

---

Electronic Thesis and Dissertation Repository

---

1-19-2015 12:00 AM

## Gamma-Radiation Induced Redox Reactions and Colloidal Formation of Chromium and Cobalt Oxide Nanoparticles

Leena M. Alrehaily  
*The University of Western Ontario*

Supervisor  
J.C.Wren  
*The University of Western Ontario*

Graduate Program in Chemistry  
A thesis submitted in partial fulfillment of the requirements for the degree in Doctor of Philosophy  
© Leena M. Alrehaily 2015

Follow this and additional works at: <https://ir.lib.uwo.ca/etd>

 Part of the [Materials Chemistry Commons](#), and the [Physical Chemistry Commons](#)

---

### Recommended Citation

Alrehaily, Leena M., "Gamma-Radiation Induced Redox Reactions and Colloidal Formation of Chromium and Cobalt Oxide Nanoparticles" (2015). *Electronic Thesis and Dissertation Repository*. 2673.  
<https://ir.lib.uwo.ca/etd/2673>

This Dissertation/Thesis is brought to you for free and open access by Scholarship@Western. It has been accepted for inclusion in Electronic Thesis and Dissertation Repository by an authorized administrator of Scholarship@Western. For more information, please contact [wlsadmin@uwo.ca](mailto:wlsadmin@uwo.ca).

**GAMMA-RADIATION INDUCED REDOX REACTIONS AND  
COLLOIDAL FORMATION OF CHROMIUM AND COBALT  
OXIDE NANOPARTICLES**

(Thesis format: Integrated Article)

by

Leena M. Alrehaily

Graduate Program in Chemistry

A thesis submitted in partial fulfillment  
of the requirements for the degree of  
Doctor of Philosophy

The School of Graduate and Postdoctoral Studies  
The University of Western Ontario  
London, Ontario, Canada

© Leena M. Alrehaily 2015

## Abstract

The main goal of this thesis research is to develop a mechanistic understanding of radiation-induced chromium oxide and cobalt oxide nanoparticle formation in aqueous solutions containing initially dissolved metal ions. When exposed to ionizing radiation, water decomposes to form a range of chemically reactive radical and molecular products. These redox agents can readily change the oxidation state of dissolved metal ions. The solubility of a transition metal ion can vary by several orders of magnitude depending on its oxidation state and the solution pH. Thus, reactions that can alter the oxidation state of a dissolved ion can lead to the condensation of insoluble species and the formation of solid particles.

The formation of  $\text{Co}_3\text{O}_4$  nano-scale colloid particles by gamma irradiation of  $\text{CoSO}_4$  solutions was investigated as a function of pH, initial  $\text{Co}^{\text{II}}$  concentration and radical scavenger environment. Particle formation was observed only in aerated solutions. Analysis of the particle formation as a function of irradiation time and information from the scavenger studies shows that the particles evolve from  $\text{Co}(\text{OH})_2$  to  $\text{CoOOH}$  and then to  $\text{Co}_3\text{O}_4$  with oxidation of  $\text{Co}^{2+}$  to  $\text{Co}^{3+}$  by  $\bullet\text{OH}$  being the most important process. Transmission electron microscopy (TEM) images show that the final particle sizes depend on the initial conditions of the solution. The formation of chromium oxide nanoparticles by gamma radiolysis of  $\text{Cr}^{\text{VI}}$  solutions was investigated as a function of pH, initial  $\text{Cr}^{\text{VI}}$  concentration and scavenger environment. The results show that  $\text{Cr}^{\text{VI}}$  is easily reduced to  $\text{Cr}^{\text{III}}$  by a homogeneous aqueous reaction with  $\bullet\text{e}_{\text{aq}}^-$ , but, due to the stability of  $\text{Cr}^{\text{III}}$  colloids, the growth of the  $\text{Cr}(\text{OH})_3$  particles is very slow. However, after

some time the  $\text{Cr}(\text{OH})_3$  is converted to  $\text{Cr}_2\text{O}_3$ . Again for this system, the sizes of the particles formed depend on the solution conditions.

Keywords:

Chromium oxide, cobalt oxide, gamma-radiolysis, scavenger, pH, nitrous oxide, t-butanol, nanoparticles, water radiolysis

## Dedication

This thesis dedicated to the persons who supported me

To the persons who encourages me to study abroad

To my father

and to my brother, Amr

For their love and compassion

May Allah be merciful to them

## Co-Authorship statement

All articles presented in this thesis were co-authored with my supervisor, Dr. J.Clara Wren. The roles of the others authores are discussed below:

Chapter 3: J. Joseph assisted with experimental measerment, M.Biesinger performed XPS analysis, D. Guzonas and J.C. Wren assisted with editing.

Chapter 4: J. Joseph assisted with experimental measerment, A.Y. Musa assisted with DFT calculation, M. Biesinger performed XPS analysis, D. Guzonas and J.C. Wren assisted with editing.

Chapter 5: J. Joseph assisted with experimental measerment, M.Biesinger performed XPS analysis and J.C. Wren assisted with writing and editing.

Chapter 6: J. Joseph assisted with experimental measerment, M.Biesinger performed XPS analysis and J.C. Wren assisted with writing and editing.

## Acknowledgments

First and foremost, praise and gratitude be to ALLAH, the Almighty, who has blessed me and given me the strength and patience to complete my study.

I owe much gratitude and sincere to my supervisor Prof. Clara Wren for giving me this unique opportunity to work in her group and for her generous support, encouragement, suggestions, patience and assistance.

I would like to acknowledge Saudi Arabia and Saudi bureau for granting and providing the scholarship for my PhD program at Western University.

Special thanks are extended to Dr. Jiju Joseph for her constructive comments, helpful suggestions, and excellent support in many aspects of this research.

My thanks go to my colleagues and friends at UWO. Special thanks go to Dr. Veena Subramanian, Dr. Sriya Peiris and Dr. Ahmed Musa for their assistance and cooperation during my work. Special thanks go to Dr. Dave Wren for his support during the writing process.

I am obliged to offer my indebtedness and sincere appreciation to my mother, sisters (Mahasen and Ebtessam) and brothers (Bsam and Zuhair). With their support, love and encouragement this work is a success. Lastly, but by no means the least, my lovely husband, Mowffaq, for his Love, support, patient and advice and my sweet girls, Tala and Jana, for their encouraging smiles and warm hugs every day.

## Table of Contents

Abstract .....	ii
Dedication .....	iv
Co-Authorship Statement .....	v
Acknowledgements .....	vi
Table of Contents .....	vii
Symbols and Acronyms .....	xiii
List of Tables .....	xiv
List of Figures .....	xv
List of Appendices .....	xxi
<b>Chapter 1. Introduction.....</b>	<b>1</b>
1.1 THESIS OBJECTIVE, METHODS and OUTLINE .....	1
1.2 MATERIALS BACKGROUND .....	10
1.2.1 Forced hydrolysis method for the synthesis of metal nanoparticles....	10
1.2.2 Radiation-induced nanoparticle formation .....	12
1.2.3 Cobalt and Chromium Oxides .....	15
1.2.3.1 Cobalt oxide (Co <sub>3</sub> O <sub>4</sub> ).....	15
1.2.3.2 Chromium oxide .....	17
1.3 RADIATION CHEMISTRY .....	19
1.3.1 Ionizing radiation and its interaction with matter .....	20



1.3.2 Radiolysis process .....	20
1.3.3 Water radiolysis: process, species and G-value.....	22
1.4 RADIOLYSIS OF PURE WATER WITHOUT ANY ADDITIVE .....	26
1.5 SCAVENGERS .....	31
1.5.1 Scavenger of •OH, t-butanol .....	31
1.5.2 Scavenger of hydrated electrons ( $\bullet e_{aq}^-$ ), Nitrous oxide, N <sub>2</sub> O .....	31
1.6 REFERENCES .....	32
<b>Chapter 2. Experimental Principle and Details .....</b>	<b>37</b>
2.1 EXPERIMENTAL TECHNIQUES .....	37
2.1.1 Gas Chromatography (GC) .....	37
2.1.2 UV-Visible Spectrophotometry .....	40
2.2.3 Raman Spectroscopy .....	41
2.2.4 Fourier Transform Infrared Spectroscopy (FTIR) .....	43
2.2.5 Transmission Electron Microscopy (TEM) .....	44
2.2.6 X-ray Photonelectron Spectroscopy (XPS) .....	45
2.2 EXPERIMENTAL PROCEDURES .....	47
2.2.1 Solution preparation .....	47
2.2.2 Irradiation procedure .....	48
2.2.3 Sample analysis .....	49



3.3.4 Reaction of H <sub>2</sub> O <sub>2</sub> with Co <sup>II</sup> under un-irradiated condition.....	86
3.3.5 Kinetic behaviour of radiolysis product H <sub>2</sub> O <sub>2</sub> and H <sub>2</sub> .....	87
3.4 MECHANISM OF RADIOLYTIC PRODUCTION OF Co <sub>3</sub> O <sub>4</sub> NANOPARTICLES.....	89
3.4.1 Mechanism for Co <sub>3</sub> O <sub>4</sub> nanoparticles formation.....	89
3.4.2 Comparison of the mechanism for cobalt and iron system .....	91
3.5 CONCLUSION .....	92
3.6 REFERENCES .....	93

#### **Chapter 4. Gamma-Radiation Induced Formation of Chromium Oxide**

<b>Nanoparticles from Dissolved Dichromate .....</b>	<b>96</b>
4.1 INTRODUCTION .....	96
4.2 EXPERIMENTAL .....	99
4.3 RESULT AND DISCUSSION .....	102
4.3.1 Experimental observations .....	102
4.3.2 Kinetic analysis.....	114
4.3.3 Particle growth mechanism .....	122
4.4 CONCLUSION .....	123
4.5 REFERENCES .....	124

**Chapter 5. Radiation-Induced Cobalt-Oxide Nanoparticle Formation: Kinetics of Particle Size Control .....128**

5.1 INTRODUCTION .....	128
5.2 EXPERIMENTAL .....	131
5.3 RESULT .....	133
5.3.1 Effect of Scavenger on the Type, Shape and Size of Nanoparticles .	133
5.3.2 Effect of Scavenger on the Kinetics of Radiolysis conversion of $\text{Co}^{\text{II}}$ to $\text{Co}^{\text{III}}$ .....	136
5.4 DISCUSSION .....	142
5.4.1 Radiolytic production of oxidants and reductants .....	142
5.4.2 Thermal conversion and equilibrium of cobalt species .....	143
5.4.3 Radiation-induced cobalt oxide nanoparticles formation .....	145
5.5 CONCLUSION .....	153
5.6 REFERENCES .....	154

**Chapter 6. Radiation-Induced Formation of Chromium-Oxide Nanoparticles: Role of Radical Scavengers on the Redox Kinetics and Particle Size.....157**

6.1 INTRODUCTION .....	157
6.2 EXPERIMENTAL .....	160
6.3 RESULT .....	162
6.3.1 Effect of Scavenger on the Type, Shape and Size of Nanoparticles .	162

6.3.2 Effect of Scavenger on Cr <sup>VI</sup> (aq) to Cr <sup>III</sup> particles conversion.....	170
6.4 DISCUSSION .....	177
6.5 CONCLUSION .....	185
6.6 REFERENCES .....	186
<b>Chapter 7. Summary and Future work .....</b>	<b>190</b>
7.1 Summary .....	190
7.2 Future Work .....	194
<b>Appendix A. ....</b>	<b>196</b>
<b>Curriculum Vitae .....</b>	<b>214</b>

## Symbols and Acronyms

### Symbols

A	Absorbance
C	Concentration of sample
$D_R$	Gamma radiation dose rate
$E_k$	Kinetic energy
$E_B$	Binding energy
$\Delta E_{\text{vibration}}$	Energy gap between the vibrational levels
h	Planck's constant
$I_0$	Light intensity of the incident radiation
I	Light intensity of transmitted radiation
l	Path length of the measuring cell
$\rho$	Resolution
$\nu'$	Scattered light frequency
$\nu''$	Excitation light frequency
$\nu$	Frequency
$\lambda$	Wavelength
$\alpha$	Maximum angle between the incident and deflected beam
$\epsilon$	Extinction coefficient of sample under study
$\phi$	Work function

### Acronyms

FTIR	Fourier Transform Infrared spectroscopy
GC	Gas Chromatography
LET	Linear Energy Transfer
TEM	Transmission Electron Microscope
TCD	Thermal conductivity detector
UV-Vis	Ultraviolet and visible absorption spectroscopy
XPS	X-ray photon spectroscopy

## List of Tables

<b>Table 4.1:</b> Size ranges of the chromium oxide nanoparticles determined from TEM images.....	108
<b>Table 5.1:</b> Test solutions studied.....	134
<b>Table 6.1:</b> Test solutions studied.....	163

## List of Figures

<b>Figure 1.1:</b> Schematic of a CANDU nuclear reactor [1].....	2
<b>Figure 1.2:</b> Schematic of the redox potential of radiolysis products and their reactions to make condensable material [4,5].....	6
<b>Figure 1.3 :</b> $\gamma$ -FeOOH nanoparticles formed by forced hydrolysis and by radiolytic oxidation, reproduced from [6] and [7] with permission of The Royal Society of Chemistry.....	8
<b>Figure 1.4:</b> Unit cell (on the left) and primitive cell (on the right) of $\text{Co}_3\text{O}_4$ . Light cyan and navy blue spheres indicate $\text{Co}^{2+}$ and $\text{Co}^{3+}$ ions, red ones indicate $\text{O}^{2-}$ ions [50].....	16
<b>Figure 1.5:</b> Crystal structure of $\text{Cr}_2\text{O}_3$ with (a) the rhombohedral primitive cell and (b) the hexagonal structure. The $\text{Cr}^{\text{III}}$ ions are grey while the $\text{O}^{2-}$ ions are red (adopted from reference [9]).....	18
<b>Figure 1.6:</b> Schematic of a radiation track resulting from a $\gamma$ -photon [3].....	22
<b>Figure 1.7:</b> Schematics of the initial reactions that occur in water following absorption of ionizing radiation. The species in the green bar are designated the primary radiolysis products [60].....	24
<b>Figure 1.8:</b> Schematic representation of continuous gamma-radiolysis kinetics.....	25
<b>Figure 1.9:</b> The radiolytic production of $\text{H}_2$ (a) and $\text{H}_2\text{O}_2$ (b) in deaerated water case at different pHs as a function of irradiation time. (Figure reproduced from reference [61]).....	30
<b>Figure 2.1:</b> Schematic of Gas Chromatography system (GC-MS, 6580 Agilent Technologies) used in this work.....	38



<b>Figure 2.2:</b> Chromatogram showing the H <sub>2</sub> peak eluting at a retention time of 2.66 min determined with a GS-GASPRO column and using N <sub>2</sub> as the carrier gas at a flow rate of 4.6 ml/min.....	39
<b>Figure 2.3:</b> Illustration showing Rayleigh scattering, Stokes scattering and anti-Stokes scattering.....	42
<b>Figure 2.4:</b> Schematic representation of a single photon/electron ejection process.....	46
<b>Figure 2.5:</b> The sample vials with the custom designed sample holder for the gamma cell experiment.....	48
<b>Figure 2.6:</b> Calibration curve for H <sub>2</sub> O <sub>2</sub> using Ghormley tri-iodide method.....	51
<b>Figure 3.1:</b> Calibration curve obtained for [Co <sup>II</sup> ] using the method used in the study.....	63
<b>Figure 3.2:</b> Photographs of irradiated aerated solutions initially containing 0.3 mM CoSO <sub>4</sub> at pH 10.6.....	65
<b>Figure 3.3:</b> UV-Vis spectra of irradiated aerated solutions initially containing 0.3 mM CoSO <sub>4</sub> at pH 10.6: (a) raw spectra and (b) empty-cell background-subtracted spectra. The reference spectrum of Co <sub>3</sub> O <sub>4</sub> is shown as the dashed curve.....	66
<b>Figure 3.4:</b> Concentration of Co <sup>III</sup> (sol) as a function of irradiation time for aerated (squares) and deaerated (circles) solutions initially containing 0.3 mM Co <sup>II</sup> (sol) at pH 10.6. The concentrations were determined by the PAR method (solid symbols) and UV-Vis absorbance (open symbols).....	68
<b>Figure 3.5:</b> (a) Concentrations of Co <sup>II</sup> (sol) and Co <sup>III</sup> (sol) as a function of irradiation time. (b) The Δ[Co <sup>II</sup> (sol)] and [Co <sup>III</sup> (sol)] in the irradiated solutions initially containing 0.3 mM Co <sup>II</sup> (sol) under air-saturated pH 10.6 conditions.....	70
<b>Figure 3.6:</b> TEM images of the particles collected at different irradiation times from aerated solutions initially containing 0.3 mM Co <sup>II</sup> (sol) at pH 10.6.....	72

- Figure 3.7:** High resolution XPS spectra of the (a) O 1s, (b) C 1s, and (c) Co 2p bands obtained from particles collected after 5-min of irradiation of a deaerated solution initially containing 0.3 mM  $\text{Co}^{\text{II}}(\text{sol})$  at pH 10.6. Deconvoluted reference spectra and the composite spectra are also shown.....74
- Figure 3.8:** Composition determined by XPS of particles collected as a function of irradiation time from aerated solutions initially containing 0.3 mM  $\text{Co}^{\text{II}}(\text{sol})$  at pH 10.6.....76
- Figure 3.9:** (a) Raman spectra of particles collected as a function of irradiation time from aerated solutions initially containing 0.3 mM  $\text{Co}^{\text{II}}(\text{sol})$  at pH 10.6. (b) Raman spectra of particles prepared from several pure cobalt oxides.....77
- Figure 3.10:** Concentrations of (a)  $[\text{Co}^{\text{II}}(\text{sol})]$ , (b)  $[\text{H}_2\text{O}_2]$  and (c)  $[\text{H}_2]$  as a function of irradiation time at pHs 6.0 and 10.6 aerated solutions initially containing 0.3 mM  $\text{Co}^{\text{II}}(\text{sol})$ . The  $[\text{H}_2\text{O}_2]$  and  $[\text{H}_2]$  as a function of irradiation time in pure water are also shown for comparison.....80
- Figure 3.11:** Overall solubility of  $\text{Co}^{\text{II}}$  hydroxide as a function of pH and the concentrations of the contributing hydroxide species.....83
- Figure 3.12:** Schematic of the mechanism proposed for radiation-induced cobalt oxide colloid formation.....90
- Figure 4.1:** Photographs of argon-purged solutions initially containing 0.1 mM  $\text{Cr}^{\text{VI}}$  at pH 8.5 that were irradiated for different durations, and UV- Vis spectra showing the decrease in the intensity of the absorbance peak of  $\text{Cr}^{\text{VI}}$  over the same time period.....103
- Figure 4.2:** The decrease in the height of the UV-Vis absorption peak at 370 nm and the decrease in  $[\text{Cr}^{\text{VI}}]$  as a function of irradiation time for deaerated solutions initially containing 0.1 mM  $\text{Cr}^{\text{VI}}$  at pH 8.5.....104
- Figure 4.3:** The concentrations of  $\text{Cr}^{\text{VI}}$  (a),  $\text{Cr}^{\text{III}}$  (b) and  $\text{H}_2$  (c) measured as a function of irradiation time at pHs 6.0 (■), 8.5 (▲) and 10.6 (●) for solutions initially

containing  $[\text{Cr}^{\text{VI}}]$  of 0.1 mM (solid symbols), 0.3 mM (half filled symbols) and 0.5 mM (open symbols) lines to indicate the stages.....106

**Figure 4.4:** TEM images of chromium oxide nanoparticles formed after 300 min irradiation for (a) 0.1 mM  $[\text{Cr}^{\text{VI}}]_0$ , (b) 0.5 mM  $[\text{Cr}^{\text{VI}}]_0$  and (c) 10 mM  $[\text{Cr}^{\text{VI}}]_0$ .....110

**Figure 4.5:** (a) Photographs before and after irradiation of an Ar-purged 10 mM  $\text{Cr}^{\text{VI}}$  solution at pH 8.5 and (b) Raman spectrum of unwashed chromium oxide nanoparticles formed in the irradiated solution. The reference spectra of  $\text{CrO}_4^{2-}$  dissolved in solution and  $\text{Cr}_2\text{O}_3$  powder are also shown.....111

**Figure 4.6:** The FTIR spectrum and TEM image of chromium oxide nanoparticles after washing (a) prior to and (b) after heating. Also included are spectra for  $\text{Cr}_2\text{O}_3$  and  $\text{Cr}(\text{OH})_3$  for comparison.....112

**Figure 4.7:** XPS spectra of washed chromium oxide nanoparticles showing the fit to the different components of the particles (a) with no heating and (b) with heating.....113

**Figure 4.8:** Schematic representation of the proposed mechanism for the radiolytic formation of chromium oxide nanoparticles under steady state radiolysis.....121

**Figure 5.1:** TEM images of cobalt oxide nanoparticles formed in 0.1 mM  $\text{CoSO}_4$  solutions (5 h irradiation) in different scavenging environments: (a) aerated only, (b) aerated and 0.1 M *t*-butanol, and (c)  $\text{N}_2\text{O}/\text{Ar}$  purged.....135

**Figure 5.2:** (a) Raman spectra of the particles collected after 5 h irradiation of 0.1 mM  $\text{CoSO}_4$  solutions at pH 10.6 in different scavenging environments (shifted vertically for presentation) and (b) Raman spectra of standard cobalt oxides/hydroxides.....135

- Figure 5.3:** Concentrations of  $\text{Co}^{\text{II}}$  (solid symbols) and  $\text{Co}^{\text{III}}$  (open symbols) as a function of irradiation time for 0.1 mM  $\text{CoSO}_4$  solutions at pH 10.6 in different scavenging environments: aerated only ( $\blacktriangle$  &  $\triangle$ ), aerated and 0.1 M *t*-butanol ( $\blacksquare$  &  $\square$ ), and purged with  $\text{N}_2\text{O}/\text{Ar}$  ( $\bullet$  &  $\circ$ ).....136
- Figure 5.4:** Concentrations of  $\text{Co}^{\text{II}}$  (solid symbols) and  $\text{Co}^{\text{III}}$  (open symbols) as a function of irradiation time observed for 0.1 mM  $\text{CoSO}_4$  solutions at pH 10.6 in different scavenging environments: aerated only ( $\blacktriangle$  &  $\triangle$ ), deaerated only ( $\blacktriangledown$  &  $\triangledown$ ), deaerated and 0.1 M *t*-butanol ( $\blacksquare$ ), and purged with  $\text{N}_2\text{O}/\text{Ar}$  ( $\bullet$  &  $\circ$ ).....139
- Figure 5.5:** Composition determined by XPS of particles collected as a function of irradiation time from aerated solutions initially containing 0.3 mM  $\text{Co}^{\text{II}}$  at pH 10.6. The corresponding TEM images of the particles formed at different times are shown on top. These figures are adopted from Alrehaily et al [20].....140
- Figure 5.6:** Concentrations of  $\text{Co}^{\text{II}}$  (solid symbols) and  $\text{Co}^{\text{III}}$  (open symbols) as a function of irradiation time in aerated solutions containing 0.1 mM (red) and 0.3 mM (black)  $\text{CoSO}_4$  at pH 10.6.....141
- Figure 5.7:** Schematic of a mechanism for radiation-induced cobalt oxide colloid formation.....146
- Figure 6.1:** TEM images of chromium oxide nanoparticles formed by irradiation (5 h) of 0.1 mM  $\text{K}_2\text{Cr}_2\text{O}_7$  solution at pH 6.0 in solutions with different scavengers: (a) none, (b) 0.1 M *t*-butanol, and (c)  $\text{O}_2$  + 0.1 M *t*-butanol.....164
- Figure 6.2:** TEM images of chromium oxide nanoparticles formed in 0.1 mM  $\text{K}_2\text{Cr}_2\text{O}_7$  solutions with deaerated and 0.1 M *t*-butanol added as a function of irradiation time: (a) 20 min, (b) 60 min and (c) 300 min.....165
- Figure 6.3:** TEM images of (a) unwashed particles, (b) washed particles, and (c) washed and heated particles.....166

- Figure 6.4:** FTIR spectra of (a) the nanoparticles formed in the solutions with 0.1 M butanol followed by different post-radiolysis treatments, unwashed (black line), washed (blue line) and washed and heated (red line); and (b) the reference spectra of the  $\text{Cr}_2\text{O}_3$ ,  $\text{Cr}(\text{OH})_3$  and  $\text{K}_2\text{Cr}_2\text{O}_7$  powders.....167
- Figure 6.5:** High resolution XPS Cr-2p spectra of (a) the washed particles and (b) the washed and heated particles, and (c) the relative contributions of  $\text{Cr}^{\text{VI}}$ ,  $\text{Cr}(\text{OH})_3$  and  $\text{Cr}_2\text{O}_3$  to the Cr-2p band intensity obtained for the particles. The deconvoluted peaks of the individual components are also shown and the composite spectra are compared with the actual spectra in (a) and (b).....169
- Figure 6.6:** Concentrations of  $\text{Cr}^{\text{VI}}(\text{aq})$  (solid symbols) and  $\text{Cr}^{\text{III}}$  (open symbols) observed as a function of time during radiolysis of deaerated solutions initially containing 0.1 M  $\text{CrO}_4^{2-}$  at pH 6.0. Three different sets of data are presented on two different time scales.....171
- Figure 6.7:** Concentrations of  $\text{Cr}^{\text{VI}}(\text{aq})$  (solid symbols) and  $\text{Cr}^{\text{III}}$  (open symbols) observed as a function of time during radiolysis of 0.1 mM  $\text{K}_2\text{Cr}_2\text{O}_7$  solutions at pH 6.0 in solutions containing only one-type of scavenger: none ( $\blacktriangle$ ,  $\triangle$ ); 0.1 M *t*-butanol ( $\blacksquare$ ,  $\square$ );  $\text{O}_2$  ( $\blacklozenge$ ) and  $\text{N}_2\text{O}$  ( $\blackstar$ ). The data are presented on two different time scales.....174
- Figure 6.8:** Concentrations of  $\text{Cr}^{\text{VI}}(\text{aq})$  (solid symbols) and  $\text{Cr}^{\text{III}}$  (open symbols) observed as a function of time during radiolysis of 0.1 mM  $\text{K}_2\text{Cr}_2\text{O}_7$  solutions with different scavengers: none ( $\blacktriangle$ ,  $\triangle$ ); 0.1 M *t*-butanol ( $\blacksquare$ ,  $\square$ ); and  $\text{O}_2$  + 0.1 M *t*-butanol ( $\bullet$ ,  $\circ$ ). The two sets of graphs present the data on two different time scales.....177
- Figure 6.9:** Schematic of a mechanism for radiation-induced chromium oxide nanoparticle formation.....184

## List of Appendices

Appendices A: copyrights

# Chapter 1

## Introduction

### 1.1 THESIS OBJECTIVE, METHODS and OUTLINE

The main goal of this thesis research is to develop a mechanistic understanding of radiation-induced chromium oxide and cobalt oxide nanoparticle formation in aqueous solutions containing initially dissolved metal ions. The application of the research is to provide a technical basis that can be used in assessments of corrosion products and activity transport in a nuclear reactor coolant circuit. The understanding gained through this research can be also used to tailor the size of nanoparticles and optimize radiation-induced nanoparticle synthesis.

Nuclear power provides a large fraction of the electricity needed to meet the energy requirements of Canada and many other industrialized countries. While there is substantial growth in alternative sources of energy supply, nuclear energy remains one of the few proven technologies that can supply the very large quantities of base-load electricity needed by industrialized countries. This is particularly important in the province of Ontario where nuclear power already supplies 50% of the electrical energy consumed and presents a real alternative for replacement of fossil fuel electrical generating plants that release large quantities of greenhouse gases. Sustained operation of nuclear power plants is expected to be a part of any balanced energy supply strategy.

One of the key issues in the public acceptance of continued nuclear power production is the safe operation of reactors over an extended lifetime. One of the major

issues for nuclear power plants arises from corrosion products and activity transport in the reactor coolant circuit. Figure 1.1 shows a schematic of a CANDU<sup>®</sup> reactor.

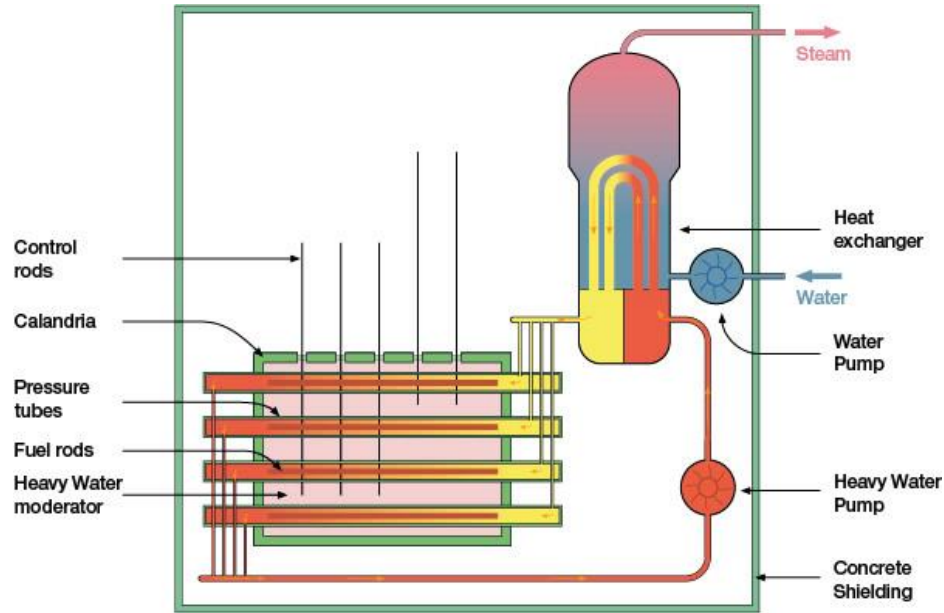


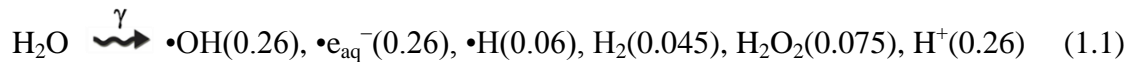
**Figure 1.1:** Schematic of a CANDU nuclear reactor [1].

The materials that are in contact with coolant include steel, nickel and cobalt alloys. Corrosion of coolant circuit materials releases dissolved metal ions (such as  $\text{Fe}^{3+}$ ,  $\text{Co}^{3+}$ ,  $\text{Cr}^{6+}$ , etc.) into the coolant. These elements can exist either as dissolved ions or as suspended particulates. In the circuit the reactor coolant is subjected to a high radiation field and a temperature gradient. Since the solubility of metal species depends strongly on temperature, the concentration of dissolved metal ions in the coolant can exceed its solubility limit as the coolant passes through a lower temperature region. This can lead to the precipitation or co-precipitation of these corrosion products on the walls of the coolant circuit piping.



The corrosion products can also deposit on the fuel cladding or other in-core surfaces (e.g., the pressure tubes of a CANDU reactor). In the reactor core, the corrosion products can be neutron activated to form hazardous radionuclides, which, if re-released into the coolant at later times, can be transported and deposit outside the biological shield of the reactor core where they pose a radiological hazard to the reactor maintenance workers [2]. On-line coolant purification systems (typically consisting of ion exchange and filtration) are used to control the concentrations of dissolved ions and particles in these systems, but the efficacy of filters depends on the sizes of the particles that are present; they are often not effective for removing colloids (particles with sizes less than 0.1  $\mu\text{m}$ ).

In addition to a temperature gradient, the coolant is exposed to a high flux of ionizing radiation. Exposed to ionizing radiation, water decomposes into a range of oxidizing ( $\text{O}_2$ ,  $\bullet\text{OH}$ ,  $\text{HO}_2\bullet$ ,  $\text{H}_2\text{O}_2$ ) to reducing ( $\bullet\text{e}_{\text{aq}}^-$ ,  $\bullet\text{O}_2^-$ ,  $\bullet\text{H}$ ) species [3]. For  $\gamma$ -radiolysis at room temperature, the primary radiolysis products (formed within  $\sim 100$  ns following the absorption of radiation energy) and their yields per absorbed radiation energy at 25  $^\circ\text{C}$  (in brackets in units of  $\mu\text{mol}\cdot\text{J}^{-1}$ ) are [3]:



As these primary radiolysis products are produced they react with one another, water molecules and, if present, any solutes such as corrosion products, and additional reactive (secondary) species such as  $\text{O}_2$ ,  $\bullet\text{O}_2^-$  and  $\bullet\text{O}_3^-$ , can be formed. Although slower than the primary radiolysis process, the aqueous phase reactions of the radiolytically-produced radicals and ions are still fast for chemical reactions. The speciation of water radiolysis

products changes rapidly, following an initial interaction of the radiation particle (or photon) with the water molecules.

In the presence of a constant radiation source, water decomposition products are continuously produced at a constant rate. However, as the concentrations of the radiolysis products increase the reaction rates of the radiolysis products increase, eventually matching their radiolytic production rates. Thus, the aqueous chemical system under continuous irradiation reaches a pseudo-steady state on a time scale on the order of milliseconds. It then more slowly reaches an actual steady state over a longer period of time which is controlled by slow processes such as surface reactions and interfacial transport. It is the pseudo steady-state aqueous concentrations of the radiolytically-produced species that control corrosion and colloid formation since these processes involve solid state reactions and are typically slower than the homogeneous aqueous reactions.

Colloid formation from dissolved corrosion products in the reactor coolant has an additional impact on the coolant chemistry that controls corrosion. Since corrosion products are often transition metal ions that can exist in different oxidation states, they can interact catalytically with water radiolysis products. The solubility of a transition metal ion can vary by several orders of magnitude depending on pH and the oxidation state of the ion. Thus, reactions that can alter this oxidation state are important in controlling the concentrations of metal ions in solution and their condensation to form solid particles.

In addition to its importance to nuclear reactor safety, gamma radiation-induced nanoparticle synthesis has attracted attention due to its unique features. Radiation-

induced nanoparticle formation is better, compared to conventional methods of nanoparticle formation, in controlling the size, structure, and purity of nanoparticles. The formation of metallic nanoparticles using ionizing radiation has been reported by several groups. These studies have focused mainly on synthesis of noble metal nanoparticles by utilizing the strong reducing power of radiolytically-produced  $\bullet e_{aq}^-$  (or  $\bullet H$ ) (which have the standard redox potentials of  $E^0(H_2O/\bullet e_{aq}^-) = -2.87 V_{NHE}$  and  $E^0(H^+/\bullet H) = -2.3 V_{NHE}$ , respectively) to reduce the metal ions to a zero-valence state. Scavengers are used in these syntheses to remove hydroxyl radicals (a powerful oxidizing agent,  $E^0(\bullet OH/H_2O) = + 2.8 V_{NHE}$ ) to prevent the back oxidation of the metal atom [3].

In a nuclear reactor environment radiation is not present as short-term pulses, but rather as a continuous steady-state radiation field. Under this condition both the oxidizing and reducing water radiolysis products co-exist and cannot be manipulated by the addition of selected radical scavengers. Therefore, the mechanism of nanoparticle formation by a continuous radiation source without the scavenging of any oxidizing or reducing species power will be entirely different.

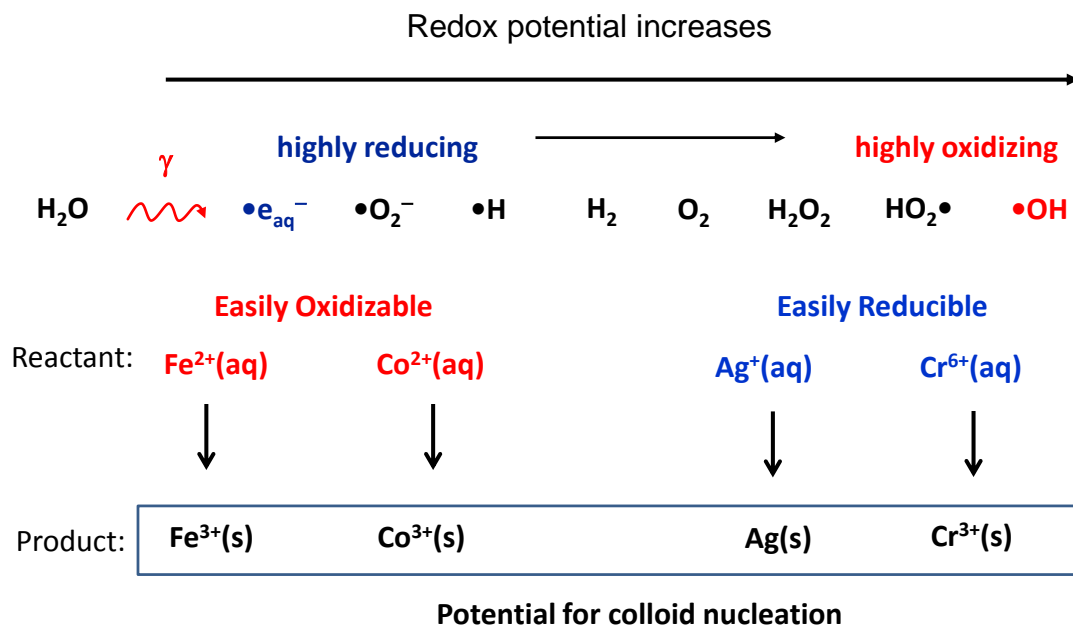


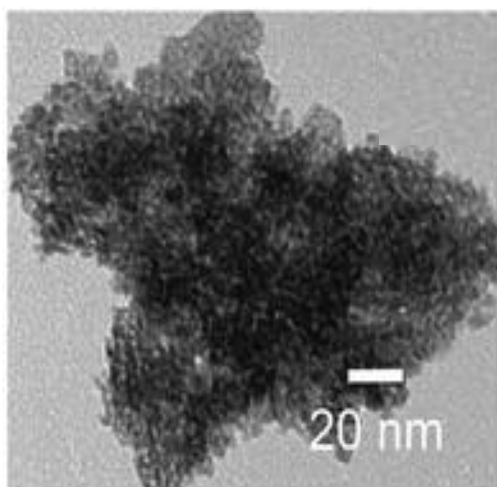
**Figure 1.2:** Schematic of the redox potential of radiolysis products and their reactions to make condensable material [4,5].

Under continuous radiation both reducing as well as oxidizing species are generated. Depending on the standard reduction potential of the metal ion redox pair dissolved metal ions can be oxidized (by any species whose redox potentials lie higher than that of the metal ion redox pair), or reduced (by any species whose redox potentials lie lower than that of the metal ion redox pair). For example, the redox potential of  $\text{Fe}^{2+}/\text{Fe}^{3+}$  is  $0.77 \text{ V}_{\text{NHE}}$  and the soluble  $\text{Fe}^{2+}$  can therefore be easily oxidized to insoluble  $\text{Fe}^{3+}$  by any species the powerful oxidizing agent  $\bullet\text{OH}$  as well as by less powerful oxidizing agent  $\text{H}_2\text{O}_2$  ( $E^0(\text{H}_2\text{O}_2 + 2\text{H}^+)/2 \text{H}_2\text{O}) = 1.763 \text{ V}_{\text{NHE}}$ ). For cobalt the redox potential of  $\text{Co}^{2+}/\text{Co}^{3+}$  is  $1.81 \text{ V}_{\text{NHE}}$  and therefore radiolytic oxidation of dissolved  $\text{Co}^{2+}$  to less soluble  $\text{Co}^{3+}$  oxides/hydroxides requires the more powerful oxidizing agent  $\bullet\text{OH}$ . On the other hand, the soluble  $\text{Cr}^{\text{VI}}$  ( $E^0(\text{Cr}^{3+}/\text{Cr}_2\text{O}_7^{2-}) = 1.33 \text{ V}_{\text{NHE}}$ ) is easily reduced to

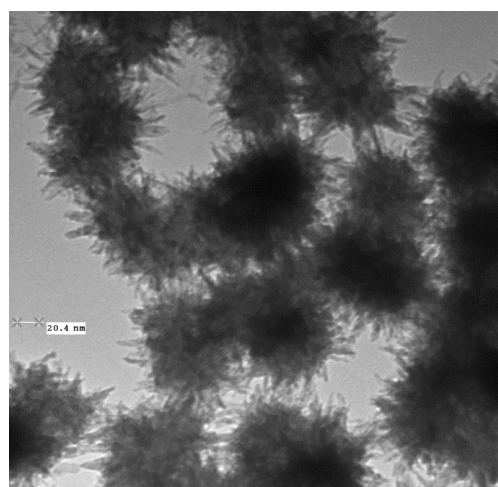
insoluble  $\text{Cr}^{\text{III}}$  by  $\bullet\text{e}_{\text{aq}}^-$  or  $\bullet\text{O}_2^-$  ( $E^0(\text{O}_2/\bullet\text{O}_2^-) = -0.33 \text{ V}_{\text{NHE}}$ ) while soluble  $\text{Ag}^+$  is reduced to insoluble Ag by  $\bullet\text{e}_{\text{aq}}^-$  and less effectively by  $\bullet\text{O}_2^-$ , Figure 1.2 [4,5]. If the solubility of metal ion varies considerably depending on its oxidation state, the insoluble redox products can quickly condense and provide nucleation sites onto which soluble metal ions continuously adsorb and undergo redox reaction, growing a solid particle phase.

The formation of iron oxide nanoparticles has been previously studied [6]. In this system the oxidizing power of the hydroxyl radical is mainly utilized for the nanoparticle formation. Uniform-sized colloidal particles of  $\gamma\text{-FeOOH}$  can be formed from the oxidation of dissolved  $\text{Fe}^{\text{II}}$  by radiolytically-produced  $\bullet\text{OH}$  or  $\text{H}_2\text{O}_2$  [6]. This occurs by rapid radiolytic oxidation of dissolved  $\text{Fe}^{\text{II}}$  to less soluble  $\text{Fe}^{\text{III}}$  hydroxides, leading to particle nucleation via spontaneous condensation. This promotes the adsorption of ferrous ions on the nucleates. Radiolytically-induced electrochemical oxidation of these nucleates leads to the growth of  $\gamma\text{-FeOOH}$  (lepidocrocite) in a dendritic structure whose final size is regulated. The  $\gamma\text{-FeOOH}$  nanoparticles formed by forced hydrolysis and by  $\gamma$ -radiation are compared in Figure 1.3. This figure illustrates that the different synthesis methods can affect the size, shape and morphology of the particles that are formed. This thesis work extends studies on radiolytic particle formation to other transition metal ions, cobalt and chromium.

## $\gamma$ -FeOOH nanoparticles



Forced hydrolysis



Radiolytic oxidation

**Figure 1.3 :**  $\gamma$ -FeOOH nanoparticles formed by forced hydrolysis and by radiolytic oxidation, reproduced from [6] and [7] with permission of The Royal Society of Chemistry.

The synthesis of chromium and cobalt oxide nanoparticles has been explored by others using chemical and physical methods [8-24], but there have been no prior studies on the radiation-induced synthesis of cobalt and chromium nanoparticles. To address this void, the experimental studies have performed on the irradiation of aqueous solutions containing initially dissolved  $\text{Co}^{\text{II}}$  and/or  $\text{Cr}^{\text{VI}}$  in a gamma-irradiation cell. The reaction kinetics have been followed by measuring the concentrations of molecular water radiolysis products ( $\text{H}_2$ ,  $\text{O}_2$  and  $\text{H}_2\text{O}_2$ ) and metal ions in solution, and by characterizing the size, and chemical and phase composition of particles that are formed, as a function of irradiation time and test conditions (pH, initial concentration of dissolved metal ions, and addition of scavengers (dissolved  $\text{O}_2$ ,  $\text{N}_2\text{O}$  and t-butanol)).

The remainder of this chapter provides further background on water radiolysis chemistry, and Co and Cr nanoparticle chemistry. The experimental design and analysis

techniques employed in the thesis study are documented in Chapter 2. The experimental findings are presented and discussed in a series of chapters as follows.

- Chapter 3. The effects of pH, dissolved O<sub>2</sub> and the initial concentration of dissolved Co<sup>II</sup> on the formation of cobalt oxide nanoparticles and the behaviour of water radiolysis products are investigated. A mechanism for radiation-induced Co<sub>3</sub>O<sub>4</sub> nanoparticle formation and growth is proposed.
- Chapter 4. The effects of pH, dissolved O<sub>2</sub> and the initial concentration of dissolved Cr<sup>VI</sup> on the formation of chromium oxide nanoparticles are investigated. A mechanism for the radiation-induced Cr<sub>2</sub>O<sub>3</sub> nanoparticle formation and growth is proposed.
- Chapter 5. The radiolytic formation of Co<sub>3</sub>O<sub>4</sub> nanoparticles was investigated using the radical scavengers, *t*-butanol, nitrous oxide and dissolved oxygen. A mechanism is proposed that is consistent with the observed effects of the scavengers on the kinetics of oxidation of Co<sup>II</sup> and the sizes of the Co<sub>3</sub>O<sub>4</sub> nanoparticles that are formed.
- Chapter 6. The roles of radiolytically-produced redox agents in the formation mechanism of chromium oxide nanoparticles are investigated. This study used the radical scavengers, *t*-butanol, nitrous oxide and dissolved oxygen. A mechanism is proposed that is consistent with the observed effects of scavengers on the kinetics of reduction of Cr<sup>VI</sup> in solution to solid Cr<sup>III</sup> and the final sizes of Cr<sub>2</sub>O<sub>3</sub> nanoparticles that are formed.

The final chapter include summarize of the findings of our work and provide some ideas for future studies.

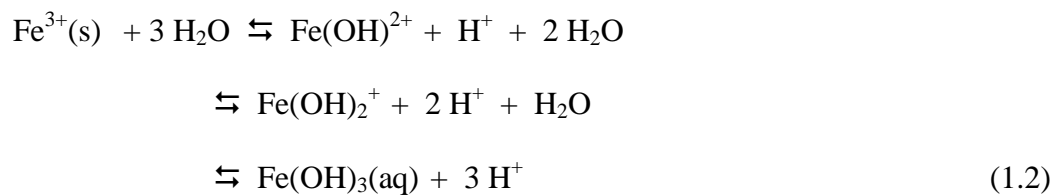
## 1.2 MATERIALS BACKGROUND

### 1.2.1 Forced hydrolysis method for the synthesis of metal nanoparticles

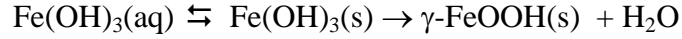
Transition metal oxide nanoparticles can be synthesized by different chemical methods that include forced hydrolysis, sol-gel synthesis, microemulsion, hydrothermal reactions, sonochemical reactions, and electrochemical methods [8-24]. The pros and cons of all of these alternative fabrication routes are not reviewing here. Instead it will briefly consider some of the work that has been done using forced hydrolysis to fabricate metal oxide nanoparticles. The Forced hydrolysis technique is chosen for review because it involves the same reaction phases (aqueous solution and solid nanoparticle phases) as those occurring in radiation-induced particle formation and hence the chemistry and physical processes to be considered in both techniques are similar. Forced hydrolysis is also considered to be the easiest way to prepare metal (hydrous) oxide nanoparticles, and gives a platform for identifying some of the significant challenges facing nanoparticle fabrication.

The forced hydrolysis technique involves the hydrolysis of a metal ion at an elevated temperature and aging of the resulting metal hydroxide gel to form particles with a narrow size distribution [25]. Polyvalent cations can be easily hydrolyzed and the deprotonation of coordinated water molecules can be achieved at elevated temperatures.

For example,







In forced hydrolysis the precipitation of the hydroxide phase is achieved by increasing the pH of the solution. Hydrolysis creates intermediates that are present prior to the precipitation of the oxide phase. The rate of formation of these intermediate complexes can be controlled by adjusting the pH and temperature to yield uniform particles [14].

Forced hydrolysis is the simplest chemical method used for the synthesis of iron oxide nanoparticles starting from  $\text{Fe}^{\text{III}}$  cations. The aging of a freshly prepared ferric solution containing NaOH or KOH has to take place at a temperature of 60-80 °C for a period of time ranging from a few days to weeks [25]. Iron oxide as spherical hematite ( $\text{Fe}_2\text{O}_3$ ) has also been prepared by forced hydrolysis of a  $\text{FeCl}_3$  and HCl solution at 100 °C with aging for 24 hours [26, 27]. In forced hydrolysis the product composition or structure is affected by small variations in conditions such as pH, concentration of the reagents, method of mixing, temperature, etc. This sensitivity of the method complicates both the reproducibility of the process and the challenges in scaling the process for industrial applications.

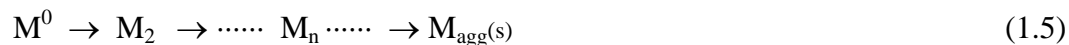
The presence of other anions besides  $\text{OH}^-$  in the solution can also affect the homogeneous precipitation of the metal ions. These anions can sometimes affect the particle morphology without being incorporated into the precipitate [28]. For example, mono-dispersed cubic cobalt oxide,  $\text{Co}_3\text{O}_4$  particles have been prepared by forced hydrolysis of Co(II)-acetate solutions at 100 °C in the presence of oxygen. However, similar particles could not be formed by using  $\text{CoSO}_4$ ,  $\text{Co(NO}_3)_2$ , or  $\text{CoCl}_2$  as precursors [28, 29].

Forced hydrolysis has been used for the preparation of colloidal particles of chromium oxides by controlled addition of KOH to a Cr<sup>III</sup> solution at elevated temperature until precipitation was achieved [26, 30]. The crystallinity of the particles was further improved by calcination at an even higher temperature [31]. Musić et al. synthesized Cr<sub>2</sub>O<sub>3</sub> using the forced hydrolysis method starting from Cr(NO<sub>3</sub>)<sub>3</sub> in a solution containing urea. In this method, the required increase in pH of the solution was achieved by the thermal decomposition of the urea and this leads to the hydrolysis of the Cr<sup>III</sup> [32]. A surfactant poly-vinyl pyrrolidone (PVP) was used in this particular case to prevent aggregation of chromium nanoparticles that were formed.

Even though forced hydrolysis is considered to be a simple technique for synthesizing nanoparticles, there are known issues with this method regarding control of particle size and purity, and prevention of agglomeration [31]. As noted above, the size and composition of the particles is affected by small variations in solution pH, concentration of the reagents, method of mixing, temperature, and adsorption of impurities.

### 1.2.2 Radiation-induced nanoparticle formation

Several groups have investigated radiation-induced nanoparticle synthesis in aqueous solutions, but most studies have been limited to noble metal nanoparticles [34-43]. These nanoparticles are prepared by the reduction of their metal salts in aqueous solution by hydrated electrons ( $\bullet e_{aq}^-$ ) and hydrogen atoms ( $\bullet H$ ) to form insoluble metallic particles ( $M^0$ ). These neutral metal atoms coalesce to form aggregates in the presence of a capping agent, such as a polymer, ligand, or surfactant. The process is given by the following reactions:



where  $n$  is the aggregation number of a growing particle and  $M_{agg}$  is the aggregate in its final size. Since radiolysis also generates oxidizing species (like  $\bullet OH$ ) the reverse oxidation by  $\bullet OH$  will compete with metal ion reduction. To create a more reducing condition specific scavengers such as the formate ion or an alcohol (like 2-propanol or t-butanol) are added to remove the  $\bullet OH$ .

The use of ionizing radiation to fabricate, in particular, metallic nanoparticles has several advantages compared to the conventional methods used for nanoparticle synthesis. Radiolysis involves the in-situ generation of the highly reducing species ( $\bullet e_{aq}^{-}$ ) homogeneously distributed throughout the reagent system with uniformity in time and space that is hard to achieve by other chemical methods.

The syntheses of some metal oxide nanoparticles by radiolysis have been reported recently [44-47]. In these studies, metal-oxide nanoparticles were still fabricated via radiolytic reduction of a metal ion from a higher oxidation state to a lower oxidation state, generally using a short-duration radiation pulse and chemical scavengers to optimize the reducing radical concentrations in solution. Under continuous steady-state irradiation conditions, the presence of these scavengers complicates the water radiolysis chemistry on longer time scales and their use can then be more challenging.

Y. Ni et al. [34] synthesized cobalt oxide nanoparticles ( $Co_3O_4$ ) via a simple reduction-oxidation route at room temperature using cobalt chloride as the reactant and sodium acetate as the basic agent. No extra reducing reagent was introduced into the

system. The mechanism of nanoparticle formation involved two steps: first, the cobalt (II) ions were reduced to cobalt atoms by  $\gamma$ -irradiation in a deaerated solution. In the second step the cobalt atoms were oxidized to cobalt oxide ( $\text{Co}_3\text{O}_4$ ) with air.

The synthesis of colloidal  $\text{Fe}_3\text{O}_4$  nanoparticles by the gamma radiolysis of a ferric chloride solution in presence of polyvinyl alcohol as a colloid stabilizer and isopropyl alcohol as an  $\bullet\text{OH}$  scavenger has been reported by Abedini et al. [39]. Again the oxide nanoparticles were prepared relying on solely the reducing power of  $\bullet\text{e}_{\text{aq}}^-$ .

I am not aware of any studies, other than those performed by Wren's research group, on the formation of uniform-sized colloidal particles of  $\gamma\text{-FeOOH}$  by the radiolytic oxidation of dissolved  $\text{Fe}^{\text{II}}$  in the absence of any stabilizer and scavenger [6]. In this work and the studies reported in this thesis, the synthesized of transition metal oxide nanoparticles from dissolved metal ions have taking advantage of either the strong reducing power of  $\bullet\text{e}_{\text{aq}}^-$  or the strong oxidizing power of  $\bullet\text{OH}$ , depending on the redox potential of the initially dissolved metal species.  $\gamma\text{-FeOOH}$  have been fabricated from  $\text{Fe}^{2+}$  [6],  $\text{Co}_3\text{O}_4$  from  $\text{Co}^{2+}$  [48], and  $\text{Cr}_2\text{O}_3$  from  $\text{Cr}_2\text{O}_7^{2-}$  [49]. This work has shown that water radiolysis products are very effective in inducing redox reactions that convert dissolved transition metal ions into less soluble species which then form metal oxide nanoparticles.

If the product of a reaction of a dissolved species with a radiolysis-generated species has a significantly different solubility from that of the reactant, then a solid product can be formed. Rapid condensation can create homogeneously distributed nucleation sites onto which the radiolysis-induced oxidation or reduction product can continue to deposit and grow the particle size. Because a very large number of nucleation

sites are generated simultaneously and homogeneously this process leads to the formation of nanoparticles with a narrow, uniform size distribution.

### 1.2.3 Cobalt and Chromium Oxides

The work of this thesis examined the radiolytic formation of cobalt and chromium oxide nanoparticles. These metal oxides are of interest due to their unique electrical, optical, magnetic and catalytic properties. Knowledge of how the particle fabrication process can be focused to control the morphology and structure of the metal oxide particles is important because all of the unique properties depend on the shape, size and chemical composition of the nanostructures. A brief overview of some of the properties and applications of metal oxide nanoparticles addressed in this thesis are provided below.

#### 1.2.3.1 Cobalt oxide ( $\text{Co}_3\text{O}_4$ )

Cobalt has two normally stable oxidation states,  $\text{Co}^{\text{II}}$  and  $\text{Co}^{\text{III}}$ . The more stable cobalt oxides are  $\text{Co}_3\text{O}_4$  and  $\text{CoO}$ , and both oxides are used in industrial application; the more important is  $\text{Co}_3\text{O}_4$ . Tricobalt tetroxide ( $\text{Co}_3\text{O}_4$ ) is a black oxide that has a normal spinel crystal structure. This structure is a cubic close-packed array in which  $\text{Co}^{\text{II}}$  ions occupy the tetrahedral sites and  $\text{Co}^{\text{III}}$  ions occupy the octahedral sites, Figure 1.4. [50]. This oxide is a p-type semiconductor [51]. It has a band gap of 1.4 to 1.8 eV and is antiferromagnetic. The spinel structure is stable up to 800°C. The mixed oxide decomposes to form cobalt (II) oxide,  $\text{CoO}$ , above 900°C.

Cobalt oxide, as  $\text{Co}_3\text{O}_4$ , is a promising candidate for application in high-power lithium ion batteries and for smart windows as a result of its electrochromic properties

[8]. Cobalt oxides have been used in many other industrial applications such as pigments and catalysts.

Cobalt oxide nanoparticles have been synthesized by many different techniques including spray pyrolysis [10], chemical vapour deposition [11], sol–gel techniques [12], pulsed laser deposition [13], thermal decomposition of solid cobalt nitrate [14] and hydrothermal synthesis [8]. These methods tend to be complex and require chemically harsh conditions and/or high processing temperatures for the synthesis of nano-scale crystalline  $\text{Co}_3\text{O}_4$  particles.

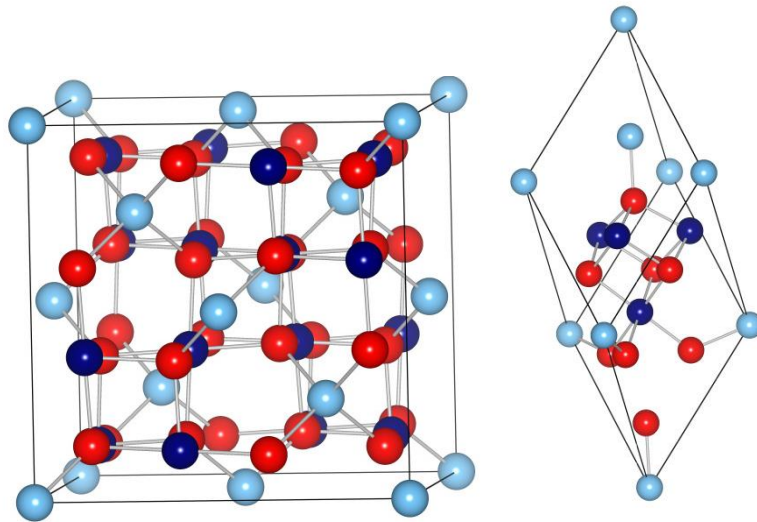


**Figure 1.4:** Unit cell (on the left) and primitive cell (on the right) of  $\text{Co}_3\text{O}_4$ . Light cyan and navy blue spheres indicate  $\text{Co}^{2+}$  and  $\text{Co}^{3+}$  ions, red ones indicate  $\text{O}^{2-}$  ions [50].

### 1.2.3.2 Chromium oxide

Chromium (III) oxide ( $\text{Cr}_2\text{O}_3$ ) is the only stable chromium oxide of interest. It adopts a corundum (rhombohedral) structure [52] that has a hexagonal close-packed array of oxygen atoms, Figure 1.5 [9]. In this structure, the metal ions occupy two thirds of the sites in the crystal lattice [9]. The band gap of  $\text{Cr}_2\text{O}_3$  is 3.3 eV [9] and this makes it an insulator. Depending on the crystal size and morphology, chromium oxide particles are used as green pigments [54], heterogeneous catalysts [55], coating materials for thermal protection [56], coatings for wear resistance [57], and electrochromic materials [58]. The high melting point of chromium oxide ( $2435^\circ\text{C}$ ) and its oxidation resistance makes this oxide an important refractory material, although its sintering properties are poor [57]. In addition to improving pigment opacity and catalytic activity, reducing the chromium oxide particle size could improve its sintering ability by decreasing the required sintering temperature and by increasing the density of the pre-sintered powder [57].

Chromium oxide nanoparticles have been synthesized by a number of techniques including hydrothermal reduction [14], solution combustion synthesis [15], sonochemical reaction [16], laser-induced pyrolysis [17], hydrazine reduction and thermal treatment [18], supercritical alcohol synthesis [19], condensation-polymerization [20], precipitation-gelation [21], gas condensation [22], microwave plasma chemistry [23], and sol-gel techniques [24]. The major drawbacks of most of these methods are a large particle size distribution, a low yield, and agglomeration of the particles. The methods also tend to be complex and require chemically harsh conditions and/or high processing temperatures.

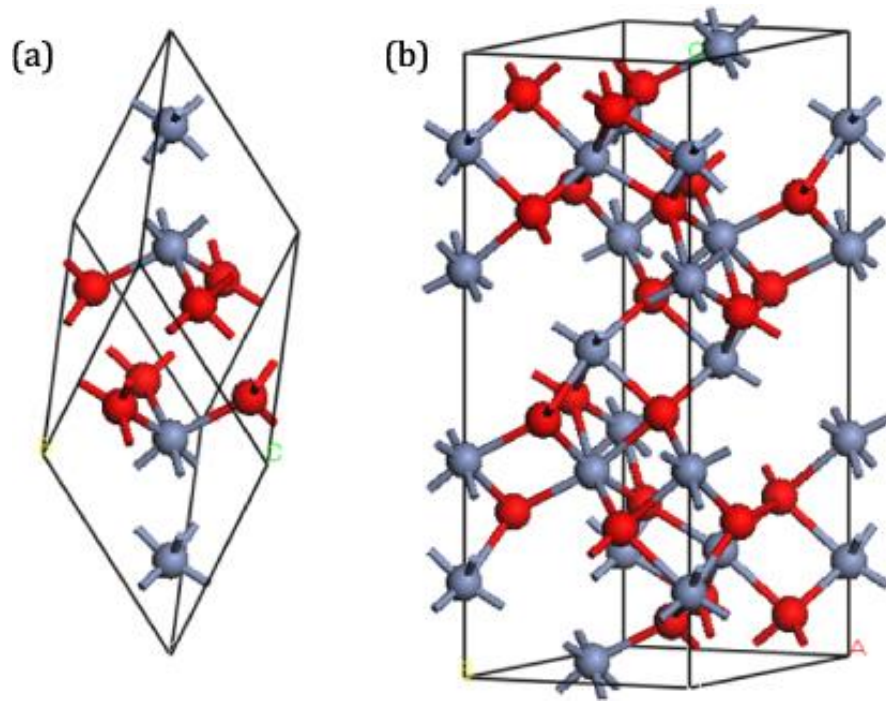


**Figure 1.5:** Crystal structure of  $\text{Cr}_2\text{O}_3$  with (a) the rhombohedral primitive cell and (b) the hexagonal structure. The  $\text{Cr}^{III}$  ions are grey while the  $\text{O}^{2-}$  ions are red (adopted from [9]).



### 1.3 RADIATION CHEMISTRY

High-energy charged particles and photons emitted during radioactive decay (alpha ( $\alpha$ ) or beta ( $\beta$ ) particles, or gamma ( $\gamma$ ) or X-ray electromagnetic radiation) are termed ionizing radiation because of their ability to ionize atoms and molecules. Ionizing radiation interacts with matter very differently from lower-energy radiation such as infrared (IR) and ultraviolet (UV). The low energy radiation interacts with molecules via a dipole moment transition between different energy states. Hence this type of radiation tends to cause specific molecular vibrational or electronic excitations in specific target molecules. These types of interactions occur in a one-to-one manner, in which a single photon can interact with only one molecule. The frequency (or wavelength) of the radiation can be tuned to interact with a selected molecular group. Due to the high specificity and singular interaction involved, the chemistry induced by low energy radiation is a solute-oriented process in which the bulk solution is largely unaffected by the radiation [3].

Radiation with energy in the keV-MeV range excites or ionizes a large number of molecules randomly distributed along a radiation track. Due to the non-specific interaction of this type of radiation (all molecules are equally likely to interact with the radiation), the bulk solution is most affected by the presence of the radiation and radiation chemistry is therefore referred to as a solvent oriented process.

### 1.3.1 Ionizing radiation and its interaction with matter

Ionizing radiation interacts with matter via a series of collisions with the electrons in the matter. For a  $\gamma$ -photon its initial interaction with matter is an inelastic Compton scattering. The most probable Compton scattering is either near zero or  $\sim 100\%$  energy transfer from the photon to an electron initially bound to a molecule. The Compton scattered electron has energy similar to the original  $\gamma$ -photon and hence behaves very much like a  $\beta$ -particle or fast electron generated from an electron-beam accelerator. Each collision of a fast electron transfers a small amount of energy ( $\sim 100$  eV) to the interacting matter and produces initially an ion pair (cation and electron). Since the electrons ejected from the bound states of a molecule tend to have a kinetic energy of the order of 100 eV, they can ionize or excite nearby solvent molecules. Thus, one encounter of a radiation particle with an molecule can lead to the formation of a cluster of 2-3 ion pairs (electron and solvent cations), known as a spur. Alternatively a collision can lead to the formation of an electronically excited molecule that can be stabilized or decompose into radical fragments [59]. Due to its high energy, a radiation particle interacts with a large number targets, resulting in a large number of excited species and ions being formed, distributed along the radiation track.

### 1.3.2 Radiolysis process

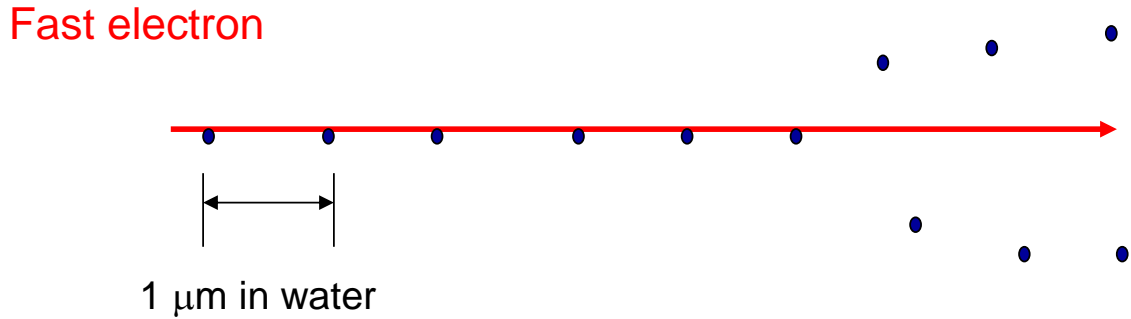
The fast-moving radiation particle interacts indiscriminately with the electron clouds of target atoms or molecules. As such the probability of interaction is related to the electron density (or mass density) of the target species. The chemical effect induced by radiation in the interacting medium depends on the rate of radiation energy transfer

per unit radiation track length (the rate of linear energy transfer, LET). The LET depends on the nature of the radiation particle and is higher for  $\alpha$ -particles than  $\beta$ -particles or  $\gamma$ -photons. The LET is a measure of the penetration depth of the radiation, with this depth ranging from 20-25  $\mu\text{m}$  for  $\alpha$ -particles to 0.5-1.0 cm for  $\beta$ -particles and fast electrons, and to tens of cm for  $\gamma$ -rays in water at room temperature.

Linear energy transfer (LET) is defined as the rate of energy loss per unit length of a radiation track. Since energy loss is correlated with spur formation, the distance between two sequential spurs depends on the type of radiation. In the case of a high LET radiation the distance between two sequential spurs is extremely short and the species created in separate spurs tend to intermingle. On the other hand, low LET radiation produces spurs that are sufficiently far apart along the radiation track that the species created do not interact immediately. In water the electrons, cations and excited species produced in a spur can interact with nearby water molecules to form radicals within the solvent cages. Alternatively some of the radicals can combine to form molecular products such as  $\text{H}_2$  and  $\text{H}_2\text{O}_2$  [2, 59].

In the case where spurs are initially formed close together (for  $\alpha$ -particles), the free radicals (or ions) formed from one spur will rapidly encounter the free radicals (or ions) formed from in a neighbouring spur and radical-radical (or ion-molecule) recombination can occur before these species can diffuse from the region around the radiation track into the bulk phase. For low LET radiation the spurs are spread out along the radiation track (Figure 1.6) and the highly reactive radicals can diffuse into the bulk phase, reducing the probability of recombination to form molecular products. As a result high LET radiation generates a characteristically higher proportion of molecular products

than low LET radiation. The chemical yields when homogeneous species distribution along a track is achieved are referred to as the primary radiolysis yields and the species created are known as the primary radiolysis products.



● Spur = 2-3 ions/excited solvent molecules

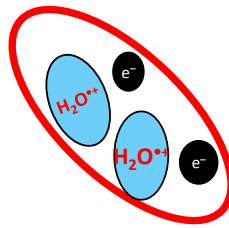
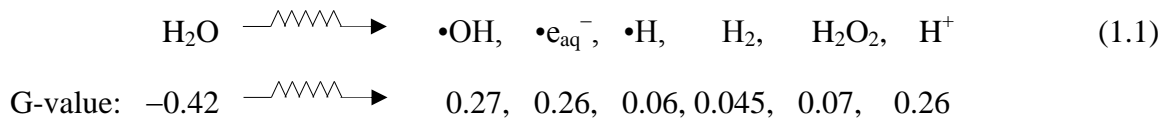


**Figure 1.6:** Schematic of a radiation track resulting from a  $\gamma$ -photon [3].

### 1.3.3 Water radiolysis: process, species and G-values

Ionizing radiation initially produces a series of spurs of 2-3 ion pairs (electrons and water cations) or excited water molecules along a radiation track. While these species diffuse out of expanding the spurs, they can undergo dissociation, recombination and ion-molecule reactions to form radical and the molecular products as schematically

represented in Figure 1.7 [3, 60]. The distribution of the radiolysis products along the track is initially inhomogeneous but it becomes homogeneous as the spurs expand. The homogeneous distribution is reached in less than  $10^{-6}$  s in water [2]. This time is shorter than the time required for bulk aqueous phase chemistry to take place. For this reason, the products formed at this stage are referred to as the primary radiolysis products, even though they are not the very first species created by the interaction of a radiation particle. The chemical yields per absorbed energy at this stage are known as the primary radiolysis yields, commonly referred to as G-values ( $\mu\text{mol}\cdot\text{J}^{-1}$ ) [2, 61]. For gamma-radiolysis of water at room temperature the G-values are [61]:



Most of the primary radiolysis products are highly reactive and can react with each other, with water molecules (and  $\text{H}^+$  and  $\text{OH}^-$ ) and, if present, solute species. The reactions of the radiolysis products occurring after 1  $\mu\text{s}$  follow typical bulk aqueous phase kinetics. The production rates of primary radiolysis products are not affected by the presence of other dissolved species at levels  $< 0.01$  M since the probability of the solute species interacting with radiation is very small compared to the probability of water radiolysis. If there is a continuous radiation flux, primary water radiolysis products are continuously generated at a rate determined by the absorbed radiation dose rate and the G values. As their concentrations increase, the rates of the subsequent reactions of the primary radiolysis products also increase, and the irradiated system approaches steady state, Figure 1.8. The concentrations of the radiolysis products can reach (pseudo) steady

state quickly, typically on the order of ms. True steady state may be reached only at longer times in the presence of slow reactions such as interfacial processes.

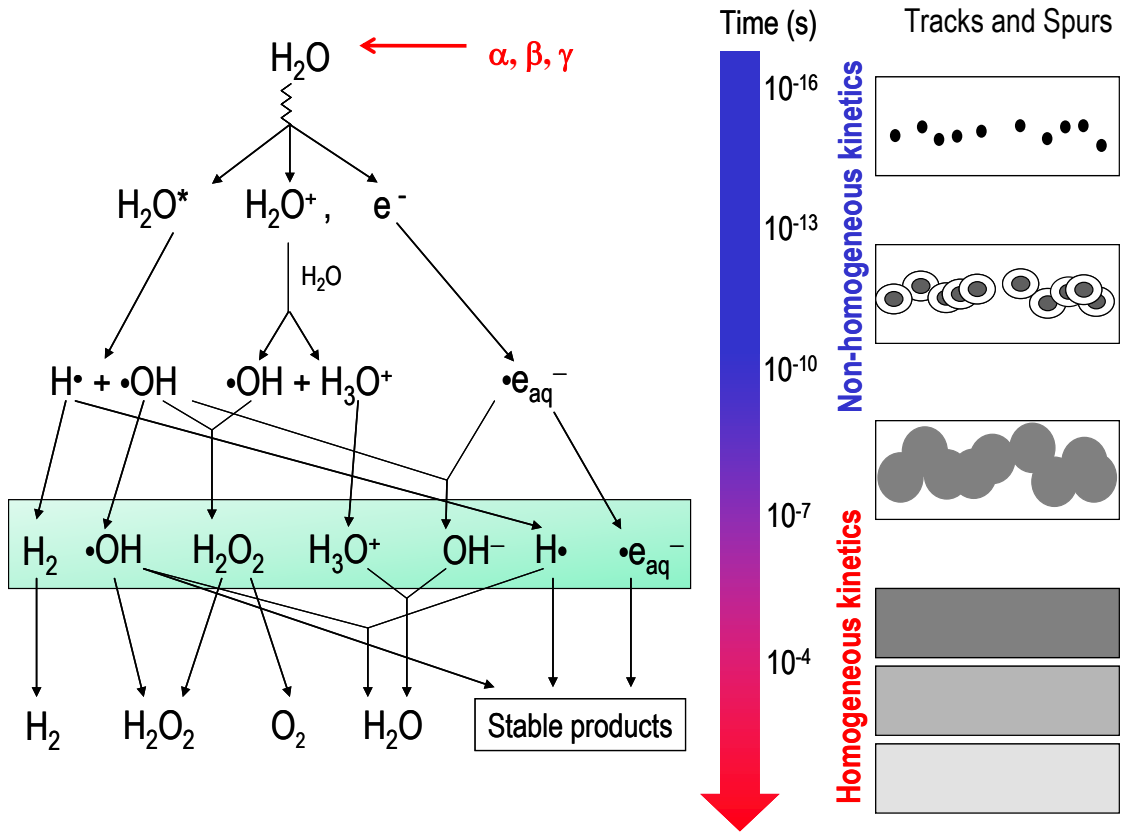


**Figure 1.7:** Schematics of the initial reactions that occur in water following absorption of ionizing radiation. The species in the green bar are designated the primary radiolysis products adopted from reference [60].

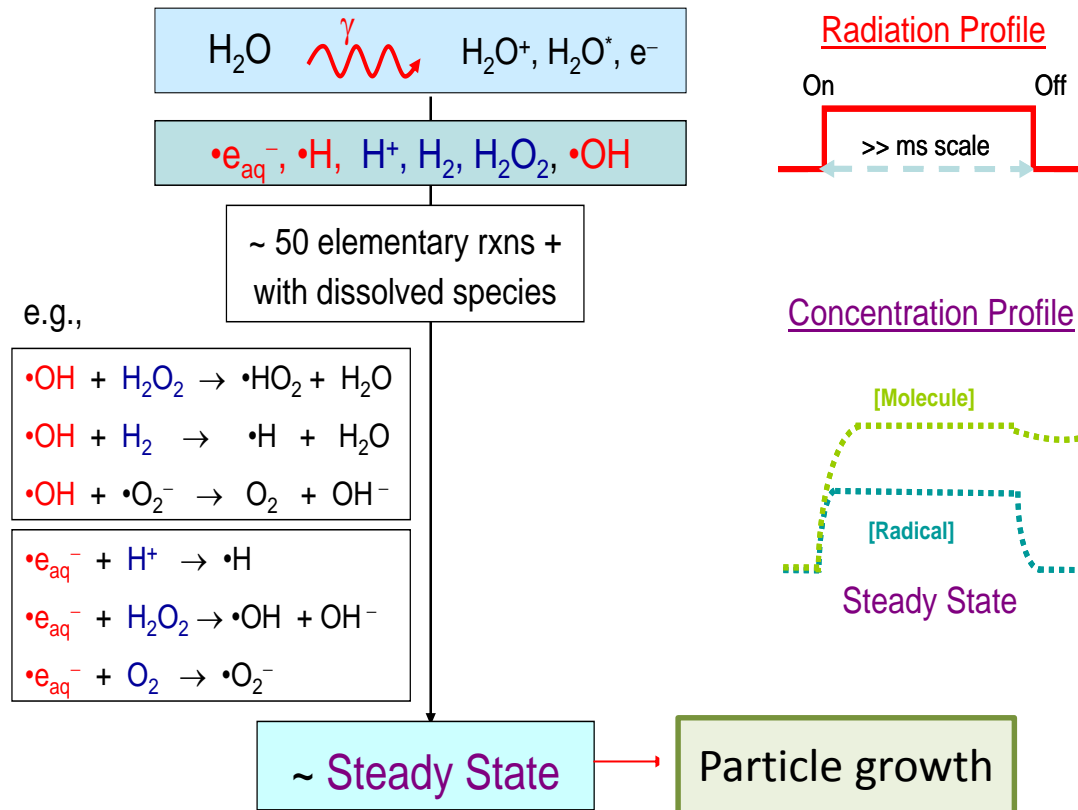


**Figure 1.8:** Schematic representation of continuous gamma-radiolysis kinetics.

Interfacial reactions and the mass transport involved in corrosion and colloid formation are slow processes. Thus, it is the steady state concentrations and not the primary radiolysis yields that determine the kinetics of these processes. Dissolved impurities provide additional reaction pathways for the radiolysis products and their presence can significantly alter the steady-state chemistry of an irradiated system. If the dissolved impurities can participate in reactions with water radiolysis products in a catalytic manner they can, even at very low levels, have a significant impact on the concentrations of the radiolysis products and redox conditions. The possible reactions of

all species in a system must be taken into account to determine the radiation-induced chemistry in the system.

#### 1.4 RADIOLYSIS OF PURE WATER WITHOUT ANY ADDITIVES

The radiolysis of pure water has been studied previously [61]. That work combined both experiments and kinetic model simulations to understand the complex radiolysis kinetics that occurs under long-term continuous irradiation. A radiolysis kinetic model that includes the primary radiolysis production reactions (whose rates are expressed using primary homogeneous yields multiplied by the radiation dose rate), ~40 elementary homogeneous reactions with well-defined rate constants, hydrolysis reactions and the related acid-base equilibria of the primary water decomposition products has been validated. The kinetics of the coupled reactions was solved using the software package FACSIMILE [61]. This model has been shown to reproduce the steady-state radiolysis chemistry in liquid water for a wide range of conditions [61]. The key findings regarding the behaviour of the molecular and radical species of primary interest in this work are discussed here, to aid in interpreting the chemistry seen in irradiation of chromium and cobalt systems.

The key reactions that determine the concentrations of molecular water radiolysis products,  $H_2$  and  $H_2O_2$  are as follows [61]:

For  $H_2$





For H<sub>2</sub>O<sub>2</sub>



where reactions (1.6) and (1.8) represent production by radiolysis and the other reactions are aqueous chemical reactions.

Except at very short times (< ms), the steady-state approximation can be applied to these reactions to obtain analytical solutions for the species concentrations. Using only the main reactions listed above, the results are [61]:

$$[\text{H}_2(\text{aq})]_{\text{ss}} \approx \frac{k_{\text{Rad}}^{\text{H}_2}}{k_{1.7} \cdot [\bullet\text{OH}]_{\text{ss}}} \quad (1.11)$$

$$[\text{H}_2\text{O}_2]_{\text{ss}} \approx \frac{k_{\text{Rad}}^{\text{H}_2\text{O}_2}}{k_{1.9} \cdot [\bullet\text{OH}]_{\text{ss}} + k_{1.10} \cdot [\bullet\text{e}_{\text{aq}}^-]_{\text{ss}}} \quad (1.12)$$

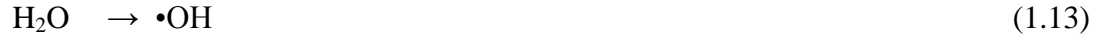
where  $k_{\text{Rad}}^{\text{H}_2} \approx C_R \cdot G_{\text{H}_2} \cdot D_R \cdot \rho_{\text{H}_2\text{O}}$  and  $k_{\text{Rad}}^{\text{H}_2\text{O}_2} \approx C_R \cdot G_{\text{H}_2\text{O}_2} \cdot D_R \cdot \rho_{\text{H}_2\text{O}}$  represent the zeroth-order radiolytic production rates for H<sub>2</sub> and H<sub>2</sub>O<sub>2</sub>. These rates are determined by the primary radiolysis yields (the G-values), the gamma-radiation dose rate, D<sub>R</sub>, and the density of water (ρ<sub>H<sub>2</sub>O</sub>), with a unit conversion factor C<sub>R</sub> (1.04 × 10<sup>-7</sup> mol·eV·molecules<sup>-1</sup>·J<sup>-1</sup>) The other rate constants (k<sub>1.7</sub>, k<sub>1.9</sub>, and k<sub>1.10</sub>) are second-order bimolecular rate constants.

These analytical equations state that, in the absence of any other dissolved species, the concentrations of H<sub>2</sub> and H<sub>2</sub>O<sub>2</sub> are inversely proportional to the radical concentrations. These inverse relationships were confirmed by experimental results [60].

It is important to examine the behaviour of radical species  $\bullet\text{e}_{\text{aq}}^-$  and  $\bullet\text{OH}$ . These radicals

can be consumed by other reactions in addition to those with the molecular species discussed above as follows [61]:

For  $\bullet\text{OH}$



For  $\bullet\text{e}_{\text{aq}}^-$



Note that although reaction (1.7) is an important removal path for  $\text{H}_2$ , it is not important for the removal of  $\bullet\text{OH}$  because reactions (1.9) and (1.14) are faster. Reaction (1.7) is only important if  $\text{H}_2$  is initially present at a high concentration prior to the build-up of  $\text{H}_2\text{O}_2$  and  $\bullet\text{O}_2^-$ .

The interaction between the molecular and the radical radiolysis products leads to regeneration of some species that can establish a catalytic reaction cycle. This changes the relative contributions of different reactions to the net removal of the radicals as water radiolysis progresses, making it difficult to predict the chemistry at longer times. For example, in initially de-aerated pure water at pH 6.0, the concentrations of the molecular products are below the detection limits as shown in Figure 1.8.

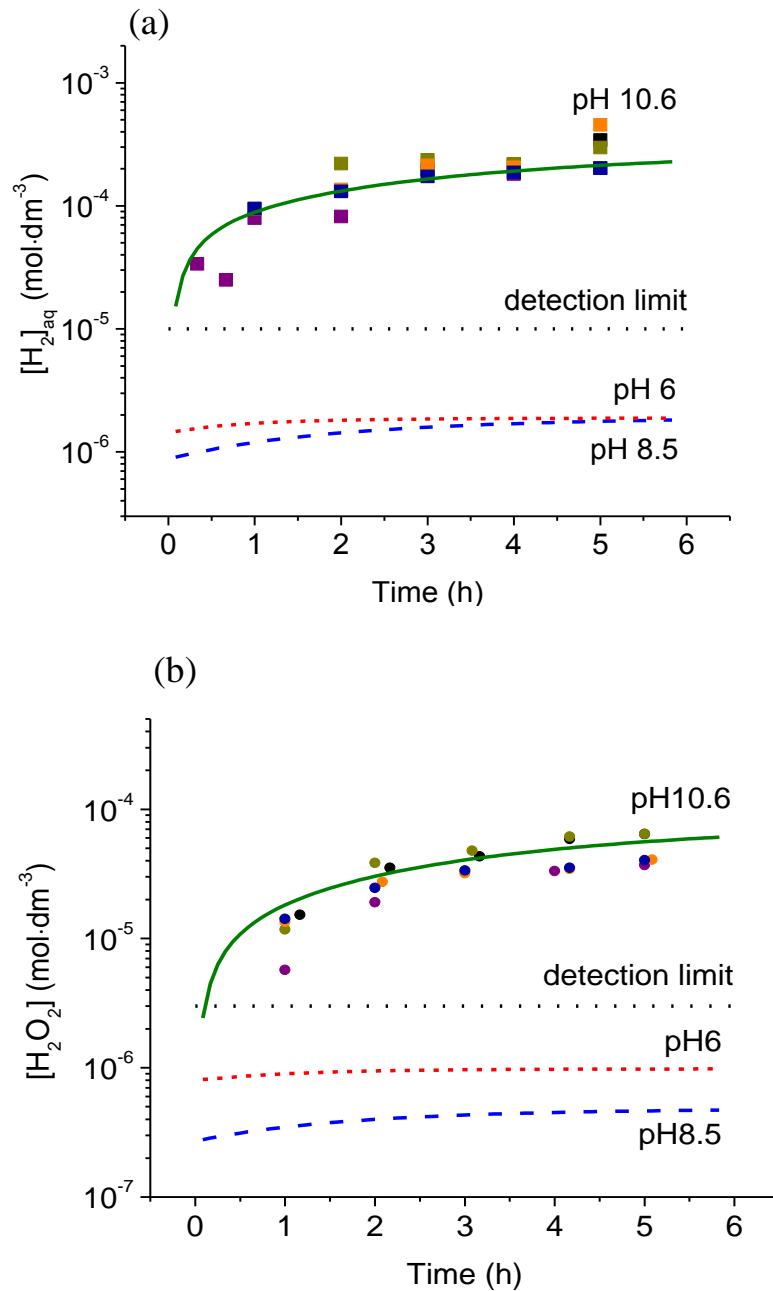


**Figure 1.9:** The radiolytic production of  $H_2$  (a) and  $H_2O_2$  (b) in deaerated water at different pHs as a function of irradiation time. (Reprinted from reference [61], Copyright (2008), with permission from Elsevier).

The molecular species concentrations remain low at pH 8.5 (model predictions are shown in Figure 1.8). However, at pH 10.6 the molecular product concentrations are about three orders of magnitude larger (Figure 1.9). At pH 10.6, a pH higher than the  $pK_a$  of  $\bullet H$  of 9.7 ( $\bullet H \rightleftharpoons \bullet e_{aq}^- + H^+$ ), reaction (1.16) is very slow and the reaction of  $\bullet e_{aq}^-$  with the secondary radiolysis product  $O_2$  (reaction (1.18)) becomes an important removal path for  $\bullet e_{aq}^-$ . The product of reaction (1.18),  $\bullet O_2^-$ , however, reacts with  $\bullet OH$  (reaction (1.14)) to reform  $O_2$ . Once this catalytic cycle is established, the secondary radiolysis product  $O_2$  can build up to a significant level while continuously reacting with the radicals. This results in a reduction in the loss rates of molecular products at high pH, thus increasing their steady-state concentrations [61].

Introduction of other chemical species into water that can react with the radical species (scavengers) can upset the chemistry by providing additional removal pathways for those radicals. If the added species can be regenerated by back reactions such that they can establish a (semi-) catalytic cycle with the radical species before they are totally consumed or removed from the aqueous phase, their influence on radiolysis product concentrations can be significant and last for a long time.

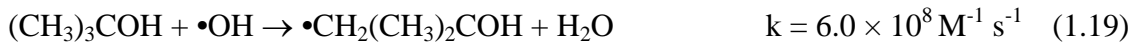
Corrosion products of steel alloys are transition metal ions that can exist in different oxidation states. Dissolved, ions (such as  $Cr^{VI}$ ,  $Co^{II}$ ,  $Fe^{II}$ ) can affect water radiolysis chemistry via their interactions with the radical species present during radiolysis and thereby influence the concentrations of key molecular oxidants and reductants ( $H_2O_2$  and  $H_2$ ). Some dissolved metal ions can significantly alter the solution redox conditions.

## 1.5 SCAVENGERS

In this thesis, scavengers have been used to investigate the role played by the redox active radicals  $\bullet\text{OH}$  and  $\bullet\text{e}_{\text{aq}}^-$  on the formation of  $\text{Cr}_2\text{O}_3$  and  $\text{Co}_3\text{O}_4$  nanoparticles. Different scavengers were used to selectively remove  $\bullet\text{OH}$  or  $\bullet\text{e}_{\text{aq}}^-$  from the irradiated system. For scavenging  $\bullet\text{OH}$  *t*-butanol was used and for removal of  $\bullet\text{e}_{\text{aq}}^-$  nitrous oxide ( $\text{N}_2\text{O}$ ) was used.

### 1.5.1 Scavenger of $\bullet\text{OH}$ , *t*-butanol

The radiolysis of *t*-butanol (2-methyl-2-propanol) solutions has been investigated using the pulse radiolysis technique [62, 63]. This chemical has been widely used as a preferential scavenger of  $\bullet\text{OH}$  because the scavenging reaction produces a relatively inert radical ( $\bullet\text{CH}_2(\text{CH}_3)_2\text{COH}$ ), reaction (1.19), [62, 63].



However, in aerated solutions, the  $\bullet\text{CH}_2(\text{CH}_3)_2\text{COH}$  radical does react rapidly with  $\text{O}_2$  to form a peroxy radical,



### 1.5.2 Scavenger of hydrated electron ( $\bullet\text{e}_{\text{aq}}^-$ ), Nitrous Oxide, $\text{N}_2\text{O}$

Nitrous oxide ( $\text{N}_2\text{O}$ ) has been widely used in radiation chemical studies to promote the abundance of  $\bullet\text{OH}$  (and create a more oxidizing environment) by selectively removing  $\bullet\text{e}_{\text{aq}}^-$  [64]. Nitrous oxide reacts with a hydrated electron to produce the  $\text{N}_2\text{O}^-$

anion and this dissociates to release the  $O^-$  anion. The  $O^-$  can then react with water to form  $\bullet OH$ . Studies have shown that  $N_2O$  has a relative high reactivity toward  $\bullet e_{aq}^-$  [64].



The overall reaction can be presented as



The rate constant of reaction (1.21) is reported as  $9.1 \times 10^9 \text{ M}^{-1}\text{s}^{-1}$  [64]. In comparison  $\bullet H$  is much less reactive with  $N_2O$  (rate constant reported as  $2.1 \times 10^6 \text{ M}^{-1}\text{s}^{-1}$  [64]). In this research work,  $N_2O$  is used to produce a more oxidizing system by scavenging  $\bullet e_{aq}^-$ .

## 1.6 REFERENCES

- [1] Description of different types of nuclear reactor: PWR, BWR, CANDU. Retrieved from <http://coursenligne.chimie-paristech.fr/cinch/1.php>
- [2] R.J. Woods, A.K. Pikaev, *Applied Radiation Chemistry: Radiation Processing*, John Wiley & Sons, Inc., New York, 1994.
- [3] J.W.T. Spinks, R.J. Woods, *An Introduction to Radiation Chemistry*, Wiley-Interscience, New York, 1990.
- [4] J.C. Wren, Steady-state radiolysis: effect of dissolved additives in ACS Symposium Series: *Nuclear Energy and the Environment*, 2010.
- [5] A.J. Bard, L.R. Faulkner, *Electrochemical Methods: Fundamentals and Applications*. (2<sup>nd</sup> Ed.) John Wiley & Sons, Inc, New York, 2001.

- [6] P.A. Yakabuskie, J.M Joseph, P. Keech, G.A. Botton, D. Guzonas, J.C. Wren, *Phys. Chem. Chem. Phys.*, 13 (2011) 7198.
- [7] D. Fu, P. Keech, X. Sun, J.C. Wren, *J. Phys. Chem. Chem. Phys.*, 13 (2011) 18523.
- [8] M.M. Rahman, J.-Z. Wang, X.-L. Deng, Y. Li, H.-K. Liu, *Electrochim. Acta*, 55 (2009) 504.
- [9] Y. Guo, S. J Clark, J. Robertson, *J. Phys.: Condens. Matter*, 24 (2012) 325504.
- [10] C.S. Cheng, M. Serizawa, H. Sakata, T. Hirayama, *Mater. Chem. Phys.*, 53 (1998) 225.
- [11] A.U. Mane, K. Shalini, A. Wohlfart, A. Devi, S.A. Shivashankar, *J. Cryst. Growth*, 240 (2002) 157.
- [12] S.R. Ahmed, S.B. Ogale, G.C. Papaefthymiou, R. Ramesh, P. Kofinas, *Appl. Phys. Lett.*, 80 (2002) 1616.
- [13] B. Orel, V. Kauc, *Electrochim. Acta*, 45 (2000) 4359.
- [14] Z. Pei, H. Xu, Y. Zhang, *J. Alloys Compd.*, 468 (2009) L5.
- [15] M.D. Lima, R. Bonadimann, M.J. de Andrade, J.C. Toniolo, C.P. Bergmann, *J. Eur. Ceram. Soc.*, 26 (2006) 1213.
- [16] N.A. Dhas, Y. Koltypin, A. Gedanken, *Chem. Mater.*, 9 (1997) 3159.
- [17] G. Peters, K. Jerg, B. Schramm, *Mater. Chem. Phys.*, 55 (1998) 197.
- [18] L. Qiao, H.Y. Xiao, H.M. Meyer, J.N. Sun, C.M. Rouleau, A.A. Puretzky, D.B. Geohegan, I.N. Ivanov, M. Yoon, W.J. Weber, M.D. Biegalski, *J. Mater. Chem. C*, 1 (2013) 4628
- [19] L. Znaidi, C. Pommier, *Eur. J. Solid State Inorg. Chem.*, 35 (1998) 405.

- [20] A. Kawabata, M. Yoshinaka, K. Hirota, O. Yamaguchi, *J. Am. Ceram. Soc.*, 78 (1995) 2271.
- [21] D. Kim, S. Shin, J. Lee, S. Oh, *Mater. Lett.*, 58 (2004) 1894.
- [22] U. Balachandran, R.W. Siegel, Y. X. Liao, T.R. Askew, *Nanostruct. Mater.*, 5 (1995) 505.
- [23] D. Vollath, D.V Szab, J.O. Willis, *Mater, Lett.*, 29 (1996) 271.
- [24] C. Zhu, Y. Hong, J. Zhang, B. Zhou, *Key Eng. Mater*, 353 (2007) 2111.
- [25] M. Mohapatra, S. Anand, *Int. J. Eng. Sci. Technol.*, 2 (2010) 127.
- [26] E. Matijevic, *Annu. Rev. Mater. Sci.*, 15 (1985) 483.
- [27] T. Sugimoto, E. Matijevic, *J. Colloid Interface Sci.*, 74 (1980) 227.
- [28] K. Sinkó, G. Szabó, M. Zrínyi, *J. Nanosci. Nanotechnol.*, 11 (2011) 4127.
- [29] Y. Liu, Z.L. Wang, Z. Zhang, in *Handbook of Nanophase and Nanostructured Materials*, Springer –Verlag, New York, 2012.
- [30] H.J. Gulley-Stahl, W.L. Schmidt, H.A. Bullen, *J. Mater. Sci.*, 43 (2008) 7066.
- [31] A.E. Onjia, S.K. Milonjić, D. Čokeša, M. Čomor, N. Miljević, *Mater. Res. Bull.*, 38 (2003) 1329.
- [32] S. Musić, M. Maljković, S. Popvić, R. Trojko, *Croatica Chemica Acta*, 72 (1999) 789.
- [33] A. Henglein, M. Giersig, *J. Phys. Chem. B*, 103 (1999) 9533.
- [34] Y. Ni, X. Ge, Z. Zhang, H. Liu, Z. Zhu, Q. Ye, *Mater. Res. Bull.*, 14 (2002) 1048.
- [35] J. Belloni, M. Mostafavi, H. Remita, J.-L. Marignier, M.-O. Delcourt, *New J. Chem.*, 22 (1998) 1239.



- [36] S. Chen, Y. Liu, G. Wu, *Nanotechnology*, 16 (2005) 2360.
- [37] H. Remita, M. Tréguer, J. Amblard, J. Belloni, J. Khatouri, *Z. Phys. D*, 40 (1997) 127.
- [38] M. Treguer, C. De Cointet, H. Remita, J. Khatouri, M. Mostafavi, J. Amblard, J. Belloni, R. De Keyzer, *J. Phys. Chem. B*, 102 (1998) 4310.
- [39] A. Abedini, A.R. Daud, M.A. Abdul Hamid, N. Kamil Othman, E. Saion, *Nanoscale Res. Lett.*, 8 (2013) 474.
- [40] M. Mirdamadi-Esfahani, M. Mostafavi, B. Keita, L. Nadjo, P. Kooyman, H. Remita, *Gold Bull.*, 43 (2010) 49.
- [41] S. Gasaymeh, S. Radiman, *Am. J. Applied Sci.*, 7 (2010) 892.
- [42] K. Torigoe, H. Remita, P. Beaunier, J. Belloni, *Radiat. Phys. Chem.*, 64 (2002) 215.
- [43] G.R. Dey, H. Remita, M. Mostafavi, *Chem. Phys. Lett.*, 431 (2006) 83.
- [44] P. Yadav, R.T. Olsson, M. Jonsson, *Radiat. Phys. Chem.*, 78 (2009) 939.
- [45] E.B. Gracien, Z. Ruimin, X. Lihui, L.K. Kanza, I. Lopaka, *Radioanal. Nucl. Chem.*, 270 (2006) 473.
- [46] N. Misra, J. Biswal, V.P. Dhamgaye, G.S. Lodha, S. Sabharwal, *Adv. Mater. Lett.*, 4 (2013) 458.
- [47] A.A. Athawale, M. Majumdar, H. Singh, K. Navinkiran, *Defence Sci. J.*, 60 (2010) 507.
- [48] L.M. Alrehaily, J.M. Joseph, M.C. Biesinger, D. Guzonas, J.C. Wren, *Phys. Chem. Chem. Phys.*, 15 (2013) 1014.
- [49] L.M. Alrehaily, J.M. Joseph, A.Y. Musa, D.A. Guzonas, J.C. Wren, *Phys. Chem. Chem. Phys.*, 15 (2013) 98.

- [50] J. Chen, X. Wu, A. Selloni, *Phys. Rev. B.*, 83 (2011) 245204.
- [51] Y. Ikedo, J. Sugiyama, H. Nozaki, H. Itahara, J. Brewer, E. Ansaldo, G. Morris, D. Andreica, A. Amato, *Phys. Rev. B*, 75 (2007) 054424.
- [52] C.N.R. Rao, B. Raveau (2nd Ed.). *Transition metal oxides : structure, properties, and synthesis of ceramic oxides*, Wiley-VCH, New York, 1998.
- [53] T. Ivanova, K. Gesheva, A. Cziraki, A. Szekeres, E. Vlaikova, in *Journal of Physics: Conference Series*, 113 (2008) 012030.
- [54] B. Abu-Zied, *Appl. Catal. A Gen.*, 198 (2000) 139.
- [55] P. Berdahl, *J. Heat Transfer*, 117 (1995) 355.
- [56] H. Kitsunai, K. Hokkirigawa, N. Tsumaki, K. Kato, *Wear*, 51 (1991) 279.
- [57] P. Gibot, L. Vidal, *J. Eur. Ceram. Soc.*, 30 (2010) 911.
- [58] T. Brock, M. Groteklaes, P. Mischke, *European Coating Handbook*. Hannover, Germany, 2000.
- [59] R.L. Cowan, *Water Chemistry of Nuclear Reactor System 7*, Nuclear Energy Society, London: British, 1996.
- [60] Farhataziz, M. A. J. Rodgers, *Radiation chemistry: principles and applications*, VCH, New York, 1987.
- [61] J.M. Joseph, B. Seon Choi, P.A. Yakabuskie, J.C. Wren, *Radiat. Phys. Chem.*, 77 (2008) 1009.
- [62] M. Von Piechowski, M.-A. Thelen, J. Hoigné, R. E. Bühler, *Berichte der Bunsengesellschaft für Phys. Chemie*, 96 (1992) 1448.
- [63] M. Schuchmann, C. Von Sonntag, *J. Phys. Chem.*, 83 (1979) 780.
- [64] G. Scholes, M. Simic, *J. Phys. Chem.*, 68 (1964) 1731.

## Chapter 2

### Experimental Principle and Details

General information regarding the experimental techniques and analysis used in this thesis work are provided in this chapter. The common experimental procedures applicable for all experimental work are also described in this chapter. Detailed experimental information, as required, is provided in the experimental sections of later chapters.

#### 2.1 EXPERIMENTAL TECHNIQUES

##### 2.1.1 Gas Chromatography (GC)

Gas chromatography (GC) is a technique used for analyzing a mixture of chemicals. Gas chromatography separates the components of a mixture of chemicals into individual components through the selective partitioning of each component between the mobile and the stationary phase; after that the components can be characterized for each of the isolated molecules individually. In all chromatographic techniques, separation occurs due to differential partitioning between the mobile (gas) phase and the stationary phase on the walls of the gas chromatograph column. When a gas sample is injected into a mobile phase (which is usually an inert gas such as helium or nitrogen gas) the mobile phase carries the sample into a column containing stationary phase. The stationary phase is usually made of chemical that can selectively attract components in a sample mixture; it is usually contained in a tube made of a glass or steel. As the mixture of compounds in

the mobile phase passes through the column, each compound interacts with the stationary phase at different rates depending on component molecule's affinity. The separation is also controlled by changing the temperature of the stationary phase and the flow rate of the mobile phase [1]. Figure 2.1 represents a schematic diagram of gas chromatography used in this work. The GC system (GC-MS, 6580 Agilent Technologies) contained a 60 m long GS-GASPRO column (diameter 0.32  $\mu\text{m}$ ) connected to a micro fluid three-way splitter to allow simultaneous analysis by three detectors: Thermal Conductivity Detector (TCD),  $\mu$ -Electron Capture Detector ( $\mu$ -ECD) and Mass Selective Detector (MSD). The resulting GC spectra can be used to identify species eluting at a specific retention time as illustrated in Figure 2.2. The peak area is proportional to the amount of the component in the mixture.

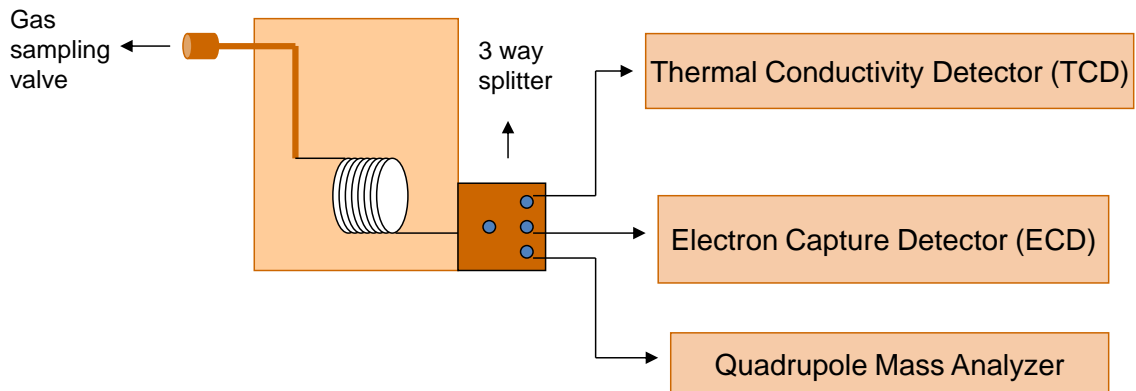


**Figure 2.1:** Schematic of Gas Chromatography system (GC-MS, 6580 Agilent Technologies) used in this work.

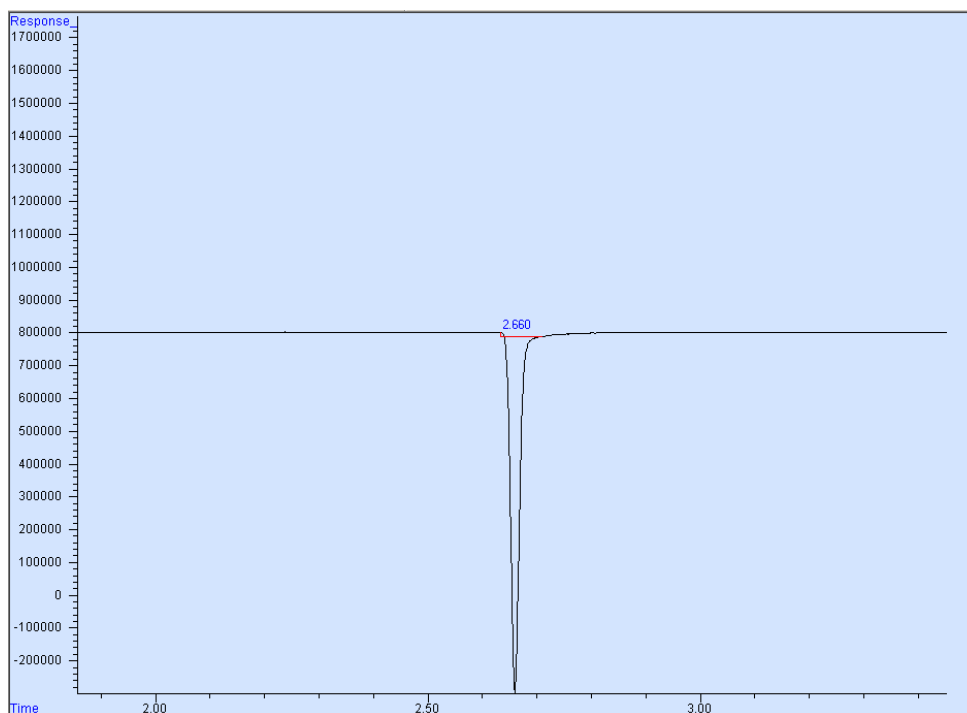


**Figure 2.2:** Chromatogram showing the H<sub>2</sub> peak eluting at a retention time of 2.66 min determined with a GS-GASPRO column and using N<sub>2</sub> as the carrier gas at a flow rate of 4.6 ml/min.

In this work a TCD detector and ECD detector were used. The GC-MS TCD detector was calibrated by injecting certified gas mixtures with concentrations of 0.1%, 1%, 3% and 5% H<sub>2</sub> (Praxair), and the ECD detector was calibrated by injecting gas mixtures of 2%, 5% 10% and 35% O<sub>2</sub> (Praxair).

The thermal conductivity detector (TCD) was used to measure the amount of H<sub>2</sub> in a sample. A TCD detects the difference in the thermal conductivities of two gas flows: the column effluent (the carrier gas + sample component) and the carrier gas alone. The magnitude of the TCD signal (measured as a voltage) is proportional to the concentration in the sample.

An electron capture detector responds to electron-capturing substances like O<sub>2</sub>. The electron capture detector uses a radioactive source, <sup>63</sup>Ni (beta emitter), to form

thermal electrons in the gas flow. The current generated by the production of these electrons can be measured. Species which contain an electronegative functional group, such as halogens, phosphorous or oxygen will capture some electrons and reduce the measured current. The reduction in current is proportional to the quantity of the species in the sample.

### 2.1.2 UV-Visible Spectrophotometry

Ultraviolet and visible (UV-Vis) absorption spectroscopy is a useful technique to characterize the metal nanoparticles that possess bright colour. The UV-Vis technique measures the attenuation of a beam of light passing through a sample or by measurement of reflection from a sample surface. This spectroscopy uses light in the UV, (200 nm - 400 nm) and visible (400 nm - 800 nm) regions.

The concentration of an absorbing species is quantitatively determined using the Beer-Lambert law. The ratio of amount of light of the incident radiation ( $I_0$ ) to the transmitted radiation ( $I$ ) is called absorbance [2]. The absorbance depends on the concentration of the sample ( $c$ ) ( $\text{mol.L}^{-1}$ ), path length of the measuring cell ( $l$ ) (cm), and extinction coefficient ( $\epsilon$ ) of sample under study ( $\text{L.mol}^{-1}.\text{cm}^{-1}$ ), (2.1).

$$A = \log \frac{I_0}{I} = \epsilon c l \quad (2.1)$$

In this project, the UV-Vis technique was used to detect the concentration of metallic species ( $\text{Co}^{\text{II}}$ ,  $\text{Co}^{\text{III}}$ ,  $\text{Cr}^{\text{III}}$  and  $\text{Cr}^{\text{VI}}$ ) and hydrogen peroxide ( $\text{H}_2\text{O}_2$ ) in the aqueous phase as discussed in section 2.2.3.

### 2.1.3 Raman Spectroscopy

Raman spectroscopy is used to analyze the chemical composition of materials that are Raman active. The Raman spectrometer instrumentation consists of a laser source, a sample illumination and scattered light collection system, and a light detection system. Raman spectroscopy detects changes induced in the polarizability of the electron cloud around a molecule on interaction with light [3,4].

The irradiation of the sample by an intense laser beam leads to the scattering of light. Elastic or Rayleigh scattering is the most probable interaction. However, a small fraction of the incident light undergoes inelastic scattering. If the molecule, after absorbing the incident photons, is excited to a virtual excited electronic energy state and quickly decays back to its original state, the scattered photon will have the same energy as the incident photon; this is called Rayleigh scattering, Figure 2.3. Stokes scattering occurs when a molecule, after absorbing the incident photon, relaxes back to its original electronic energy state, but to a higher vibrational state than the initial state (Figure 2.3). In this case the scattered photon has less energy than the incident photon. If the excited molecule relaxes to lower vibrational state than the initial state, the scattered photon has more energy than the incident photon; this is called anti-inelastic Stokes scattering. The ratio of Stokes and anti-Stokes scattering depends on the original vibrational energy distribution of the target species and this distribution is linked to the sample temperature through the Boltzmann distribution.

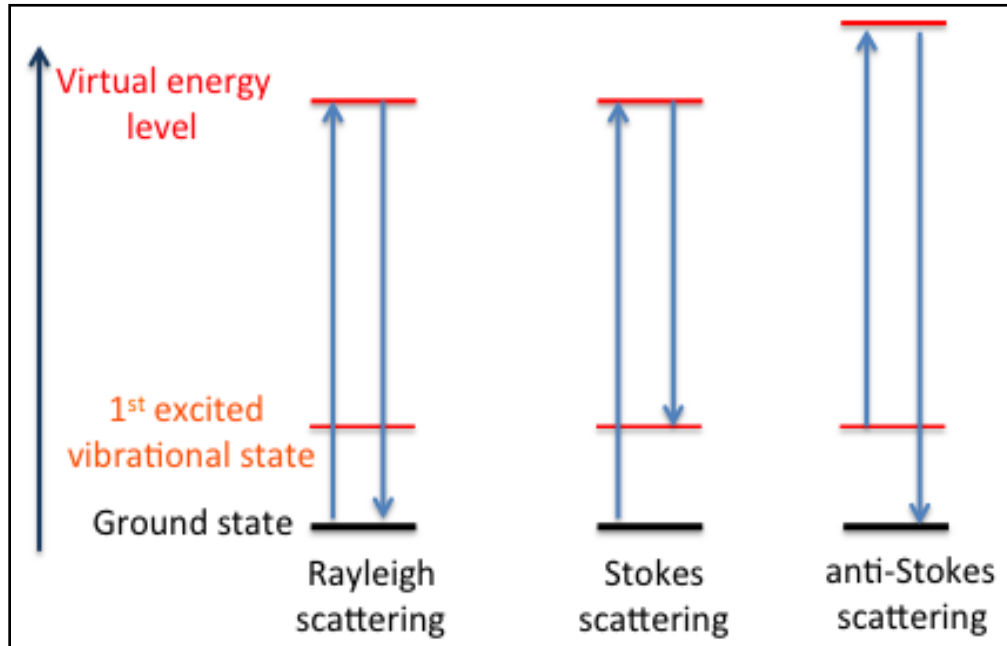


**Figure 2.3:** Illustration showing Rayleigh scattering, Stokes scattering and anti-Stokes scattering.

The energy difference between the incident and scattered light is termed the frequency shift. The relation between the scattered light frequency ( $\nu'$ ) and the excitation light frequency ( $\nu''$ ) is given by

$$h\nu' = h\nu'' + \Delta E_{vibration} \quad (2.2)$$

where  $\Delta E_{vibration}$  is the energy gap between the vibrational levels (initial and final). Since vibrational state energies are a characteristic of a chemical species, Raman spectroscopy can be used to identify a chemical species and the intensity of any spectral peaks can be linked to the abundance of the species.



In this thesis, Raman spectroscopy was used to characterize the oxide and hydroxide phases of the metal of interest, both in nanoparticle form as well as in the aqueous phase. Raman spectroscopy is particularly suited for the latter analysis because water does not generate any Raman scattering.

#### **2.1.4 Fourier Transform Infrared Spectroscopy (FTIR)**

Fourier transform infrared spectroscopy (FTIR) is one of the common analytical techniques used in molecular structure investigation. The infrared region extends from 500 to 1500  $\text{cm}^{-1}$ . An infrared spectrum contains peaks characteristic of specific bonds within specific compounds. An infrared spectrum is obtained by passing radiation through a sample and measuring the absorbance.

In FTIR technique, the molecular bond must have an electrical dipole moment in order for the light energy to be absorbed [5, 6]. This allows the molecule to interact with incoming photons and absorb energy at frequencies associated with transitions between vibrational and rotation states within the molecule [7]. The vibrational frequency depends on the bond strength and the masses of the atoms.

The FTIR instrumentation consists of four components: a light source, a beam splitter, a sample, and a detector. Light from the source is split by a stationary mirror and a moving mirror and is combined again to form an interferogram [5]. After interaction with the sample, the light beam reaches the detector.

The FTIR technique is sensitive to water and water peaks can block other peaks in the spectra. However, FTIR technique has number of advantages compared to Raman,

fluorescence of the sample can interfere with the Raman signal. In this thesis, the two complementary techniques (FTIR and Raman) were used to identify the chemical phases and compositions of metal nanoparticles.

### 2.1.5 Transmission Electron Microscopy (TEM)

The size and morphology of nanoparticles can be determined using transmission electron microscopy (TEM) [8]. A transmission electron microscope is based on the same principles as a light microscope but it uses a beam of electrons instead of visible photons. A TEM instrument is composed of a monoenergetic electron source (80 keV), two condenser lenses for electron beam focus and to adjust magnification, and magnetic coils to align the electron beam. The resolution ( $\rho$ ) of a microscope is related to the wavelength of the light by the relation [8]

$$\rho = \frac{0.61 \lambda}{\sin \alpha} \quad (2.3)$$

where  $\lambda$  is the wavelength of the light and  $\alpha$  is the maximum angle between the incident and deflected beams. TEM resolution is limited by the de Broglie wavelength of the electrons. The standard electron energy of 100 keV provides a maximum resolution of 37 pm, which is much smaller than the near neighbour atomic separation in crystals [8]. In TEM a beam of electrons is transmitted through an ultra thin specimen and to obtain an image. For the electron to transit through the sample, the sample must be thin enough (20-200 nm).

Images of the samples are taken in bright field mode (the most common mode). The brightness of the image is dictated by the flux of incident electrons on a detector. Thicker areas, where nanoparticles are present, will appear dark and the areas where no sample is present will appear bright.

### 2.1.6 X-ray Photoelectron Spectroscopy (XPS)

X-ray photoelectron spectroscopy (XPS) is a surface sensitive quantitative spectroscopic technique. Information regarding the element composition, chemical state, electronic state, and empirical formulas can be obtained by XPS. This technique was used in this project to obtain information on the oxide composition of nanoparticles.

XPS is based on photoelectric effect, wherein an incident X-ray interacts with the core electron shell of an atom causing ejection of an electron (a photoelectron), Figure 2.4. In XPS, the sample is illuminated with a soft (~1.5 kV) X-ray beam in an ultrahigh vacuum. The ejected photoelectrons have an energy spectrum that is characteristic of the source atom and its surrounding electronic environment. This energy spectrum is used to determine the composition of the sample. The kinetic energy of the ejected photoelectron is defined as the difference between the energy of the X-ray and the binding energy of the electron plus the work function.

$$E_k = h\nu - (E_B + \varphi) \quad (2.4)$$

where  $E_k$  is the kinetic energy,  $E_B$  is the binding energy of the electron in the ionized atom,  $h$  is the Planck constant,  $\nu$  is the frequency of the X-ray and  $\varphi$  is the work function [8]. The work function here is the combined work function induced by the analyzer and the sample work function. By using this equation and by knowing the photon energy  $h\nu$ ,

and the work function of the system, the binding energies (B.E) of the photoelectrons can be calculated.

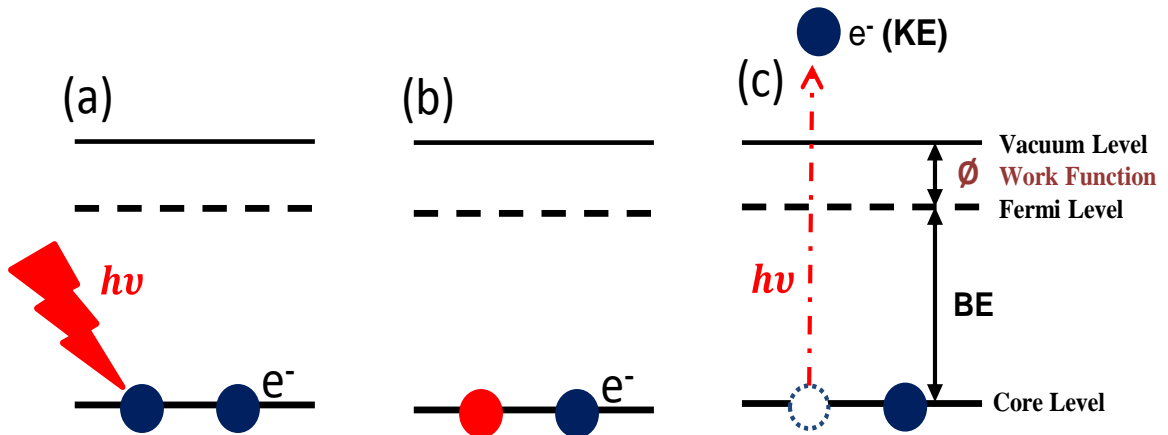


**Figure 2.4:** Schematic representation of a single photon/electron ejection process.

An XPS spectrum is a plot of the measured photoelectron intensity as a function of the binding energy. Since the binding energies of the electron orbitals in atoms are known, the positions of the peaks in the spectrum allow the qualitative identification of the elemental composition of the sample surface. The intensity of the peaks is related to the concentrations of the elements under study. The binding energies of a particular element depend on its chemical state (the electronic environment of the element). Very small shifts in the binding energies can be utilized in determining the oxidation states of an element.

## 2.2 EXPERIMENTAL PROCEDURES

### 2.2.1 Solution preparation

All solutions were freshly prepared before each experiment using water purified using a NANOpure Diamond UV ultrapure water system (Barnstead International). The purified water had a consistent resistivity of 18.2 M $\Omega$ -cm. High-purity potassium dichromate (K<sub>2</sub>Cr<sub>2</sub>O<sub>7</sub>) obtained from Sigma-Aldrich (purity  $\geq$  99%) was used without further purification for the formation of chromium nanoparticles. Cobalt solutions were prepared by dissolving high-purity cobalt (II) sulfate obtained from Sigma-Aldrich (purity  $\geq$  99%) for the formation of cobalt nanoparticles. Pure water was first purged with ultra high purity argon (Praxair, impurity content 0.001%) for more than one hour and then transferred to an argon-filled glove box for a de-aerated solution preparation. The oxygen level in the glove box was maintained below 0.1 volume percent. Solutions containing dissolved Cr<sup>VI</sup> or Co<sup>II</sup> were prepared and the pH of the solution (measured using a Toledo pH meter) was adjusted to 6.0, 8.5 and 10.6 using a sodium hydroxide solution inside the glove box. The solutions were then transferred into test vials in the glove box (20 ml, pyrex, Agilent Technologies) and sealed using PTFE silicon septa. For aerated sample tests, solutions were first prepared and then purged high purity air (Praxair, hydrocarbon free air) for one hour. Using a syringe, this aerated solution was transferred to pre-sealed vials leaving no headspace.

### 2.2.2 Irradiation procedure

The sample vials were placed in a custom-designed sample holder to ensure a uniform radiation dose to all of the samples throughout the irradiation period, as illustrated in Figure 2.5. The irradiation was carried out in a  $^{60}\text{Co}$  gamma cell 220 Excel (MDS Nordion) that provided the irradiation chamber with a uniform absorption dose rate between 4 and 6.7  $\text{kGy}\cdot\text{h}^{-1}$  determined by using Fricke Dosimetry [9, 10]. The dose rate varied over the period in which the experiments were conducted due to decay of the  $^{60}\text{Co}$  source.

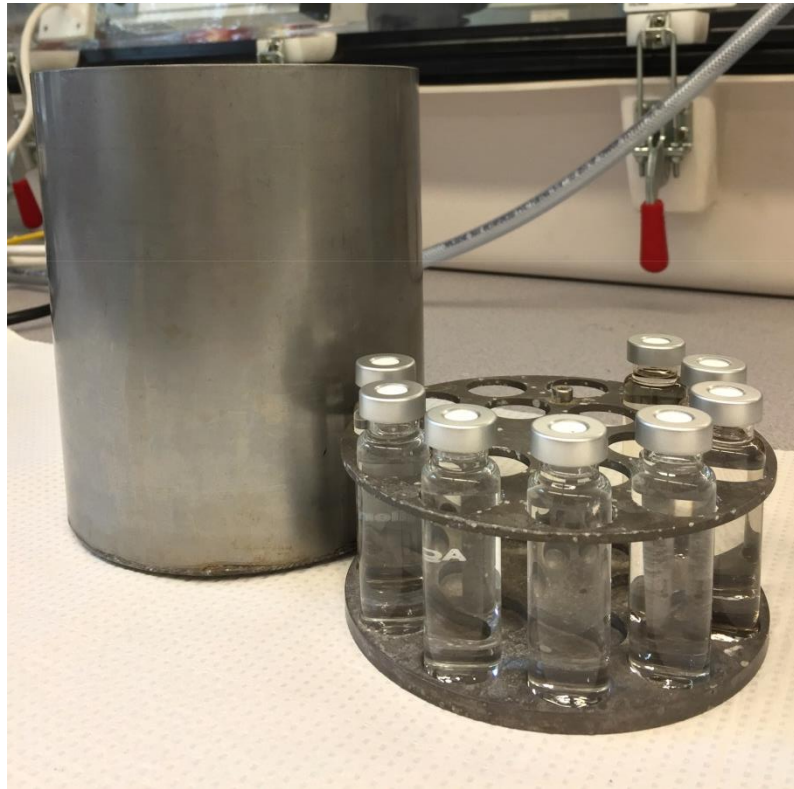


**Figure 2.5:** The sample vials with the custom designed sample holder for the gamma cell experiments.

The  $^{60}\text{Co}$  isotope has a half-life of 5.27 years and emits two characteristic  $\gamma$ -rays at 1.332 MeV and 1.173 MeV. A  $\beta$ -particle is also emitted with energy of 0.318 MeV, but this particle is blocked by the metal shielding around the sample container.

### 2.2.3 Sample analysis

Following irradiation for a desired period, individual vials were removed from the irradiation chamber to allow for gas and aqueous phase analysis. These chemical analyses were performed before the colloidal particles were collected for analysis.

#### 2.2.3.1 Gas phase analysis

For analysis of dissolved  $\text{H}_2$ , one half (10 mL) of the irradiated test solution was transferred to a new 20 mL vacuum-tight vial using a gas-tight syringe (Hamilton). Equilibration of the gas concentrations in the headspace above the solution and in the aqueous phase was quickly established. A gas sample was extracted from the headspace using a gas-tight syringe with a Luer lock (Agilent Technologies) and was analyzed using a gas chromatograph with a thermal conductivity detector (GC-TCD, 6580 Agilent Technologies) [11]. The GC consists of a GS-GASPRO column and nitrogen was used as the carrier gas at a flow rate of 4.6 ml/min. The aqueous phase  $\text{H}_2$  concentrations were calculated from the measured gas phase concentrations using the known aqueous-gas partition coefficients (0.019 for  $\text{H}_2$  at  $25^\circ\text{C}$  ( $[\text{C}_{\text{aq}}]/[\text{C}_{\text{g}}]$ , both concentrations in  $\text{mol}\cdot\text{dm}^{-3}$  [12])). Using this method, the detection limit for the aqueous  $[\text{H}_2]$  was  $1.0 \times 10^{-5}$   $\text{mol}\cdot\text{dm}^{-3}$  and the uncertainties in the measurement arising from sampling and

instrumental errors were estimated to be  $\pm 50\%$  at the low end of the measured concentration range and  $\pm 0.005\%$  at the high end of the concentration range.

### **2.2.3.2 Aqueous phase analysis**

The aqueous phase was analyzed by UV spectrophotometry for hydrogen peroxide and dissolved metal (Cr and Co) speciation. All spectrophotometric measurements were performed using a diode array UV spectrophotometer (BioLogic Science Instruments). The colorimetric methods used for the analysis of hydrogen peroxide and Cr and Co speciation are described in detail below.

#### **2.2.3.2.1 Hydrogen peroxide analysis (Ghormley tri-iodide method)**

The hydrogen peroxide analysis was performed immediately after the termination of irradiation to minimize the thermal decomposition of  $\text{H}_2\text{O}_2$  in the sample vials. The concentration of hydrogen peroxide was determined by the Ghormley tri-iodide method [13]. In the presence of an ammonium molybdate catalyst,  $\text{I}^-$  is oxidized to  $\text{I}_3^-$  by  $\text{H}_2\text{O}_2$ . The  $\text{I}_3^-$  ion has a maximum absorption at 350 nm with a molar extinction coefficient of  $25500 \text{ M}^{-1}\cdot\text{cm}^{-1}$  [14]. From a calibration curve that was obtained, the detection limit for  $[\text{H}_2\text{O}_2]$  was determined to be  $3 \times 10^{-6} \text{ mol}\cdot\text{dm}^{-3}$ , Figure 2.6.



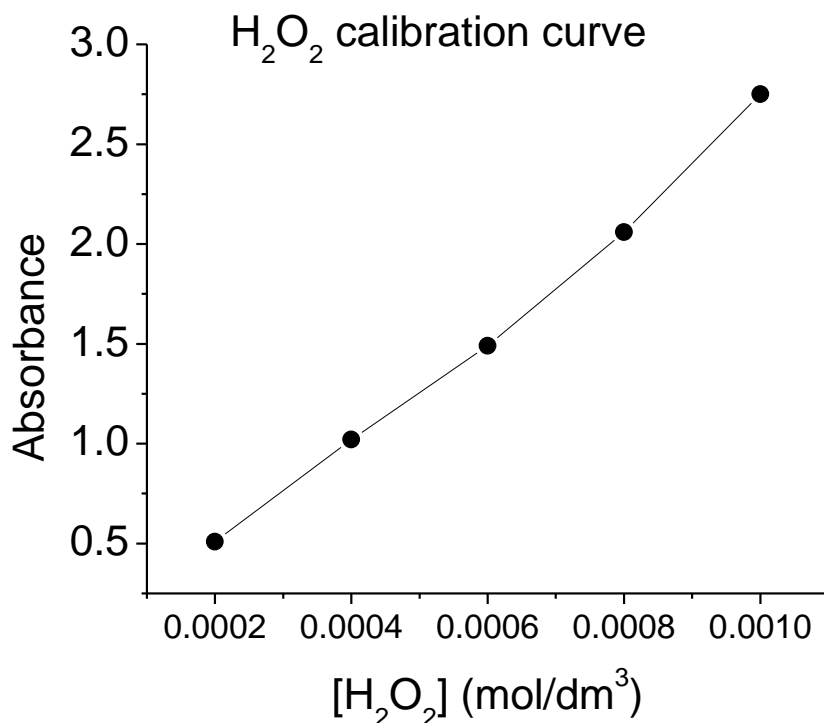


**Figure 2.6:** Calibration curve for H<sub>2</sub>O<sub>2</sub> using Ghormley tri-iodide method.

#### 2.2.3.2.2 Cobalt (Co<sup>II</sup> and Co<sup>III</sup>) analysis (PAR colorimetric method)

The total concentration of Co<sup>III</sup> present in a sample (dissolved or dispersed as a colloidal solid) was determined by reacting the sample with 4-(2-pyridylazo) resorcinol (PAR) (Sigma-Aldrich (ACS reagent)). This form a coloured complex that absorbs light at 510 nm with a molar extinction coefficient of  $5.6 \times 10^4 \text{ M}^{-1}\cdot\text{cm}^{-1}$  [15]. To determine the concentration of Co<sup>II</sup> present, the Co<sup>II</sup> in the sample was first oxidized to Co<sup>III</sup> using a 3% hydrogen peroxide solution. Then the solution was heated to 100 °C in a boiling water bath to remove any unreacted hydrogen peroxide. The Co<sup>III</sup> concentration of this

solution was then determined by the PAR method. The difference between this total cobalt concentration (measured after oxidation) and the concentration of  $\text{Co}^{\text{III}}$  measured before oxidation gives the concentration of  $\text{Co}^{\text{II}}$  in the sample.

#### 2.2.3.2.3 Chromium ( $\text{Cr}^{\text{VI}}$ and $\text{Cr}^{\text{III}}$ ) analysis (DPC colorimetric method)

The concentration of  $\text{Cr}^{\text{VI}}$  was determined using the diphenylcarbazide (DPC) colorimetric method (Sigma-Aldrich (ACS reagent)). Here DPC reacts with  $\text{Cr}^{\text{VI}}$  to form a coloured complex that absorbs light at 540 nm [16]. A calibration curve for  $\text{Cr}^{\text{VI}}$  over the concentration range of 0.01 to 1mM was generated. The molar extinction coefficient of  $39032 \text{ M}^{-1}\cdot\text{cm}^{-1}$  obtained from the calibration curve is comparable to the reported value of  $34400 \text{ M}^{-1}\cdot\text{cm}^{-1}$  [16]. Gamma-irradiation reduces  $\text{Cr}^{\text{VI}}$  to  $\text{Cr}^{\text{III}}$  which then forms colloidal particles that are comprised of  $\text{Cr}(\text{OH})_3$ ,  $\text{CrOOH}$ , and  $\text{Cr}_2\text{O}_3$ . The concentration of  $\text{Cr}^{\text{III}}$  particles dispersed in the solution samples was determined by first oxidizing a sample solution containing  $\text{Cr}^{\text{III}}$  particles with a potassium permanganate solution (Sigma-Aldrich (ACS reagent)) to form dissolved  $\text{Cr}^{\text{VI}}$ , and then by measuring the  $\text{Cr}^{\text{VI}}$  concentration in the sample using the DPC method. The  $\text{Cr}^{\text{III}}$  particle concentration was calculated by subtracting the dissolved  $\text{Cr}^{\text{VI}}$  concentration (measured before oxidation) from the total  $\text{Cr}^{\text{VI}}$  concentration determined after oxidation.

### 2.2.3.3 Particle analysis

Particles collected from the sample vials were analyzed by transmission electron microscopy, X-ray photoelectron spectroscopy, Fourier transform infrared spectroscopy and Raman spectroscopy.

Samples for TEM were prepared by dipping a carbon-coated copper grid into the irradiated test solution and then drying the sample grid in air. The TEM images were obtained with a Philips Electronics Ltd. electron microscope operated at 80 keV.

For the XPS, FTIR and Raman analyses particles were collected by centrifuging a test solution. The particles were then dried on a glass plate in an argon-purged glove box. FTIR spectroscopy was performed with a Bruker, Vertex 70v instrument in the 400 to 4000  $\text{cm}^{-1}$  range. The dried particle sample was incorporated into a KBr pellet for the FTIR measurement. A standard  $\text{Cr}_2\text{O}_3$  spectrum was measured using the same method. XPS spectra were acquired on a KRATOS Axis Nova spectrometer using monochromatic  $\text{Al K}_\alpha$  radiation and operating at 210 W with a base pressure of  $10^{-8}$  Pa. The analysis depth of the XPS instrument is 6-7 nm. Raman measurements were performed using a Renishaw model 2000 Raman spectrometer with a laser excitation wavelength of 633 nm.

## 2.3 REFERENCES

- [1] D.D.A. Skoog, F.J. Holler, S.R. Crouch (6th Ed.). *Principles of Instrument Analysis*, Thomson Brooks Cole, Belmont, CA, 2007.
- [2] T. Owen, *Fundamentals of Modern UV-visible Spectroscopy*, Agilent Technologies, Germany, 2000.
- [3] R.L. McCreery, *Raman Spectroscopy for Chemical Analysis*, John Wiley & Sons, New York, NY, 2000.
- [4] J.R. Ferraro, *Introductory Raman Spectroscopy*, Academic Press, San Diego, CA, 1994.
- [5] D.R. Vij, *Handbook of Applied Solid State Spectroscopy*, Springer, New York, 2006.
- [6] D.L. Pavia, G.M. Lampman, G.S. Kriz (3<sup>rd</sup> Ed.). *Introduction to Spectroscopy*, Thomson Learning Inc., Toronto, ON, 2001.
- [7] C. Berthomieu, R. Hienerwadel, *Photosynth. Res.*, 101 (2009) 157.
- [8] D.J. O'Connor, B.A. Sexton, *Surface Analysis Methods in Materials Science*, Springer-Verlag, Berlin, Germany, 1992.
- [9] S.N. Upadhaya, N.K. Ray, H.C. Goel, *Indian J. Nucl. Med.*, 17 (2002) 35.
- [10] J.W.T. Spinks and R.J. Woods, *An Introduction to Radiation Chemistry*, Wiley-Interscience, New York, 1990.
- [11] J.M. Joseph, B. Seon Choi, P.A. Yakabuskie, J.C. Wren, *Radiat. Phys. Chem.*, 77 (2008) 1009.
- [12] P.A. Yakabuskie, J.M. Joseph, J.C. Wren, *Rad. Phys. Chem.*, 79 (2010) 777.
- [13] C.J. Hochanadel, *J. Phys. Chem.*, 56 (1952) 587.

- [14] I. Stefanic, J.A. Laverne, *J. Phys. Chem. A*, 106 (2002) 447.
- [15] T. Yotsuyanagi, R. Yamashita, K. Aomura, *Anal. Chem.*, 44 (1972) 1091.
- [16] T. Shigematsu, S. Gohda, H. Yamazaki, Y. Nishikawa, *Bull. Inst. Chem. Res., Kyoto Univ.*, 55 (1977) 429.

## Chapter 3

### Gamma-Radiolysis-Assisted Cobalt Oxide Nanoparticle Formation<sup>1</sup>

#### 3.1 INTRODUCTION

Recently synthesis of nano-scale structured transition metal oxides has been an area of active research due to the many technological applications of such oxide particles. The magnetic, catalytic, optical, and electronic properties of these metal oxides are determined by the size, structure and shape of the particles that they form [1,2]. Nanoparticles containing magnetic materials (such as iron, nickel and cobalt oxides) have potential applications in medical biotechnology, drug delivery and hyperthermic cancer treatment. They can also be used as contrast agents for magnetic resonance imaging (MRI) [3-7]. This type of oxide is a magnetic *p*-type semiconductor with a cubic spinel crystal structure in which  $\text{Co}^{\text{II}}$  occupies the tetrahedral sites and the octahedral sites are occupied by  $\text{Co}^{\text{III}}$  [8]. The properties of  $\text{Co}_3\text{O}_4$  nanoparticles make them promising materials for electronic devices [9], gas sensors [10], magnetic materials [11], electrochromic devices [12], electrochemical anodes for sensors [13], high temperature selective absorbers of solar radiation [14] and anode materials for rechargeable Li ion batteries [1]. Cobalt nanoparticles have also been proposed for use as an alternative to iron oxide nanoparticles as the contrast agent for MRI due to their greater impact on proton relaxation times [1,15].

---

<sup>1</sup> [L.M. Alrehaily, J.M Joseph, M.C. Biesinger, D. Guzonas, J.C. Wren, *Phys. Chem. Chem. Phys.*, 15 (2013) 1014.]-Reproduced by permission of the PCCP Owner Societies.

Cobalt oxide nanoparticles have been synthesized by different techniques including chemical vapour deposition [16], sol-gel techniques [17], pulsed laser deposition [18], thermal decomposition of solid cobalt nitrate [19], and hydrothermal synthesis [1]. These methods are either complex or require chemically harsh conditions and/or high processing temperatures for the synthesis of nano-scale crystalline  $\text{Co}_3\text{O}_4$  particles. Radiolytic particle formation is a promising new technique for the synthesis of  $\text{Co}_3\text{O}_4$  nanoparticles that avoids the need for chemically and thermally extreme conditions.

The potential formation of insoluble cobalt particles is also a particular concern for water-cooled nuclear reactors. Corrosion of metal alloys (and particularly Co-based alloys such as Stellites) can release dissolved Co ions into the reactor coolant water. Dissolved Co species can deposit in the reactor core where neutron activation can convert  $^{59}\text{Co}$  to radioactive  $^{60}\text{Co}$ . Subsequent resuspension/dissolution of the  $^{60}\text{Co}$  and its transport by the coolant to out-of-core piping where it can redeposit can give rise to high radiation fields around system piping. Radiolytic conversion of dissolved  $^{60}\text{Co}$  to colloidal particles will affect the transport and deposition of this radioactive isotope.

Understanding the mechanisms for the formation of cobalt particulates is particularly important because of the radiological hazard posed by the formation of  $^{60}\text{Co}$  [20, 21]. On-line purification systems are used to control the concentrations of dissolved ions (using ion exchange resins) and particulates (using mechanical filters) in the coolant; the efficacy of filters for particle removal depends on the size of the particles present. Therefore, it is important to understand the various mechanisms that can convert dissolved Co species to particles.

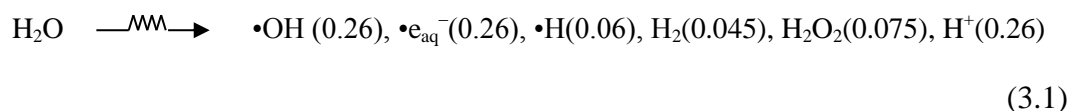
Ionizing radiation includes high energy charged particles (such as  $\alpha$ -particles and fast electrons) and electromagnetic radiation ( $x$ - and  $\gamma$ -rays). Due to its high energy (typically greater than 10 keV), when passing through matter, individual radiation particles or photons lose their energy continuously through a large number of collisions, mostly with electrons in the matter. The initial interaction of ionizing radiation with matter is thus to ionize the molecules or atoms on its track. Since the interaction is indiscriminant, radiolysis is considered as a non-selective, solvent-oriented process [22,23]. This contrasts with the selective, solute-oriented process that occurs in photolysis, where the energy of photons is on the order of a few eVs and can be tuned to the excitation energy of a target solute molecule. One important implication of this difference is that the reactions of dilute chemical species in water exposed to ionizing radiation occur primarily via reactions with radiolytic decomposition products of the solvent water [23]. Their direct interaction with incident radiation is negligible.

The initial consequence of each collision between a radiation particle and a water molecule is to form ion pairs ( $\text{H}_2\text{O}^{\bullet+}$  and  $e^-_{\text{hot}}$ ) or excited species ( $\text{H}_2\text{O}^*$ ) along the radiation track where  $e^-_{\text{hot}}$  represents an energetic electron [22,23]. These hot electrons may themselves have sufficient energy to produce secondary ion pairs ( $\text{H}_2\text{O}^{\bullet+}$  and  $e^-$ ) and excited species before they are thermalized. Any secondary ionization they produce will be situated close to the original ionization (within a few nm or a few atom lengths) in a small cluster, or spur, of excited and ionized species. For water molecules, typically 2-3 ion pairs or excited species are formed in a spur. These energetic species undergo a range of chemical reactions as the spur expands. The distribution of radiolytic decomposition products of water becomes homogeneous along the radiation track on a



time scale on the order of  $10^{-7}$  s. The water decomposition products at this stage are referred to as the primary radiolysis products; while they are not the first species formed upon absorption of radiation energy, they are the first set of relatively stable, longer-lived species.

For a given type of radiation, the chemical yields of the primary radiolysis products at this stage depend mainly on the net absorption energy and, hence, the primary yields are expressed in G-values or the number of molecules produced per absorbed energy. The primary yields depend on the type of radiation and solvent properties. For the  $\gamma$ -radiolysis at room temperature, the primary products and their yields (in bracket in units of  $\mu\text{mol}\cdot\text{J}^{-1}$ ) are [22]:



These chemical yields per unit energy input are very high. Such high yields, particularly for the radicals, cannot be obtained by thermal processes. Gamma-radiolysis is the most effective way of producing these reactive species. Due to the long penetration depth of a typical  $\gamma$ -ray in water ( $\sim 20$  cm for a half reduction in intensity), these species are also produced uniformly over a large volume of water. The high yields and the uniform production of the chemically reactive species at room temperature can provide ideal conditions for certain chemical reactions.

The primary radiolysis products continue to react each other to form secondary products such as  $\cdot\text{HO}_2$ ,  $\text{O}_2$  and  $\cdot\text{O}_2^-$  and eventually the stable products  $\text{H}_2$ ,  $\text{O}_2$  and  $\text{H}_2\text{O}_2$ . Under continuous irradiation, in pure water, the concentrations of radiolysis products quickly reach a pseudo-equilibrium state where the steady-state concentrations of the

radiolysis products depend on radiation energy absorption rate, the solution pH, and temperature [24,25]. The radiolysis products are highly redox active and include both oxidizing (e.g.,  $\bullet\text{OH}$ ,  $\text{H}_2\text{O}_2$  and  $\text{O}_2$ ) and reducing (e.g.,  $\bullet\text{H}$ ,  $\bullet\text{e}_{\text{aq}}^-$  and  $\bullet\text{O}_2^-$ ) species. These species can readily interact with dissolved transition metal ions to change their oxidation states. Since the solubility of a transition metal ion can vary by several orders of magnitude depending on its oxidation state, reactions that can alter the oxidation state can control the concentrations of metal ions in solution. Conversion of dissolved metal species to oxidation states with low solubilities can lead to condensation and the formation of colloidal particles.

The formation of  $\gamma\text{-FeOOH}$  nanoparticles using steady-state radiolysis previously studied [25]. This study has shown that radiolytic oxidation of  $\text{Fe}^{\text{II}}(\text{aq})$  to less soluble  $\text{Fe}(\text{OH})_3$  provides nucleation sites for particle growth and that this oxidation is very fast. Subsequently ferrous ions are continuously oxidized and adsorbed on the nucleates, growing into nano-scale  $\gamma\text{-FeOOH}$  particles. The final size and morphology of the particles is regulated by the radiolytically-induced steady-state redox conditions at the water-solid particle interface and the phase of the oxide.

This chapter describes the mechanism of the formation of  $\text{Co}_3\text{O}_4$  nanoparticles from the Co-containing solutions when exposed to  $\gamma$ -radiation. The effects of pH and dissolved oxygen are investigated. Similarities and differences in particle formation and growth in the iron and cobalt systems are discussed.

## 3.2 EXPERIMENTAL

### 3.2.1 Sample preparation and irradiation process

Cobalt solutions (0.2 and 0.3 mM) were prepared by dissolving high-purity cobalt (II) sulfate obtained from Sigma-Aldrich (purity  $\geq 99\%$ ). All solutions were freshly prepared with water purified using a NANOpure Diamond UV ultrapure water system with a resistivity of 18.2 M $\Omega$ -cm. The pH was adjusted to 6.0 and 10.6 using a concentrated NaOH solution. These pH values were chosen based on the solubilities of Co<sup>II</sup> and Co<sup>III</sup> species [26]. The solubility of Co<sup>II</sup> is at a minimum ( $\sim 10^{-6}$  M) at pH 10.6 whereas it is several orders of magnitude higher ( $\sim 1$  M) at pH 6.0. The solutions were either aerated by purging with high purity air (Praxair) or de-aerated by purging with Ar for one hour. Using a syringe, the test solution was transferred to a pre-sealed 20-ml vial leaving no headspace. The sample vials were irradiated in a <sup>60</sup>Co gamma cell (MDS Nordion) as described in chapter 2. The gamma source provided a uniform absorption dose rate of 5.5 kGy·h<sup>-1</sup> in the water samples at the time of this study.

### 3.2.2 Sample analysis preparation

Following irradiation for the desired period, a series of chemical analyses of solution species were first performed. Colloid particles were then collected for various particle analyses. For the analysis of dissolved H<sub>2</sub> and O<sub>2</sub>, one half (10 ml) of the irradiated test solution was transferred to a new 20 ml vacuum-sealed vial using a gas-tight syringe. Equilibration of the gas concentrations in the headspace above the solution with the gases in the aqueous phase was quickly established. A gas sample was extracted

from the headspace using a gas-tight syringe with a Luer lock (Agilent Technologies) and was analyzed using gas chromatography with a thermal conductivity detector (GC-TCD, 6580 Agilent Technologies) [24]. The solutions were first analyzed for  $\text{Co}^{\text{III}}$  species by direct UV-VIS absorption (BioLogic Science Instruments). The solution cobalt species and  $\text{H}_2\text{O}_2$  were subsequently quantified by colorimetric analysis.

The total concentration of  $\text{Co}^{\text{III}}$  present in the sample (dissolved or dispersed as a colloidal solid) was determined by reacting the sample with 4-(2-pyridylazo) resorcinol (PAR) to form a coloured complex that absorbs light at 510 nm with a molar extinction coefficient of  $5.6 \times 10^4 \text{ M}^{-1} \cdot \text{cm}^{-1}$  [27]. To determine the concentration of  $\text{Co}^{\text{II}}$  present, the  $\text{Co}^{\text{II}}$  in the sample was first oxidized to  $\text{Co}^{\text{III}}$  using a 3% hydrogen peroxide solution and then the solution was heated to  $100^\circ\text{C}$  in a boiling water bath to boil off any unreacted hydrogen peroxide. The  $\text{Co}^{\text{III}}$  concentration of this solution was then determined by the PAR method. The calibration curve for  $\text{Co}^{\text{II}}$  in the concentration range of  $5 \mu\text{M}$  to  $1 \text{ mM}$  obtained by this method is shown in Figure 3.1. The difference between the total cobalt concentration (after oxidation) and the concentration of  $\text{Co}^{\text{III}}$  determined prior to the hydrogen peroxide treatment was taken to be the concentration of  $\text{Co}^{\text{II}}$  in the solution phase. Using this method, the detection limits for both  $[\text{Co}^{\text{II}}]$  and  $[\text{Co}^{\text{III}}]$  were  $1 \mu\text{M}$  [10]. Note that although the experiment tests started with  $0.2$  to  $0.3 \text{ mM}$   $\text{CoSO}_4$  solutions, the total amount of Co found in solution at pH 10.6 was actually less due to the loss of some Co through precipitation. The concentrations determined by the PAR method including the initial  $\text{Co}^{\text{II}}$  concentration,  $[\text{Co}^{\text{II}}(\text{sol})]_0$  are used throughout this chapter.

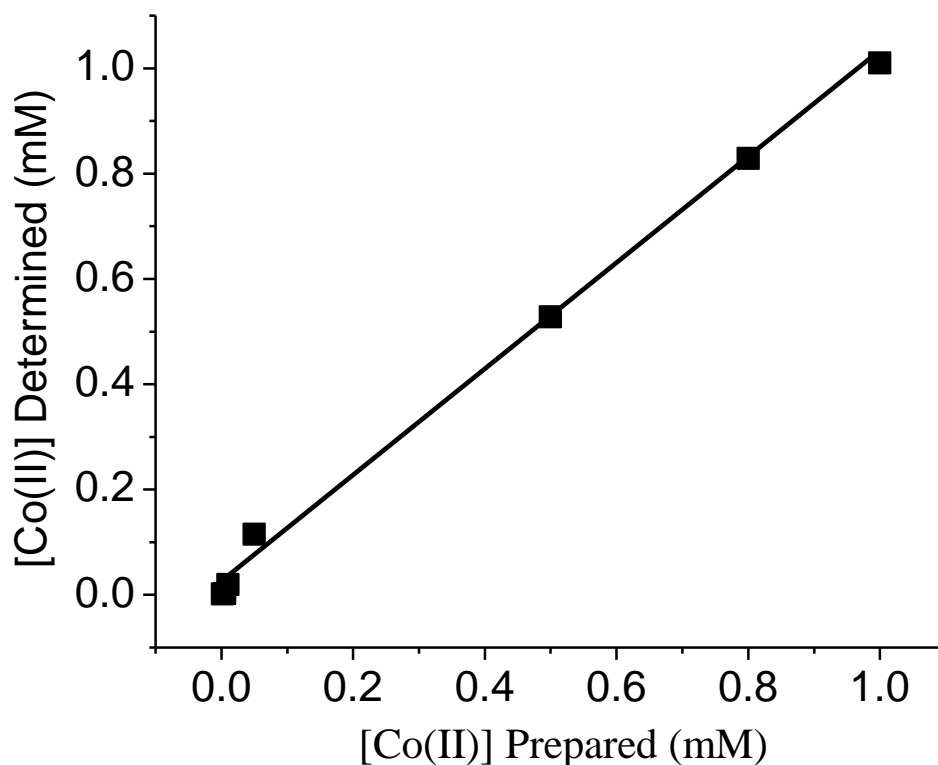


**Figure 3.1:** Calibration curve obtained for  $[\text{Co}^{\text{II}}]$  using the method used in the study.

The concentration of hydrogen peroxide in the test solution was determined by the Ghormley tri-iodide method [28] in which  $\text{I}^-$  is oxidized to  $\text{I}_3^-$  by  $\text{H}_2\text{O}_2$  in the presence of ammonium molybdate as a catalyst, followed by spectrophotometric measurement of the  $\text{I}_3^-$  concentration;  $\text{I}_3^-$  has a maximum absorption at 350 nm with a molar extinction coefficient of  $25500 \text{ M}^{-1} \cdot \text{cm}^{-1}$  [29]. The solution tested for and observed no oxidation of  $\text{I}^-$  to  $\text{I}_3^-$  by  $\text{Co}(\text{III})$  in the test solutions.

### 3.2.3 Particle analysis process

Particles were collected from the sample vials for analyses by transmission electron microscopy (TEM), x-ray photoelectron spectroscopy (XPS) and Raman spectroscopy. For TEM the particles were collected by dipping a carbon-coated copper grid into the irradiated test solution and drying the sample grid in air. Samples for the XPS and Raman analyses were collected by centrifuging the solution and then drying the precipitate on a glass plate in an Ar-purged glove box. The sizes and shapes of the particles were measured using TEM with the microscope operating at 80 keV by dipping TEM grid to the solution. X-ray photoelectron spectra were acquired on a KRATOS Axis Nova spectrometer using monochromatic Al K(alpha) radiation and operating at 210 W, with a base pressure of  $10^{-8}$  Pa. Raman scattering measurements to determine the particle chemical composition were performed using a Renishaw model 2000 Raman Spectrometer with a laser excitation wavelength of 633 nm.

## 3.3 RESULT AND DISCUSSION

### 3.3.1 Solution analyses

No conversion of dissolved  $\text{Co}^{\text{II}}$  to particles was observed at pH 6.0 either in the absence or presence of dissolved oxygen; see further discussion on the effect of pH in Section 3.3.2. Photographs of solutions that initially contained 0.32 mM  $\text{Co}^{\text{II}}(\text{sol})$  at pH 10.6, irradiated for different times, are shown in Figure 3.2. Note that for the photographs the solutions were transferred to new, clear sample vials because the test sample vials darken when exposed to  $\gamma$ -radiation. The corresponding UV-Vis spectra of the test

solutions are shown in Figure 3.3. The pre-irradiated  $\text{CoSO}_4$  solution is colorless but the sample vial contained some precipitate at the bottom due to the conversion of some of the  $\text{CoSO}_4$  to insoluble  $\text{Co}(\text{OH})_2$ . With increasing irradiation time,  $t_{\text{RAD}}$ , the solution becomes increasingly brown in colour and more opaque. The amount of precipitate appeared to increase with  $t_{\text{RAD}}$  up to ~60 min. After this time, the amount of precipitate appeared to decrease (not quantitatively determined) while the solution continued to darken.

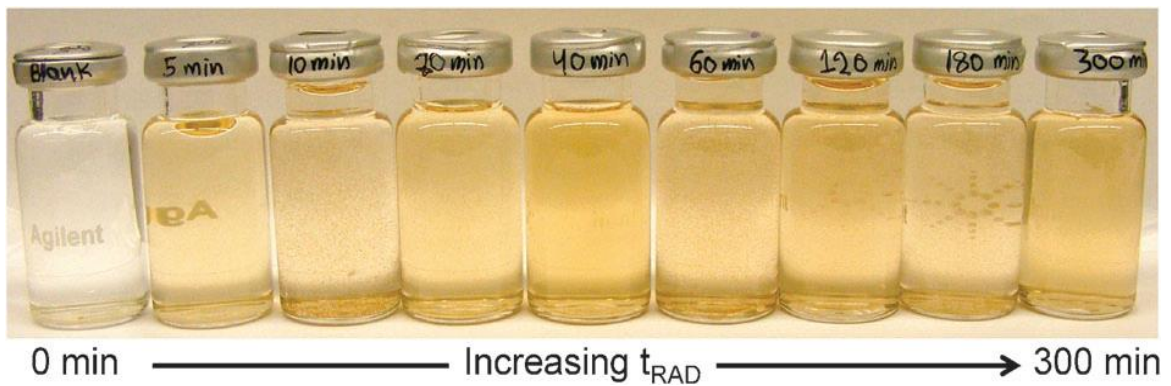


**Figure 3.2:** Photographs of irradiated aerated solutions initially containing 0.3 mM  $\text{CoSO}_4$  at pH 10.6.

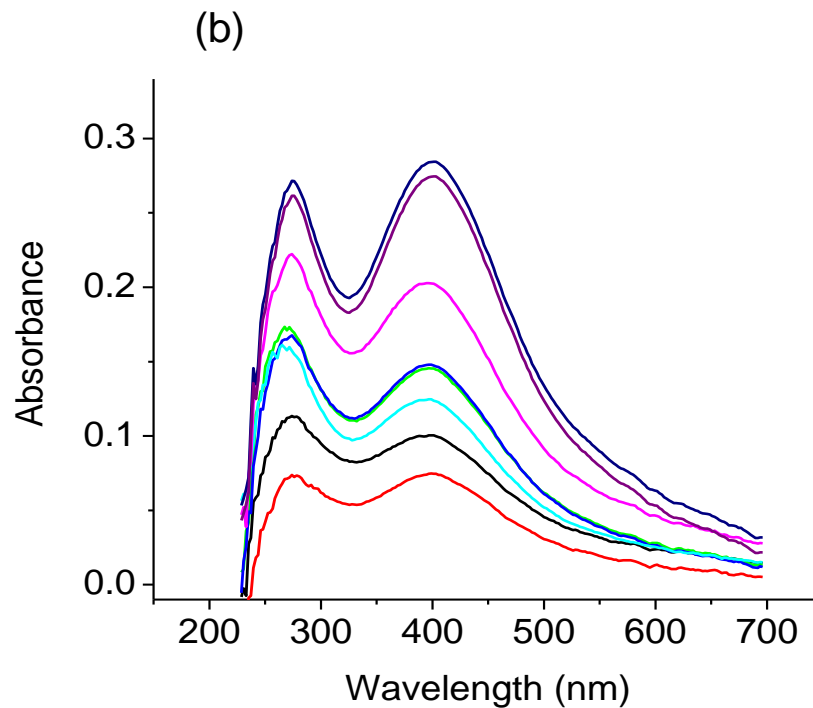
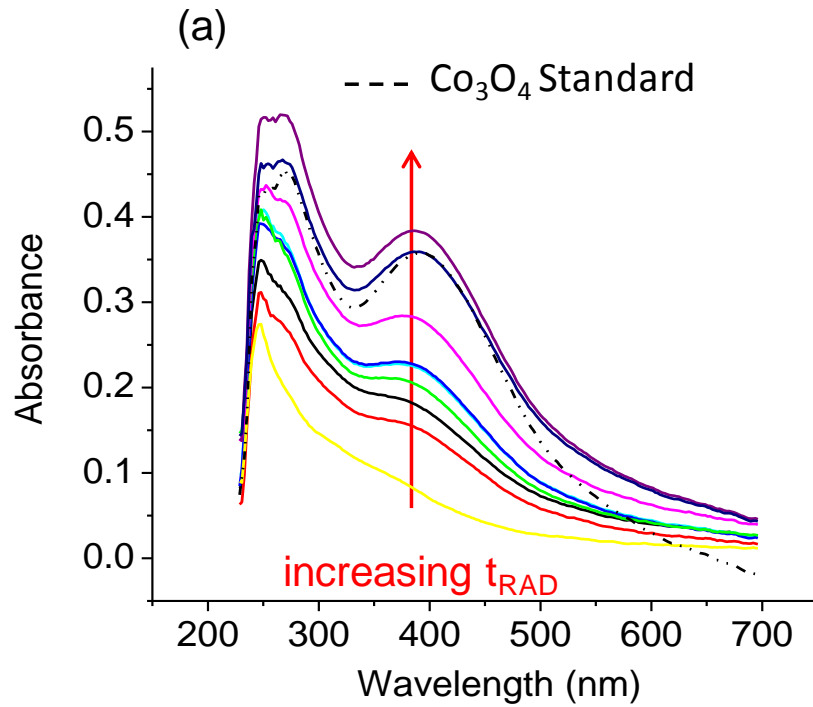


**Figure 3.3:** UV-Vis spectra of irradiated aerated solutions initially containing 0.3 mM  $\text{CoSO}_4$  at pH 10.6: (a) raw spectra and (b) empty-cell background-subtracted spectra. The reference spectrum of  $\text{Co}_3\text{O}_4$  is shown as the dashed curve.



The UV-Vis spectra of the test solutions show increases in the intensities of absorption bands with maxima at ~280 and 400 nm, Figure 3.3a. These spectra match very well with a reference spectrum taken with a solution that was prepared with dispersed  $\text{Co}_3\text{O}_4$  particles. The  $\text{Co}_3\text{O}_4$  used for the reference spectrum was purchased from Alfa Aesar and TEM analysis showed that the diameter of the particles was in the range of 8-20 nm. The similarity indicates that the irradiated test solutions contain  $\text{Co}_3\text{O}_4$  particles and that the colloidal particle density increases with irradiation time. The good agreement between the reference spectrum and the test solution spectra also indicates that  $\text{Co}_3\text{O}_4$  is the only colored species present. The other  $\text{Co}^{\text{III}}$  species,  $\text{CoOOH}$ , does not absorb in the 200 to 700 nm range.

The peak intensity of the background-subtracted band centered at ~400 nm is plotted as a function of  $t_{\text{RAD}}$  in Figure 3.4. These results are compared in the same figure with the concentrations of  $\text{Co}^{\text{III}}$  determined by the PAR method. The two sets of data match very well except at long irradiation times (> 250 min) in deaerated solutions. Compared to the aerated solution cases, the radiolytic conversion of  $\text{Co}^{\text{II}}(\text{sol})$  to  $\text{Co}_3\text{O}_4$  in deaerated solutions is negligible at pH 10.6.

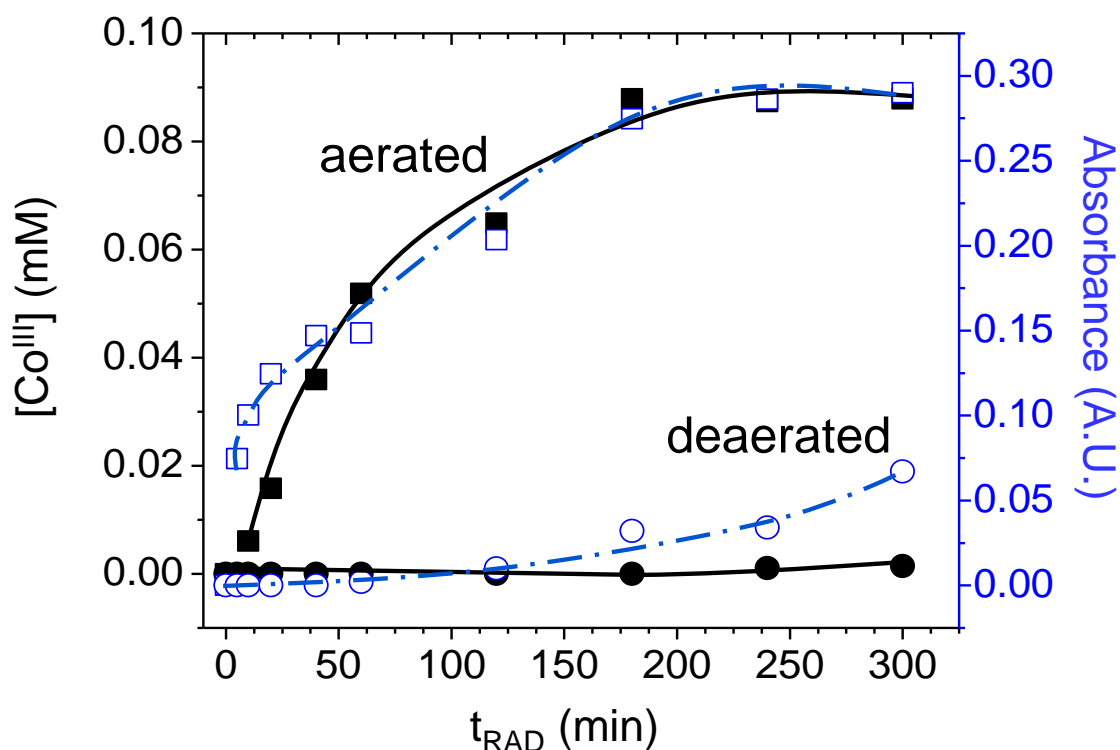


**Figure 3.4:** Concentration of  $\text{Co}^{\text{III}}(\text{sol})$  as a function of irradiation time for aerated (squares) and deaerated (circles) solutions initially containing 0.3 mM  $\text{Co}^{\text{II}}(\text{sol})$  at pH 10.6. The concentrations were determined by the PAR method (solid symbols) and UV-Vis absorbance (open symbols).

The change in the oxidation state of the cobalt in solution as a function of  $t_{\text{RAD}}$  is shown in Figure 3.5. The  $[\text{Co}^{\text{III}}(\text{sol})]$  increases while the  $[\text{Co}^{\text{II}}(\text{sol})]$  decreases before they reach the near plateau regions. The sudden drop in  $\log [\text{Co}^{\text{II}}(\text{sol})]$  at 200 min is attributed to a continuous linear decrease in  $[\text{Co}^{\text{II}}(\text{sol})]$  with time and not due to a change in the mechanism. However, the total cobalt concentration in solution at any given time is not equal to  $[\text{Co}^{\text{II}}(\text{sol})]_0$ . This discrepancy can be better appreciated in Figure 3.5 where the change in  $[\text{Co}^{\text{II}}(\text{sol})]$  ( $\Delta[\text{Co}^{\text{II}}(\text{sol})] = [\text{Co}^{\text{II}}(\text{sol})]_0 - [\text{Co}^{\text{II}}(\text{sol})]$ ) is shown as well as the

curve for  $[\text{Co}^{\text{III}}]$ . The discrepancy increases with irradiation time and then reaches a steady-state value after the test solution has been irradiated for approximately 55 min. This discrepancy is attributed to the loss of cobalt that has settled as a solid precipitate at the bottom of the test vial (Figure 3.2).

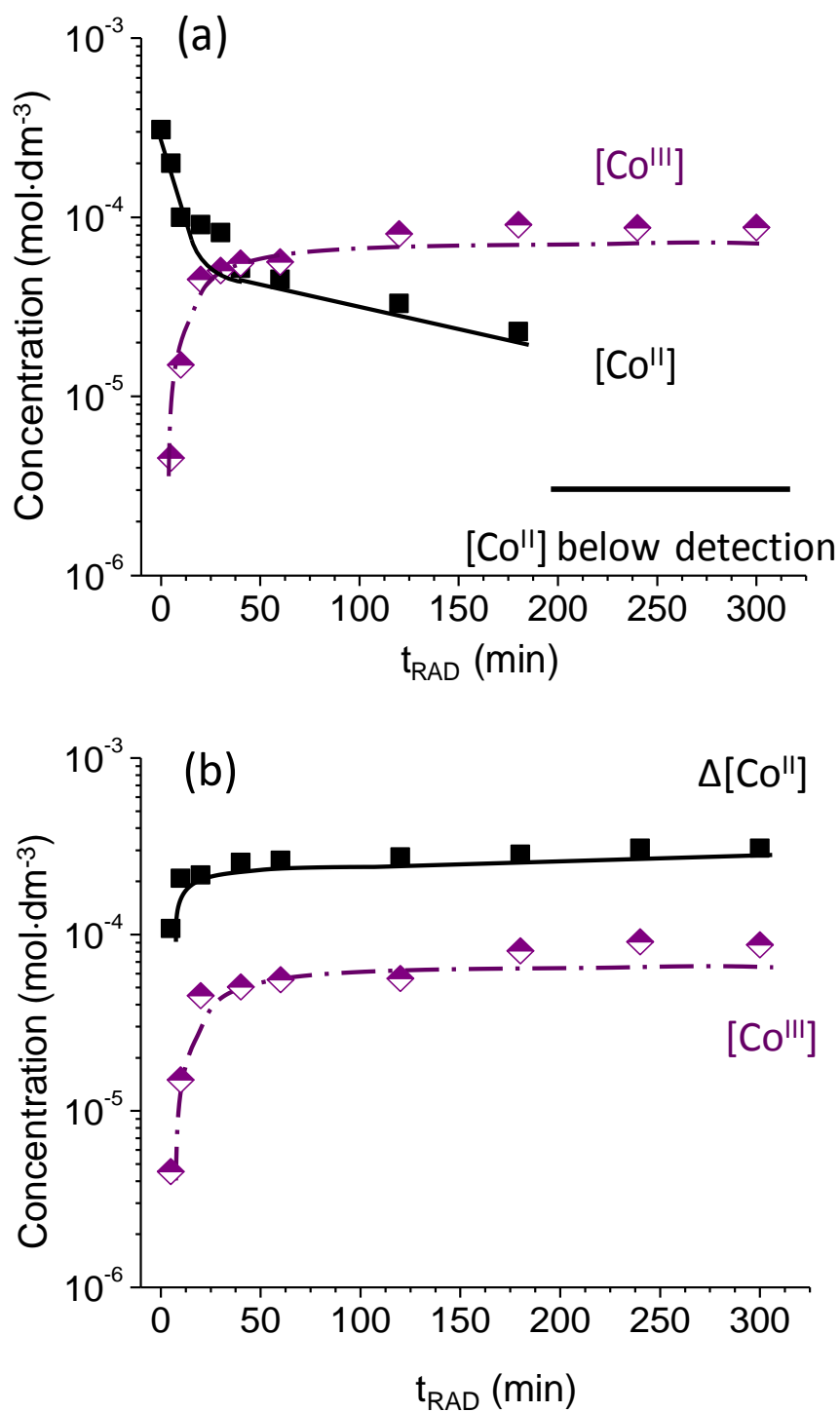
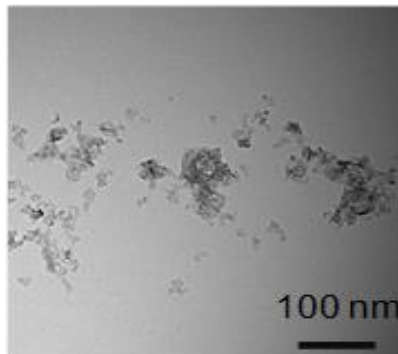


**Figure 3.5:** (a) Concentrations of  $\text{Co}^{\text{II}}(\text{sol})$  and  $\text{Co}^{\text{III}}(\text{sol})$  as a function of irradiation time. (b) The  $\Delta[\text{Co}^{\text{II}}(\text{sol})]$  and  $[\text{Co}^{\text{III}}(\text{sol})]$  in the irradiated solutions initially containing 0.3 mM  $\text{Co}^{\text{II}}(\text{sol})$  under air-saturated pH 10.6 conditions.

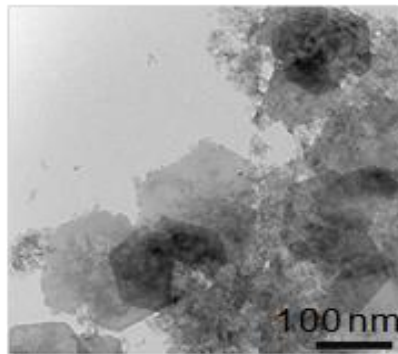
### 3.3.2 Particle analyses

The colloid particles formed by  $\gamma$ -irradiation of the  $\text{Co}^{\text{II}}$  solutions were collected for various particle analyses. Solid particles of  $\text{Co}(\text{OH})_2$  formed in aerated solutions at pH 10.6 without irradiation were also collected for analysis. The TEM images of the particles formed as a function of  $t_{\text{RAD}}$  are shown in Figure 3.6. The TEM images show the presence of two types of particles that have very different sizes. The larger particles are  $\sim 200$  nm in width and have a thin hexagonal shape. These particles are present in non-irradiated solutions and in irradiated solutions at irradiation times  $< \sim 60$  min. At longer irradiation times, few of these particles are present. They are replaced by smaller particles, 8-20 nm in size and spherical in shape.

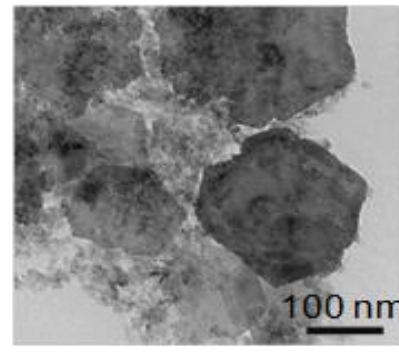
$t_{\text{RAD}} = 0 \text{ min}$



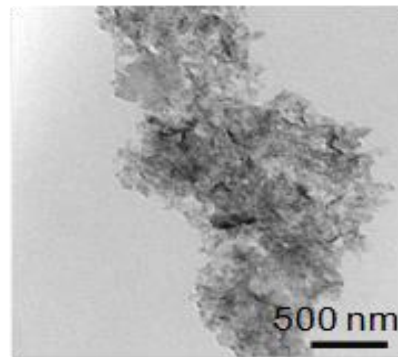
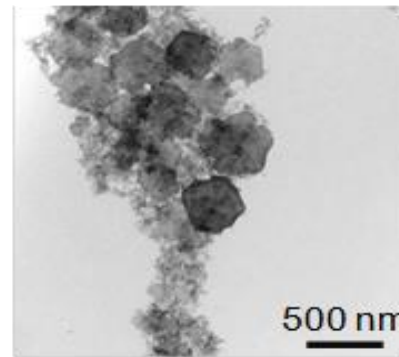
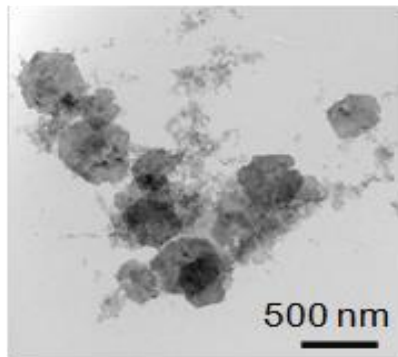
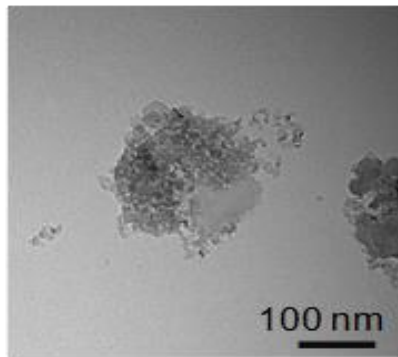
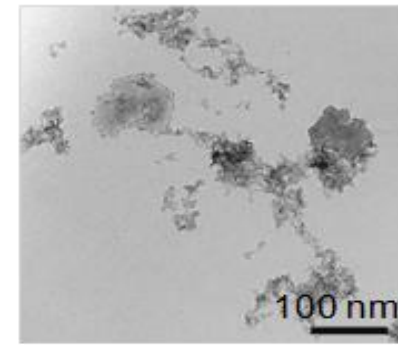
5 min



10 min

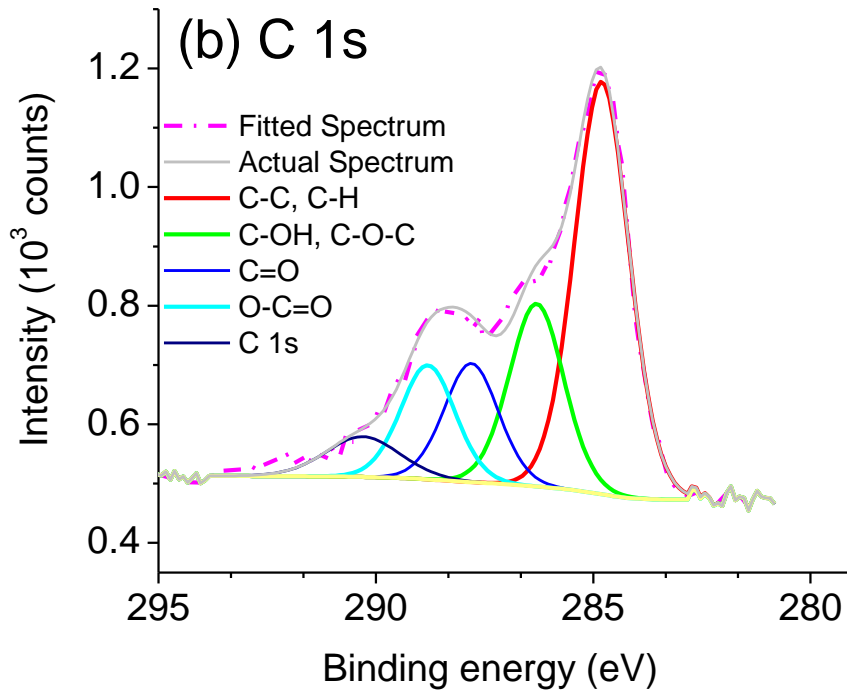
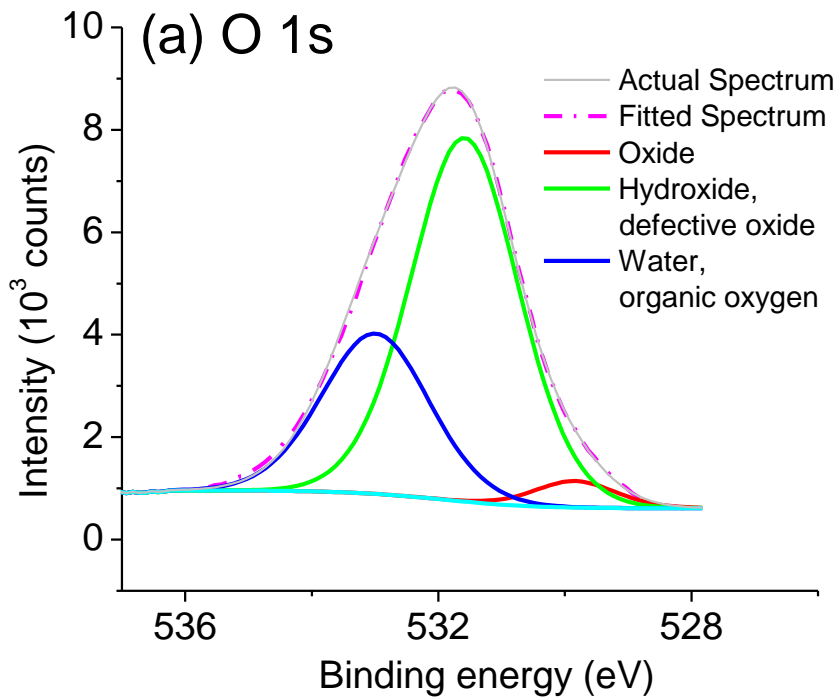


60 min

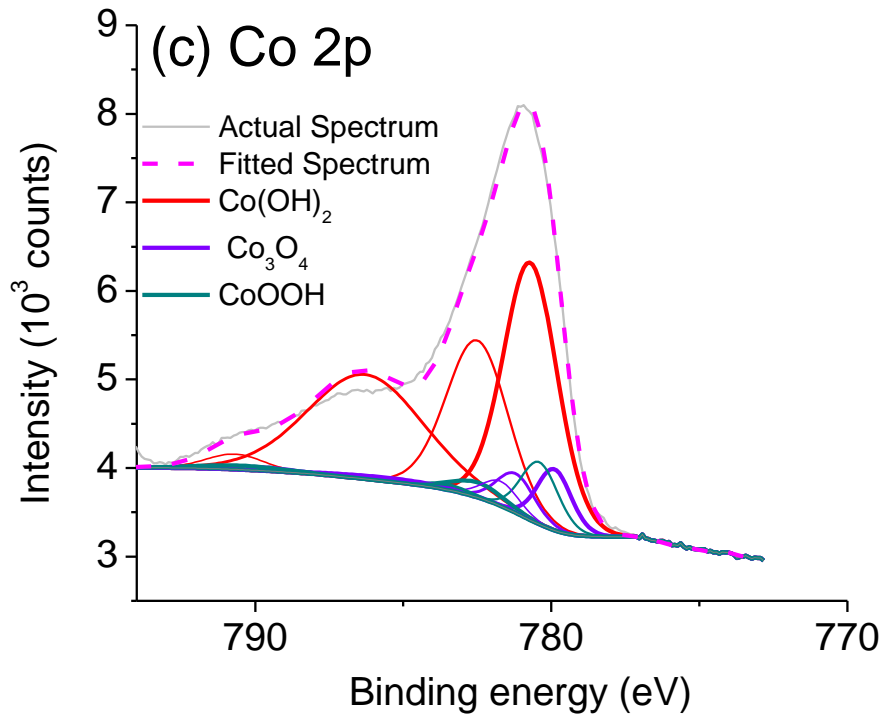


**Figure 3.6:** TEM images of the particles collected at different irradiation times from aerated solutions initially containing 0.3 mM  $\text{Co}^{\text{II}}(\text{sol})$  at pH 10.6.

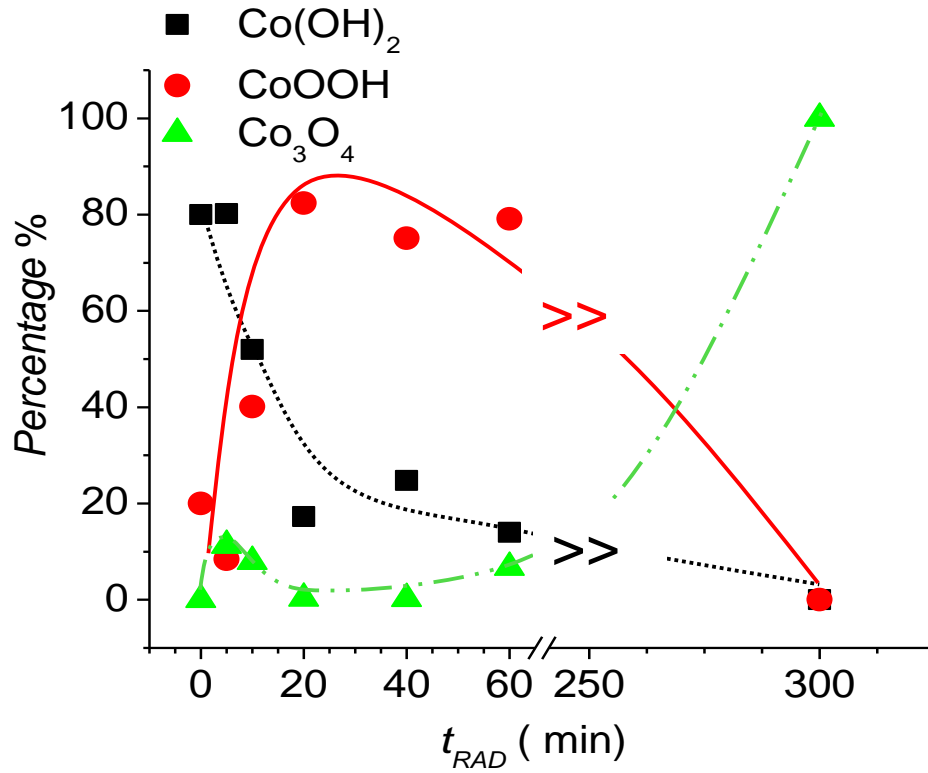
The particles were further examined by XPS and Raman spectroscopy to determine their chemical and phase composition. Typical high resolution XPS spectra of the regions containing the O 1s, C 1s and Co 2p bands are shown in Figure 3.7. The high resolution XPS spectra of the Co 2p band were deconvoluted using reference spectra of standard single-phase samples of  $\text{Co}^0$ ,  $\text{Co(OH)}_2$ ,  $\text{CoO}$ ,  $\text{Co}_3\text{O}_4$ ,  $\text{CoOOH}$ , and  $\text{CoCr}_2\text{O}_4$  (which have binding energies of 778.1 eV, 780.4 eV, 780.0 eV, 779.6 eV, 780.1 eV and 778.8 eV, respectively) [30]. Similarly, the O 1s and C 1s bands were deconvoluted to identify the different O components. The deconvolution of XPS bands using multiple-peak reference spectra with a Shirley-type background subtracted has been successfully applied for cobalt oxide analysis [30]. Commercial software (CASAXPS®) was used for the deconvolution fitting analysis. The weighting factors yield the relative concentrations of individual species in the Co oxide particles and the results are summarized in Figure 3.8. It should be noted that the analysis depth of the XPS instrument is 6-7 nm so that the derived compositions strictly apply only to the outer layer of the particles. The XPS results show that the fraction of  $\text{Co(OH)}_2$  in the particle decreases with irradiation time while the fraction of  $\text{Co}_3\text{O}_4$  increases. The fraction of the particle that is  $\text{CoOOH}$  initially increases, reaching a maximum at ~50 min, and then decreases. The particles collected from the solutions irradiated for long times (> 300 min) contain only  $\text{Co}_3\text{O}_4$ . The XPS analyses of particles collected from test solutions that were not subject to irradiation show that they contain ~80%  $\text{Co(OH)}_2$  and ~20%  $\text{CoOOH}$  by percentage. This composition did not change with time over a period of a few weeks.



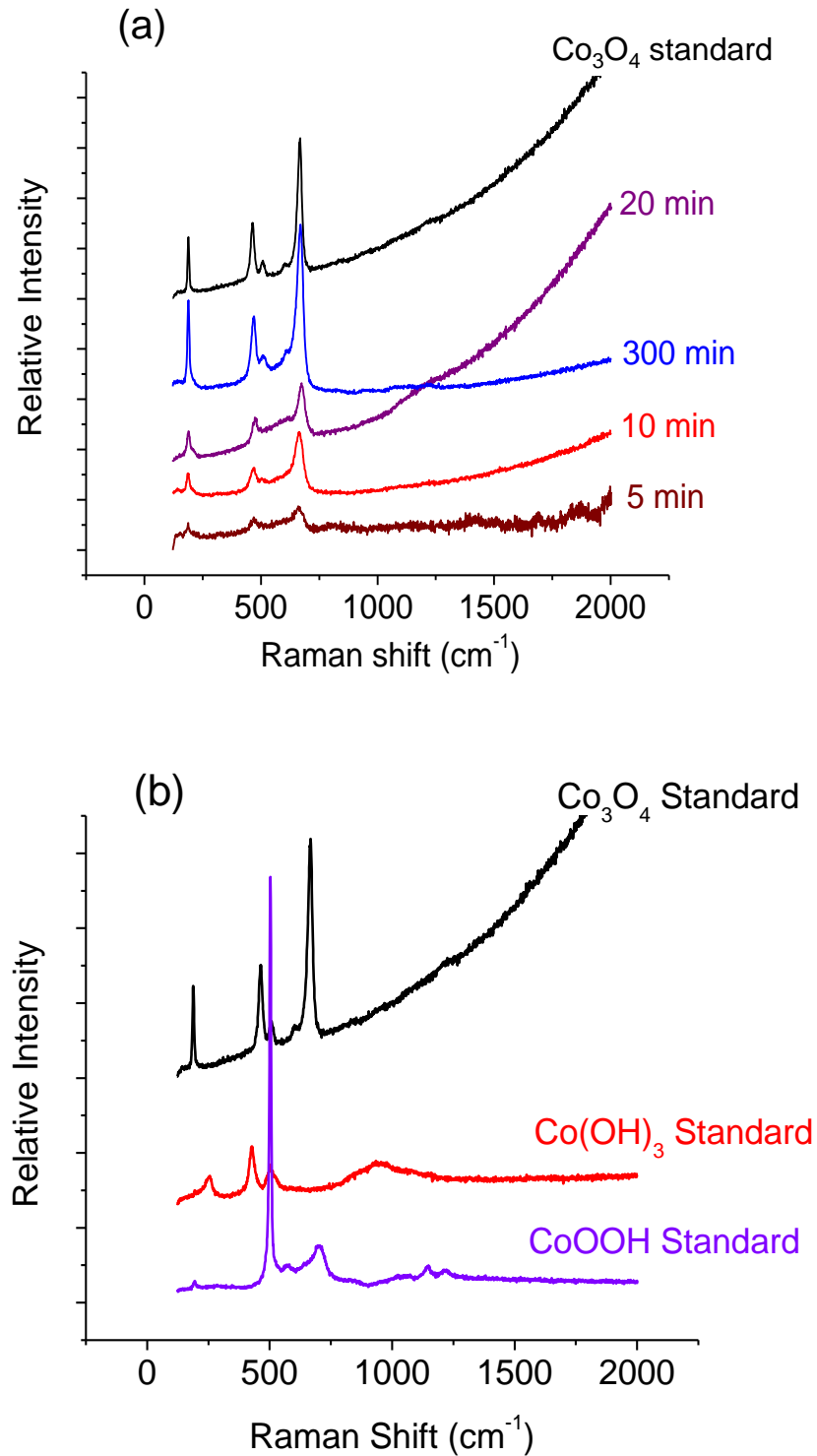




**Figure 3.7:** High resolution XPS spectra of the (a) O 1s, (b) C 1s, and (c) Co 2p bands obtained from particles collected after 5-min of irradiation of a deaerated solution initially containing 0.3 mM  $\text{Co}^{\text{II}}(\text{sol})$  at pH 10.6. Deconvoluted reference spectra and the composite spectra are also shown.

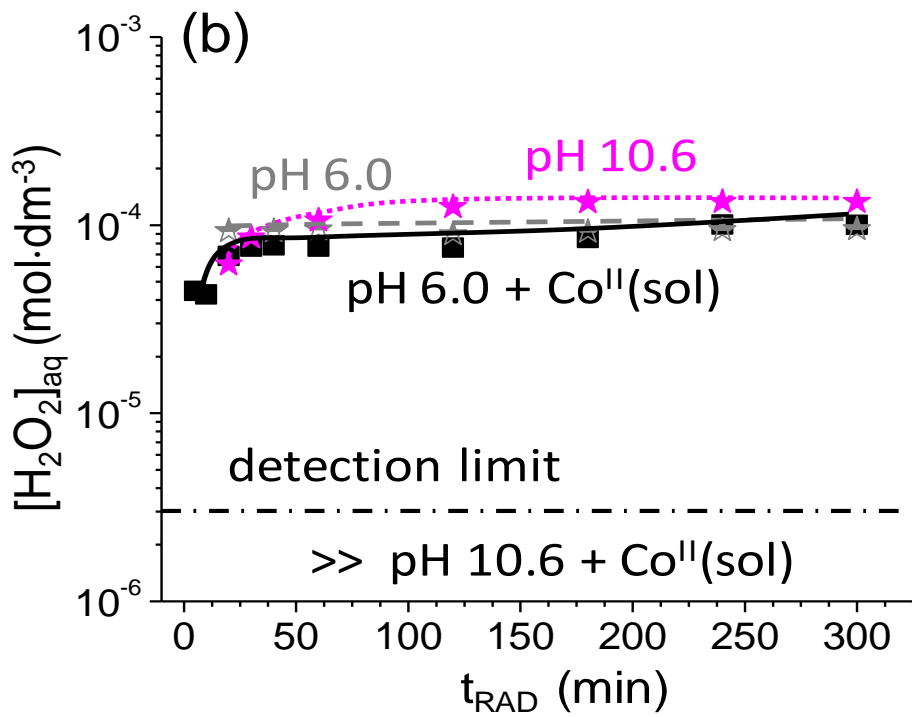
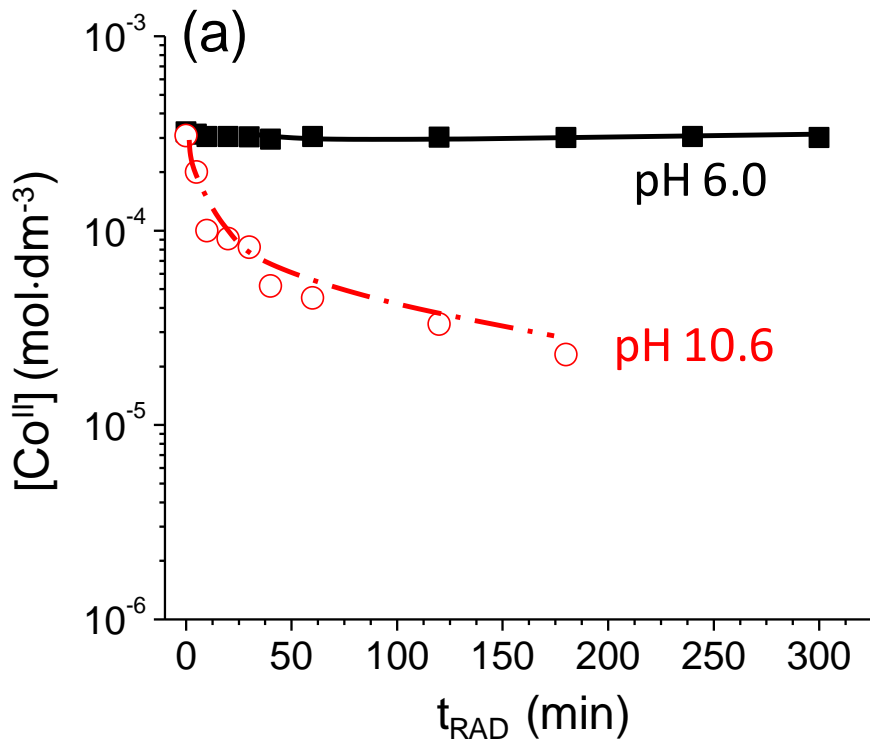


**Figure 3.8:** Composition determined by XPS of particles collected as a function of irradiation time from aerated solutions initially containing 0.3 mM  $\text{Co}^{\text{II}}(\text{sol})$  at pH 10.6 (lines just to indicate the increase and decrease of metal oxide/hydroxide).



**Figure 3.9:** (a) Raman spectra of particles collected as a function of irradiation time from aerated solutions initially containing 0.3 mM  $\text{Co}^{\text{II}}$ (sol) at pH 10.6. (b) Raman spectra of particles prepared from several pure cobalt oxides.

The Raman spectra of particles formed as a function of irradiation time are shown in Figure 3.9. The depth analysis of Raman spectroscopy could not establish, but it is generally considered to be deeper than the XPS technique (on the order of the wavelength of the exciting line depending on the absorption properties of the material) [31]. Comparison of the Raman spectra of the particles from irradiated tests with the reference spectra of different Co oxides (Figure 3.9b) also shows that the particles are composed of only  $\text{Co}_3\text{O}_4$ . A broad band centered at  $3000\text{ cm}^{-1}$  (full width of the peak not shown in Figure 3.9) grows at short irradiation times and then decreases. The origin of this band is not clear but may be attributed to the fluorescence of  $\text{Co}_3\text{O}_4$ , since the broad band also appears in the reference spectrum of  $\text{Co}_3\text{O}_4$  and the Raman excitation laser wavelength (633 nm) is on the edge of the UV-Vis absorption band. It is not clear why this band disappears at longer irradiation times, but it could be that changes in particle size may change the absorption cross section at the excitation wavelength.



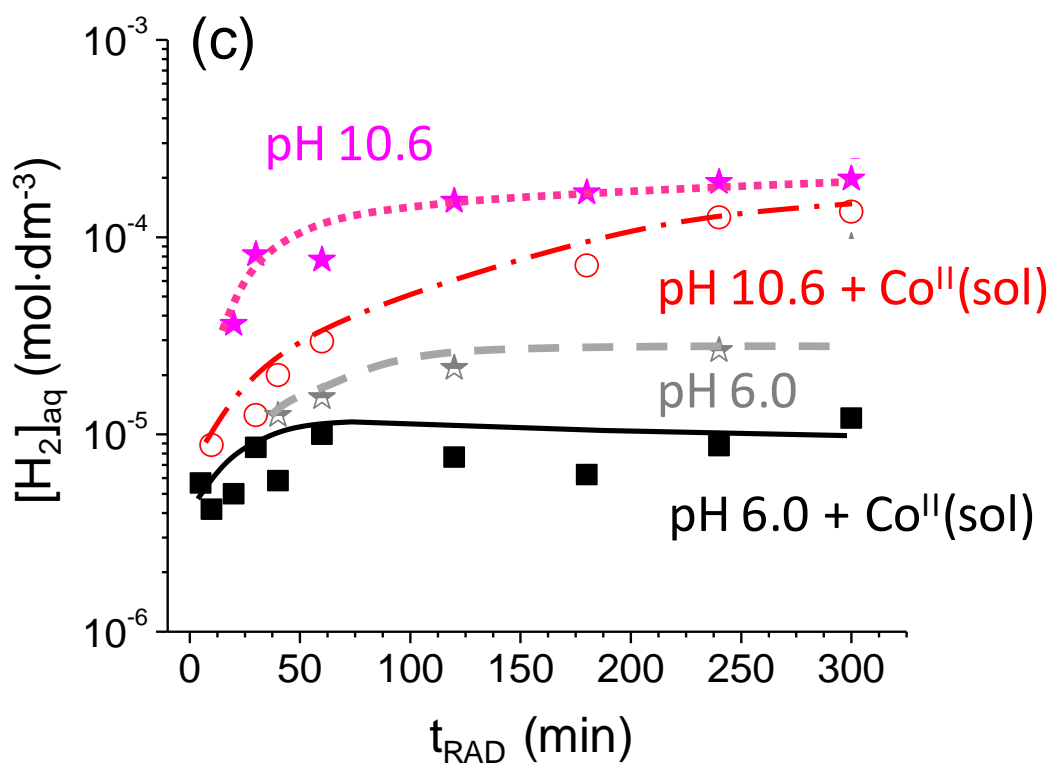


**Figure 3.10:** Concentrations of (a)  $[\text{Co}^{\text{II}}(\text{sol})]$ , (b)  $[\text{H}_2\text{O}_2]$  and (c)  $[\text{H}_2]$  as a function of irradiation time at pHs 6.0 and 10.6 aerated solutions initially containing 0.3 mM  $\text{Co}^{\text{II}}(\text{sol})$ . The  $[\text{H}_2\text{O}_2]$  and  $[\text{H}_2]$  as a function of irradiation time in pure water are also shown for comparison.

### 3.3.3 Effects of pH and dissolved oxygen

The solution pH and dissolved oxygen concentration affect the net radiolytic production of  $\text{H}_2\text{O}_2$  and  $\text{H}_2$  under long-term steady-state irradiation even in the absence of other dissolved species [24]. In the absence of any cobalt ions, the net radiolytic production of  $\text{H}_2\text{O}_2$  as a function of  $t_{\text{RAD}}$  in aerated solution is similar at both pHs, see Figure 3.10. The presence of  $\text{Co}^{\text{II}}(\text{sol})$  in aerated solution does not significantly affect  $[\text{H}_2\text{O}_2]$  at pH 6.0, but significantly reduces  $[\text{H}_2\text{O}_2]$  below  $3 \mu\text{M}$  (the detection limit) at pH 10.6 at all times ( $> 5$  min, at first measurement time). The presence of  $\text{Co}^{\text{II}}(\text{sol})$  in solution also lowers  $[\text{H}_2]$  in an aerated solution but not as dramatically. In deaerated solutions,  $[\text{H}_2\text{O}_2]$  is still below the detection limit at all irradiation times while  $[\text{H}_2]$  is the same as that observed for pure water.

The large change in  $[H_2O_2]$  with  $Co^{II}$  present indicates that  $H_2O_2$  (and its oxidizing radiolysis product precursors) is involved in a reaction with  $Co^{II}(sol)$ . However, since conversion of  $Co^{II}(sol)$  to  $Co^{III}(sol)$  was not observed at pH 6.0 (where equal concentrations of radiolytic  $H_2O_2$  are normally present), the oxidation of  $Co^{II}$  to  $Co^{III}$  observed at pH 10.6 must have an additional requirement. This requirement is the existence of a solid surface on which a heterogeneous oxidation process can occur. The solid surface is initially created by the nucleation and condensation of  $Co(OH)_2$  from the solution. The  $Co(OH)_2$  is formed by hydrolysis of the  $Co^{II}$  initially introduced into the solution as dissolved  $CoSO_4$ :



The overall solubility and the contributions of the various  $Co^{II}$  hydrolysis species to the solubility were calculated as a function of pH based on Baes and Mesmer [26] and are shown in Figure 3.11. The overall solubility of these hydrolyzed  $Co^{II}$  species is low at pH 10.6 ( $\sim 10^{-6}$  M). The solution will be quickly supersaturated with hydrolyzed  $Co^{II}$  species and excess  $Co^{II}$  species will condense as solid  $Co(OH)_2$  when starting with  $\sim 0.3$  mM  $CoSO_4$  solution. Ionic  $Co^{II}$  species are easily adsorbed on the surface of the condensation nucleus and condensed  $Co(OH)_2$  is more likely to form stable nucleates or clusters of  $Co^{II}$  species ( $Co_x(OH)_{2y}^{(x-y)+}$ ) dispersed in solution. Because particles do not grow, no particles could collect when the test solutions were initially deaerated.



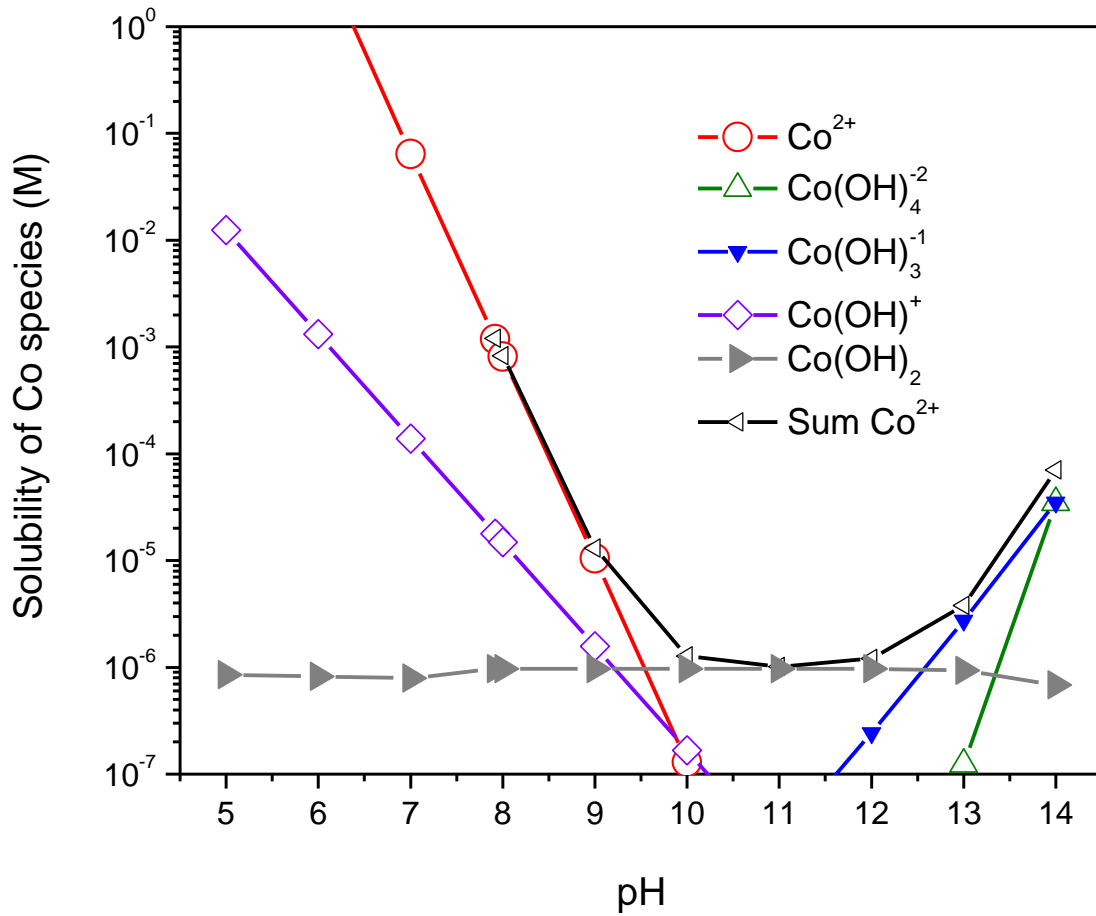
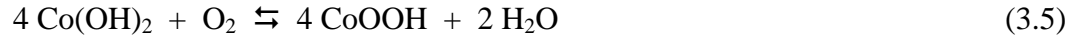


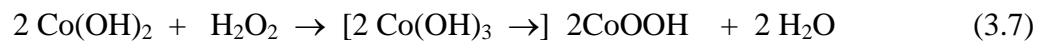
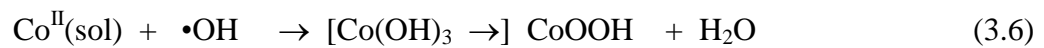
**Figure 3.11:** Overall solubility of  $\text{Co}^{\text{II}}$  hydroxide as a function of pH and the concentrations of the contributing hydroxide species.

The presence of an oxidizing agent ( $O_2$ ) in aerated solutions allows a small fraction of the initial clusters of  $Co_x(OH)_{2y}^{(x-y)+}$  to oxidize to  $Co^{III}$  and form nearly insoluble  $CoOOH$ :



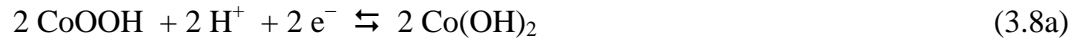
The solubility of  $CoOOH$  is negligible at all pHs [26]. The formation and precipitation of  $CoOOH$  accelerates agglomeration of the  $Co_x(OH)_{2y}^{(x-y)+}$  clusters in solution. The result can be seen in the TEM image (Figure 3.6) and XPS analysis (Figure 3.7) of the particles collected from aerated test solutions without irradiation. The TEM image of the particles collected at  $t_{RAD} = 0$  min shows small particulates congregated in a hexagonal shape and XPS analysis identifies them mostly as  $Co(OH)_2$  with a small fraction as  $CoOOH$ . At pH 6.0 the solubility of  $Co^{II}$  is sufficiently high (Figure 3.11) that no condensation (or precipitation) was observed.

At pH 10.6, no significant reduction in  $[H_2O_2]$  in both aerated and deaerated irradiated solutions (Figure 3.10b) although the conversion of  $Co^{II}(sol)$  to  $Co^{III}(sol)$  is much slower in deaerated solutions (Figure 3.4). These observations can be explained by the difference in the rate of reduction of  $CoOOH$  to  $Co(OH)_2$  in aerated versus deaerated solutions. Upon exposure to  $\gamma$ -irradiation, the  $Co^{II}(sol)$  or  $Co^{II}$  adsorbed on the particles will be quickly oxidized to  $CoOOH$  by  $\bullet OH$  and  $H_2O_2$ :



The electrochemical equilibrium potential for the  $Co(OH)_2$  and  $CoOOH$  redox reaction (reaction (3.8c)) is relatively high, 0.36  $V_{SHE}$  at pH 10.6, where  $V_{SHE}$  is the potential with

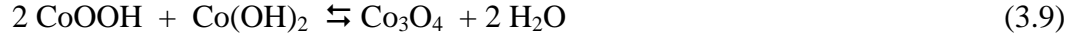
respect to standard hydrogen electrode potential [21]. The  $\text{Co}^{\text{II}}/\text{Co}^{\text{III}}$  equilibrium potential is still lower than the equilibrium potentials for the redox reactions of  $\text{OH}^-/\bullet\text{OH}$  and  $\text{OH}^-/\text{H}_2\text{O}_2$ , and hence  $\text{Co}^{\text{II}}$  can be oxidized by  $\bullet\text{OH}$  and  $\text{H}_2\text{O}_2$ . However,  $\text{H}_2\text{O}_2$  can also oxidize to  $\text{O}_2$ , reaction (3.8b). This reaction can thus couple with the reduction of  $\text{CoOOH}$  (3.8a):



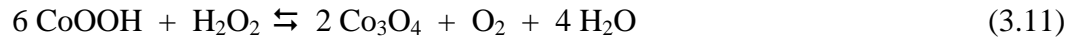
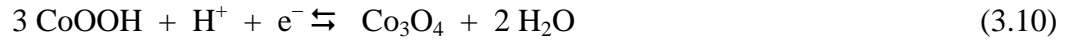
The standard potential for equilibrium (3.8a) is  $E^\circ = 0.695 \text{ V}_{\text{SHE}}$  [32]. The equilibrium (or Nernst) potential depends on pH and the concentrations of  $\text{H}_2\text{O}_2$  and dissolved  $\text{O}_2$ . At pH 10.6, the equilibrium potential for the  $\text{H}_2\text{O}_2$  oxidation equilibrium is  $\sim 0.20 \text{ V}_{\text{SHE}}$  when  $[\text{O}_2]/[\text{H}_2\text{O}_2] = 10^{-3}$  and  $\sim 0.38 \text{ V}_{\text{SHE}}$  when  $[\text{O}_2]/[\text{H}_2\text{O}_2] = 1$ . Thus, at a low dissolved oxygen concentration, the equilibrium potential for (3.8a) lies below that of  $\text{Co(OH)}_2/\text{CoOOH}$ . That shifts the equilibrium (3.8c) to the right and the net production of  $\text{CoOOH}$  will be slow, and so will be the subsequent irreversible conversion of  $\text{CoOOH}$  to  $\text{Co}_3\text{O}_4$ . Consequently no observation of any  $\text{Co}_3\text{O}_4$  formation in deaerated solutions. At a higher  $[\text{O}_2]$  the equilibrium of reaction (3.8c) shifts to the left. The net production of  $\text{CoOOH}$  is increased in aerated solutions, and we in turn see production of  $\text{Co}_3\text{O}_4$ .

The mixed  $\text{Co}^{\text{II/III}}$  oxide,  $\text{Co}_3\text{O}_4$ , is thermodynamically more stable than  $\text{CoOOH}$ . However, the oxidation of  $\text{Co(OH)}_2$  to  $\text{CoOOH}$  is kinetically more facile than oxidation to  $\text{Co}_3\text{O}_4$ . Thus,  $\text{CoOOH}$  will be formed first. At longer times  $\text{CoOOH}$  will be converted

to the thermodynamically more stable  $\text{Co}_3\text{O}_4$  by irreversible processes such as polycondensation of  $\text{CoOOH}$  and  $\text{Co}(\text{OH})_2$ :



The conversion of  $\text{CoOOH}$  to  $\text{Co}_3\text{O}_4$  is also accelerated by the radiolytic reduction of  $\text{CoOOH}$ , reaction (3.10) coupled with reaction (3.8a) resulting in the net reaction (3.11):



The reactions of  $\text{H}_2\text{O}_2$  with cobalt species (reactions 3.7, 3.8 and 3.10) are similar to the Fenton reactions with iron species [33]. We think the Fenton-like reaction occurs more readily under irradiation since the semi-conducting oxide nanoparticles become conducting due to photons with a wide range of energy. The band gap of  $\text{CoO}/\text{Co}_3\text{O}_4$  has been reported to be in a range of 1.4-2.1 eV [8] and electrocatalytic properties of cobalt oxides [33,34] have been reported in literature.

### 3.3.4 Reaction of $\text{H}_2\text{O}_2$ with $\text{Co}^{\text{II}}$ under un-irradiated conditions

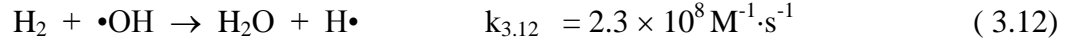
To isolate the role of  $\text{H}_2\text{O}_2$  from that of  $\bullet\text{OH}$  as an oxidizing agent, the reaction of  $\text{Co}^{\text{II}}$  and  $\text{H}_2\text{O}_2$  was studied as a function of  $[\text{H}_2\text{O}_2]$  in a range of 0.1 mM to 10 mM in aerated or deaerated solutions at pH 10.6 with no radiation present. For all test conditions, even after a few weeks of reaction time, we could not detect the formation of any  $\text{Co}_3\text{O}_4$  particles by the PAR method, TEM or XPS. These results confirm that some

radiolysis product, and most likely the hydroxyl radical, is necessary in the mechanism to form cobalt oxide nanoparticles. Normally radical species are not very effective in participating in reactions on particle surfaces due to their low concentrations and the distances required to diffuse to a particle surface. However, under  $\gamma$ -irradiation, nanometer-sized colloid particles will be evenly dispersed in the solution and  $\bullet\text{OH}$  is produced continuously and uniformly throughout the solution. Thus,  $\bullet\text{OH}$  does not have to diffuse far to reach the particle interface where it can react to form  $\text{Co}^{\text{III}}$  species which can then adsorb on the particle. Hydrogen peroxide is also involved in the oxidation of hydrated  $\text{Co}^{\text{II}}$  in the aqueous phase or on the surface of the  $\text{Co}_x(\text{OH})_{2y}^{(x-y)+}$  clusters (reaction (3.7)). However,  $\text{H}_2\text{O}_2$  is also equally effective in reducing  $\text{Co}^{\text{III}}$  back to hydrated  $\text{Co}^{\text{II}}$  (reaction (3.8)) but the net rate of reduction is greatly reduced with  $\text{O}_2$  present. The conversion of hydrated  $\text{Co}^{\text{II}}$  and  $\text{CoOOH}$  is fast due to the reactions (3.6) and (3.7) under irradiation, and their concentrations reach pseudo equilibrium. Once formed  $\text{CoOOH}$  is irreversibly converted to  $\text{Co}_3\text{O}_4$  via reactions (3.9) and (3.11). Reaction (3.9) is, however, slow, whereas surface reduction of  $\text{CoOOH}$  to  $\text{Co}_3\text{O}_4$  by  $\text{H}_2\text{O}_2$  (3.11) is fast. Hydrogen peroxide alone cannot produce enough  $\text{CoOOH}$  to form  $\text{Co}_3\text{O}_4$ , and consequently no particle formation was observed in the absence of radiation.

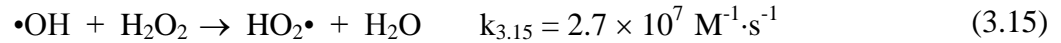
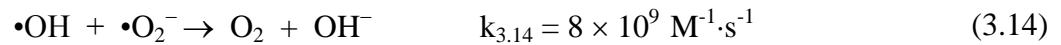
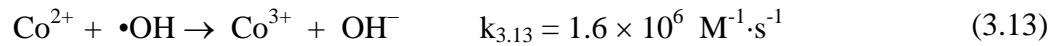
### 3.3.5 Kinetic behaviour of radiolysis products, $\text{H}_2\text{O}_2$ and $\text{H}_2$

Previous radiolysis kinetic studies [21,35,36] have shown that the concentration of  $\text{H}_2$  produced by continuous  $\gamma$ -radiolysis is determined mainly by the primary radiolysis

production rate of H<sub>2</sub> (the primary yield for H<sub>2</sub> multiplied by the dose rate) and the rate of its reaction with •OH:



The decrease in [H<sub>2</sub>] in irradiated solutions of Co<sup>II</sup>(sol) (Figure 3.10) thus indicates that there is an increase in [•OH] in the solutions. This increase in [•OH] is attributed to a decrease in [H<sub>2</sub>O<sub>2</sub>]. In addition to reaction with H<sub>2</sub> (reaction (3.12)), •OH reacts with Co<sup>II</sup>, •O<sub>2</sub><sup>-</sup>, and H<sub>2</sub>O<sub>2</sub> [36]:



The presence of Co<sup>II</sup> in solution will decrease the [H<sub>2</sub>O<sub>2</sub>] due to reactions (3.7), (3.8) and (3.11). A decrease in [H<sub>2</sub>O<sub>2</sub>] leads to a reduction in the rate of reaction (3.15). This compensates for the rate of loss of •OH due to reaction (3.6) (or 3.13) and causes an increase in [•OH] which then causes a decrease in [H<sub>2</sub>].

## 3.4 MECHANISM OF RADIOLYTIC PRODUCTION OF $\text{Co}_3\text{O}_4$ NANOPARTICLES

### 3.4.1 Mechanism for $\text{Co}_3\text{O}_4$ nanoparticle formation

A mechanism for  $\text{Co}_3\text{O}_4$  particle formation that is consistent with all of the observations is summarized schematically in Figure 3.12. Radiation-induced formation of  $\text{Co}_3\text{O}_4$  nanoparticles requires the presence of stable nucleates of  $\text{Co}^{\text{II}}$  species ( $\text{Co}_x(\text{OH})_{2y}^{(x-y)+}$ ). Upon exposure to  $\gamma$ -irradiation, the  $\text{Co}^{\text{II}}$  adsorbed on the nucleate will be quickly oxidized to  $\text{CoOOH}$  by the oxidizing radiolysis products  $\bullet\text{OH}$  and  $\text{H}_2\text{O}_2$ , via reactions (3.6) and (3.7). The  $\text{CoOOH}$  then undergoes polycondensation with  $\text{Co}(\text{OH})_2$  to form  $\text{Co}_3\text{O}_4$ . The conversion of  $\text{CoOOH}$  to  $\text{Co}_3\text{O}_4$  is accelerated in the presence of  $\text{H}_2\text{O}_2$  via reaction (3.11). The proposed mechanism can explain the pH dependence (via its influence on the formation of  $\text{Co}^{\text{II}}$  nucleates), and the dissolved oxygen dependence of the process (via its influence on the stability of  $\text{H}_2\text{O}_2$  (reaction (3.8b)) and the observed behaviour of water radiolysis products of  $\text{H}_2$  and  $\text{H}_2\text{O}_2$ ).

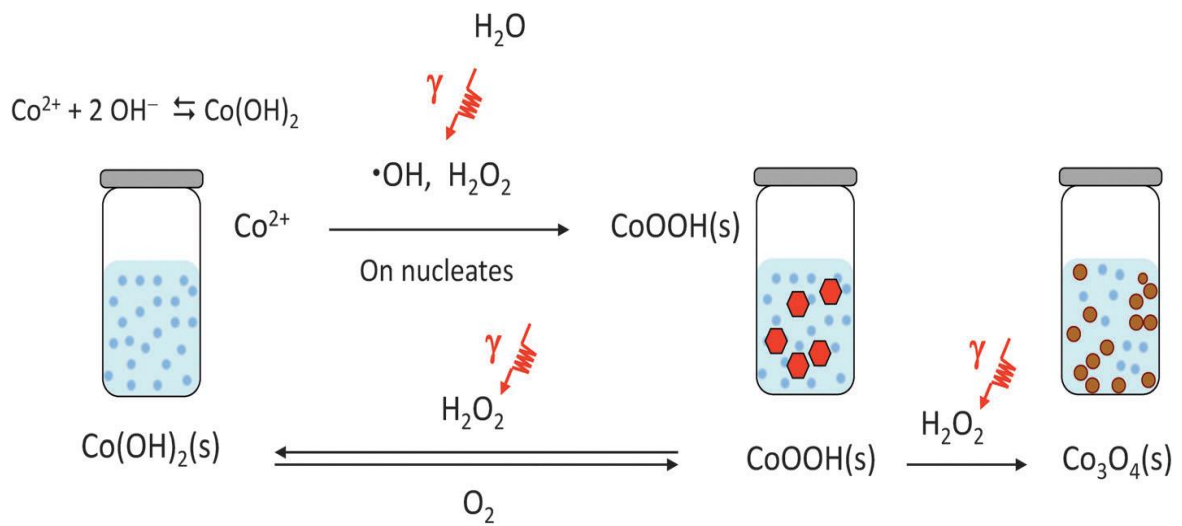


**Figure 3.12:** Schematic of the mechanism proposed for radiation-induced cobalt oxide colloid formation.



### 3.4.2 Comparison of the mechanisms for cobalt and iron systems

Previous studies on the radiolytic formation of iron oxide colloids from dissolved ferrous ions have shown that oxidation of  $\text{Fe}^{\text{II}}(\text{aq})$  to less soluble  $\text{Fe}(\text{OH})_3$  provides nucleation sites for particle growth and that this oxidation is very fast [25]. Compared to the analogous cobalt reaction (3.12), the rate of  $\text{Fe}^{\text{II}}(\text{aq})$  reaction with  $\bullet\text{OH}$  is two orders of magnitude higher with a rate constant of  $2.3 \times 10^8 \text{ M}^{-1}\cdot\text{s}^{-1}$ [36]. Likewise, the net oxidation of  $\text{Fe}^{\text{II}}$  by  $\text{H}_2\text{O}_2$  is faster than the similar oxidation of  $\text{Co}^{\text{II}}$  as discussed earlier. Subsequently ferrous ions are continuously adsorbed and oxidized on the nucleate, growing them into nano-scale  $\gamma\text{-FeOOH}$  particles. The final size and morphology of the particles is regulated by the radiolytically-induced steady-state redox conditions at the water-solid particle interface and the phase of the oxide.

The cobalt system behaves similarly to the iron system in the sense that the formation of the final nanoparticles occurs via an oxidation process, oxidation of the  $\text{Co}^{\text{II}}(\text{sol})$  to  $\text{CoOOH}$  in the case of cobalt. The differences between the particle formation process for the two transition metals lie with the particle nucleation stage. In the case of cobalt, the presence of  $\text{O}_2$  in solution is required to drive the formation of insoluble  $\text{CoOOH}$ . For iron this oxidation step is not required and radiolytic oxidation of  $\text{Fe}^{\text{II}}$  to less soluble  $\text{Fe}(\text{OH})_3$  provides nucleation sites. The radiolytic conversion of  $\text{Co}^{\text{II}}(\text{sol})$  to insoluble  $\text{Co}^{\text{III}}$  oxides/hydroxides is also slower than the solution production of iron species due to the high redox potential of this process for Co. Direct oxidation of  $\text{Co}^{\text{II}}$  by  $\text{O}_2$  is therefore required to supplement slow radiolytic oxidative production of nucleates

in the cobalt system. Thus, for the cobalt system, the  $\text{Co}^{\text{II}}$  clusters formed at high pH act as the nucleation sites on which further oxidation of  $\text{Co}^{\text{II}}(\text{sol})$  to  $\text{CoOOH}$  occurs.

For the iron system, even though the initial nucleation step is fast and the growth of dendritic  $\gamma\text{-FeOOH}$  particles is also fast ( $\leq 60$  min), the conversion of  $\gamma\text{-FeOOH}$  to the thermodynamically more stable  $\text{Fe}_3\text{O}_4$  is slow due to the stability of  $\gamma\text{-FeOOH}$ . Hence no observation of  $\text{Fe}_3\text{O}_4$  formation in irradiation tests lasting 300 min. In contrast, for cobalt the reduction of  $\text{CoOOH}$  to  $\text{Co}_3\text{O}_4$  (reaction (3.10)) can be effectively coupled with the oxidation of  $\text{H}_2\text{O}_2$  to  $\text{O}_2$  (reaction (3.8b)) and the conversion of  $\text{CoOOH}$  to  $\text{Co}_3\text{O}_4$  within 300 min of irradiation time observed.

### 3.5 CONCLUSION

This study demonstrates that radiolysis of dilute cobalt solutions can produce highly uniform, nanometer-sized cobalt oxide particles. The particle formation process has implications for those interested in controlling or removing dissolved cobalt from water systems. The particle formation process has the potential to be used as a practical method of production of cobalt nanoparticles for many applications.

At high pH, the presence of insoluble  $\text{Co}(\text{OH})_2$  in an aerated solution subjected to gamma irradiation creates nucleation sites on which further oxidation of  $\text{Co}^{\text{II}}$  by the water radiolysis products ( $\bullet\text{OH}$ ,  $\text{H}_2\text{O}_2$ ) can occur. The resulting  $\text{CoOOH}$  then rapidly converts to more stable  $\text{Co}_3\text{O}_4$  nanoparticles. The formation of the nanoparticles is accelerated by the presence of  $\text{O}_2$  in solution as this drives an equilibrium that favours the formation of  $\text{CoOOH}$ .

A key difference controlling the particle formation process in the iron and cobalt systems is the electrochemical potential of the oxidation of  $M^{II}$  to  $M^{III}$ . This influences the rate of formation of insoluble  $M^{3+}$  nucleation sites on which further oxidation can occur leading to the formation of metal oxide nanoparticles.

### 3.6 REFERENCES

- [1] M.M. Rahman, J.-Z. Wang, X.-L. Deng, Y. Li, H.-K. Liu, *Electrochim. Acta*, 55 (2009) 504.
- [2] Y. Zhang, Y. Chen, T. Wang, J. Zhou, Y. Zhao, *Microporous and Mesoporous Mater.*, 114 (2008) 257.
- [3] E. Papis, F. Rossi, M. Raspanti, I. Dalle-Donne, G. Colombo, A. Milzani, G. Bernardini, R. Gornati, *Toxicol. Lett.*, 189 (2009) 253.
- [4] S. Mandal, S. Phadtare, M. Sastry, *Curr. Appl. Phys.*, 5 (2005) 118.
- [5] Q.A. Pankhurst, J. Cononolly, S.K. Jones, J. Dobson, *J. Phys. D: Appl. Phys.*, 36 (2003) R167.
- [6] L. LaConte, N. Nitin, G. Bao, *Nanotoday*, 19 (2005) 32.
- [7] A. Ito, M. Shinkai, H. Honda, T. Kobayashi, *J. Biosci. Bioeng.*, 100 (2005) 1.
- [8] L. Qiao, H.Y. Xiao, H.M. Meyer, J.N. Sun, C.M. Rouleau, A.A. Poretzky, D.B. Geohegan, I.N. Ivanov, M. Yoon, W.J. Weber, M.D. Biegalski, *J. Mater. Chem. C*, 1 (2013) 4628.
- [9] C.S. Cheng, M. Serizawa, H. Sakata, T. Hirayama, *Mater. Chem. Phys.*, 53 (1998) 225.
- [10] M. Ando, T. Kobayashi, S. Iijima, M. Haruta, *J. Mater. Chem.*, 7 (1997) 1779.

- [11] C. Pirovano, S. Trasatti, *J. Electroanal. Chem.*, 180 (1984) 171.
- [12] S. Sakamoto, M. Yoshinaka, K. Hirota, O. Yamaguchi, *J. Am. Ceram. Soc.*, 80 (1997) 267.
- [13] V.R. Shinde, S.B. Mahadik, T.P. Gujar, C.D. Lokhande, *Appl. Surf. Sci.*, 252 (2006) 7487.
- [14] K. Shalini, A.U. Mane, S.A. Shivashankar, M. Rajeswari, S. Choopun, *J. Cryst. Growth*, 231 (2001) 242.
- [15] L.M. Parkes, R. Hodgson, L.T. Lu, L.D. Tung, I. Robinson, D.G. Fernig, N.T. Thanh, *Contrast Media Mol. Imaging*, 3 (2008) 150.
- [16] C.S. Cheng, M. Serizawa, H. Sakata, T. Hirayama, *Mater. Chem. Phys.*, 53 (1998) 225.
- [17] A.U. Mane, K. Shalini, A. Wohlfart, A. Devi, S.A. Shivashankar, *J. Cryst. Growth*, 240 (2002) 157.
- [18] S.R. Ahmed, S.B. Ogale, G.C. Papaefithymiou, R. Ramesh, P. Kofinas, *Appl. Phys. Lett.*, 45 (2000) 4359.
- [19] B. Orel, V. Kauc, *Electrochim. Acta*, 45 (2000) 4359.
- [20] R.J. Woods, A.K. Pikaev, *Applied Radiation Chemistry: Radiation Processing*, John Wiley & Sons, Inc., New York, 1994.
- [21] M. Behazin, M.C. Biesinger, J.J. Noël, J.C. Wren, *Corros. Sci.*, 63 (2012) 40.
- [22] J.W.T. Spinks and R.J. Woods, *An Introduction to Radiation Chemistry*, Wiley-Interscience, New York, 1990.
- [23] J.C. Wren, Steady-state radiolysis: effect of dissolved additives in ACS Symposium Series: *Nuclear Energy and the Environment*, 2010.

- [24] J.M. Joseph, B.S. Choi, P.A. Yakabuskie, J.C. Wren, *Radiat. Phys. Chem.*, 77 (2008) 1009.
- [25] P.A. Yakabuskie, J.M. Joseph, P. Keech, G.A. Botton, D. Guzonas, J.C. Wren, *Phys. Chem. Chem. Phys.*, 13 (2011) 7198.
- [26] C.F. Baes, R.E. Mesmer (2<sup>nd</sup> Ed.). *Hydrolysis of Cations*, Krieger Pub. Co. Malabar, Florida, 1986.
- [27] T. Yotsuyanagi, R. Yamashita, K. Aomura, *Anal. Chem.*, 44 (1972)1091.
- [28] C.J. Hochanadel, *J. Phys. Chem.*, 56 (1952) 44.
- [29] I. Stefanic, J.A. Laverne, *J. Phys. Chem. A*, 106 (2002) 47.
- [30] M. Biesinger, B. Payne, A. Grosvenor, L. Lau, A. Gerson, R. Smart, *Appl. Surf. Sci.*, 257 (2011) 2717.
- [31] E. Le Ru, P. Etchegoin, *Principle of Surface-Enhanced Raman Spectroscopy*. Elsevier, 2008.
- [32] A. Brad, L.R. Faulkner (2nd ED). *Electrochemical Methods: Fundamental and Applications*., John Wiley & Sons, New York, 2001.
- [33] A.P. Murphy, W.J. Boegli, M.K. Price, D. Moody, C.D. Moody, *Environ. Sci. Technol.*, 23 (1989) 166.
- [34] A.N. Kamkin, Z. Guo-ding, A.D. Davydov, *Protection of Metals*, 37 (2001) 72.
- [35] L. Schumacher, I. Holzhueter, I. Hill, M. Dignam, *Electrochim. Acta*, 35 (1990) 975.
- [36] G.V. Buxton, R.M. Sellers, D.R. McCracken, *J. Chem. Soc. Faraday Trans. 1*, 72 (1975) 1464.

## Chapter 4

### Gamma-radiation induced formation of chromium oxide nanoparticles from dissolved dichromate<sup>2</sup>

#### 4.1 INTRODUCTION

Nano-scale chromium oxide particles have numerous applications. Depending on their crystalline size and morphology, they are used as green pigments [1], heterogeneous catalysts [2], coating materials for thermal protection [3], coatings for wear resistance [4], and as electrochromic materials [5]. The high melting point (2435 °C) and the oxidation resistance of this oxide also makes it an important refractory material, although its sintering ability is poor [6,7]. In addition to improving pigment opacity and catalytic activity, reducing the chromium oxide particle size could improve its sintering ability by decreasing the required sintering temperature and by increasing the density of the sintered powder [6,7].

Chromium oxide nanoparticles have been synthesized by various techniques such as hydrothermal reduction [8], solution combustion synthesis [9], sonochemical reaction [10], laser-induced pyrolysis [11], hydrazine reduction and thermal treatments [12], supercritical alcohol synthesis [13], condensation-polymerization [14], precipitation-gelation [15], gas condensation [16], microwave plasma chemistry [17], and sol-gel methods [18]. The major drawbacks of most of these methods are a broad particle size

---

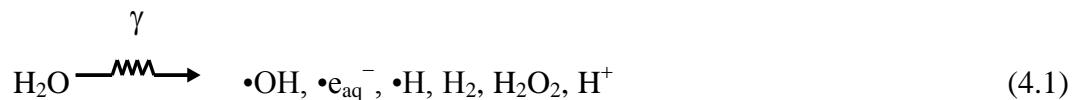
<sup>2</sup> [L.M. Alrehaily, J.M. Joseph, A.Y. Musa, D.A. Guzonas, J.C. Wren, *Phys. Chem. Chem. Phys.*, 15 (2013) 98.]-Reproduced by permission of the PCCP Owner Societies.

distribution, low yield, and agglomeration of the particles. The methods also tend to be complex and require chemically harsh conditions and/or high processing temperatures.

Radiolysis is a promising new technique for generating nano-scale particles with a narrow size distribution [19,20]. Radiation-induced nanoparticle formation also does not require the chemical additives and stabilizers for particle size control that are used in other conventional methods [21]. This eliminates undesired effects of these chemicals on the nanoparticle structure and chemical composition.

The conversion of  $\text{Cr}^{\text{VI}}$  to  $\text{Cr}^{\text{III}}$  using ionizing radiation could be used as an environmental protection process. Chromium, as  $\text{Cr}^{\text{VI}}$ , is toxic and considered to be carcinogenic, while chromium, as  $\text{Cr}^{\text{III}}$ , is an essential micronutrient for humans [22].  $\text{Cr}^{\text{VI}}$  is used in a wide range of industrial processes such as electroplating, tanning, and steel manufacturing [23]. Any  $\text{Cr}^{\text{VI}}$ -contaminated wastewater has to be treated to reduce  $\text{Cr}^{\text{VI}}$  to less harmful  $\text{Cr}^{\text{III}}$  before it can be safely discharged into the environment. Common techniques used for this reduction include electrolysis [24], photochemical reduction [25], chemical reduction [26] and biological reduction [27]. These methods require the use of reagents, can have a low efficiency, and can be dependent on the water chemistry (particularly pH). Radiation-induced reduction of  $\text{Cr}^{\text{VI}}$  to  $\text{Cr}^{\text{III}}$  is a technique for the treatment of  $\text{Cr}^{\text{VI}}$ -contaminated waste water that does not have these disadvantages [28].

When exposed to ionizing radiation, water decomposes to form a range of chemically reactive radical and molecular products [29,30]:



These products react with one another to form secondary species such as  $\text{O}_2$ ,  $\cdot\text{O}_2^-$  and  $\cdot\text{O}_3$ . The water radiolysis products range from highly oxidizing (e.g.,  $\cdot\text{OH}$ ,  $\text{H}_2\text{O}_2$  and  $\text{O}_2$ ) to highly reducing (e.g.,  $\cdot\text{H}$ ,  $\cdot\text{e}_{\text{aq}}^-$  and  $\cdot\text{O}_2^-$ ) and can readily change the oxidation state of dissolved metal ions. The solubility of a transition metal ion can vary by several orders of magnitude depending on its oxidation state and the solution pH. Thus, reactions that can alter the oxidation state of a dissolved ion can lead to the condensation of insoluble species and the formation of solid particles.

Nanoparticle synthesis by ionizing radiation has been reported by various groups [31-33], but mechanistic studies of the nanoparticle formation process are very limited [20]. The short-term pulse irradiation technique provides very useful information on the initial homogeneous aqueous reactions that occur, but does not provide information on particle growth and heterogeneous surface reactions that occur at longer times (orders of magnitude beyond the duration of the irradiation pulse).

Recent studies have shown that uniform-sized colloidal particles of  $\gamma$ -FeOOH can be formed by the radiolytic oxidation of dissolved  $\text{Fe}^{\text{II}}$  using continuous gamma irradiation. the formation of nano-scale  $\text{Co}_3\text{O}_4$  particles from the radiolysis of hydrated  $\text{Co}^{\text{II}}$  demonstrated[20,34]. In these processes the oxidizing power of water radiolysis products is utilized for particle formation. This study report on the formation of  $\text{Cr}_2\text{O}_3$  nanoparticles using water radiolysis to drive reduction of dissolved chromate ions. In addition to demonstrating nanoparticle synthesis, This study provide a mechanistic understanding of particle formation and growth kinetics. The particles that are formed



are well characterized and the effects of the initial concentration of Cr<sup>VI</sup> ions and pH on the particle growth were investigated.

This chapter reports the formation of Cr<sub>2</sub>O<sub>3</sub> nanoparticles using water radiolysis to drive reduction of dissolved chromate ions. In addition to demonstrating nanoparticle synthesis, A mechanistic understanding of particle formation and growth kinetics was provided. The particles that are formed are well characterized and the effects of the initial concentration of Cr<sup>VI</sup> ions and pH on the particle growth were investigated.

## 4.2 EXPERIMENTAL

Solutions were prepared by dissolving an appropriate amount of high-purity potassium dichromate salt purchased from Sigma-Aldrich (purity  $\geq$  99%). The salt is highly soluble and the anion is present as either CrO<sub>4</sub><sup>2-</sup> or Cr<sub>2</sub>O<sub>7</sub><sup>2-</sup> depending on the pH [35, 36]. The solutions are referred to as Cr<sup>VI</sup> solutions hereafter. The concentration of Cr<sup>VI</sup> ranged from 0.1 to 10 mM. Concentrated NaOH solution was added to a Cr<sup>VI</sup> solution to obtain the three pHs (6.0, 8.5 and 10.6) explored in this study. All solutions were freshly prepared with water purified using a NANOpure Diamond UV Ultrapure water system, with a resistivity of 18.2 M $\Omega$ -cm. All deaerated solutions were prepared inside an Ar-filled glove box (where the oxygen level was maintained below 0.1 vol %) using pure water that was purged with ultra-high purity argon (impurity content less than 0.001%) for an hour [37]. The solutions were then transferred into 20-ml glass vials leaving no headspace and sealed using aluminum crimp caps with PTFE silicon septa (Agilent Technologies). The sample vials were irradiated in a <sup>60</sup>Co gamma cell (MDS

Nordion) as described in chapter 2. The gamma source provided a uniform absorption dose rate of  $6.7 \text{ kGy}\cdot\text{h}^{-1}$  in the water samples at the time of this study as determined using Fricke dosimetry [30]. Since  $\text{Cr}^{\text{VI}}$  is a hazardous ion, handling precautions were taken in preparing test solutions to prevent exposure to the skin or inhalation.

Following irradiation for a desired period, a series of chemical analyses of the test solution were performed. Colloid particles were then collected for analysis (see below for details). For analysis of dissolved  $\text{H}_2$ , one half (10 mL) of the irradiated test solution was transferred to a new 20 mL vacuum-tight vial using a gas-tight syringe (Hamilton). Equilibration of the gas concentrations in the headspace above the solution and in the aqueous phase was quickly established. A gas sample was extracted from the headspace using a gas-tight syringe with a Luer lock (Agilent Technologies) and was analyzed using a gas chromatograph with a thermal conductivity detector (GC-TCD, 6580 Agilent Technologies) [37]. The aqueous phase  $\text{H}_2$  concentrations were calculated from the measured gas phase concentrations using the known aqueous-gas partition coefficients ( $0.019$  for  $\text{H}_2$  at  $25^\circ\text{C}$  ( $[\text{C}_{\text{aq}}]/[\text{C}_{\text{g}}]$ , both concentrations in  $\text{mol}\cdot\text{dm}^{-3}$ )). Using this method, the detection limit for the aqueous  $[\text{H}_2]$  was  $1.0 \times 10^{-5} \text{ mol}\cdot\text{dm}^{-3}$  and the uncertainties in the measurement arising from sampling and instrumental errors were estimated to be  $\pm 50\%$  at the low end of the measured concentration range and  $\pm 0.005\%$  at the high end of the concentration range. The concentration of hydrogen peroxide in the test solution was determined by the Ghormley tri-iodide method [38,39], as previously reported in chapter 2.

The solutions were analysed for their  $\text{Cr}^{\text{VI}}$  content using a UV-VIS Spectrophotometer (BioLogic Science Instruments). The concentration of  $\text{Cr}^{\text{VI}}$  was

determined by adding diphenylcarbazide (DPC) to a solution sample more details in reference [40]. This reacts with  $\text{Cr}^{\text{VI}}$  to form a coloured complex that absorbs light at 540 nm [40]. A calibration curve for  $\text{Cr}^{\text{VI}}$  over the concentration range of 0.01 to 1mM was generated. The molar extinction coefficient of  $39032\text{M}^{-1}\cdot\text{cm}^{-1}$  obtained from our calibration curve is comparable to the reported value of  $34400\text{M}^{-1}\cdot\text{cm}^{-1}$  [40], and our calibration value was used to determine the concentration of chromium in our samples. This colorimetric method is referred to as the DPC method hereafter. Gamma-irradiation reduces  $\text{Cr}^{\text{VI}}$  to  $\text{Cr}^{\text{III}}$  which then forms colloidal particles that are comprised of  $\text{Cr}(\text{OH})_3$ ,  $\text{CrOOH}$ , and  $\text{Cr}_2\text{O}_3$ . The particles are collectively referred to as  $\text{Cr}^{\text{III}}(\text{col})$ . The concentration of  $\text{Cr}^{\text{III}}(\text{col})$  dispersed in the solution samples was determined by first oxidizing the  $\text{Cr}^{\text{III}}(\text{col})$  with potassium permanganate to form dissolved  $\text{Cr}^{\text{VI}}$  and then by measuring the  $\text{Cr}^{\text{VI}}$  concentration in the samples using the DPC method. The  $\text{Cr}^{\text{III}}(\text{col})$  concentration was calculated by subtracting the initially-determined dissolved  $\text{Cr}^{\text{VI}}$  concentration from the total  $\text{Cr}^{\text{VI}}$  concentration determined after  $\text{Cr}^{\text{III}}(\text{col})$  oxidation.

Particles were collected from the sample vials for analysis by transmission electron microscopy (TEM), x-ray photoelectron spectroscopy (XPS), Fourier transform infrared spectroscopy (FTIR) and Raman spectroscopy. For the XPS, FTIR and Raman analyses the particles were collected by centrifuging the solution and then drying the precipitate on a glass plate in an Ar-purged glove box. Samples for TEM were collected by dipping a carbon-coated copper grid into the irradiated test solution and then drying the sample grid in air. FTIR spectroscopy was performed with a Bruker, Vertex 70v in the  $400$  to  $4000\text{cm}^{-1}$  range. The TEM images were obtained with a Philips Electronics Ltd. TEM with the electron microscope operated at 80 keV. XPS spectra were acquired

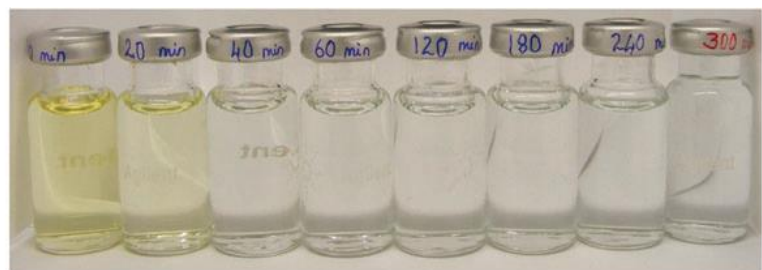
on a KRATOS Axis Nova spectrometer using monochromatic Al K (alpha) radiation and operating at 210 W with a base pressure of  $10^{-8}$  Pa. The analysis depth of the XPS instrument is 6-7 nm. Raman scattering measurements were performed using a Renishaw model 2000 Raman spectrometer with a laser excitation wavelength of 633 nm.

## 4.3 RESULTS AND DISCUSSION

### 4.3.1 Experimental observations

A series of tests was performed with  $\text{Cr}^{\text{VI}}$  solutions that were aerated (by purging with air) for 1 h prior to testing. These tests included a range of  $\text{Cr}^{\text{VI}}$  concentrations and solution pHs. In all of these tests no changes in the test solutions were observed, with and without extended periods of gamma irradiation, and no particle formation was observed. All the data presented and discussed below are for tests that were performed using de-aerated solutions.

Figure 4.1 shows the photographs and UV-Vis spectra of 0.1 mM  $\text{Cr}^{\text{VI}}$  solutions at pH 8.5 that were irradiated for different time periods ( $t_{\text{RAD}}$ ). These images were taken after transferring the solutions from the irradiated test vials to new, clear vials because the test vials darken during irradiation. The solutions change from yellow, characteristic of dissolved  $\text{CrO}_4^{2-}/\text{Cr}_2\text{O}_7^{2-}$ , to colourless as the irradiation time increases. The colour change is shown more quantitatively by the decrease in the UV-Vis absorption intensity of the solutions at 370 nm (the known absorption peak for  $\text{CrO}_4^{2-}$ ) with increasing  $t_{\text{RAD}}$ . The good agreement between the decrease in the UV-Vis absorbance and the change in  $[\text{Cr}^{\text{VI}}]$  as determined using the DPC method is shown in Figure 4.2.



0 min — Increasing  $t_{\text{RAD}}$  —> 300 min

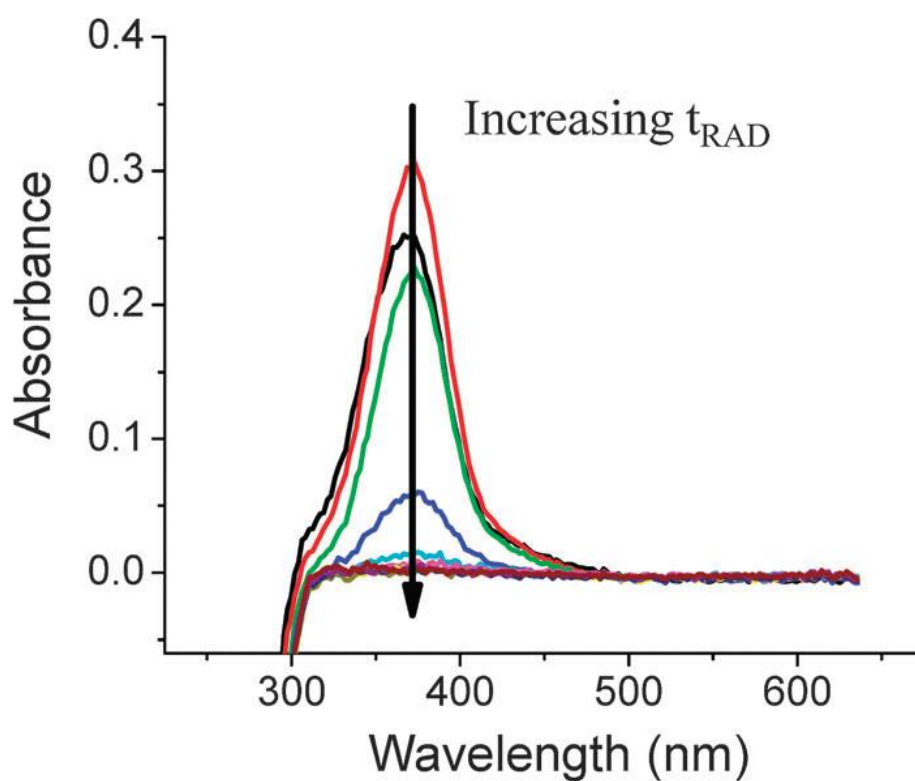


**Figure 4.1:** Photographs of argon-purged solutions initially containing 0.1 mM  $\text{Cr}^{\text{VI}}$  at pH 8.5 that were irradiated for different durations, and UV-Vis spectra showing the decrease in the intensity of the absorbance peak of  $\text{Cr}^{\text{VI}}$  over the same time period.

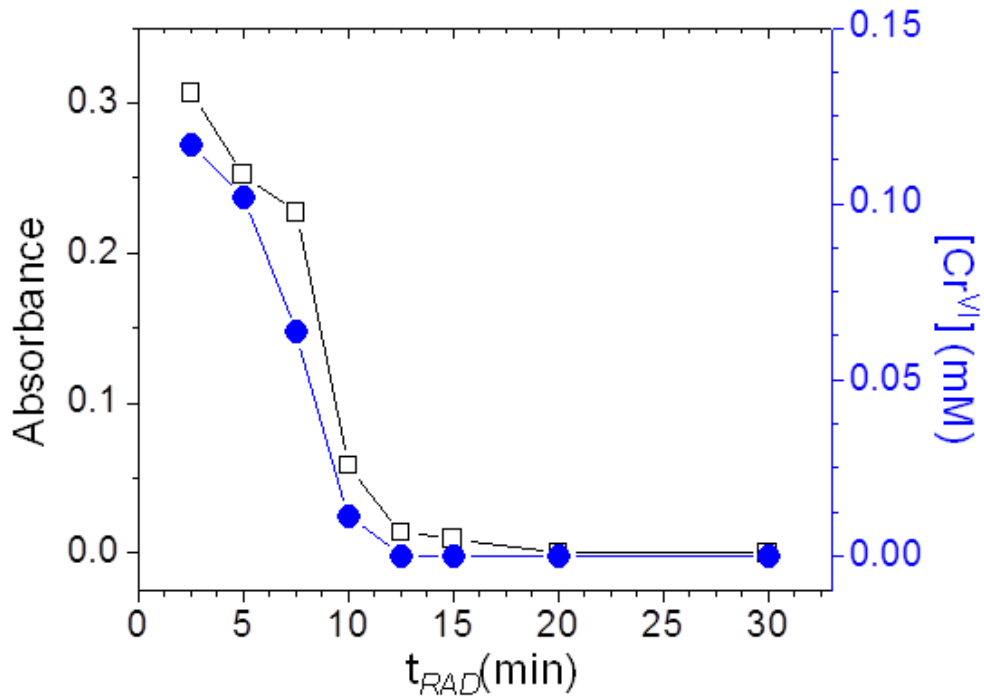


**Figure 4.2:** The decrease in the height of the UV-Vis absorption peak at 370 nm and the decrease in  $[Cr^{VI}]$  determined using the DPC method shown as a function of irradiation time for deaerated solutions initially containing 0.1 mM  $Cr^{VI}$  at pH 8.5.

The concentrations of  $\text{Cr}^{\text{VI}}$ ,  $\text{Cr}^{\text{III}}(\text{col})$  and  $\text{H}_2$ , in the test solutions as a function of  $t_{\text{RAD}}$  are presented in Figure 4.3. The results for three different initial  $\text{Cr}^{\text{VI}}(\text{aq})$  concentrations (0.1, 0.3 and 0.5 mM) at three different pHs (6.0, 8.5 and 10.6) are shown. The concentration of another molecular radiolysis product,  $\text{H}_2\text{O}_2$ , measured also but its concentration was below our detection limit ( $\leq 3 \times 10^{-6}$  M) in all tests. The data show the presence of two stages in the particle formation process. In stage 1, at any given  $[\text{Cr}^{\text{VI}}]_0$  and pH,  $[\text{Cr}^{\text{VI}}]$  decreases linearly with time while  $[\text{Cr}^{\text{III}}(\text{col})]$  increases until most of the initial  $\text{Cr}^{\text{VI}}$  is converted to  $\text{Cr}^{\text{III}}(\text{col})$ . The chromium concentrations reach steady state values in stage 2. The time to reach stage 2 increases with an increase in  $[\text{Cr}^{\text{VI}}]_0$  but is independent of pH (over the range studied). The rates of change of the chromium species concentrations in stage 1 were independent of  $[\text{Cr}^{\text{VI}}]_0$  or pH; the concentration vs. time plots all have the same slopes:

$$-\frac{d[\text{Cr}^{\text{VI}}]}{dt} = \frac{d[\text{Cr}^{\text{III}}(\text{col})]}{dt} = (1.8 \pm 0.2) \times 10^{-7} \text{ M} \cdot \text{s}^{-1} \quad (4.2)$$

The  $[\text{H}_2]$  also increased with irradiation time in stage 1, but it did not reach a steady state and continued to increase at a faster rate in stage 2.

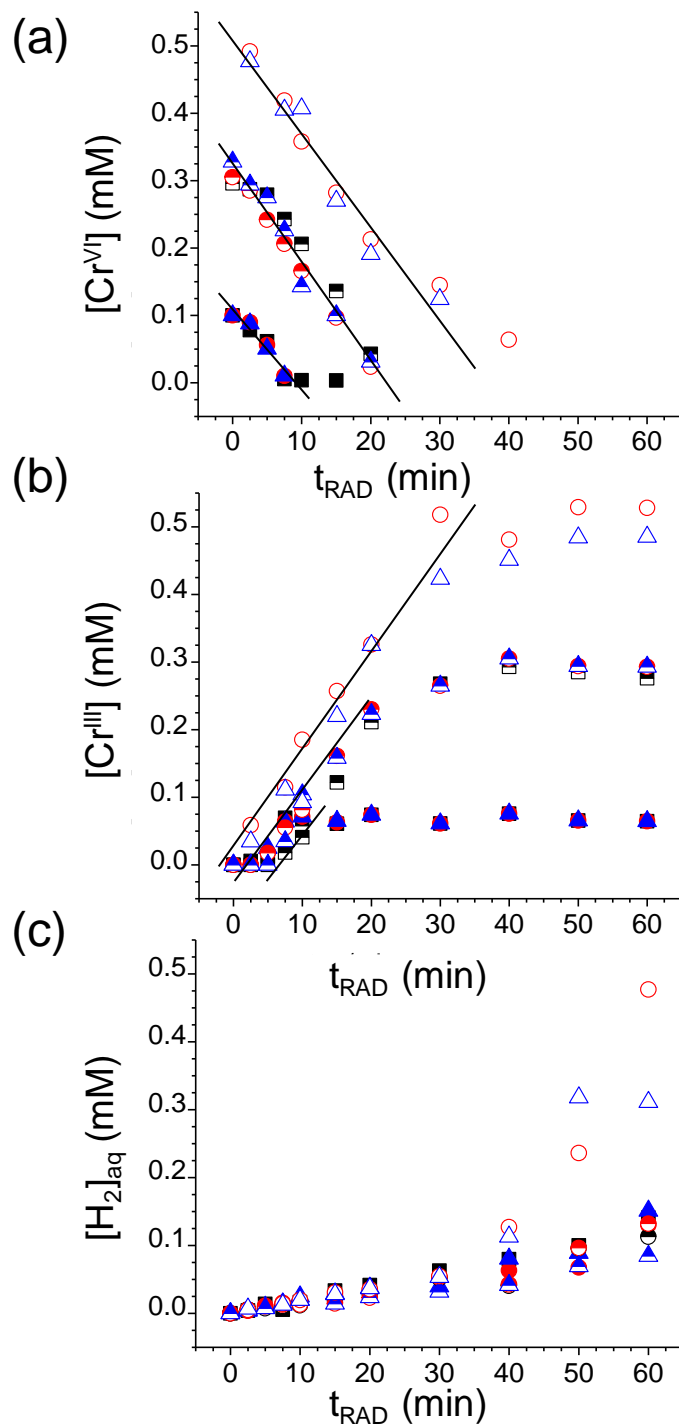


**Figure 4.3:** The concentrations of  $\text{Cr}^{\text{VI}}$  (a),  $\text{Cr}^{\text{III}}$  (b) and  $\text{H}_2$  (c) measured as a function of irradiation time at pHs 6.0 (■), 8.5 (▲) and 10.6 (●) for solutions initially containing  $[\text{Cr}^{\text{VI}}]$  of 0.1 mM (solid symbols), 0.3 mM (half filled symbols) and 0.5 mM (open symbols) lines to indicate the stages.



All of the species that comprise the  $\text{Cr}^{\text{III}}(\text{col})$  ( $\text{Cr}(\text{OH})_3$ ,  $\text{CrOOH}$  and  $\text{Cr}_2\text{O}_3$ ) are insoluble at all of the pHs used here [41]. However, the photographs of the test solutions (Figure 4.1) show no evidence of any precipitate. There is no evidence that the test solutions were supersaturated (no spontaneous formation of a solid precipitate was observed at any time). The  $\text{Cr}^{\text{III}}$  species must have condensed as particles less than 0.1  $\mu\text{m}$  in size (not visible to the naked eye) and formed a stable dispersed phase in the solution (hence the designation of  $\text{Cr}^{\text{III}}(\text{col})$  as colloid). The presence of colloid particles was confirmed by TEM analysis of particles collected from the irradiated test solutions. The size and morphology of the colloid particles formed at various irradiation times were examined. Figure 4.4 shows TEM images of chromium particles formed after 300 min irradiation; three different  $[\text{Cr}^{\text{VI}}]_0$  (0.1, 0.5 and 10 mM) are compared. The particles are relatively uniform in size, ranging from 9 to 30 nm and approximately spherical with jagged edges. The average size of the particles is nearly independent of pH but increases with  $[\text{Cr}^{\text{VI}}]_0$ . The size of the particles also appears to increase with time until reaching a final size (Table 4.1) and the time needed to reach the final size is longer for a higher  $[\text{Cr}^{\text{VI}}]_0$  (Figure 4.3). It was difficult to collect particles when  $[\text{Cr}^{\text{VI}}]_0$  was less than 0.1 mM (hence the lower limit for the  $[\text{Cr}^{\text{VI}}]_0$  used in our study). Also, when the irradiation time was very short the number density of the particles larger than a few nm was small.

**Table 4.1:** Size ranges of the chromium oxide nanoparticles determined from TEM images.

[Cr <sup>VI</sup> ] <sub>0</sub>	Irradiation time (t <sub>RAD</sub> )			
	60 min	300 min	60 min	300 min
	pH 8.5		pH 10.6	
0.5 mM	12-24.5 nm	21-22 nm	10-20 nm	15-28 nm
0.1 mM	9-13 nm	9-38 nm	8-20 nm	9-20 nm

The chemical and phase compositions of the Cr<sup>III</sup>(col) particles were analyzed using Raman, FTIR and XPS. Due to the small particle size it was impossible to collect sufficient particles for the spectroscopic characterization when [Cr<sup>VI</sup>]<sub>0</sub> was below 0.5 mM. For the spectroscopic analyses, only the particles formed from the solutions initially containing 10 mM Cr<sup>VI</sup> that were irradiated for 300 min were analyzed. The colour of the irradiated solution (Figure 4.5 a) is visibly green which is characteristic of chromium (III) oxide [42] (Note that the green colour is not visible in Figure 4.1 due to low concentration.) The particles collected from the irradiated solution were subjected to three different treatments prior to analysis: (1) as collected (unwashed), (2) washing with distilled water, and (3) washing followed by heating at 500 °C for 5 h in air. The particles collected were washed with distilled water to remove any Cr<sup>VI</sup> adsorbed on the particles. The heating treatment was performed to remove any hydrated species on the particle surface layers. The Raman spectrum of the unwashed particles whose TEM image is shown in Figure 4.4 is shown in Figure 4.5. The unwashed particles have jagged edges and a very narrow size distribution. The Raman spectrum of these particles

shows the presence of Cr<sup>VI</sup> species (as CrO<sub>4</sub><sup>2-</sup> or Cr<sub>2</sub>O<sub>7</sub><sup>2-</sup> depending on pH). Note that Figure 4.5 shows the reference spectrum of Cr<sup>VI</sup> dissolved in solution and not as adsorbed Cr<sup>VI</sup>.

The TEM images and the FTIR spectra of washed particles, and washed and heated particles are shown in Figure 4.6. The reference spectra of Cr<sub>2</sub>O<sub>3</sub> (purchased from Alfa Aesar) and Cr(OH)<sub>3</sub> (synthesized according to Biesinger *et al.* [43]) are also shown in the figure. The spectrum of the washed particles matches the reference spectrum of Cr(OH)<sub>3</sub> while the spectrum of the washed and heated particles matches the reference spectrum of Cr<sub>2</sub>O<sub>3</sub>. Similar results obtained by XPS are shown in Figure 4.7. Deconvolution of the XPS band for Cr 2-p (see reference [35] for deconvolution analysis process) shows that the washed particles contain a higher fraction of Cr(OH)<sub>3</sub> (72.9%) than Cr<sub>2</sub>O<sub>3</sub> (18.5%) while the washed and heated particles are almost pure Cr<sub>2</sub>O<sub>3</sub> (98.6%). The heating removes adsorbed water and converts Cr(OH)<sub>3</sub> to Cr<sub>2</sub>O<sub>3</sub>.

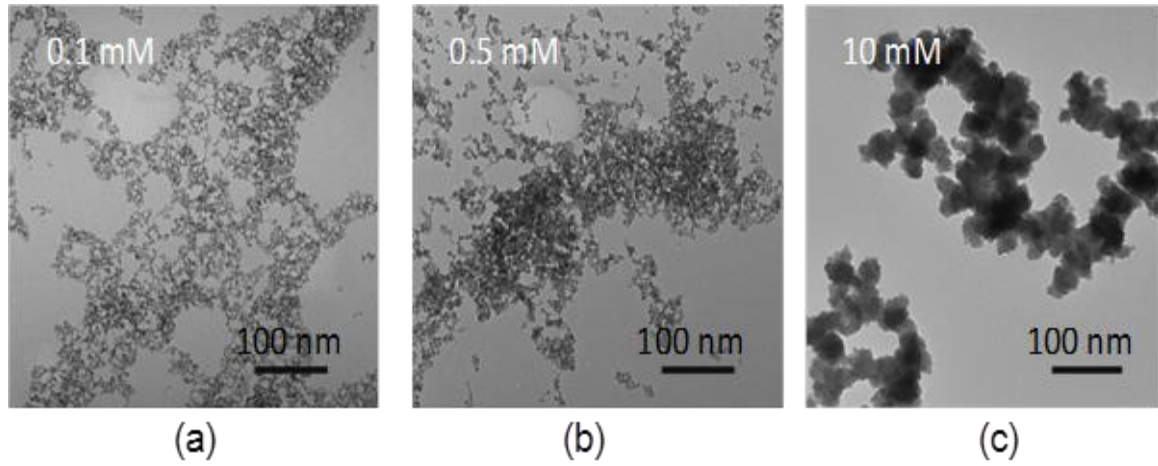
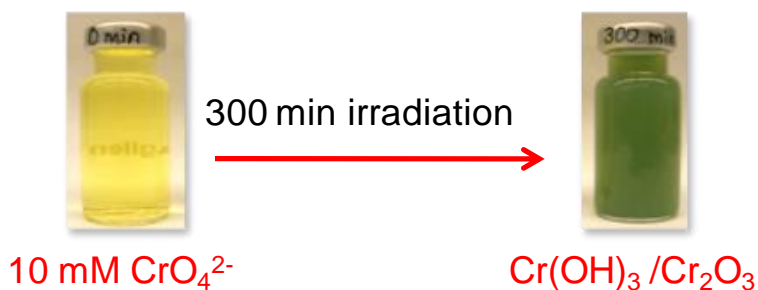


**Figure 4.4:** TEM images of chromium oxide nanoparticles formed after 300 min irradiation for (a) 0.1 mM  $[\text{Cr}^{\text{VI}}]_0$ , (b) 0.5 mM  $[\text{Cr}^{\text{VI}}]_0$  and (c) 10 mM  $[\text{Cr}^{\text{VI}}]_0$ .

(a) Change in the solution phase



(b) Particle analysis

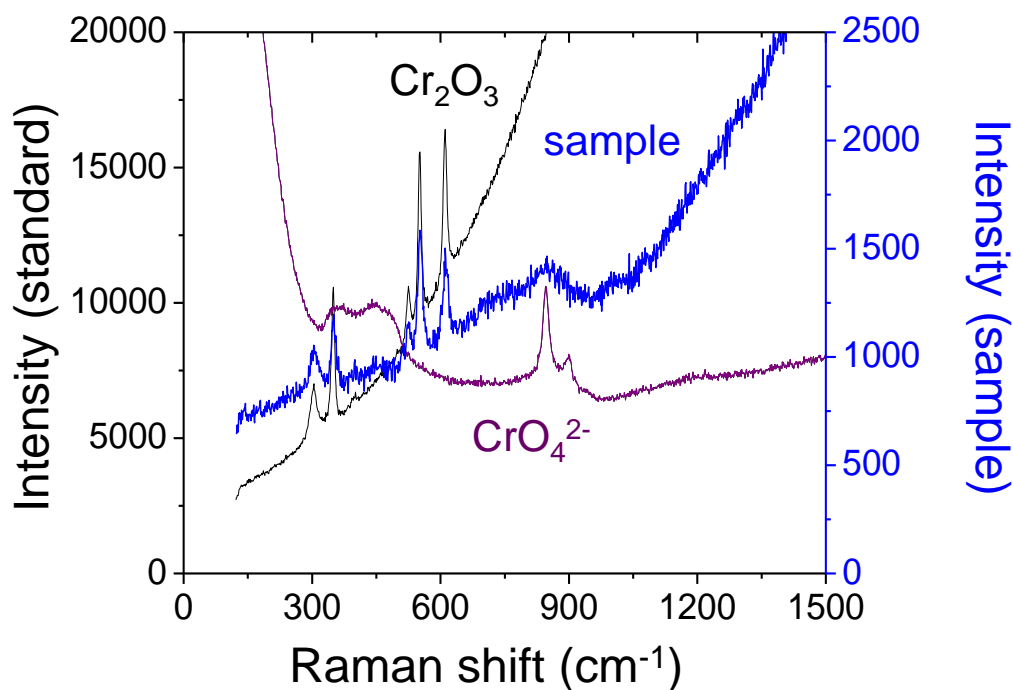


**Figure 4.5:** (a) Photographs before and after irradiation of an Ar-purged 10 mM  $\text{Cr}^{\text{VI}}$  solution at pH 8.5 and (b) Raman spectrum of unwashed chromium oxide nanoparticles formed in the irradiated solution. The reference spectra of  $\text{CrO}_4^{2-}$  dissolved in solution and  $\text{Cr}_2\text{O}_3$  powder are also shown.

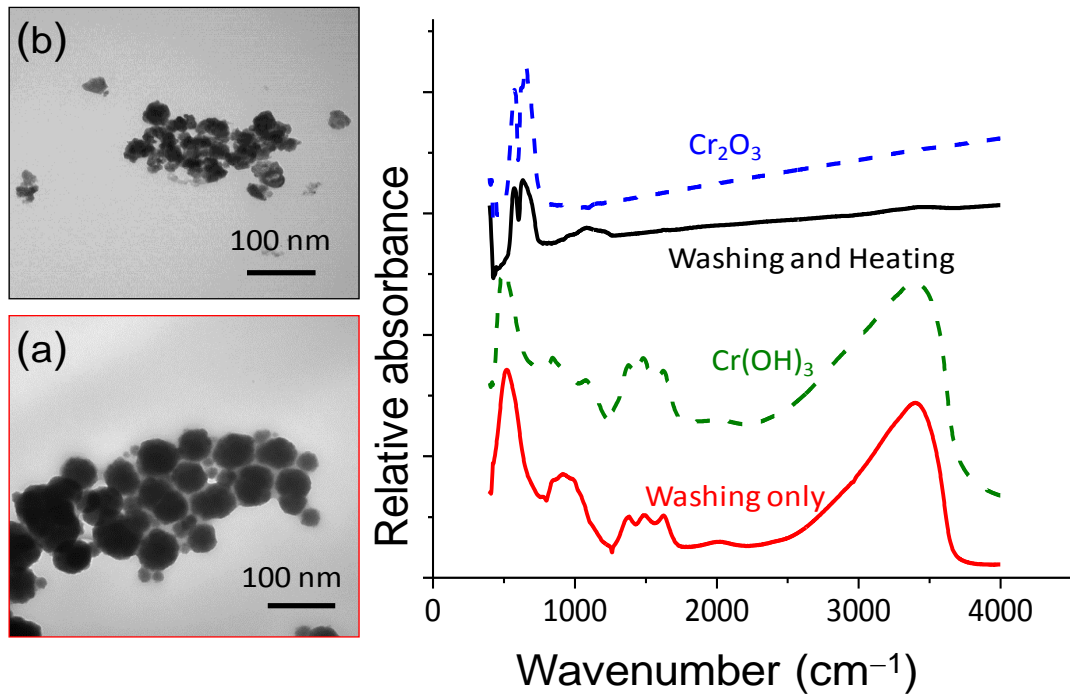


**Figure 4.6:** The FTIR spectrum and TEM image of chromium oxide nanoparticles after washing (a) prior to and (b) after heating. Also included are spectra for  $\text{Cr}_2\text{O}_3$  and  $\text{Cr}(\text{OH})_3$  for comparison.

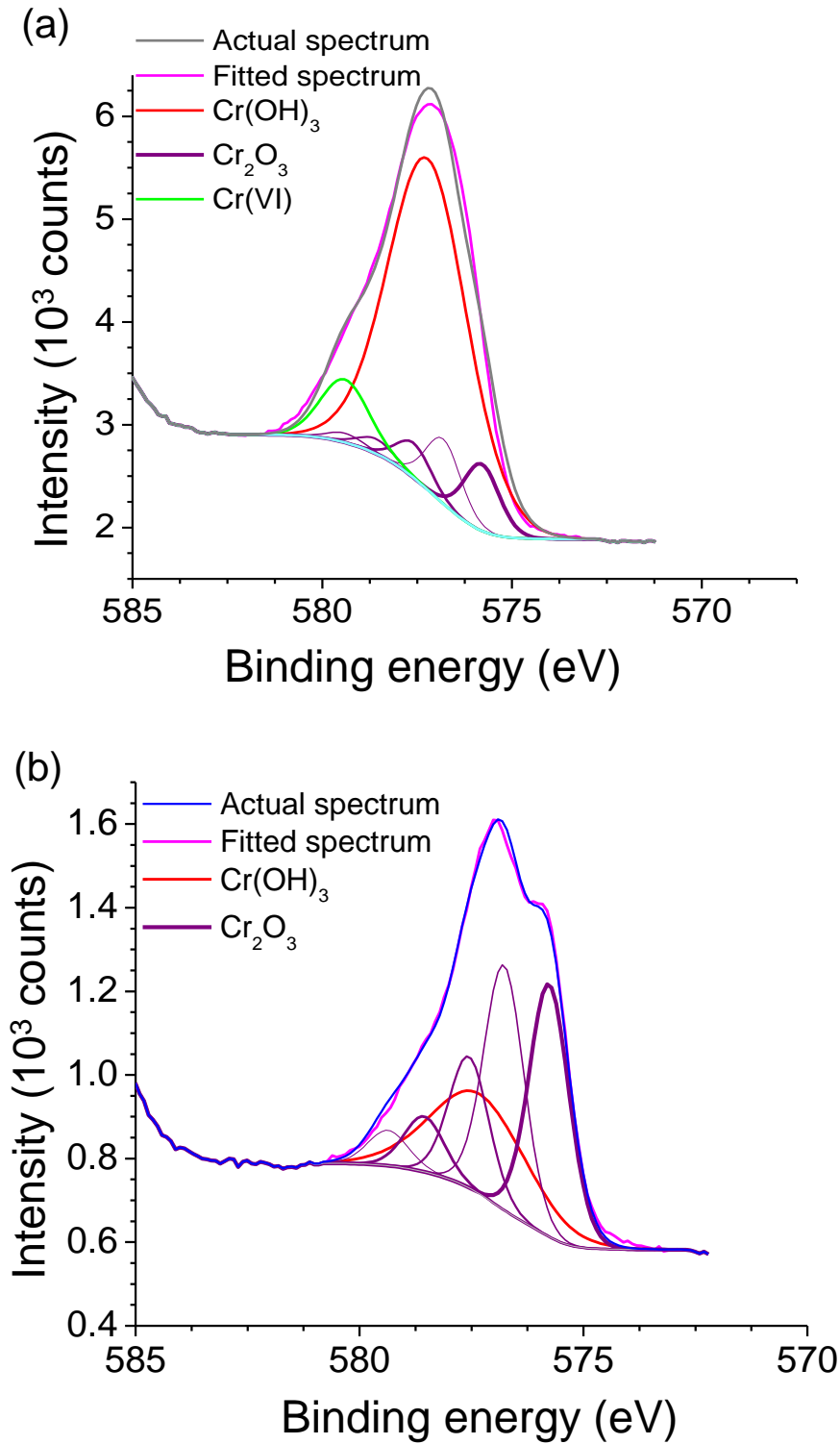
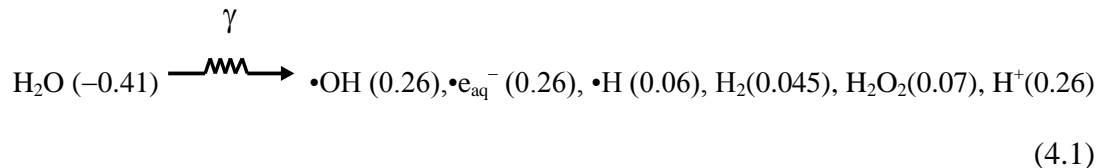


**Figure 4.7:** XPS spectra of washed chromium oxide nanoparticles showing the fit to the different components of the particles (a) with no heating and (b) with heating.

### 4.3.2 Kinetic analysis

The results presented in Figure 4.3 show that the radiolytic conversion of  $\text{Cr}^{\text{VI}}(\text{aq})$  to  $\text{Cr}^{\text{III}}(\text{col})$  follows linear kinetics in stage 1. During the conversion  $[\text{H}_2]$  also increases linearly albeit at a slower rate. The particle analysis results indicate that the particle growth occurs at a much slower rate than the reductive conversion and continues long after most of the  $\text{Cr}^{\text{VI}}(\text{aq})$  has been converted to  $\text{Cr}^{\text{III}}(\text{col})$ . What reaction mechanism can explain these observations?

When exposed to ionizing radiation, water decomposes to form a range of chemically reactive species. The physical and physicochemical processes occurring in water within the  $\mu\text{s}$  time scale following the absorption of radiation energy have been studied extensively [29, 44]. These studies have established that the distribution of the water radiolysis products reaches homogeneity along the radiation track within  $10^{-9}$  to  $10^{-6}$  s. The chemical species formed at this time scale are referred to as primary radiolysis products, and the primary radiolysis yields (often referred to as G-values) are expressed as species formed per unit of absorbed energy ( $\mu\text{mol}\cdot\text{J}^{-1}$ ). For gamma-radiolysis of water, the primary radiolysis products and corresponding G-values (in parenthesis) are given below [37]:



These primary radiolysis yields are not affected by the presence of a solute at a concentration less than  $10^{-2}$  M [37]. Since the primary yields are reached at a very short



time scale ( $< \mu\text{s}$ ) while chemical reactions in solution are slow, the yields can be multiplied by the radiation dose rate ( $\text{J} \cdot (\text{kg H}_2\text{O})^{-1} \cdot \text{s}^{-1} = \text{Gy} \cdot \text{s}^{-1}$ ) to be the production rate of these species by the incident radiation. Homogeneous aqueous phase chemical kinetics under continuous gamma irradiation combines these yields with the subsequent reactions of these species with each other, with water molecules, and, if present, with solute species.

The main water radiolysis product that is involved in the reduction of  $\text{Cr}^{\text{VI}}$  is the hydrated electron,  $\bullet\text{e}_{\text{aq}}^-$ . In de-aerated solutions free of chromium species, the main removal reaction for  $\bullet\text{e}_{\text{aq}}^-$  is (rate constant from reference [30] at  $25^\circ\text{C}$ )



The kinetics of the radiolytic reduction of  $\text{Cr}^{\text{VI}}$  by  $\bullet\text{e}_{\text{aq}}^-$  have been studied using pulse radiolysis techniques [45]:



The rate constant of this process is comparable to that of the reaction of  $\bullet\text{e}_{\text{aq}}^-$  with  $\text{H}_3\text{O}^+$  and it is higher than the typical rate constant for a diffusion-limited reaction. The very high rate constant is attributed to electron tunnelling [46]. Thus, when  $[\text{Cr}^{\text{VI}}] > [\text{H}_3\text{O}^+]$  (4.4) becomes the main route for removal of  $\bullet\text{e}_{\text{aq}}^-$ .

The reduction of the poly-oxygenated  $\text{CrO}_4^{2-}$  or  $\text{Cr}_2\text{O}_7^{2-}$  to  $\text{Cr}(\text{OH})_{3-n}^{n+}$  ( $n = 1, 2, 3$ ) in water requires a change in the coordination structure of the chromium atom from tetrahedral to octahedral [47]. The reduction also requires the loss of an oxygen atom from the Cr coordination structure. In their pulse radiolysis study of  $\text{Cr}^{\text{VI}}$  reduction, Buxton and Djouider found that intermediate  $\text{Cr}^{\text{V}}$  and  $\text{Cr}^{\text{IV}}$  species appear within a few  $\mu\text{s}$

after the radiation pulse and the change in the coordination structure of the Cr atom occurred when the chromium was in the Cr<sup>V</sup> state [48]. In their study, they could not follow the evolution of the chromium species to final products. Thus, it is difficult to determine whether the overall reduction rate of Cr<sup>VI</sup> to Cr<sup>III</sup> is as fast as the rate of reaction (4.4) (effectively the rate for the first step in the Cr<sup>VI</sup> reduction) or if there is a slower rate-determining step later in the reduction.

The rate of the radiolytic reduction can then be expressed as:

$$-\frac{d[CrO_4^{2-}]}{dt} = \frac{d[Cr^{III}]}{dt} = k_{Cr^{VI}-\bullet e_{aq}^-} \cdot [CrO_4^{2-}] \cdot [\bullet e_{aq}^-] \quad (4.5)$$

where  $k_{Cr^{VI}-\bullet e_{aq}^-}$  is the rate constant for reaction (4.4). The data in the top graph of Figure 4.3 show that the rate of loss of Cr<sup>VI</sup> follows a straight line with a slope that is independent of pH and  $[CrO_4^{2-}]_0$ . This slope is also the same in value, but with the opposite sign, as the slope of the rate of increase in  $[Cr^{III}(col)]$ . This result can also be explained by radiolysis kinetics. Under continuous radiolysis conditions, the concentration of a radical radiolysis product is determined by the primary radiolysis production rate and the removal rates of the products [29, 37]:

$$\frac{d[\bullet e_{aq}^-]}{dt} = C_R \cdot D_R \cdot G_{\bullet e_{aq}^-} - \sum_i k_{i-\bullet e_{aq}^-} \cdot [i] \cdot [\bullet e_{aq}^-] \quad (4.6)$$

where  $C_R$  is a unit conversion factor,  $D_R$  is the radiation energy absorption rate (1.87 Gy·s<sup>-1</sup> in this study where Gy = J·kg<sup>-1</sup>),  $G_{\bullet e_{aq}^-}$  is the primary production yield for  $\bullet e_{aq}^-$  (0.26 μmol·J<sup>-1</sup>) and  $k_{i-\bullet e_{aq}^-}$  is the second order rate constant for the reaction of  $\bullet e_{aq}^-$  with species  $i$ . At the studied pHs (> 6.0) and for  $[CrO_4^{2-}]_0$  (> 0.1 mM), reaction (4.4) is the

main removal path for  $\bullet e_{aq}^-$ . This allows to simplify equation (4.6) using the approximation

$$\sum_i k_{i-\bullet e_{aq}} \cdot [i] \cdot [\bullet e_{aq}^-] \approx 3 \cdot k_{Cr^{VI}-\bullet e_{aq}} \cdot [CrO_4^{2-}] \cdot [\bullet e_{aq}^-] \quad (4.7)$$

The rate constant  $k_{Cr^{VI}-\bullet e_{aq}}$  in equation (4.7) is the same rate constant used in equation (4.5). The factor of three is necessary because the reduction of  $Cr^{VI}O_4^{2-}$  to  $Cr^{III}$  requires reaction with three hydrated electrons ( $\bullet e_{aq}^-$ ).

The rapid removal of  $\bullet e_{aq}^-$  ensures that  $[\bullet e_{aq}^-]$  will be at steady state during continuous irradiation:

$$\frac{d[\bullet e_{aq}^-]}{dt} = C_R \cdot D_R \cdot G_{\bullet e_{aq}} - 3 \cdot k_{Cr^{VI}-\bullet e_{aq}} \cdot [CrO_4^{2-}] \cdot [\bullet e_{aq}^-] \approx 0 \quad (4.8)$$

so that

$$C_R \cdot D_R \cdot G_{\bullet e_{aq}} \approx 3 \cdot k_{Cr^{VI}-\bullet e_{aq}} \cdot [CrO_4^{2-}] \cdot [\bullet e_{aq}^-] \quad (4.9)$$

and

$$[\bullet e_{aq}^-] = \frac{C_R \cdot D_R \cdot G_{\bullet e_{aq}}}{3 \cdot k_{Cr^{VI}-\bullet e_{aq}} \cdot [CrO_4^{2-}]} \quad (4.10)$$

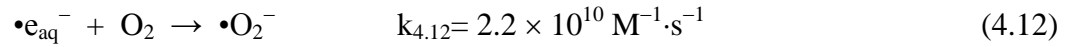
Substitution of equation (4.9) into equation (4.5) yields:

$$-\frac{d[CrO_4^{2-}]}{dt} = \frac{d[Cr^{III}]}{dt} = \frac{1}{3} \cdot C_R \cdot D_R \cdot G_{\bullet e_{aq}} \quad (4.11)$$

This analysis also shows that the rate of radiolytic reduction of  $CrO_4^{2-}$  to  $Cr^{III}$  is constant with time, and independent of pH and  $[CrO_4^{2-}]_0$ , consistent with the data shown in Figure 4.3.

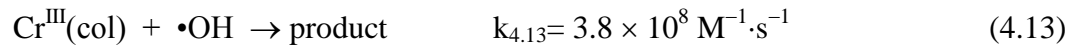
Equation (4.11) also predicts that the slope of the plot of  $[\text{CrO}_4^{2-}]$  versus time will be 1/3 of the primary production rate of  $\bullet\text{e}_{\text{aq}}^-$ . The absolute values of the slopes of the lines for the plots of  $[\text{CrO}_4^{2-}]$  vs t and  $[\text{Cr}^{\text{III}}]$  vs t in Figure 4.3 are  $(1.8 \pm 0.2) \times 10^{-7} \text{ M}\cdot\text{s}^{-1}$ . At the dose rate used in this study, the production rate  $C_R \cdot D_R \cdot G_{\bullet\text{e}_{\text{aq}}^-}$  is  $5.2 \times 10^{-7} \text{ M}\cdot\text{s}^{-1}$ . This value is close to three times the slopes obtained from the data in Figure 4.3, consistent with the prediction of equation (4.5).

In all tests with an aerated solution no conversion of  $\text{Cr}^{\text{VI}}$  to  $\text{Cr}^{\text{III}}$  was observed. This is because the  $\text{O}_2$  that is present in the solution provides a preferential partner for removal of  $\bullet\text{e}_{\text{aq}}^-$  through the reaction:[37]



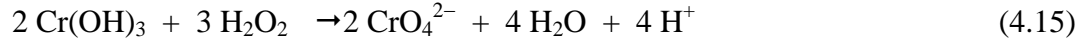
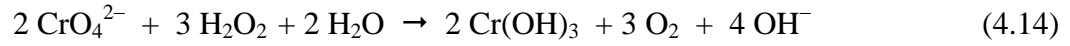
The dissolved oxygen concentration in a fully aerated solution is  $\sim 2 \times 10^{-4} \text{ M}$  and can effectively compete with  $\text{CrO}_4^{2-}$  for  $\bullet\text{e}_{\text{aq}}^-$ .

Any chromium reduction products ( $\text{Cr}^{\text{V}}$ ,  $\text{Cr}^{\text{IV}}$  or  $\text{Cr}^{\text{III}}$ ) can also react with  $\bullet\text{OH}$  to reform  $\text{Cr}^{\text{VI}}$ ; the rate constant for the oxidation reaction of  $\text{Cr}^{\text{III}}(\text{aq})$  with  $\bullet\text{OH}$  has been reported to be in the range of  $3.1$  to  $3.8 \times 10^8 \text{ M}^{-1}\cdot\text{s}^{-1}$ : [49,50]



The steady-state concentration of  $\bullet\text{OH}$  would be only slightly higher than that of  $\bullet\text{e}_{\text{aq}}^-$  [37] (see further analysis below). Thus, this reaction is slow compared to the reduction of  $\text{Cr}^{\text{VI}}$  (4.4) and hence will not influence the kinetics of the net conversion of  $\text{Cr}^{\text{VI}}$  to  $\text{Cr}^{\text{III}}$  until most of the  $\text{Cr}^{\text{VI}}$  has been converted. Consequently, linear slopes were observed in Figure 4.3 until most of the  $\text{CrO}_4^{2-}$  was reduced.

Hydrogen peroxide is another important water radiolysis product and it can act as both a reductant and an oxidant in reactions with chromium ions:



These Fenton-like reactions can explain the negligible net production of  $\text{H}_2\text{O}_2$ . These reactions are important for determining  $[\text{H}_2\text{O}_2]$ , but are much slower than reactions (4.4) and (4.12) and hence their contributions to the chromium redox chemistry are negligible.

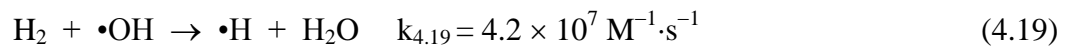
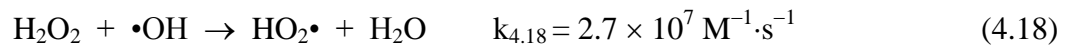
As  $[\text{Cr}^{\text{III}}]$  increases, reaction (4.13) provides a pathway for removal of  $\bullet\text{OH}$ . At steady state the time independent behaviour of  $[\bullet\text{OH}]$  is given by: [37]

$$\frac{d[\bullet\text{OH}]}{dt} = C_R D_{RG} \bullet\text{OH} - \sum_i k_i \bullet\text{OH}[i][\bullet\text{OH}] \approx 0 \quad (4.16)$$

and

$$[\bullet\text{OH}] \approx \frac{C_R D_{RG} \bullet\text{OH}}{\sum_i k_i \bullet\text{OH}[i]} \quad (4.17)$$

At the start of a test, when  $[\text{Cr}^{\text{III}}]$  is very low the main paths for removal of  $\bullet\text{OH}$  are



At early times  $[\bullet\text{OH}]$  should be nearly independent of  $[\text{Cr}^{\text{VI}}]_0$  and this is what observed in the lower graph of Figure 4.3. In stage 2, where  $[\text{Cr}^{\text{III}}]$  is high, reaction (4.13) becomes the dominant path for removal of  $\bullet\text{OH}$ . This results in a decrease in the  $[\bullet\text{OH}]$  and therefore a decrease in the rate of reaction (4.19) and a consequent increase in  $[\text{H}_2]$ , again

as seen in Figure 4.3. This is the expected behaviour of  $H_2$  as it is well established that the concentration of  $[H_2]$  is inversely proportional to  $[•OH]$  in water systems exposed to continuous gamma irradiation [37].

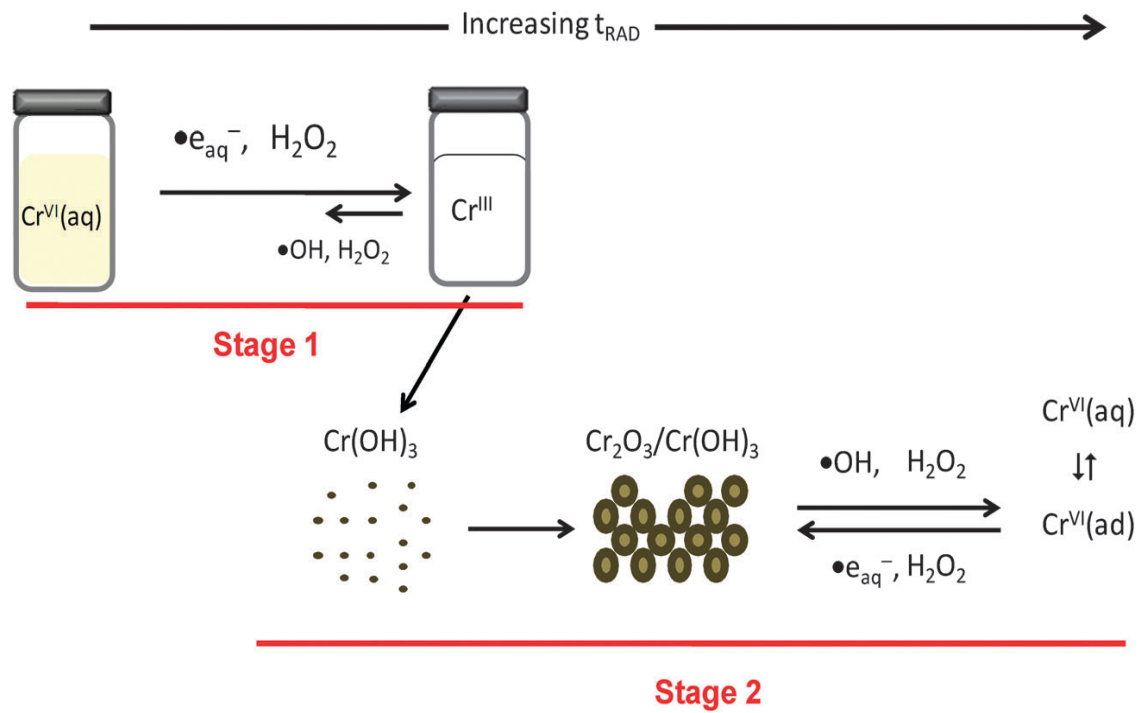
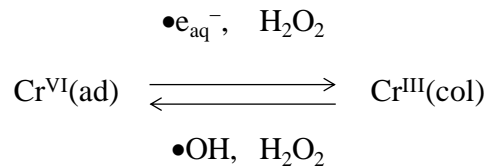


**Figure 4.8:** Schematic representation of the proposed mechanism for the radiolytic formation of chromium oxide nanoparticles under steady state radiolysis.

### 4.3.3 Particle growth mechanism

Figure 4.8 shows a schematic representation of the mechanism for the radiolytic formation of  $\text{Cr}_2\text{O}_3$  nanoparticles. Particle growth in stage 1 is very slow and no appreciable particles could be collected for particle analysis (as discussed above). The  $\text{Cr}(\text{OH})_3$  that is formed in stage 1 is homogeneously dispersed and particle growth occurs by agglomeration of  $\text{Cr}^{\text{III}}$  driven by Brownian motion. No appreciable conversion of  $\text{Cr}(\text{OH})_3$  to other oxides occurs until all of the  $\text{Cr}^{\text{VI}}$  is consumed. As the particles of  $\text{Cr}(\text{OH})_3$  grow they begin to dehydrate and the inner oxide becomes  $\text{Cr}_2\text{O}_3$ . In stage 2, when the most of the  $\text{Cr}^{\text{VI}}$  has been reduced, dehydration continues and the water radiolysis products participate in redox reactions with chromium species on the particle surface. Eventually the system will reach a steady state in which the particles are largely  $\text{Cr}_2\text{O}_3$  and cyclic reactions of  $\text{Cr}^{\text{III}}$  with  $\bullet\text{OH}$  and  $\text{H}_2\text{O}_2$  and  $\text{Cr}^{\text{VI}}$  with  $\bullet\text{e}_{\text{aq}}^-$  and  $\text{H}_2\text{O}_2$  occur at the liquid-solid interface:



The final size of the particles formed is determined by the steady-state redox conditions at the particle liquid-solid interface. The existence of adsorbed  $\text{Cr}^{\text{VI}}$  on the particles is confirmed by the observation of  $\text{Cr}^{\text{VI}}$  on the unwashed particles that were collected (washing removes the soluble  $\text{Cr}^{\text{VI}}$ ). Distilled water not only dissolves the adsorbed  $\text{Cr}^{\text{VI}}$  but also provides a different redox environment, changing the surface potential of the particles. This can promote agglomeration of  $\text{Cr}^{\text{III}}$  particles by Ostwald ripening [24]. Thus, when the particles were washed with distilled water after irradiation a wider range of size was observed (Figure 4.6).



#### 4.4 CONCLUSION

Uniform-sized Cr<sup>III</sup> colloidal particles, 9-30 nm in diameter, were formed by gamma-irradiation of de-aerated solutions of dissolved Cr<sup>VI</sup> (as K<sub>2</sub>Cr<sub>2</sub>O<sub>7</sub>) at pHs 6.0, 8.5 and 10.6. A radiation-induced Cr<sub>2</sub>O<sub>3</sub> particle formation and growth mechanism is proposed based on the observed time-dependent behaviours of [Cr<sup>VI</sup>], [Cr<sup>III</sup>(col)] and [H<sub>2</sub>], particle analyses by TEM and a range of spectroscopic techniques. In stage 1, the homogeneous aqueous reduction of Cr<sup>VI</sup> to Cr<sup>III</sup>(col) by •e<sub>aq</sub><sup>-</sup> is prevalent while particle growth by agglomeration of Cr<sup>III</sup>(col) (as Cr(OH)<sub>3</sub>) by Brownian motion is taking place at a slow rate. As the Cr(OH)<sub>3</sub> particles grow, the interior of the particles dehydrates to form Cr<sub>2</sub>O<sub>3</sub> while the outer layer remains hydrated. However, the dehydration rate is very slow since Cr(OH)<sub>3</sub> is a relatively stable phase. In stage 2, most of the initial Cr<sup>VI</sup> has been converted to Cr(OH)<sub>3</sub> and has condensed onto particles. Redox reactions of chromium species occur on the particle surfaces. The surface redox reactions reach an equilibrium state with cyclic reactions of Cr<sup>III</sup> oxidation by •OH and H<sub>2</sub>O<sub>2</sub> and Cr<sup>VI</sup> reduction by •e<sub>aq</sub><sup>-</sup> and H<sub>2</sub>O<sub>2</sub>. The final particle size distribution is determined by the steady-state redox conditions that are established at the liquid-solid interface.

#### 4.5 REFERENCE:

- [1] T. Brock, M. Groteklaes, P. Mischke, in *European Coating Handbook*, Vincentz, Hannover, Germany, 2000.
- [2] B.M. Abu-Zied, *Appl. Catal. A: Gen.*, 198 (2000) 139.
- [3] P. Berdhal, *Trans. Am. Soc. Mech. Eng. J. Heat Transfer*, 117 (1995) 355.
- [4] H. Kitsunai, K. Hokkirigawa, N. Tsumaki, K. Kato, *Wear*, 151 (1991) 279.
- [5] T. Ivanova, K. Gesheva, A. Cziraki, A. Szekeres, E. Vlaikova, *J. Phys. Conf. Ser.*, 113 (2008) 012030.
- [6] P. Gibot, L. Vidal, *J. Eur. Ceram. Soc.*, 30 (2010) 911.
- [7] A.M.L. Medeiros, M.A.R. Miranda, A.S. de Menezes, P.M. Jardim, L.R.D. de Silva, S.T. Gouveia, J.M. Sasaki, *J. Metastable Nanocryst. Mater.*, 20 (2004) 399.
- [8] Z. Pei, H. Xu, Y. Zhang, *J. Alloys. Compd.*, 468 (2009) L5.
- [9] M.D. Lima, R. Bonadimann, M.J. de Addrade, J.C. Toniolo, C.P. Bergmann, *J. Eur. Ceram. Soc.*, 26 (2006) 1213.
- [10] N. Arul Dash, Y. Koltypin, A. Gedanken, *Chem. Mater.*, 9 (1997) 3159.
- [11] G. Peters, K. Jerg, B. Schramn, *Mater. Chem. Phys.*, 55 (1998) 197.
- [12] Z. Gui, R. Fan, W. Mo, X. Chen, L. Yang, U. Hu, *Mater. Res. Bull.*, 38 (2003) 169.
- [13] L. Znaidi, C. Pommier, *Eur. J. Solid. State. Inorg. Chem.*, 35 (1998) 405.
- [14] A. Kawabata, M. Yoshinaka, K. Hirota, O. Yamaguchi, *J. Am. Ceram. Soc.*, 78 (1995) 2271.
- [15] D.W. Kim, S.I. Shin, J.D. Lee, S.G. Oh, *Mater. Lett.*, 58 (2004) 1894.

- [16] U. Balachandran, R.W. Siegel, Y.X. Liao, T.R. Askew, *Nanostruct.Mater.*, 5 (1995) 505.
- [17] D. Vollath, D.V. Szabo, J.O. Willis, *Mater. Lett.*, 29 (1996) 271.
- [18] C. Zhu, Y. Hong, J. Zhang, B. Zhou, *Key. Eng. Mater.*, 353 (2007) 2111.
- [19] M-E. Meyre, M. Treguer-Delapierre, C. Faure, *Langmuir*, 24 (2008) 4421.
- [20] P.A. Yakabuskie, J.M. Joseph, P. Keech, G.A. Botton, D. Guzonas, J.C. Wren, *Phys. Chem. Chem. Phys.*, 13 (2011) 7198.
- [21] T. Li, H.G. Park, S-H. Choi, *Mater. Chem. Phys.*, 105 (2007) 325.
- [22] J. Koatas, Z. Stasicka, *Environ. Pollut.*, 107 (2000) 263.
- [23] Y.-L. Wei, W.-J. Sun, H.-C. Huang, Y.-W. Yang, J.-F. Lee, *J. Electron Spectros. Relat. Phenomena*, 144 (2005) 303.
- [24] S. Aber, A.R. AmaniGhadim, V. Mirzajani, *J. Hazard. Mater.*, 171 (2009) 484.
- [25] E.J. Yurkow, J. Hong, S. Min, S. Wang, *Environ. Pollut.*, 117 (2002) 1.
- [26] M. Pettine, I. Barra, L. Campanella, F.J. Millero, *Wat. Res.*, 32 (1998) 2807.
- [27] E. Dermou, A. Velissariou, D. Xenos, D. Vayenas, *J. Hazard. Mater.*, 126 (2005) 78.
- [28] S-J. Yuan, Z. Zheng, Y-Y. Mu, X. Yu, Y-F. Zhao, *J. Environ.Sci.*, 18 (2006) 254.
- [29] J.W.T. Spinks, R.J. Woods, *An Introduction to Radiation Chemistry*, Wiley-Interscience, New York, 1990.
- [30] J.C. Wren, Steady-state radiolysis: effect of dissolved additives in ACS Symposium Series: *Nuclear Energy and the Enviroment*, 2010.
- [31] J. Belloni, M. Mostafavi, H. Remita, J.L. Marignier, M.O. Delcourt, *New. J. Chem.*, 22 (1998) 1239.
- [32] Y. Ni, X. Ge, Z. Zhang, Q. Ye, *Chem. Mater.*, 14 (2002) 1048.

- [33] S. Chen, Y. Liu, G. Wu, *Nanotechnology*, 16 (2005) 2360.
- [34] L.M. Alrehaily, J.M Joseph, M.C. Biesinger, D. Guzonas, J.C. Wren, *Phys. Chem. Chem. Phys.*, 15 (2013) 1014.
- [35] F. Djouider, M.S. Aljohani, *J. Radioanal. Nucl. Chem.*, 285 (2010) 417.
- [36] J.D. Ramsey, L.Xia, M.W. Kending, R. L. McCreery, *Corros. Sci.*, 43 (2001) 1557.
- [37] J.M. Joseph, B.S. Choi, P.A. Yakabuskie, J.C. Wren, *Radiat. Phys. Chem.*, 77 (2008) 1009.
- [38] C.J. Hochanadel, *J. Phys. Chem.*, 56 (1952) 587.
- [39] I. Stefanic, J.A. Laverne, *J. Phys. Chem. A*, 106 (2002) 447.
- [40] T. Shigematsu, S. Gohda, H. Yamazaki, Y. Nishikawa, *Bull. Inst. Chem. Res. Kyoto Univ.*, 55 (1977) 429.
- [41] C.F. Baes, R.E. Mesmer (2<sup>nd</sup> ED). *Hydrolysis of Cations*, Krieger Pub. Co. Malabar, Florida, 1986.
- [42] R.E. Kirk, D.F. Othmer, *Kirk-Othmer encyclopedia of Chemical Technology*. John Wiley & Sons, 2003.
- [43] M.C. Biesinger, B. Payne, A. Grosvenor, L. Lau, A. Gerson, R. Smart, *Appl. Surf. Sci.*, 257 (2011) 2717.
- [44] Farhataziz, M.A.J. Rodgers, *Radiation Chemistry: Principles and Applications*, NY:VCH, New York, 1987.
- [45] G.V. Buxton, in *Radiation Chemistry*, M. Spothem-Maurizot, M. Mostafavi, T. Douki, J. Belloni, Eds., EDP Sciences, France, 2008.
- [46] E.J. Hart, M. Anbar, *The Hydrated Electron*, Wiley Interscience, New York, 1970.
- [47] J.Y-P. Tong, E.L. King, *J. Am. Chem. Soc.*, 82 (1960) 3805.

- [48] G.V. Buxton, F. Djouider, *J. Chem. Soc., Faraday Trans.*, 92 (1996) 4173.
- [49] M. Al-Sheikhly, W.L. McLaughlin, *Radiat. Phys. Chem.*, 38 (1991) 203.
- [50] R. Boistelle, J. Astier, *J. Cryst. Growth*, 90 (1988) 14.

## Chapter 5

### Radiation-Induced Cobalt-Oxide Nanoparticle Formation: Kinetics of Particle Size Control

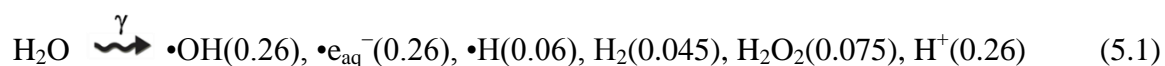
#### 5.1 INTRODUCTION

Transition metal oxide nanoparticles (such as iron oxide, chromium oxide and cobalt oxide) have many potential useful applications. The magnetic, catalytic, optical, and electronic properties of these metal oxides are determined by the size, structure and shape of the particles that they form [1,2]. For example, spinel-type cobalt oxide ( $\text{Co}_3\text{O}_4$ ) nanoparticles have been used as heterogeneous catalysts, selective absorbers of solar radiation [3], and anode materials for rechargeable Li ion batteries [1]. The properties of  $\text{Co}_3\text{O}_4$  nanoparticles make them promising materials for electronic devices [4], gas sensors [5], magnetic materials [6], electrochromic devices [7], and electrochemical anodes for sensors [8].

Cobalt oxide nanoparticles have been synthesized by several physical and chemical methods including spray pyrolysis [9], chemical vapour deposition [5], sol-gel techniques [10], pulsed laser deposition [11], thermal decomposition of solid cobalt nitrate [12], and hydrothermal synthesis [1]. These methods are either complex, or require chemically harsh conditions and/or high processing temperatures for the synthesis of nano-scale crystalline  $\text{Co}_3\text{O}_4$  particles. Drawbacks of these methods include a low level of control over particle size and composition, and a difficulty in generating a pure, single-phase product. Radiation-

induced nanoparticle formation is a promising new technique that addresses these drawbacks.

When exposed to ionizing radiation, water decomposes to yield a range of chemically reactive species. For  $\gamma$ -radiolysis at room temperature, the primary radiolysis products (formed within  $\sim 100$  ns following the absorption of radiation energy) and their yields per absorbed radiation energy (in brackets in units of  $\mu\text{mol}\cdot\text{J}^{-1}$ ) are [13,14]:



These chemical yields per unit energy input are very high. Such high yields, particularly for the radicals, cannot be obtained by thermal processes and gamma-radiolysis is the most effective way of producing these reactive species. Due to the long penetration depth of a typical  $\gamma$ -ray in water ( $\sim 20$  cm for a half reduction in intensity), these species can be produced nearly uniformly within a reasonably large volume of water. The combination of high densities of redox reactive species and their uniform production and distribution in solution can provide ideal conditions for promoting homogeneous redox reactions.

If the product of a reaction of a dissolved species with a radiolysis-generated species has a significantly different solubility from that of the reactant, then a solid product can be formed. Rapid condensation can create homogeneously distributed nucleation sites onto which the radiolysis-induced oxidation or reduction product can continue to deposit and grow the particle size. Because a very large number of nucleation sites are generated simultaneously and homogeneously, this process leads to the formation of nanoparticles with a narrow, uniform size distribution. This principle has been applied in making noble metal nanoparticles (of silver and gold) from dissolved metal ions, taking advantage of the strong reducing power of  $\cdot\text{e}_{\text{aq}}^-$  produced by radiolysis [15-19].

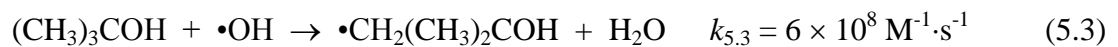
The formation of nanometer-sized  $\gamma$ -FeOOH and  $\text{Co}_3\text{O}_4$  particles by continuous  $\gamma$ -irradiation of solutions containing dissolved  $\text{Fe}^{2+}$  (added as  $\text{FeSO}_4$ ) and  $\text{Co}^{2+}$  (as  $\text{CoSO}_4$ ) respectively without any other chemical additives were recently reported [20,21]. In these studies the advantage of the strong oxidizing power of  $\bullet\text{OH}$  and  $\text{H}_2\text{O}_2$  have taken rather than the strong reducing power of  $\bullet e_{\text{aq}}^-$ , and of the large difference in the solubility of the oxidation products which then precipitate as metal oxide nanoparticles.

In the case of cobalt,  $\gamma$ -radiolysis converts soluble  $\text{Co}^{\text{II}}$  to less soluble  $\text{Co}^{\text{III}}$  oxide and hydroxide [20]:



In cobalt study the investigated of the nanoparticle formation as a function of pH and dissolved  $\text{O}_2$  concentration, and found that the nanoparticles were formed only under conditions that promote  $\text{Co}^{\text{II}}$  adsorption on the particles that grow. Based on the observed effects of pH and dissolved oxygen on the oxidation kinetics of  $\text{Co}^{\text{II}}$  to  $\text{Co}^{\text{III}}$  and the final size of the particles, a mechanism was proposed in which  $\text{Co}^{\text{II}}/\text{Co}^{\text{III}}$  hydroxide condensates act as nucleation sites on which radiolytically-induced heterogeneous oxidation processes can occur. The particles grow as a  $\text{CoOOH}$  phase which is converted to  $\text{Co}_3\text{O}_4$  at longer irradiation times.

This chapter include report on an investigation of the effects of radical scavengers, (*t*-butanol for  $\bullet\text{OH}$ ,  $\text{N}_2\text{O}$  for  $\bullet e_{\text{aq}}^-$ , and dissolved  $\text{O}_2$  for both  $\bullet\text{OH}$  and  $\bullet e_{\text{aq}}^-$ ) on  $\gamma$ -radiation-induced cobalt oxide nanoparticle formation. The intent was to confirm the role of  $\bullet\text{OH}$  in the reaction kinetics. Tertiary-butanol is a well-known scavenger for the oxidizing radical  $\bullet\text{OH}$  (rate constant from ref [22]).





On the other hand, both N<sub>2</sub>O and O<sub>2</sub> are efficient scavengers of the reducing radical, •e<sub>aq</sub><sup>-</sup> (rate constants from ref [23]):



The products of the reactions of N<sub>2</sub>O and O<sub>2</sub> with •e<sub>aq</sub><sup>-</sup> are, however, different. The N<sub>2</sub>O reaction with •e<sub>aq</sub><sup>-</sup> produces an oxidizing radical while the reaction with O<sub>2</sub> produces superoxide (•O<sub>2</sub><sup>-</sup>), a weaker reductant.

The cobalt oxidation kinetics were followed by measuring the concentrations of Co<sup>II</sup> and Co<sup>III</sup> as a function of irradiation time. The particles formed after 5 h of irradiation were collected and characterized by TEM and Raman spectroscopy.

## 5.2 EXPERIMENTAL

Cobalt solutions (0.1 mM) were prepared by dissolving high-purity cobalt (II) sulfate obtained from Sigma-Aldrich (purity ≥ 99%). The *t*-butanol obtained from Sigma-Aldrich was of high purity (purity ≥ 99%). Gas containing 50% N<sub>2</sub>O in Ar was purchased from Praxair (impurities < 0.001%). All solutions were freshly prepared with water purified using a NANOpure Diamond UV ultrapure water system, with a resistivity of 18.2 MΩ·cm. The pH was adjusted to 10.6 using a concentrated NaOH solution. The pH value was chosen based on the solubilities of Co<sup>II</sup> and Co<sup>III</sup> species [24]. The solubility of Co<sup>II</sup> is at a minimum (~10<sup>-6</sup> M) at pH 10.6 whereas it is many orders of magnitude higher (~1 M) at pH 6.0. The solutions were either aerated by purging with high purity air (Praxair) or de-aerated by purging with high purity Ar for one hour. Using a syringe, 10 ml of the test solution was transferred to a pre-sealed 20-ml vial [25]. All experiments were performed with a gas

headspace in the test vial. For experiments performed with N<sub>2</sub>O, the test solutions were purged with N<sub>2</sub>O gas for about 15- 20 min. The test vials were irradiated in a <sup>60</sup>Co gamma cell (MDS Nordion) as described in chapter 2. The gamma source provided a uniform absorption dose rate of 4.5 kGy·h<sup>-1</sup> in the water samples at the time of this study.

Following irradiation for a desired period, a series of chemical analyses of solution species was first performed. Colloid particles were then collected for various particle analyses. A liquid sample removed from the vial using a syringe was analyzed for Co<sup>III</sup> content by UV-VIS absorption (BioLogic Science Instruments). The solution cobalt species and H<sub>2</sub>O<sub>2</sub> content were subsequently quantified by colorimetric analysis.

The total concentration of dissolved Co<sup>III</sup> present in the test solution was determined by reacting a sample from the solution with 4-(2-pyridylazo) resorcinol (PAR) to form a coloured complex that absorbs light at 510 nm with a molar extinction coefficient of  $5.6 \times 10^4 \text{ M}^{-1} \cdot \text{cm}^{-1}$  [26]. To determine the concentration of Co<sup>II</sup> present, any Co<sup>II</sup> in the sample was then oxidized to Co<sup>III</sup> by adding 1 ml of 3% hydrogen peroxide solution, allowing it to react and then heating the sample to 100 °C in a boiling water bath to remove any unreacted hydrogen peroxide. The Co<sup>III</sup> concentration of this oxidized solution was then determined again by the PAR method described above. The difference between the total cobalt concentration (determined after oxidation) and the concentration of Co<sup>III</sup> determined prior to the hydrogen peroxide treatment was taken to be the concentration of Co<sup>II</sup> in the solution phase. Using this method, the detection limits for both [Co<sup>II</sup>] and [Co<sup>III</sup>] were 1 μM [26]. The validity of the PAR method was confirmed by measuring the concentration of Co<sup>II</sup> in our initially prepared CoSO<sub>4</sub> solutions.

The concentration of hydrogen peroxide in the test solution was determined by the Ghormley tri-iodide method [27] in which  $\Gamma^-$  is oxidized to  $I_3^-$  by  $H_2O_2$  in the presence of ammonium molybdate as a catalyst, followed by spectrophotometric measurement of the  $I_3^-$  concentration;  $I_3^-$  has a maximum absorption at 350 nm with a molar extinction coefficient of  $25500\text{ M}^{-1}\cdot\text{cm}^{-1}$  [28]. We tested for and observed no oxidation of  $\Gamma^-$  to  $I_3^-$  by  $Co^{III}$  in our test solutions.

Particles were collected from the sample vials for analyses by transmission electron microscopy (TEM), X-ray photoelectron spectroscopy (XPS) and Raman spectroscopy. For TEM the particles were collected by dipping a carbon-coated copper grid into the irradiated test solution and drying the sample grid in air. Samples for the XPS and Raman analyses were collected by centrifuging the solution and then drying the precipitate on a glass plate in air. The sizes and shapes of the particles were measured using TEM with the microscope operating at 80 keV. X-ray photoelectron spectra were acquired on a KRATOS Axis Nova spectrometer using monochromatic Al K (alpha) radiation and operating at 210 W, with a base pressure of  $10^{-8}$  Pa. Raman scattering measurements to determine the particle chemical composition were performed using a Renishaw model 2000 Raman Spectrometer with a laser excitation wavelength of 633 nm.

## 5.3 RESULTS

### 5.3.1 Effect of Scavengers on the Type, Shape and Size of Nanoparticles

The effect of the radical scavengers *t*-butanol,  $N_2O$  and dissolved  $O_2$  on radiation-induced cobalt oxide nanoparticle formation was investigated using solutions initially

containing 0.1 mM CoSO<sub>4</sub> at pH 10.6. The studied solutions are listed in Table 5.1. The concentration of dissolved O<sub>2</sub> in an air-saturated solution is ~ 0.25 mM at 25 °C [13]. The concentration of N<sub>2</sub>O in the N<sub>2</sub>O/Ar purged solution is estimated to be ~ 12.5 mM, half of the solubility of N<sub>2</sub>O at 1 atm at 25 °C [29].

**Table 5.1:** Test solutions studied.

	no scavengers	one type of scavenger			two types of scavenger
ID	1	2	3	4	5
Type of solution	deaerated only	deaerated & 0.1 M <i>t</i> -butanol	purged with N <sub>2</sub> O/Ar	aerated only	aerated & 0.1 M <i>t</i> -butanol

No detectable particles were formed after 5 h of irradiation without any scavengers present (solution 1) or with 0.1 M *t*-butanol only added (solution 2). The TEM images of the particles formed in the solutions of with other three scavenging environments are presented in Figure 5.1. The Raman spectra of these particles are compared with the reference spectra of standard samples of various cobalt oxides and hydroxides in Figure 5.2. The spectra of the particles all match the reference spectrum of Co<sub>3</sub>O<sub>4</sub> very well, with no unidentified peaks, and this indicates that the particles are all essentially pure Co<sub>3</sub>O<sub>4</sub>.

Although the particles formed are all the same species, their sizes depended on the nature of the test solution. TEM images in Figure 5.1 show that the particles are: 8 – 20 nm in the aerated only solutions (solution 4), 10 – 30 nm in the aerated with 0.1 M *t*-butanol solutions (solution 5), and 60 – 80 nm in the N<sub>2</sub>O/Ar purged solutions (solution 3).

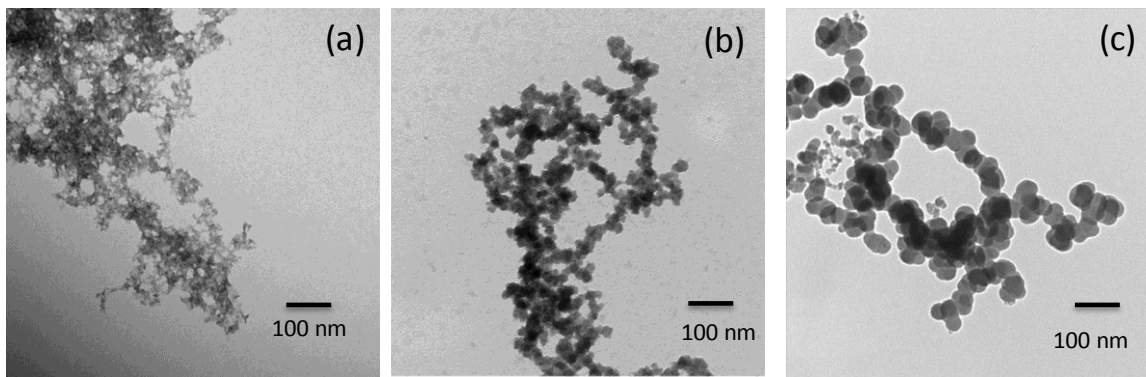


**Figure 5.1:** TEM images of cobalt oxide nanoparticles formed in 0.1 mM  $\text{CoSO}_4$  solutions (5 h irradiation) in different scavenging environments: (a) aerated only, (b) aerated and 0.1 M *t*-butanol, and (c)  $\text{N}_2\text{O}/\text{Ar}$  purged.

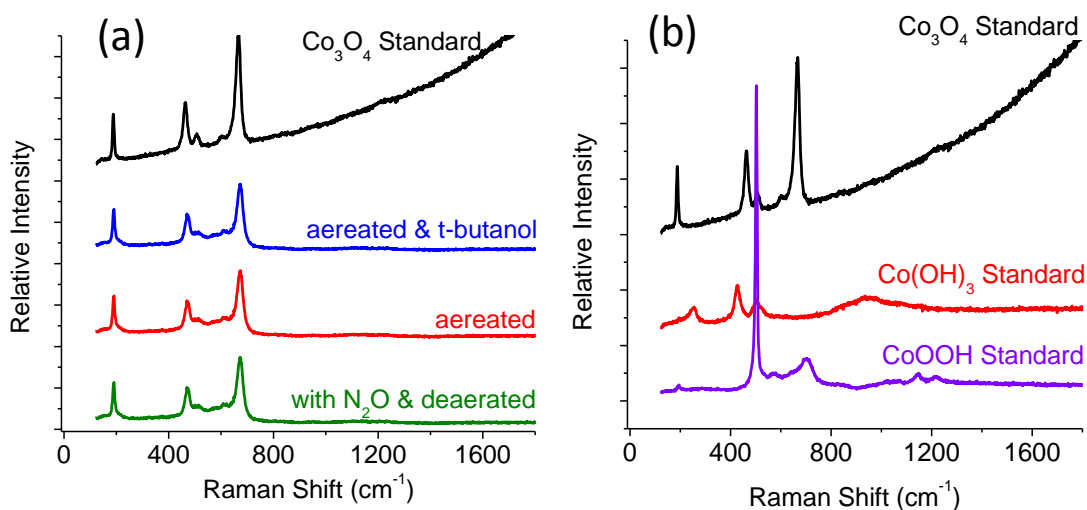


**Figure 5.2:** (a) Raman spectra of the particles collected after 5 h irradiation of 0.1 mM  $\text{CoSO}_4$  solutions at pH 10.6 in different scavenging environments (shifted vertically for presentation) and (b) Raman spectra of standard cobalt oxides/hydroxides.

### 5.3.2 Effect of Scavenger on the Kinetics of Radiolytic Conversion of $\text{Co}^{\text{II}}$ to $\text{Co}^{\text{III}}$

To determine the mechanism by which the radical scavengers influence the size of the particles that grow, the kinetics of radiolytic conversion of the initially dissolved  $\text{Co}^{2+}$  ions to  $\text{Co}_3\text{O}_4$  particles were investigated by following the concentrations of  $\text{Co}^{\text{II}}$  and  $\text{Co}^{\text{III}}$  as a function of irradiation time. The rates of change of the  $[\text{Co}^{\text{II}}]$  and  $[\text{Co}^{\text{III}}]$  obtained from the same irradiation tests that produced the particles shown in Figure 5.1 are compared in Figure 5.3.

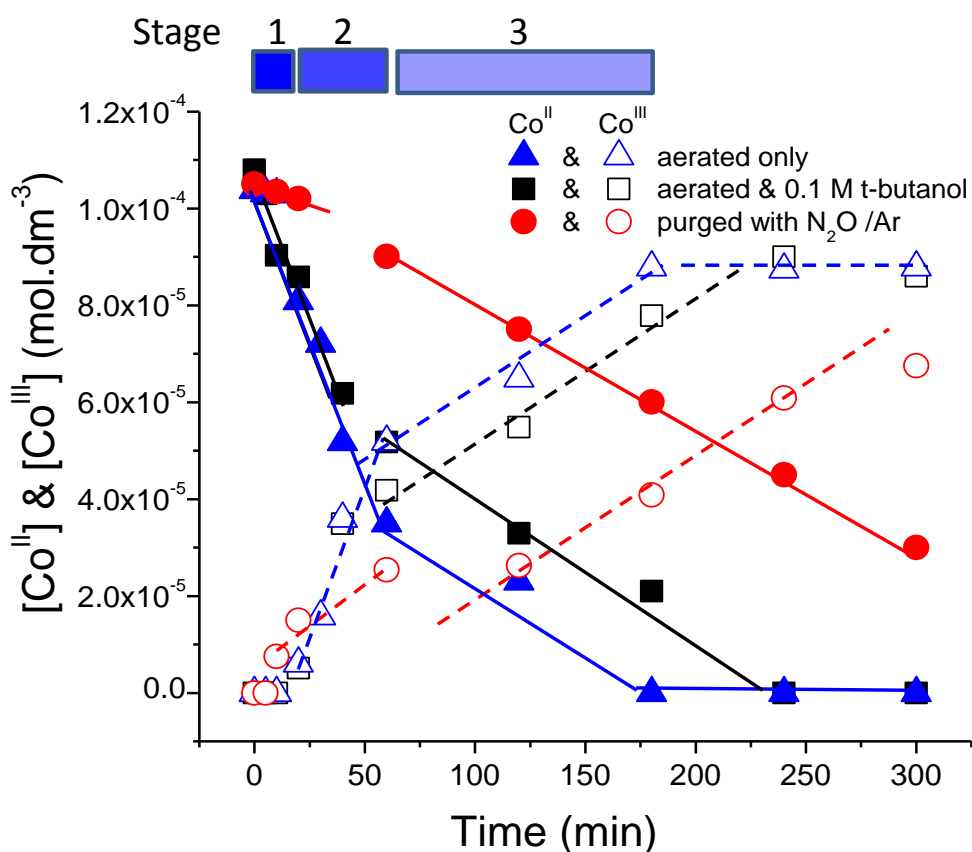


**Figure 5.3:** Concentrations of  $\text{Co}^{\text{II}}$  (solid symbols) and  $\text{Co}^{\text{III}}$  (open symbols) as a function of irradiation time for 0.1 mM  $\text{CoSO}_4$  solutions at pH 10.6 in different scavenging environments: aerated only ( $\blacktriangle$  &  $\triangle$ ), aerated and 0.1 M *t*-butanol ( $\blacksquare$  &  $\square$ ), and purged with  $\text{N}_2\text{O}/\text{Ar}$  ( $\bullet$  &  $\circ$ ).

In all three solutions that produced nanoparticles (solutions 3, 4 and 5), the changes in  $[\text{Co}^{\text{II}}]$  and  $[\text{Co}^{\text{III}}]$  during irradiation have at least two kinetic stages with distinctly different time dependences. Previously, in similar experiments performed with a higher initial  $\text{Co}^{\text{II}}$  concentration we saw three separate kinetic stages. In that study, Stage 1, during which  $[\text{Co}^{\text{II}}]$  decreased very rapidly with time while no  $\text{Co}^{\text{III}}$  was detected, was more clearly seen and this occurred in the first 10 min, see further discussion below. In this current study, there is some limited evidence in Figure 5.3 for a delay in the onset of  $\text{Co}^{\text{III}}$  production, which depends on the nature of the solution, and for consistency with the previous work it would consider this evidence of Stage 1. Mass balance for cobalt species is not always achieved in Stage 1 (the sum of  $[\text{Co}^{\text{II}}]$  and  $[\text{Co}^{\text{III}}]$  is not constant between 70-90% depended on scavenger environment of the solution). This mass imbalance is attributed to the production of solid precipitates that could not be sampled for the cobalt speciation using the PAR analysis method.

Stage 1 is followed by a faster decrease in  $[\text{Co}^{\text{II}}]$  and increase in  $[\text{Co}^{\text{III}}]$  in the first 50 min (Stage 2). This is followed by a slower linear decrease in  $[\text{Co}^{\text{II}}]$  and a linear increase in  $[\text{Co}^{\text{III}}]$  (Stage 3) until total conversion is achieved. The rate of increase in  $[\text{Co}^{\text{III}}]$  depends on the solution type in Stage 2, but it is independent of the solution type in Stage 3. In Stage 3 the rate of increase in  $[\text{Co}^{\text{III}}]$  is linear and equal to the rate of decrease in  $[\text{Co}^{\text{II}}]$ ; the slopes of  $[\text{Co}^{\text{II}}]$  and  $[\text{Co}^{\text{III}}]$  versus time are same in magnitude but with opposite signs. These rates are about  $4.5 \times 10^{-9} \text{ M}\cdot\text{s}^{-1}$  and are nearly independent of the type of scavenger that is present.

Comparison of Figure 5.1 and Figure 5.3 shows that the more  $\text{Co}^{\text{II}}$  that has been converted to  $\text{Co}^{\text{III}}$  before Stage 3 begins, the smaller the final  $\text{Co}_3\text{O}_4$  particles are. This suggests that the rate of oxidation of  $\text{Co}^{\text{II}}$  to  $\text{Co}^{\text{III}}$  in Stage 3 is controlled by the rate of

growth of the  $\text{Co}_3\text{O}_4$  particles, and that the rate of the  $\text{Co}_3\text{O}_4$  particle growth is not limited by the rate of oxidation of  $\text{Co}^{\text{II}}$  either in solution or on a particle surface. If cobalt oxidation was the rate limiting, we should see an effect of the scavenger type on the rate of particle growth. However, we do see the effect the scavenger type on the rate of  $\text{Co}^{\text{II}}$  oxidation in Stages 1 and 2.

The effect of individual scavengers on the oxidation kinetics of  $\text{Co}^{\text{II}}$  to  $\text{Co}^{\text{III}}$  can be better appreciated from the delay in the production of  $\text{Co}^{\text{III}}$ , Figure 5.4. In a deaerated solution without any scavengers (solution 1),  $\text{Co}^{\text{III}}$  was detected at very small concentrations only after 200 min. No  $\text{Co}^{\text{III}}$  was observed after 5-h irradiation in the presence of the  $\bullet\text{OH}$  scavenger, *t*-butanol, whereas  $\text{Co}^{\text{III}}$  is observed almost immediately in the presence of an  $\bullet\text{e}_{\text{aq}}^-$  scavenger,  $\text{N}_2\text{O}$  or  $\text{O}_2$ .



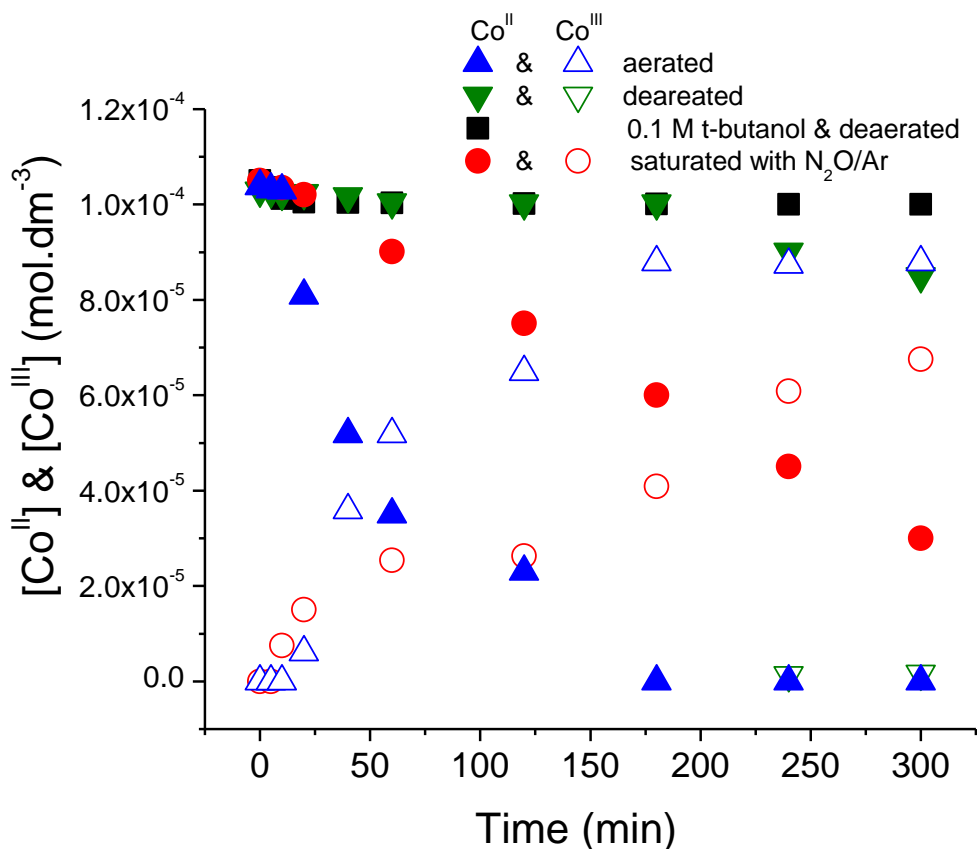


**Figure 5.4:** Concentrations of  $\text{Co}^{\text{II}}$  (solid symbols) and  $\text{Co}^{\text{III}}$  (open symbols) as a function of irradiation time observed for 0.1 mM  $\text{CoSO}_4$  solutions at pH 10.6 in different scavenging environments: aerated only ( $\blacktriangle$  &  $\triangle$ ), deaerated only ( $\blacktriangledown$  &  $\triangledown$ ), deaerated and 0.1 M *t*-butanol ( $\blacksquare$ ), and purged with  $\text{N}_2\text{O}/\text{Ar}$  ( $\bullet$  &  $\circ$ ).

Cobalt oxide nanoparticle formation in aerated solutions containing a higher initial concentration of  $\text{CoSO}_4$  (0.3 mM) previously reported [20]. The TEM images and the oxide compositions of the particles formed in those tests as a function of irradiation time are reproduced in Figure 5.5. The figure shows that particle formation progresses from initially mostly  $\text{Co}(\text{OH})_2$ , to  $\text{CoOOH}$ , and then to  $\text{Co}_3\text{O}_4$ , with the conversion of  $\text{CoOOH}$  to  $\text{Co}_3\text{O}_4$  occurring at times longer than 1 h. In the current study we could not collect enough particles at short times to observe such a progression due to the lower initial  $\text{CoSO}_4$  concentration.

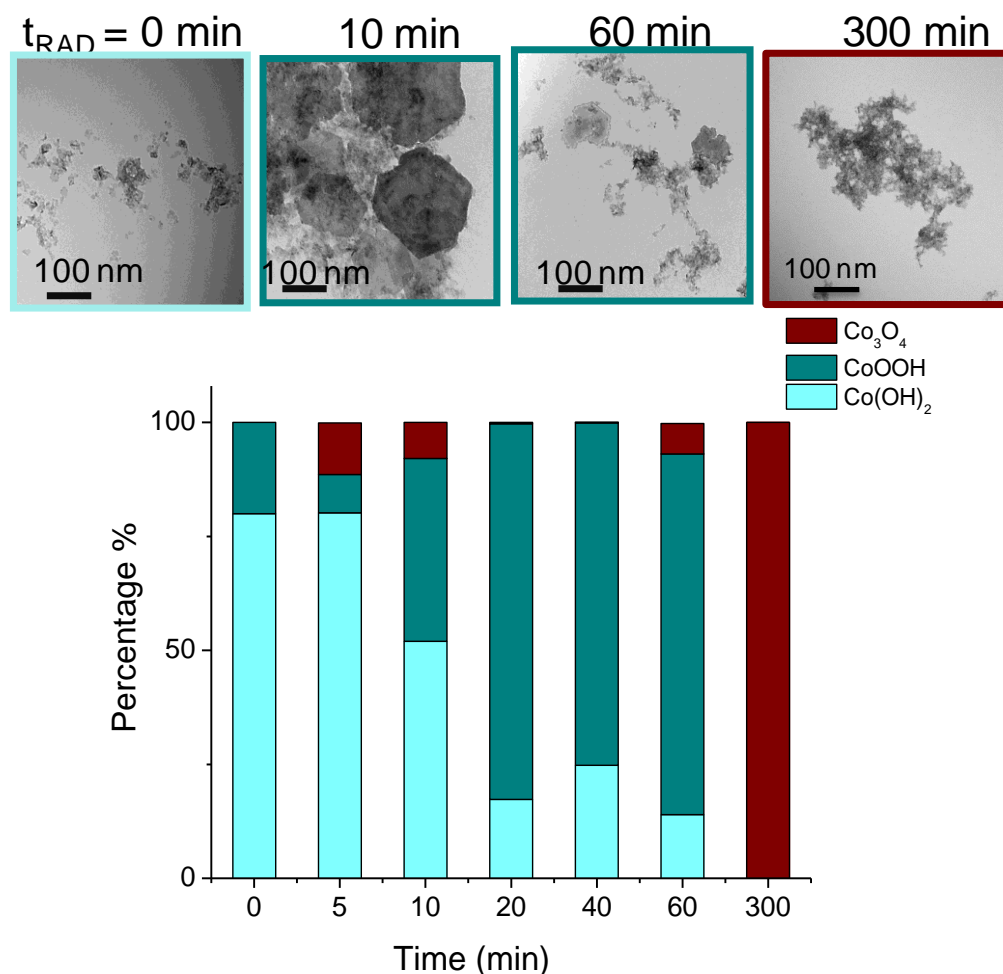


**Figure 5.5:** Composition determined by XPS of particles collected as a function of irradiation time from aerated solutions initially containing 0.3 mM Co<sup>II</sup> at pH 10.6. The corresponding TEM images of the particles formed at different times are shown on top. These figures are adopted from Alrehaily et al. [20].

The cobalt oxidation kinetics observed in a 0.3 mM CoSO<sub>4</sub> solution are compared with those observed in a 0.1 mM CoSO<sub>4</sub> solution in Figure 5.6. In a 0.3 mM CoSO<sub>4</sub> solution the [Co<sup>II</sup>] decreases to ~ 0.1 mM CoSO<sub>4</sub> within ~10 min (Stage 1) during which Co<sup>III</sup> production appears to be negligible as the concentration of dissolved Co<sup>III</sup> is very low. After this initial drop in [Co<sup>II</sup>] the rates of decrease in [Co<sup>II</sup>] in both solutions are nearly the same but [Co<sup>III</sup>] increases faster in the 0.3 mM CoSO<sub>4</sub> solution than in the 0.1 mM CoSO<sub>4</sub> solution

in Stage 2. In Stage 3 the rate of increase in  $[\text{Co}^{\text{III}}]$  is the same as the rate of decrease in  $[\text{Co}^{\text{II}}]$  independent of the initial concentration of  $\text{CoSO}_4$ . All the experiment data performed more than 3 times and it showed the results are reproducible.

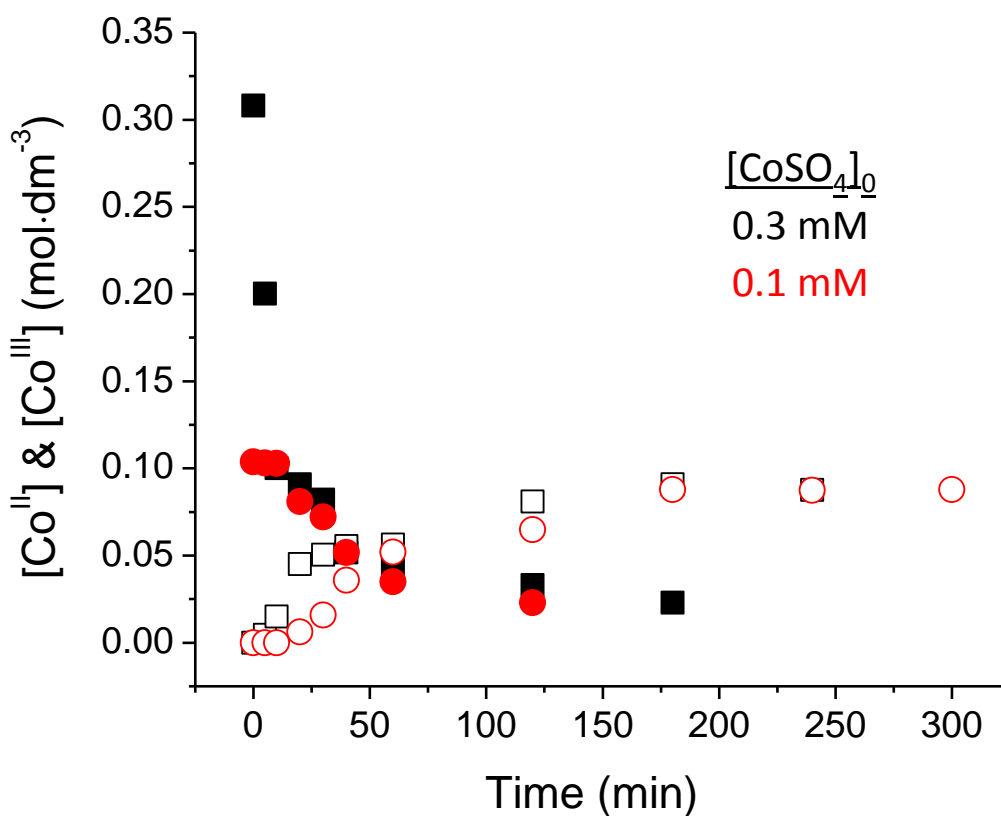


**Figure 5.6:** Concentrations of  $\text{Co}^{\text{II}}$  (solid symbols) and  $\text{Co}^{\text{III}}$  (open symbols) as a function of irradiation time in aerated solutions containing 0.1 mM (red) and 0.3 mM (black)  $\text{CoSO}_4$  at pH 10.6.

The combined results presented in Figures 5.5 and 5.6 indicate that Stage 1 ( $< 10$  min) corresponds to the formation of hexagonal particles (possibly a mixed  $\text{Co}^{\text{II}}/\text{Co}^{\text{III}}$  hydroxide, see discussion in Section 4.3), whereas Stage 2 (10 min to 60 min) corresponds to

the formation of the small CoOOH particles, and Stage 3 corresponds to the formation of slightly larger Co<sub>3</sub>O<sub>4</sub> particles.

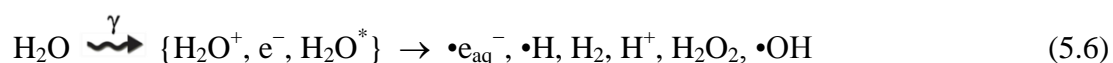
The combined results from the previous and current studies show that the rate of oxidation of Co<sup>II</sup> to Co<sup>III</sup> in Stage 3 is independent of the initial concentration of CoSO<sub>4</sub> and also independent of the type of radical scavenger that is present. The rate of radiolytic conversion of Co<sup>II</sup> to Co<sub>3</sub>O<sub>4</sub> nanoparticles in Stage 3 is not limited by the rate of oxidation of Co<sup>II</sup> to Co<sup>III</sup> (either in solution or on a particle surface), but by the rate of Co<sub>3</sub>O<sub>4</sub> particle growth.

## 5.4 DISCUSSION

The effects of different scavengers on the behaviour of irradiated cobalt solutions suggest that different redox species may control the behaviour seen at different times. To explore this, first consider the radiolytic production of oxidants and reductants, and the hydrolysis and phase equilibria of cobalt species that can occur. A mechanism of radiation-induced particle formation that is consistent with the observations is then proposed.

### 5.4.1 Radiolytic production of oxidants and reductants

Gamma radiolysis of water produces a number of redox active species [25]:



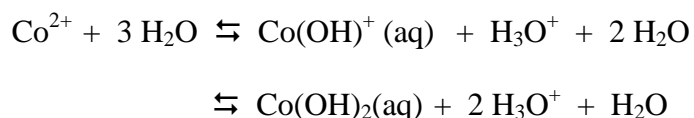
Under continuous irradiation these primary radiolysis products are continuously produced and they then undergo aqueous phase chemical reactions with each other and the water solvent species (H<sub>2</sub>O, H<sup>+</sup>, OH) to form secondary products such as O<sub>2</sub> and •O<sub>2</sub><sup>-</sup>. The

concentrations of radiolysis products typically reach steady state within minutes of initiation of a continuous  $\gamma$ -radiation flux [14, 25].

The radiolysis products can also react with redox active solutes that are present. (The probability of a solute species at a relatively low concentration ( $< 0.01$  M) directly interacting with the gamma radiation is very small and can be neglected.) These aqueous phase chemical reactions are typically much slower than the reactions leading to formation of the primary radiolysis products. (The half-life of an aqueous reaction is typically  $> 1$  ms whereas a homogeneous distribution of primary radiolysis products is achieved in  $< 1$   $\mu$ s) [13, 25]. However, solute reactions can have an impact on the longer term, steady-state concentrations of the radiolysis products. Hence, the relative concentrations of the radiolysis products and their effectiveness in driving a chemical reaction may change with time over an irradiation period lasting longer than milliseconds. Studies on steady-state radiolysis kinetics can be found in references [14, 30-32].

#### 5.4.2 Thermal conversion and equilibrium of cobalt species

Before considering the impact of radiation on a cobalt solution, it is necessary to consider the solution chemistry of cobalt. For a given oxidation state, Co will exist in a number of different chemical forms in solution. The  $\text{Co}^{2+}$  ions that enter solution following dissolution and dissociation of the  $\text{CoSO}_4$  salt are very rapidly hydrolyzed to form both neutral and ionic species, and the hydrolyzed species quickly reach equilibrium with each other [24]:





Dissolved  $\text{Co}^{\text{II}}$  species (referred to collectively as  $\text{Co}^{2+}(\text{aq})$  below) thus include  $\text{Co}^{2+}$ ,  $\text{Co(OH)}^+$ ,  $\text{Co(OH)}_2(\text{aq})$  and  $\text{Co(OH)}_3^-$ .

While the aqueous cobalt species are in hydrolysis equilibria, the neutral  $\text{Co(OH)}_2$  can condense as solid  $\text{Co}^{\text{II}}$  hydroxide ( $\text{Co(OH)}_2(\text{s})$ ) and establish a phase equilibrium:



The distribution of the  $\text{Co}^{\text{II}}$  between solution and solid states is sensitive to the pH of the solution due to the hydrolysis equilibria (reaction 5.7). The presence of a large surface area or large numbers of small particulates (nucleates) will also shift the phase equilibrium of reaction 5.8 to the right.

Similarly,  $\text{Co}^{\text{III}}$  can exist as a number of dissolved species ( $\text{Co}^{3+}(\text{aq})$ ) ( $\text{Co}^{3+}$ ,  $\text{Co(OH)}^{2+}$ ,  $\text{Co(OH)}_2^+$ ,  $\text{Co(OH)}_3(\text{aq})$  and  $\text{Co(OH)}_4^-$ ) and these aqueous species are in phase equilibrium with solid  $\text{Co(OH)}_3(\text{s})$ :



Again the distribution of the  $\text{Co}^{\text{III}}$  depends on pH. This dependence is weaker than that of  $\text{Co}^{\text{II}}$  because the solubility of  $\text{Co}^{3+}(\text{aq})$  is several orders of magnitude lower than that of  $\text{Co}^{2+}(\text{aq})$ ; in pure water free of  $\text{SO}_4^{2-}$  the solubilities of  $\text{Co}^{\text{III}}$  and  $\text{Co}^{\text{II}}$  species at pH 10.6 are  $\sim 10^{-13}$  M and  $\sim 10^{-6}$  M, respectively [24]. Hence,  $\text{Co}^{\text{III}}$  much prefers to exist in the solid state.

### 5.4.3 Radiation-induced cobalt oxide nanoparticle formation

The radiolytic production of  $\text{Co}_3\text{O}_4$  particles involves many competing oxidation and reduction reactions. The observed effects of different scavengers on the kinetics of this process and the final sizes of  $\text{Co}_3\text{O}_4$  nanoparticles that are formed can provide information on the reaction pathways and the key reactions involved.

A reaction mechanism that is consistent with the observations is proposed and schematically presented in Figure 5.7. This mechanism is similar to a mechanism proposed previously to explain the behaviour of irradiated  $\text{Co}^{\text{II}}$  in aerated solutions [20]. The mechanism is further refined here based on the evidence of the changes in reaction kinetics caused by the presence of selective radical scavengers. The mechanism consists of three stages with the following key reactions/processes:

Stage 1: Radiolytic oxidation of  $\text{Co}^{\text{II}}(\text{aq})$  to  $\text{Co}^{\text{III}}(\text{aq})$  species occur in the solution phase, followed by spontaneous co-precipitation of mixed  $\text{Co}^{\text{II}}/\text{Co}^{\text{III}}$  oxide/hydroxide nucleation particles.

Stage 2: Adsorption of  $\text{Co}^{\text{II}}$  on the particle surfaces continues while heterogeneous redox reactions of  $\text{Co}^{\text{II}}$  and  $\text{Co}^{\text{III}}$  occur at the aqueous-solid particle interface. The particles grow into a  $\text{CoOOH}$  phase.

Stage 3: Solid-state conversion from  $\text{CoOOH}(\text{s})/\text{Co}^{\text{II}}(\text{ad})$  to  $\text{Co}_3\text{O}_4(\text{s})$  becomes rate determining.

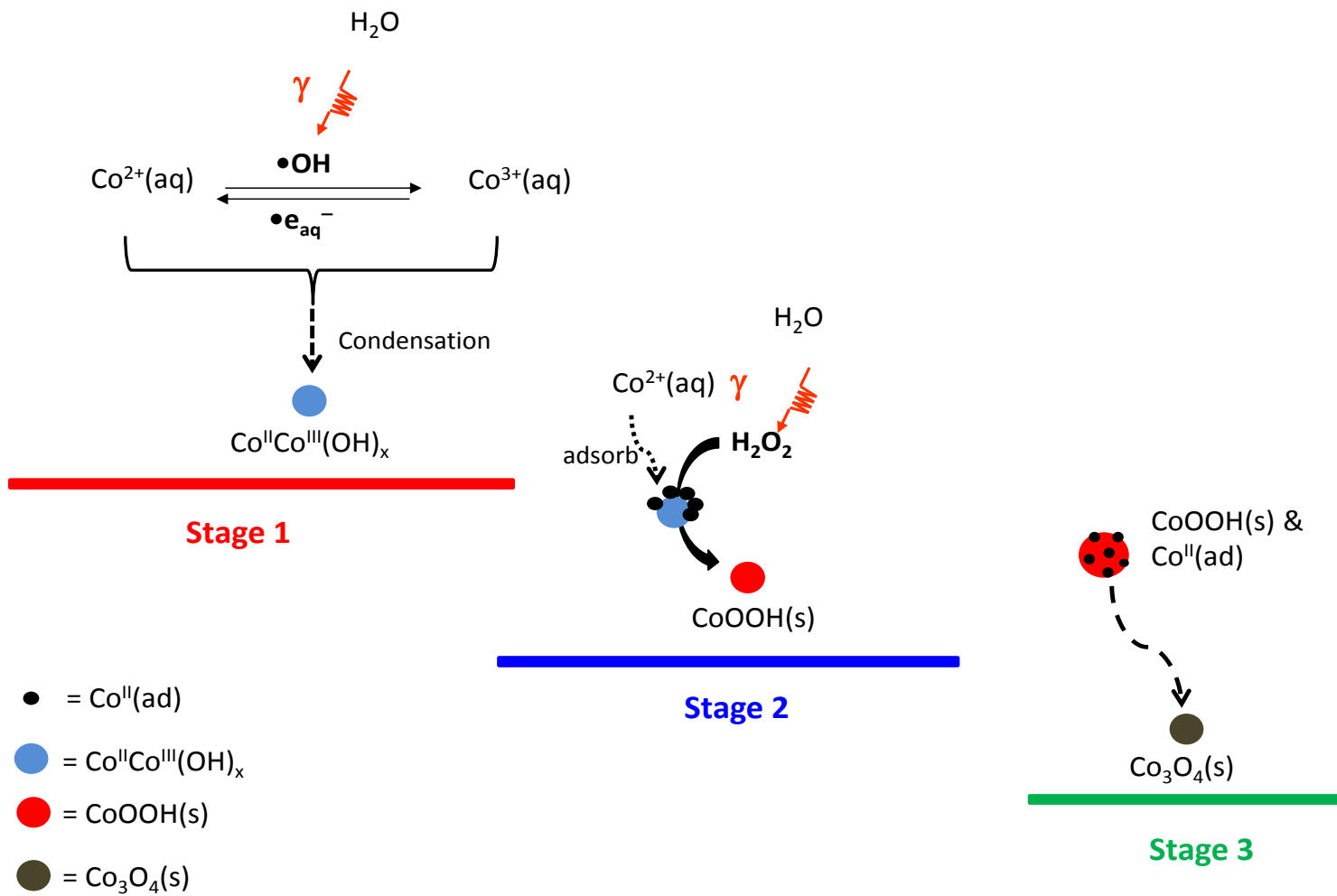


**Figure 5.7:** Schematic of a mechanism for radiation-induced cobalt oxide colloid formation.



The standard potential for the oxidation of  $\text{Co}^{2+}(\text{aq})$  to  $\text{Co}^{3+}(\text{aq})$  ( $E^{\circ}(\text{Co}^{2+}/\text{Co}^{3+})$ ) is 1.81  $V_{\text{SHE}}$ . This oxidation does not occur easily without the presence of a very strong oxidant, such as  $\bullet\text{OH}$ . Dissolved oxygen ( $\text{O}_2$ ), and even  $\text{H}_2\text{O}_2$ , are not sufficiently strong oxidants to oxidize  $\text{Co}^{2+}(\text{aq})$ . Water radiolysis produces  $\bullet\text{OH}$ , and reaction with this radical rapidly leads to oxidation (rate constant from reference [34]):



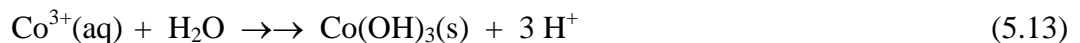
However, water radiolysis also produces strong reductants that can quickly reverse this process (rate constant from reference [34]):



Since these radical/ion reactions are very fast, the concentrations of  $\text{Co}^{2+}(\text{aq})$  and  $\text{Co}^{3+}(\text{aq})$  quickly reach pseudo equilibrium or steady state, and the ratio of their concentrations can be approximated to:

$$\frac{[\text{Co}^{3+}(\text{aq})]}{[\text{Co}^{2+}(\text{aq})]} \approx \frac{k_{5.10}[\bullet\text{OH}]}{k_{5.11}[\bullet e_{\text{aq}}^-]} \quad (5.12)$$

Since the solubility of  $\text{Co}^{3+}(\text{aq})$  is several orders of magnitude lower than that of  $\text{Co}^{2+}(\text{aq})$ , the  $\text{Co}^{3+}(\text{aq})$  that is formed will tend to condense as  $\text{Co}(\text{OH})_3(\text{s})$  (reaction 5.9). Once the concentration of  $\text{Co}^{3+}(\text{aq})$  reaches a critical mass spontaneous condensation of  $\text{Co}^{3+}(\text{aq})$  to  $\text{Co}(\text{OH})_3(\text{s})$  occurs:



This promotes adsorption or co-precipitation of  $\text{Co}^{2+}(\text{aq})$  and forms mixed hydroxide ( $\text{Co}^{\text{II}}\text{Co}^{\text{III}}(\text{OH})_x$ ) particle nucleates. The reduction of  $\text{Co}^{2+}(\text{aq})$  to  $\text{Co}^0$  by  $\bullet e_{\text{aq}}^-$  and the precipitation of  $\text{Co}^0$  may also trigger the spontaneous condensation of  $\text{Co}^{\text{II}}$  and  $\text{Co}^{\text{III}}$  species.

The condensed  $\text{Co}^{\text{II}}\text{Co}^{\text{III}}(\text{OH})_x(\text{s})$  particles become the nucleation sites for  $\text{Co}^{2+}(\text{aq})$  species to continue to adsorb and oxidize to grow, first as  $\text{CoOOH}$  and then converted to  $\text{Co}_3\text{O}_4$  particles. As discussed below, the oxidation of a solid or adsorbed  $\text{Co}^{\text{II}}$  species is kinetically easier due to a lower activation energy than the homogeneous oxidation of  $\text{Co}^{2+}(\text{aq})$  in solution. Thus, the less oxidizing species such as  $\text{H}_2\text{O}_2$  (to  $\text{OH}^-$ ) can contribute to the cobalt oxidation. The reverse redox reaction of  $\text{Co}^{\text{III}}$  to  $\text{Co}^{\text{II}}$  on surface also becomes easier, and less reducing species such as  $\text{H}_2$  (if it can accumulate in solution) can contribute to the cobalt reduction. The net conversion from  $\text{Co}^{\text{II}}$  to  $\text{Co}^{\text{III}}$  particles at this stage is thus controlled by the less redox active species that have been accumulated to sufficiently high concentrations in solution at longer times. Thus, the overall rate for the oxidative conversion of  $\text{Co}^{2+}(\text{aq})$  to  $\text{CoOOH}(\text{s})$  and  $\text{Co}_3\text{O}_4(\text{s})$  accelerates once a sufficient number of the  $\text{Co}^{\text{II}}\text{Co}^{\text{III}}(\text{OH})_x(\text{s})$  nucleation particles with sufficient total surface area are formed.

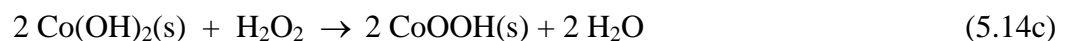
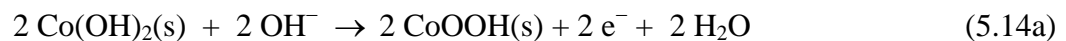
Stage 1 attribute to the time required for the spontaneous condensation of the  $\text{Co}^{\text{II}}\text{Co}^{\text{III}}(\text{OH})_x(\text{s})$  nucleation particles to occur. The delay observed in the conversion of  $\text{Co}^{\text{II}}$  to  $\text{Co}^{\text{III}}$  species can then be attributed to the time required to form a sufficient number of the  $\text{Co}^{\text{II}}\text{Co}^{\text{III}}(\text{OH})_x(\text{s})$  nucleation particles onto which  $\text{Co}^{2+}(\text{aq})$  can continually adsorb as  $\text{Co}(\text{OH})_2$ . The speed at which these nucleates with sufficient total surface area are formed will depend on  $[\text{Co}^{3+}(\text{aq})]$ . Under  $\gamma$ -irradiation the  $[\text{Co}^{3+}(\text{aq})]$  and  $[\text{Co}^{2+}(\text{aq})]$  in solution reach pseudo steady state very quickly and their concentrations depend on the rates of these species interconversion reactions, primarily by reactions (5.10) and (5.11).

The different delay in the production of a detectable amount of  $\text{Co}^{\text{III}}$  in different solutions can then be explained by a scavenger's impact on the concentrations of  $\bullet\text{OH}$

and  $\bullet e_{aq}^-$ . The presence of *t*-butanol, a well-known scavenger for the oxidizing radical  $\bullet OH$  (reaction 5.2), will reduce  $[\bullet OH]$  and decrease the ratio of  $[Co^{3+}(aq)]$  to  $[Co^{2+}(aq)]$  in equation (5.12). On the other hand, the presence of an  $\bullet e_{aq}^-$  scavenger,  $N_2O$  and/or  $O_2$  (reactions 5.3 and 5.4), will increase the ratio of  $[Co^{3+}(aq)]$  to  $[Co^{2+}(aq)]$ . Accordingly, no  $Co^{III}$  particles were formed in solutions containing only *t*-butanol, while no significant delay in the production of a detectable amount of  $Co^{III}$  was observed in these solutions (Figure 5.4).

Once a sufficient number of the  $Co^{II}Co^{III}(OH)_x(s)$  nucleates is formed, the  $Co^{2+}(aq)$  easily adsorb on the solid particles and the phase equilibrium (5.8) shifts towards the formation of solid  $Co^{II}$  or mixed  $Co^{II}/Co^{III}$  hydroxides on the surfaces of the nucleation particles. Most transition metal oxides/hydroxides, including cobalt oxides/hydroxides, are semiconductors that can continually support electrochemical oxidation of  $Co^{II}$ . Electrochemical oxidation occurs more readily than the corresponding homogeneous phase oxidation, because electron migration can occur through the semiconductor substrate to other sites on the particle where corresponding reduction of an aqueous species can occur. The standard potential for  $(Co(OH)_2(s) \rightleftharpoons CoOOH(s))$  is  $-0.695 V_{SHE}$  [33], lower than  $E^0(Co^{2+}(aq)/Co^{3+}(aq))$ . This allows weaker oxidizing species than  $\bullet OH$  such as  $H_2O_2$  to now participate in the oxidation of  $Co^{II}$  to  $Co^{III}$ .

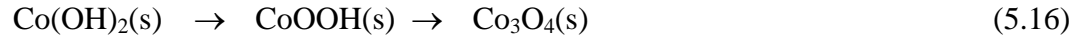
Once a sufficient number of nuclei are formed and  $Co^{II}$  begins to condense, solid state oxidation by  $H_2O_2$  will become the dominant oxidation pathway:



This is followed by solid-state conversion:



The overall particle growth following nucleation is then:



This particle growth mechanism is consistent with the observed two longer oxidation stages (Stages 2 and 3). The rate of oxidation reaction (5.12) will depend on  $[\text{H}_2\text{O}_2]$  and the surface area of  $\text{Co(OH)}_2(\text{s})$  on particles, while the rate of the solid-state conversion reaction (5.15) is limited by slow oxide lattice rearrangement rather than cobalt redox reaction. Due to its dependence on the  $[\text{H}_2\text{O}_2]$  the net rate of oxidation of  $\text{Co}^{\text{II}}$  to  $\text{Co}^{\text{III}}$  in Stage 2 ( $< 1$  h in Figure 5.3) will depend on the scavenging environment that influences  $[\text{H}_2\text{O}_2]$ . In Stage 3 after enough  $\text{CoOOH}(\text{s})$  has formed, the net oxidation of  $\text{Co}^{\text{II}}$  to  $\text{Co}^{\text{III}}$  will be determined by the rate of reaction (5.15) (the slowest step in a series of reactions) and the rate will be nearly independent of the scavenging environment but mostly on temperature. These kinetic considerations explain why Stage 3 starts at nearly the same time ( $\sim 1$  h) and the rate of conversion of  $\text{Co}^{\text{II}}$  to  $\text{Co}^{\text{III}}$  in Stage 3 is the same with different scavengers present (Figure 5.3).

The rate of oxidation of  $\text{Co}^{\text{II}}$  to  $\text{Co}^{\text{III}}$  in Stage 2 is faster in aerated solutions than in deaerated  $\text{N}_2\text{O}$  solutions. This difference can be attributed to the different effects of  $\text{O}_2$  and  $\text{N}_2\text{O}$  on the steady-state concentration of  $\text{H}_2\text{O}_2$ . As noted in Section 4.1, the concentration of  $\text{H}_2\text{O}_2$  in irradiated water depends on a complex, linked set of reactions [25]. Two key reactions are [25]:



Both N<sub>2</sub>O and O<sub>2</sub> are effective in removing •e<sub>aq</sub><sup>-</sup> and any decrease in the [•e<sub>aq</sub><sup>-</sup>] will tend to cause an increase in the [H<sub>2</sub>O<sub>2</sub>]. However, the reaction of •e<sub>aq</sub><sup>-</sup> with N<sub>2</sub>O produces •OH (reaction 5.4) and this will tend to decrease the [H<sub>2</sub>O<sub>2</sub>] via reaction 5.17. Hence, the net effect of N<sub>2</sub>O on the [H<sub>2</sub>O<sub>2</sub>] is moderate, balancing changes in •e<sub>aq</sub><sup>-</sup> and •OH. On the other hand, the reaction •e<sub>aq</sub><sup>-</sup> with O<sub>2</sub> produces •O<sub>2</sub><sup>-</sup> (reaction 5.5) and this species can react with •OH [25]:



Although the steady-state concentration of •O<sub>2</sub><sup>-</sup> is small, this reaction and reaction (5.11) can form a catalytic cycle that can substantially reduce both the [•e<sub>aq</sub><sup>-</sup>] and the [•OH] and tend to increase the [H<sub>2</sub>O<sub>2</sub>]. Thus, [H<sub>2</sub>O<sub>2</sub>] will be higher with O<sub>2</sub> present, compared to the concentration that will be seen with an equivalent amount of N<sub>2</sub>O present. This explains what we see in Figure 5.4.

For a solution with both dissolved O<sub>2</sub> and *t*-butanol present the behaviour is very similar to that seen for a solution with only O<sub>2</sub> present. With both O<sub>2</sub> and *t*-butanol present there is a competition between the reactions of the different scavengers, with the *t*-butanol suppressing oxidation and the O<sub>2</sub> supporting it. Because of the catalytic effect of reactions 5.11 and 5.17, the effect of O<sub>2</sub> on H<sub>2</sub>O<sub>2</sub> is significantly larger than that of *t*-butanol. Hence, the O<sub>2</sub> in an aerated solution is capable of causing sufficient oxidation to drive particle formation even with an oxidation suppressant present. In examining Figure 5.3 we can see that the rate of increase in the [Co<sup>III</sup>] in Stage 2 is greater for the solution that is only aerated compared to a solution with both air and *t*-butanol present. This shows the influence of the *t*-butanol in partially suppressing the oxidation by consuming •OH radicals.

Given the above mechanism for Co oxidation and particle formation we are able to understand the dependence of the particle sizes that are formed on the solution environment. The particle sizes are: 8 – 20 nm in the aerated only solutions, 10 – 30 nm in the aerated/*t*-butanol solutions, and 60 – 80 nm in the N<sub>2</sub>O purged solutions. These sizes are in the inverse order of the [Co<sup>III</sup>] that is reached at the time Stage 3 starts in the different environments (see Figures 5.3, 5.4 and 5.6).

The more oxidizing the solution, the more rapidly Co<sup>3+</sup>(aq) is initially formed and this leads to a larger number of Co<sup>II</sup>Co<sup>III</sup>(OH)<sub>x</sub> condensation nuclei being created in Stage 1. This in turn leads to a larger number of particles that are available to grow in subsequent stages. The surface to volume ratio on the particles is greater for a larger number of smaller particles and this supports faster Co<sup>III</sup> oxidation in Stage 2. It also means that because there are more small CoOOH particles, each particle is able to attract and retain less cobalt for further conversion to Co<sub>3</sub>O<sub>4</sub> in Stage 3, so the final particle sizes are smaller. In the end, the amount of Co that accumulates in particles is about the same for all oxidizing environments, with the aerated solution having many smaller particles, the N<sub>2</sub>O solution having fewer larger particles, and the particles formed in an aerated/*t*-butanol solution lying in between in size and number.

## 5.5 CONCLUSIONS

A mechanism for radiation-induced formation of  $\text{Co}_3\text{O}_4$  nanoparticles is proposed that is consistent with the observed effects of scavengers on the kinetics of oxidation of  $\text{Co}^{\text{II}}$  in solution to solid  $\text{Co}^{\text{III}}$  and the final size of  $\text{Co}_3\text{O}_4$  nanoparticles that are formed. It is proposed that the cobalt oxidation occurs in three steps: (1) the oxidation of  $\text{Co}^{2+}(\text{aq})$  to  $\text{Co}^{3+}(\text{aq})$  in solution followed by condensation of  $\text{CoOOH}$  nucleates on which  $\text{Co}(\text{OH})_2$  can be adsorbed as  $\text{Co}(\text{OH})_2(\text{s})$ , (2) the oxidation of  $\text{Co}(\text{OH})_2(\text{s})$  to  $\text{CoOOH}(\text{s})$ , and (3) the solid-state conversion of  $\text{Co}(\text{OH})_2(\text{s})$  and  $\text{CoOOH}(\text{s})$  to form  $\text{Co}_3\text{O}_4(\text{s})$  particles.

The first step is predominantly oxidation of  $\text{Co}^{2+}$  by  $\bullet\text{OH}$  formed by water radiolysis. This is confirmed by tests with an  $\bullet\text{OH}$  scavenger present (*t*-butanol) where no oxidation is seen. The initial formation of  $\text{Co}^{\text{III}}$  occurs nearly immediately after the start of irradiation with  $\text{N}_2\text{O}$  and  $\text{O}_2$  present. Scavengers also affect the rate of the solid phase oxidation by influencing the concentration of  $\text{H}_2\text{O}_2$  in the system. This species accumulates during steady-state radiolysis and is more effective at the surface oxidation of  $\text{Co}^{\text{II}}$  than  $\bullet\text{OH}$ . Scavengers do not affect the rate of solid-state conversion and hence the growth rate of  $\text{Co}_3\text{O}_4$  is nearly the same in different scavenging environments.

The different particle sizes observed in different scavenging environments are attributed to different rates of oxidation of  $\text{Co}(\text{OH})_2(\text{s})$  to  $\text{CoOOH}(\text{s})$ . The final size of  $\text{Co}_3\text{O}_4$  nanoparticles formed is larger in the  $\text{N}_2\text{O}/\text{Ar}$  purged solutions than in the aerated solutions. The size of the nanoparticles in the aerated with 0.1 M *t*-butanol is in-between.

This study shows how steady-state water radiolysis kinetics, hydrolysis and phase equilibria of cobalt ions and oxide species are linked. It also shows how appropriate

adjustment of solution conditions and radical scavenger concentrations can be used to produce  $\text{Co}_3\text{O}_4$  nanoparticles with tailored sizes.

## 5.6 REFERENCES

- [1] M.M. Rahman, J.Z. Wang, X-L. Deng, Y. Li, H-K. Liu, *Electrochim. Acta.*, 55 (2009) 504.
- [2] Y. Zhang, Y. Chen, T. Wang, J. Zhou, Y. Zhao, *Microporous and Mesoporous Mater.*, 114 (2008) 257.
- [3] K. Shalini, A.U. Mane, S.A. Shivashankar, M. Rajeswari, S. Choopun, *J. Cryst. Growth.*, 231 (2001) 242.
- [4] C.S. Cheng, M. Serizawa, H. Sakata, T. Hirayama, *Mater. Chem. Phys.*, 53 (1998) 225.
- [5] M. Ando, T. Kobayashi, S. Iijima, M. Haruta, *J. Mater. Chem.*, 7 (1997) 1779.
- [6] C. Pirovano, S. Trasatti, *J. Electroanal. Chem.*, 180 (1984) 171.
- [7] S. Sakamoto, M. Yoshinaka, K. Hirota, O. Yamaguchi, *J. Am. Ceram. Soc.*, 80 (1997) 267.
- [8] V.R. Shinde, S.B. Mahadik, T.P. Gujar, C.D. Lokhande, *Appl. Surf. Sci.*, 252 (2006) 7487.
- [9] Z.W. Zhao, K. Konstantinov, L. Yuan, H.K. Liu, S.X. Dou, *J. Nanosci. Nanotechnol.*, 4 (2004) 861.
- [10] A.U. Mane, K. Shalini, A. Wohlfart, A. Devi, S.A. Shivashankar, *J. Cryst. Growth*, 240 (2002) 157.



- [11] S.R. Ahmed, S.B. Ogale, R. Ramesh, G.C. Papaefthymiou, P. Kofinas, *Appl. Phys. Lett.*, 2002 (80)1616.
- [12] F. Švegl, B. Orel, I. Grabec-Švegl, V. Kaučič, *Electrochim. Acta.*, 45 (2000) 4359.
- [13] J.W.T. Spinks, R.J. Woods, *An Introduction to Radiation Chemistry*, Wiley, New York, 1990.
- [14] J.C. Wren, Steady-state radiolysis: effect of dissolved additives in ACS Symposium Series: *Nuclear Energy and the Environment*, 2010.
- [15] M. Treguer, C. De Cointet, H. Remita, J. Khatouri, M. Mostafavi, J. Amblard, J. Belloni, R. De Keyzer, *J. Phys. Chem. B*, 102 (1998) 4310.
- [16] A. Abedini, A. R. Daud, M. A. Abdul Hamid, N. Kamil Othman, E. Saion, *Nanoscale Res. Lett.*, 8 (2013) 474.
- [17] M. Mirdamadi-Esfahani, M. Mostafavi, B. Keita, L. Nadjo, P. Kooyman, H. Remita, *Gold Bull.*, 43 (2010) 49.
- [18] S. Gasaymeh, S. Radiman, *African Physical Review*, 4 (2010) 31.
- [19] K. Torigoe, H. Remita, P. Beaunier, J. Belloni, *Radiat. Phys. Chem.*, 64 (2002) 215.
- [20] L.M. Alrehaily, J.M. Joseph, M.C. Biesinger, D. Guzonas, J.C. Wren, *Phys. Chem. Chem. Phys.*, 15 (2013) 1014.
- [21] P.A. Yakabuskie, J.M. Joseph, P. Keech, G.A. Botton, D. Guzonas, J. C. Wren, *Phys. Chem. Chem. Phys.*, 13 (2011) 7198.
- [22] M. Von Piechowski, M.-A. Thelen, J. Hoigné, R. E. Bühler, *Berichte der Bunsengesellschaft für Phys. Chemie*, 96 (1992) 1448.
- [23] M. Schuchmann, C. Von Sonntag, *J. Phys. Chem.*, 83 (1979) 780.

- [24] C.F. Baes, R.E. Mesmer (2<sup>nd</sup> ED). *Hydrolysis of Cations*, Krieger Pub. Co. Malabar, Florida, 1986.
- [25] J.M. Joseph, B.-S. Choi, P.A. Yakabusie, J.C. Wren, *Radiat. Phys. Chem.*, 77(2008) 1009.
- [26] T. Yotsuyanagi, R. Yamashita, K. Aomura, *Anal. Chem.*, 44 (1972) 1091.
- [27] C.J. Hochanadel, *J. Phys. Chem.*, 56 (1952) 587.
- [28] I. Stefanic, J.A. LaVerne, *J. Phys. Chem. A.*, 106 (2002) 447.
- [29] W. Kunerth, *Phys. Rev.*, 19 (1922) 512.
- [30] J.C. Wren, J.M. Ball, *Rad. Phys. Chem.*, 60 (2001) 577.
- [31] P. Driver, G. Glowa, J.C. Wren, *Rad. Phys. Chem.*, 57 (2000) 37.
- [32] J.C. Wren, G.A. Glowa, *Rad. Phys. Chem.*, 58 (2000) 341.
- [33] P. Atkins, J. de Paula, (7<sup>th</sup> ED). *Atkins' Physical Chemistry*, Oxford University Press Inc., New York, 2002.
- [34] G.V. Buxton, R.M. Sellers, D.R. McCracken, *J. Chem. Soc. Faraday Trans. 1*, 72 (1975) 1464.

## Chapter 6

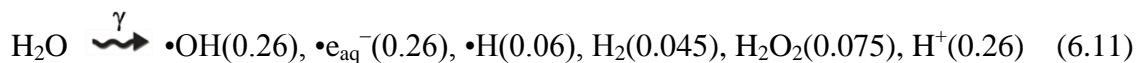
### Radiation-Induced Formation of Chromium-Oxide Nanoparticles: Role of Radical Scavengers on the Redox Kinetics and Particle Size

#### 6.1 INTRODUCTION

Chromium oxide nanoparticles have many applications. They are used in making high-temperature resistant and corrosion resistant materials, and as green pigments [1], heterogeneous catalysts [2], coating materials for thermal protection [3], coatings for wear resistance [4], and electrochromic materials [5]. Different applications require different crystalline particle size and morphology. Chromium oxide nanoparticles have been synthesized by a large number of physical and chemical techniques that include hydrothermal reduction [6], solution combustion synthesis [7], sonochemical reaction [8], laser-induced pyrolysis [9], hydrazine reduction and thermal treatments [10], supercritical alcohol synthesis [11], condensation-polymerization [12], precipitation-gelation [13], gas condensation [14], microwave plasma chemistry [15], and sol-gel methods [16]. The major drawbacks of most of these fabrication methods are a large particle-size distribution, a low yield, and agglomeration of the particles. The fabrication methods also tend to be complex and require chemically harsh conditions and/or high processing temperatures. Radiation-induced nanoparticle formation is a promising new technique that can address some of these drawbacks.

When exposed to ionizing radiation, water decomposes to yield a range of chemically reactive species. For  $\gamma$ -radiolysis at room temperature, the primary radiolysis

products (formed within ~ 100 ns following the absorption of radiation energy) and their yields per absorbed radiation energy (in brackets in units of  $\mu\text{mol}\cdot\text{J}^{-1}$ ) are [17,18]:



These chemical yields per unit energy input are very high. Such high yields, particularly for the radicals, cannot be obtained by thermal processes and gamma-radiolysis is the most effective way of producing these reactive species. Due to the long penetration depth of a typical  $\gamma$ -ray in water (~20 cm for a half reduction in intensity), these species can be produced nearly uniformly within a reasonably large volume of water. The combination of high densities of redox reactive species and their uniform production and distribution in solution can provide ideal conditions for promoting homogeneous redox reactions.

If the product of a reaction of a dissolved species with a radiolysis-generated species has a significantly different solubility from that of the reactant, then a solid product can be formed. Rapid condensation can create homogeneously distributed nucleation sites onto which the radiolysis-induced oxidation or reduction product can continue to deposit and grow the particle size. Because a very large number of nucleation sites are generated simultaneously and homogeneously, this process leads to the formation of nanoparticles with a narrow, uniform size distribution. This principle has been applied in making noble metal nanoparticles (of silver and gold) from dissolved metal ions, taking advantage of the strong reducing power of  $\bullet\text{e}_{\text{aq}}^-$  produced by radiolysis [19-28].

More recently this process have applied to making transition metal oxide nanoparticles from dissolved metal ions, taking advantage of either the strong reducing

power of  $\bullet e_{aq}^-$  or the strong oxidizing power of  $\bullet OH$ , depending on the redox potential of the initially dissolved metal species.  $\gamma$ -FeOOH have fabricated from  $Fe^{2+}$  [29],  $Co_3O_4$  from  $Co^{2+}$  [30], and  $Cr_2O_3$  from  $Cr_2O_7^{2-}$  [31]. This work has shown that water radiolysis products are very effective in inducing redox reactions that convert dissolved transition metal ions into less soluble species which then form metal oxide nanoparticles.

In the case of chromium,  $\gamma$ -radiolysis converts soluble  $Cr^{VI}$  (from dissolved dichromate  $Cr_2O_7^{2-}$ ) to less soluble  $Cr^{III}$  oxide and hydroxide [31]:

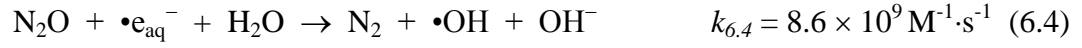


In the previous work the chromium oxide nanoparticle formation was investigated as a function of pH in deaerated or aerated solutions. That study found that no  $Cr^{III}$  particles are formed in aerated solutions this was due to the scavenging of  $\bullet e_{aq}^-$  by dissolved  $O_2$ . This would be the case if the rate controlling process in the nanoparticle formation was reduction of the  $Cr^{VI}$  ions by  $\bullet e_{aq}^-$ . In deaerated solutions, the conversion of  $Cr^{VI}(aq)$  to  $Cr^{III}$  particles is not affected by the solution pH but the average particle size that is formed increases with increase in  $[Cr^{VI}(aq)]_0$ .

In this study the effects of three different radical scavengers, *t*-butanol, dissolved  $O_2$ , and  $N_2O$ , on  $\gamma$ -radiation induced chromium oxide nanoparticle formation were investigated. The intent was to confirm the role of  $\bullet e_{aq}^-$  in the reaction kinetics. Tertiary-butanol is a well-known scavenger for the oxidizing radical  $\bullet OH$  (rate constant from ref. [32]).



On the other hand, both N<sub>2</sub>O and O<sub>2</sub> are efficient scavengers for the reducing radical, •e<sub>aq</sub><sup>-</sup> (rate constants from ref. [33]):



The products of the reactions of N<sub>2</sub>O and O<sub>2</sub> with •e<sub>aq</sub><sup>-</sup> are, however, different. The N<sub>2</sub>O reaction with •e<sub>aq</sub><sup>-</sup> produces an oxidizing radical while the reaction with O<sub>2</sub> produces superoxide (O<sub>2</sub><sup>-</sup>), a weaker reductant than •e<sub>aq</sub><sup>-</sup> but still a reductant. This work aimed at understanding why creation of this weaker reductant prevented nanoparticle formation.

## 6.2 EXPERIMENTAL

Chromium solutions were prepared by dissolving high-purity potassium dichromate, obtained from Sigma-Aldrich (purity ≥ 99%), in water purified using a NANOpure Diamond UV ultrapure water system (resistivity of 18.2 MΩ·cm). The *t*-butanol used in this work was obtained from Sigma-Aldrich (purity ≥ 99%). A 50% N<sub>2</sub>O/50% Ar gas mixture purchased from Praxair (impurities 0.001%) was used to supply N<sub>2</sub>O to the test solutions. The pH of the test solutions was adjusted to 6.0 using a NaOH solution. The solutions containing N<sub>2</sub>O or O<sub>2</sub> were prepared by purging with high purity air (Praxair) or the N<sub>2</sub>O/Ar gas mixture for 1 h prior to testing. De-aerated test solutions were prepared by purging with high purity Ar for 1 h. Using a syringe, 10 ml of the test solution was transferred to a pre-sealed 20-ml vial. Before sealing the vial was purged for 15 min with an appropriate gas (air, Ar or N<sub>2</sub>O/Ar). The test vials were irradiated in a <sup>60</sup>Co gamma cell (MDS Nordion) as described in a previous paper [34]. The gamma

radiation source provided a uniform absorption dose rate of  $4 \text{ kGy}\cdot\text{h}^{-1}$  in the water samples at the time of this study.

Following irradiation for the desired period of time, samples of the test solutions were extracted with a syringe and a series of chemical analyses was performed. The solutions were first analyzed for dissolved  $\text{Cr}^{\text{VI}}$  content using a UV-VIS spectrometer (BioLogic Science Instruments). The concentration of  $\text{Cr}^{\text{VI}}(\text{aq})$  was determined by colorimetric analysis. Diphenylcarbazide (DPC) was added to a solution sample and this reacted with  $\text{Cr}^{\text{VI}}(\text{aq})$  to form a coloured complex that absorbs light at 540 nm [35]. A calibration curve for  $\text{Cr}^{\text{VI}}(\text{aq})$  over the concentration range of 0.01 to 1 mM was generated. The molar extinction coefficient of  $39032 \text{ M}^{-1}\cdot\text{cm}^{-1}$  obtained from our calibration curve is comparable to the reported value for this complex of  $34400 \text{ M}^{-1}\cdot\text{cm}^{-1}$ [35]. This colorimetric method is referred to as the DPC method hereafter. The concentration of  $\text{Cr}^{\text{III}}$  dispersed in the solution samples was determined by first adding sufficient potassium permanganate to the sample to fully oxidize all of the  $\text{Cr}^{\text{III}}$  present to  $\text{Cr}^{\text{VI}}(\text{aq})$ . Note that we use the term  $\text{Cr}^{\text{III}}$  to refer to the combination of the  $\text{Cr}^{\text{III}}$  species that is incorporated in solid particles and any  $\text{Cr}^{\text{III}}$  species that are in solution (as hydroxides in equilibrium with condensed hydroxides on particle surfaces). The  $\text{Cr}^{\text{VI}}(\text{aq})$  concentration in the sample after this oxidation was then determined again using the DPC method. The  $\text{Cr}^{\text{III}}$  concentration in the test solution sample (combined particles and dissolved species) was the difference between the  $\text{Cr}^{\text{VI}}(\text{aq})$  concentrations determined before and after the  $\text{Cr}^{\text{III}}$  oxidation step.

The particles that were formed were analyzed by transmission electron microscopy (TEM), X-ray photoelectron spectroscopy (XPS) and Fourier transform

infrared spectroscopy (FTIR). For the XPS and FTIR analyses the particles were collected by centrifuging the solution and then washed with distilled water to remove any  $\text{Cr}^{\text{VI}}$  absorbed on the surface of the particles. A sample of the precipitate particles was then placed on a glass plate and dried in air. Samples for TEM analysis were collected by dipping a carbon-coated copper grid into the test solution and then drying the sample grid in air. The FTIR spectroscopy was performed with a Bruker, Vertex 70v instrument scanning the 400 to 4000  $\text{cm}^{-1}$  range. The TEM images were obtained with a Philips Electronics instrument with the electron microscope operated at 80 keV. The XPS spectra were acquired on a KRATOS Axis Nova spectrometer using monochromatic Al  $\text{K}\alpha$  radiation and operating at 210 W with a base pressure of  $10^{-8}$  Pa. The analysis depth of the XPS instrument for the chromium oxide is estimated to be 6-7 nm.

## 6.3 RESULTS

### 6.3.1 Effect of Scavengers on the Type, Shape and Size of Nanoparticles

The effect of the radical scavengers, *t*-butanol,  $\text{N}_2\text{O}$  and dissolved  $\text{O}_2$ , on radiation-induced chromium oxide nanoparticle formation was investigated using solutions initially containing 0.1 mM  $\text{K}_2\text{Cr}_2\text{O}_7$ . Our previous study has shown that pH has a negligible effect on the nanoparticle formation due to the highly soluble nature of  $\text{Cr}^{\text{VI}}$  while highly insoluble nature of  $\text{Cr}^{\text{III}}$  at most pHs. Thus, in the current study all tests were performed with solutions initially at pH 6.0, near neutral but a more stable pH under irradiation. The studied test solutions are listed in Table 6.1 and include: no scavengers ((1) deaerated only), solutions containing only one type of scavenger ((2) deaerated with 0.1 M *t*-butanol, (3) purged with  $\text{N}_2\text{O}$ , and (4) aerated only), and solutions containing two



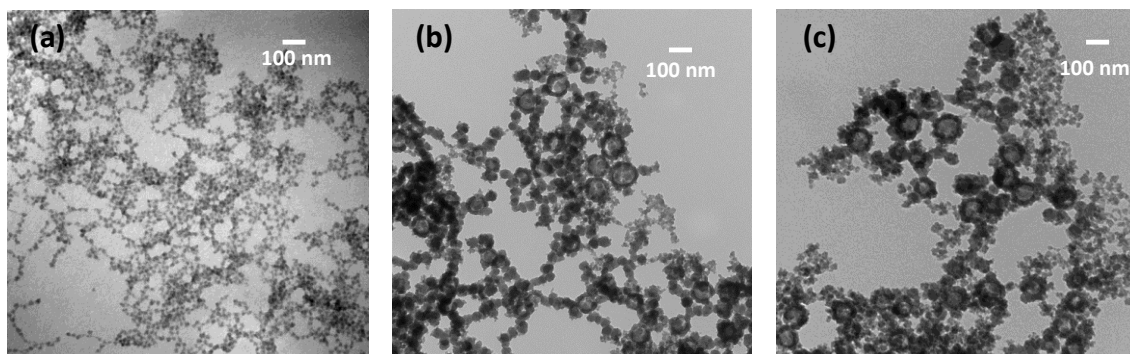
different types of scavenger ((5) aerated with 0.1 M *t*-butanol). The concentration of dissolved O<sub>2</sub> in an air-saturated solution is ~ 0.25 mM at 25 °C [17]. The concentration of N<sub>2</sub>O in the N<sub>2</sub>O/Ar (1:1 mixture) purged solution is estimated to be ~ 12.5 mM, half of the solubility of N<sub>2</sub>O at 1 atm at 25 °C [36].

**Table 6.1:** Test solutions studied.

	no scavengers	one type of scavenger			two types of scavenger
ID	1 none	2 <i>t</i> -butanol	3 N <sub>2</sub> O	4 O <sub>2</sub>	5 O <sub>2</sub> + <i>t</i> -butanol
Type of solution	deaerated only	deaerated & 0.1 M <i>t</i> -butanol	purged with N <sub>2</sub> O/Ar	aerated only	aerated & 0.1 M <i>t</i> -butanol

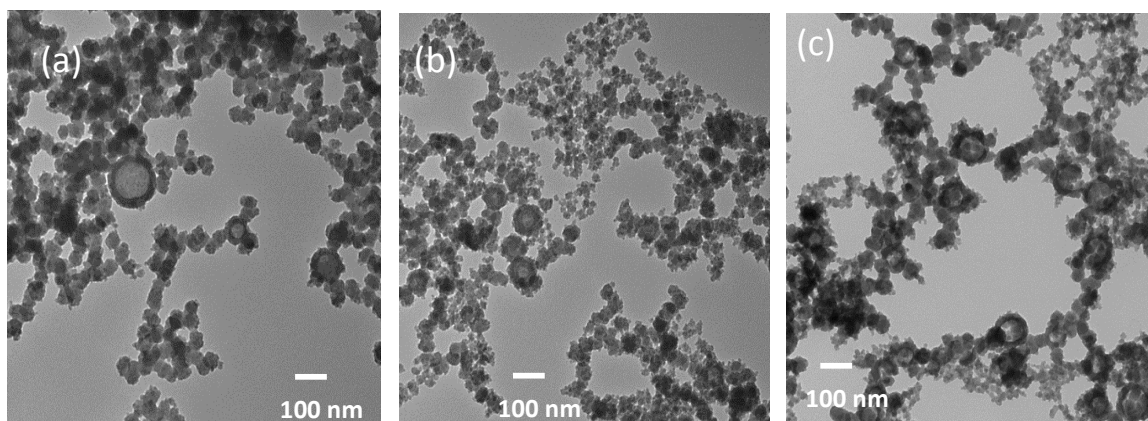
No detectable particles were formed after 5 h of irradiation for solutions purged with N<sub>2</sub>O/Ar (solution 3) and aerated only (solution 4). The TEM images of the particles formed after 5 h irradiation in the other scavenging environments are presented in Figure 6.1. The TEM images show that the particles formed in the deaerated only solutions all are very small and have a similar shape with sizes ranging 8 – 30 nm. The particles formed in the two other solutions (with *t*-butanol or O<sub>2</sub> + *t*-butanol) have bimodal size distributions, small particles with sizes ranging 10 – 30 nm and large circular disk-shaped particles with sizes ranging 140 – 200 nm. The larger circular disk-shaped particles appear to be agglomerations of the smaller particles in a micelle-like structure. The ratio of the larger to smaller particle populations appears to be higher in the solutions

with  $O_2 + t$ -butanol than in the solutions with no scavenger or only  $t$ -butanol. The smaller particles formed in the solutions with  $O_2 + t$ -butanol also have smaller sizes and sharper edges (more crystallites) than those formed in the solutions with  $t$ -butanol only. The average size of the smaller particles formed in the presence of the scavengers is larger than that observed in solutions with no scavengers.



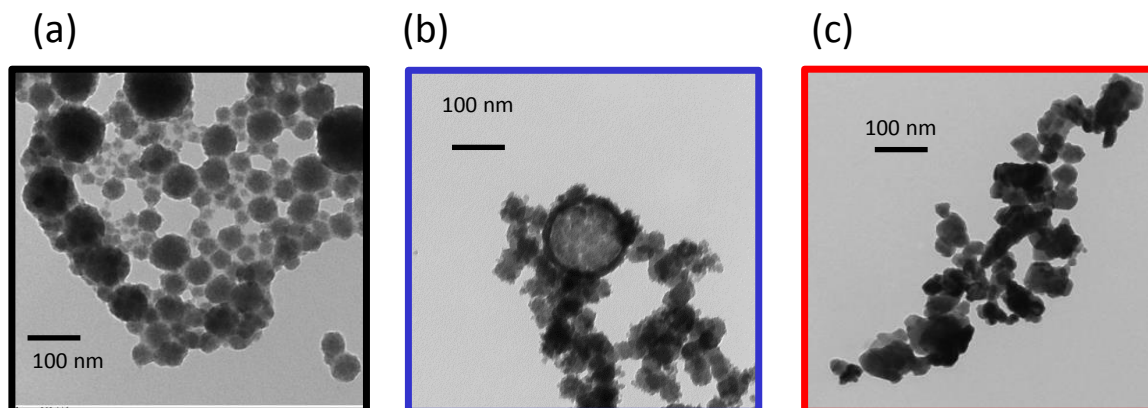
**Figure 6.1:** TEM images of chromium oxide nanoparticles formed by irradiation (5 h) of a 0.1 mM  $K_2Cr_2O_7$  solution at pH 6.0 with different scavengers: (a) none, (b)  $t$ -butanol, and (c)  $O_2 + t$ -butanol.

The changes in particle morphology and size as a function of irradiation time were explored. The TEM images of the nanoparticles formed in the solutions with  $t$ -butanol after different irradiation times are shown in Figure 6.2. The larger disk-shaped particles are present at times as early as 20 min. As irradiation time increases, these large particles appear to lose particle elements and shrink slightly with some showing holes left behind inside the micelle-like structure.



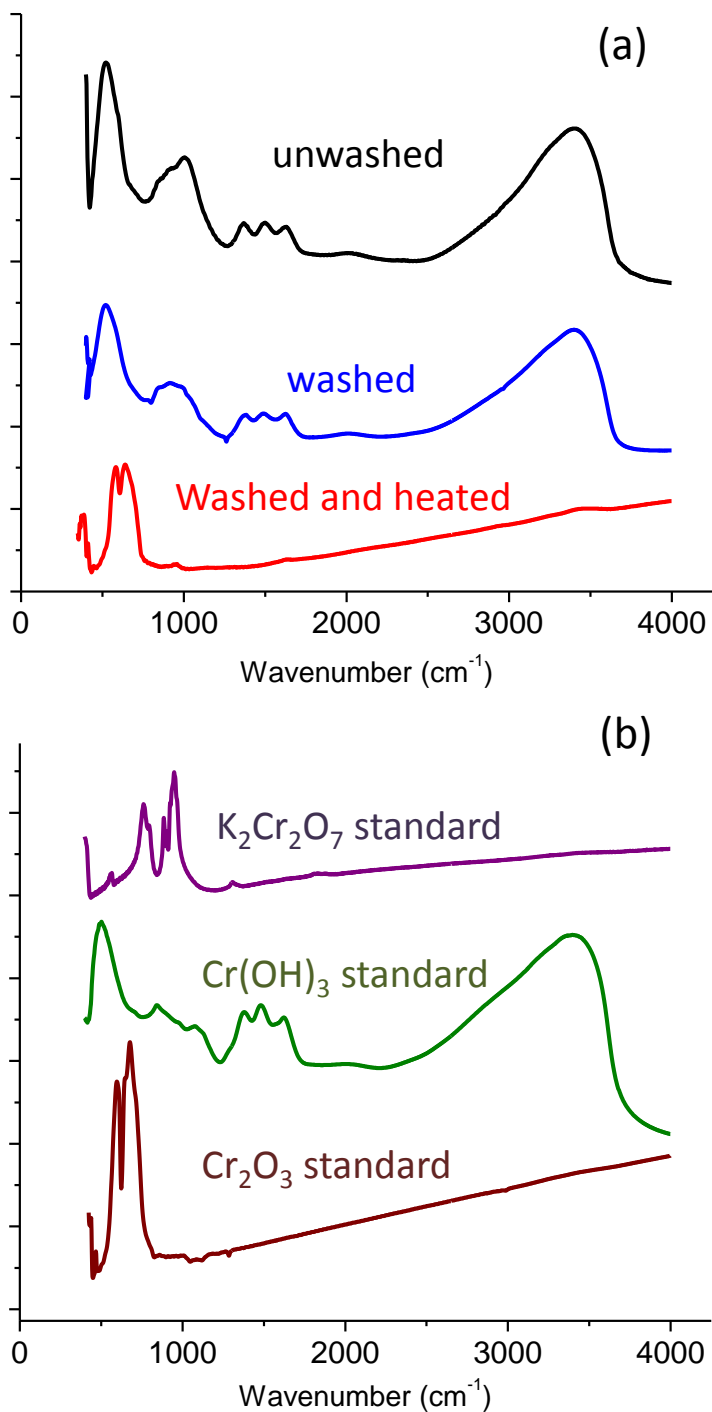
**Figure 6.2:** TEM images of chromium oxide nanoparticles formed in deaerated 0.1 mM  $K_2Cr_2O_7$  solutions with *t*-butanol added as a function of irradiation time: (a) 20 min, (b) 60 min, and (c) 300 min.

Figure 6.3 shows TEM images of the particles formed by irradiation of 0.1 mM  $K_2Cr_2O_7$  solutions with *t*-butanol that were collected by centrifuge and then subjected to different post-irradiation treatments: (1) as collected, (2) washed with distilled water (washed particles), and (3) washed with distilled water and then heated at 400 °C for 5 h in air. These particles are referred to hereafter as unwashed, washed and washed and heated particles. These treatments explored in order to see how one can address the ‘contamination’ of the particles produced by the adsorption of  $Cr^{VI}$  on the surface of the particles (see below). The unwashed particles have a similar bi-modal size distribution to the washed particles; there are large particles with sizes ranging 140 – 200 nm and smaller particles with sizes ranging 10 – 30 nm. While their sizes are similar, the unwashed particles are rounder and the larger particles appear as darker TEM images and do not reveal micelle-like structures. The washed and heated particles no longer include large micelle-like particles and they are all in the range of 10 – 30 nm with sharp edges and a defined crystal structure (cubic to hexagonal shape).



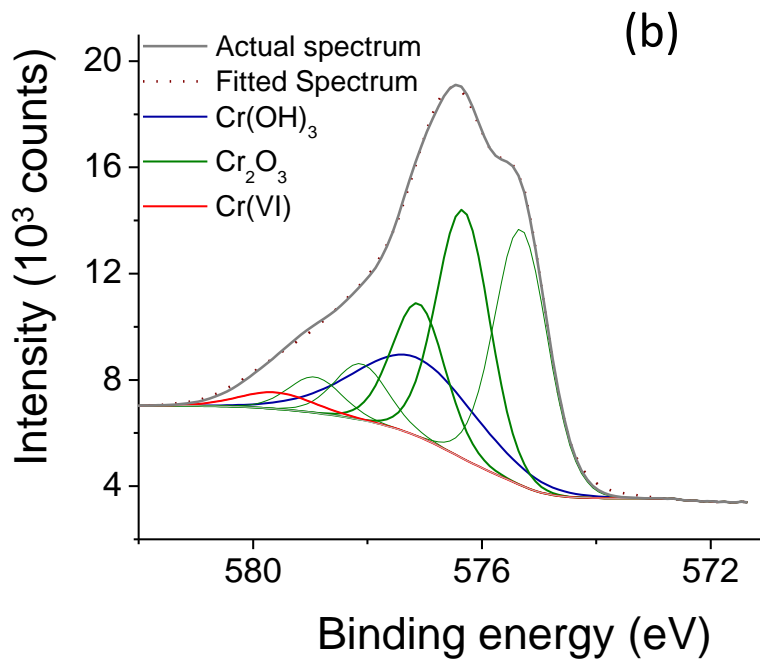
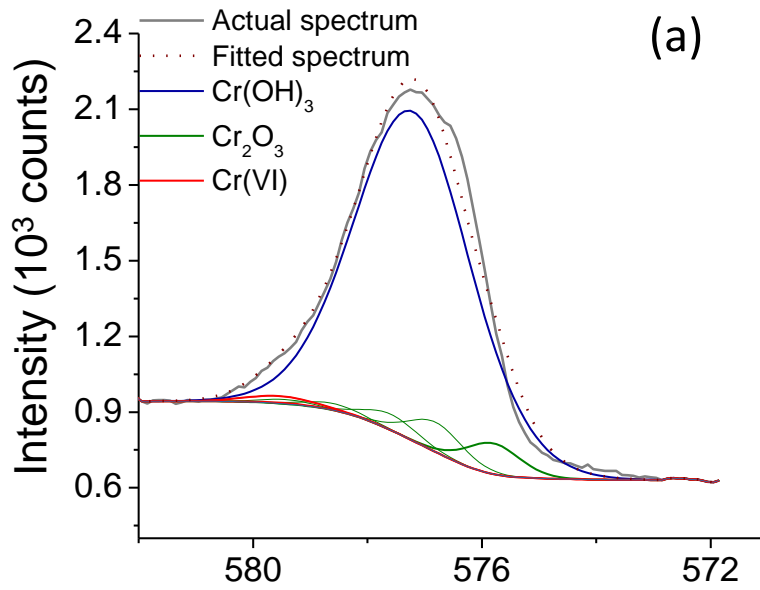
**Figure 6.3:** TEM images of (a) unwashed particles, (2) washed particles, and (3) washed and heated particles (the color of the border line related to FTIR spectra Figure 6.4)

The FTIR spectra of the particles formed from irradiation of a chromate solution with *t*-butanol added and with the different post-radiation treatments are compared in Figure 6.4a. The reference FTIR spectra of several chromium oxides/hydroxides are shown in Figure 6.4b. The reference spectra were obtained using standard powder samples of  $\text{Cr}_2\text{O}_3$  (purchased from Alfa Aesar),  $\text{Cr}(\text{OH})_3$  (synthesized according to Biesinger et al. [37]) and  $\text{K}_2\text{CrO}_4$  (purchased from Sigma-Aldrich). The FTIR spectrum of the washed and heated particles matches very well with the reference spectrum of  $\text{Cr}_2\text{O}_3$ . On the other hand the spectra of the unwashed and washed particles closely match the reference spectrum of  $\text{Cr}(\text{OH})_3$ . However, the spectra for the unwashed and washed particles also include a peak in a range of  $800$  to  $1000\text{ cm}^{-1}$  which is in the same location as a group of peaks seen in the  $\text{K}_2\text{CrO}_4$  spectrum. This may be indicative of some  $\text{Cr}^{\text{VI}}$  contamination of predominantly  $\text{Cr}^{\text{III}}$  particles, present even after washing.



**Figure 6.4:** FTIR spectra of (a) nanoparticles formed in chromate solutions with *t*-butanol followed by different post-radiolysis treatments: unwashed (black line), washed (blue line), and washed and heated (red line), and (b) the reference spectra of the Cr<sub>2</sub>O<sub>3</sub>, Cr(OH)<sub>3</sub> and K<sub>2</sub>Cr<sub>2</sub>O<sub>7</sub> powders.

The presence of Cr<sup>VI</sup> species adsorbed on the washed and unwashed particles was confirmed by XPS. The high resolution Cr-2p bands of the XPS spectra of the washed and the washed and heated particles are shown in Figure 6.5. Both the Cr-2p and O-1s (not shown) XPS bands were deconvoluted to obtain the contributions of Cr<sup>VI</sup>, Cr(OH)<sub>3</sub> and Cr<sub>2</sub>O<sub>3</sub> to the bands (see ref.[38] for the deconvolution analysis technique). The deconvoluted peaks and the composite spectra are also compared with the actual spectra obtained in Figure 6.5. The deconvolution analysis results show that for the washed particles Cr(OH)<sub>3</sub> contributes the most to the Cr-2p band intensity (88.4% Cr(OH)<sub>3</sub>, 9.8% Cr<sub>2</sub>O<sub>3</sub> and 1.8 % Cr<sup>VI</sup>), while for the heated particles the contribution from Cr<sub>2</sub>O<sub>3</sub> is the largest (88.9%) while the contribution from Cr<sup>VI</sup> remains at the same small level (2.3%). These results show that heating removes the adsorbed water and further converts Cr(OH)<sub>3</sub> to Cr<sub>2</sub>O<sub>3</sub>. This also demonstrates that the Cr<sup>III</sup> oxide particles are reasonably stable and do not oxidize to Cr<sup>VI</sup>, even during heating in air.



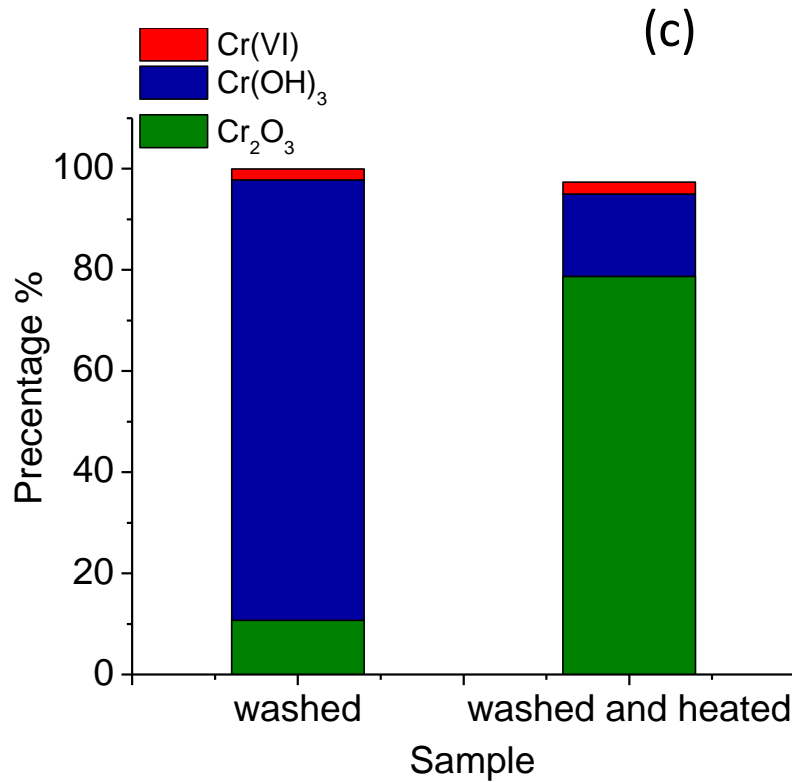


**Figure 6.5:** High resolution XPS Cr-2p bands of (a) washed particles and (b) washed and heated particles, and (c) the contributions of Cr<sup>VI</sup>, Cr(OH)<sub>3</sub> and Cr<sub>2</sub>O<sub>3</sub> to the Cr-2p band intensity obtained by deconvolution. The individual contributions to the composite bands are shown in (a) and (b).

### 6.3.2 Effect of Scavenger on Cr<sup>VI</sup>(aq) to Cr<sup>III</sup> Particle Conversion

To determine the mechanism by which the radical scavengers influence the size of the particles that grow, the kinetics of radiolytic conversion of Cr<sup>VI</sup> to Cr<sup>III</sup> were followed. The changes in [Cr<sup>VI</sup>(aq)] and [Cr<sup>III</sup>] as a function of irradiation time observed in solutions without any scavengers are first shown in Figure 6.6. The data are presented in two different time scales to better illustrate the behaviour at short times. Three different sets of data are shown to indicate the reproducibility of the concentration measurements.



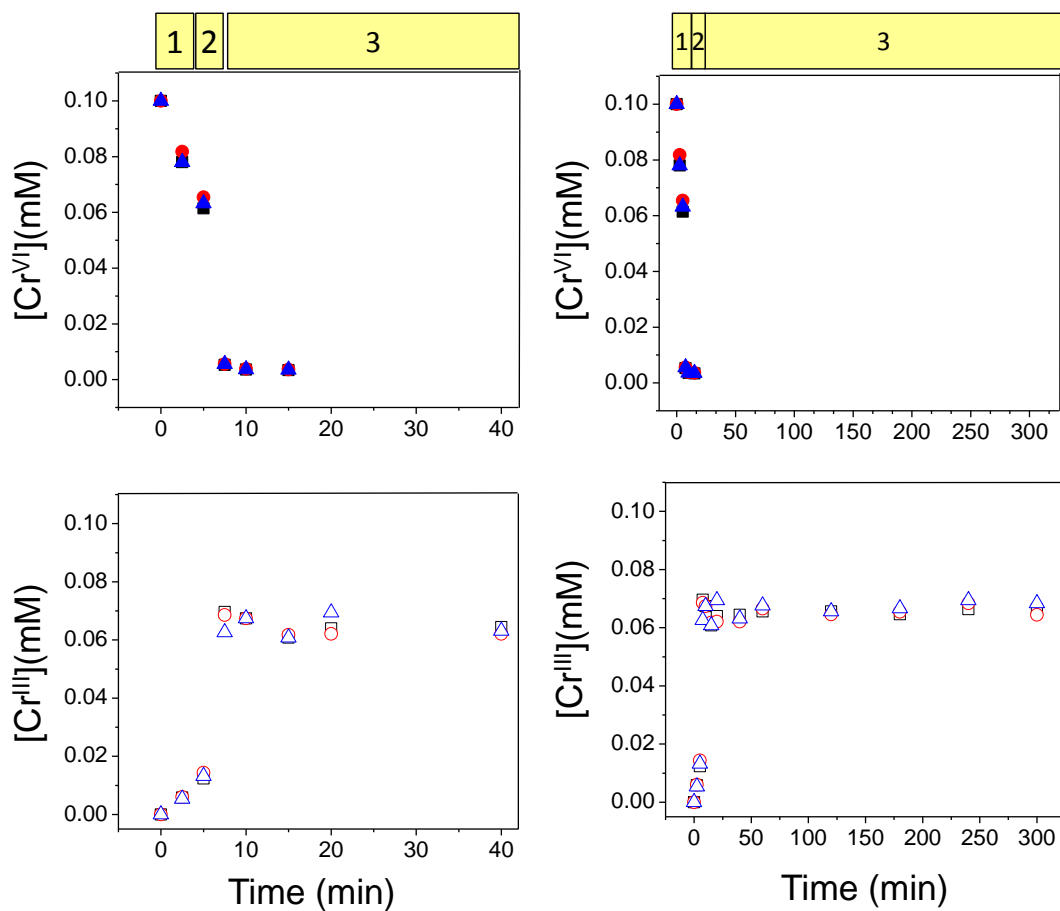


**Figure 6.6:** Concentrations of  $\text{Cr}^{\text{VI}}(\text{aq})$  (solid symbols) and  $\text{Cr}^{\text{III}}$  (open symbols) observed as a function of time during radiolysis of deaerated solutions initially containing 0.1 mM  $\text{K}_2\text{Cr}_2\text{O}_7$ . Three different sets of data show the reproducibility of the results. Stages 1, 2 and 3 are indicated on the top.

The concentrations show three kinetic stages with distinctly different time dependences. During the first 5 minutes (Stage 1) the  $[\text{Cr}^{\text{VI}}(\text{aq})]$  decreases at a linear rate while  $[\text{Cr}^{\text{III}}]$  increases at a much slower rate. As a result mass balance for Cr does not appear to be conserved in Stage 1. We attribute the apparent mass imbalance to two factors. First, adsorption of  $\text{Cr}^{\text{VI}}$  species onto the  $\text{Cr}^{\text{III}}$  condensate nucleates will remove some  $\text{Cr}^{\text{VI}}$  from solution and this will lower the apparent concentration of  $\text{Cr}^{\text{VI}}(\text{aq})$  as determined using our colorimetric technique (see discussion below on particle formation kinetics). Secondly, some of the solid  $\text{Cr}^{\text{III}}$  can precipitate on the test vial surfaces and not remain suspended in solution. The analysis for  $\text{Cr}^{\text{III}}$  is only able to quantify the  $\text{Cr}^{\text{III}}$  that is dispersed in the solution sample extracted from the test vial by syringe. Incomplete mass balance does not alter the important trends seen in the concentrations of both  $\text{Cr}^{\text{VI}}$  and  $\text{Cr}^{\text{III}}$ , see further discussion in Section 6.4.

Stage 2 refers to the short transition period between Stages 1 and 3 and lasts for only a few minutes. During this stage the concentration of  $\text{Cr}^{\text{VI}}(\text{aq})$  decreases very rapidly and the concentration of  $\text{Cr}^{\text{III}}$  increases at a similar rate in the solutions without any scavengers. Stage 3 refers to the period that starts after  $[\text{Cr}^{\text{VI}}(\text{aq})]$  becomes negligible. The time to reach Stage 3 and the  $[\text{Cr}^{\text{III}}]$  at the onset of Stage 3 depend on the solution scavenger environment. In the solutions without any scavengers, Stage 2 is very short and Stage 3 is reached in 10 min. In these solutions the  $[\text{Cr}^{\text{III}}]$  remains nearly constant in Stage 3 and is about 65% of  $[\text{Cr}^{\text{VI}}(\text{aq})]_0$ . This apparent loss of mass balance is addressed below.

Figures 6.7 and 6.8 show similar results obtained for solutions containing scavengers. Figure 6.7 shows that the  $\bullet e_{aq}^-$  scavengers,  $O_2$  and  $N_2O$ , are very effective in suppressing the reduction of  $Cr^{VI}(aq)$  to  $Cr^{III}$  as no  $Cr^{III}$  particles were observed, even after 300 min of irradiation. Addition of the  $\bullet OH$  scavenger, *t*-butanol, has a negligible effect on the reduction kinetics at short times (Stages I and II), or on the  $[Cr^{III}]$  reached at the onset of Stage 3. However, with *t*-butanol present the  $[Cr^{III}]$ , following a small decrease, increases gradually in Stage 3 and reaches ~ 90% conversion of the initially dissolved  $Cr^{VI}(aq)$  after 300 min. This is in sharp contrast to the results seen in a deaerated solution alone, where there is a greater apparent loss of mass balance.

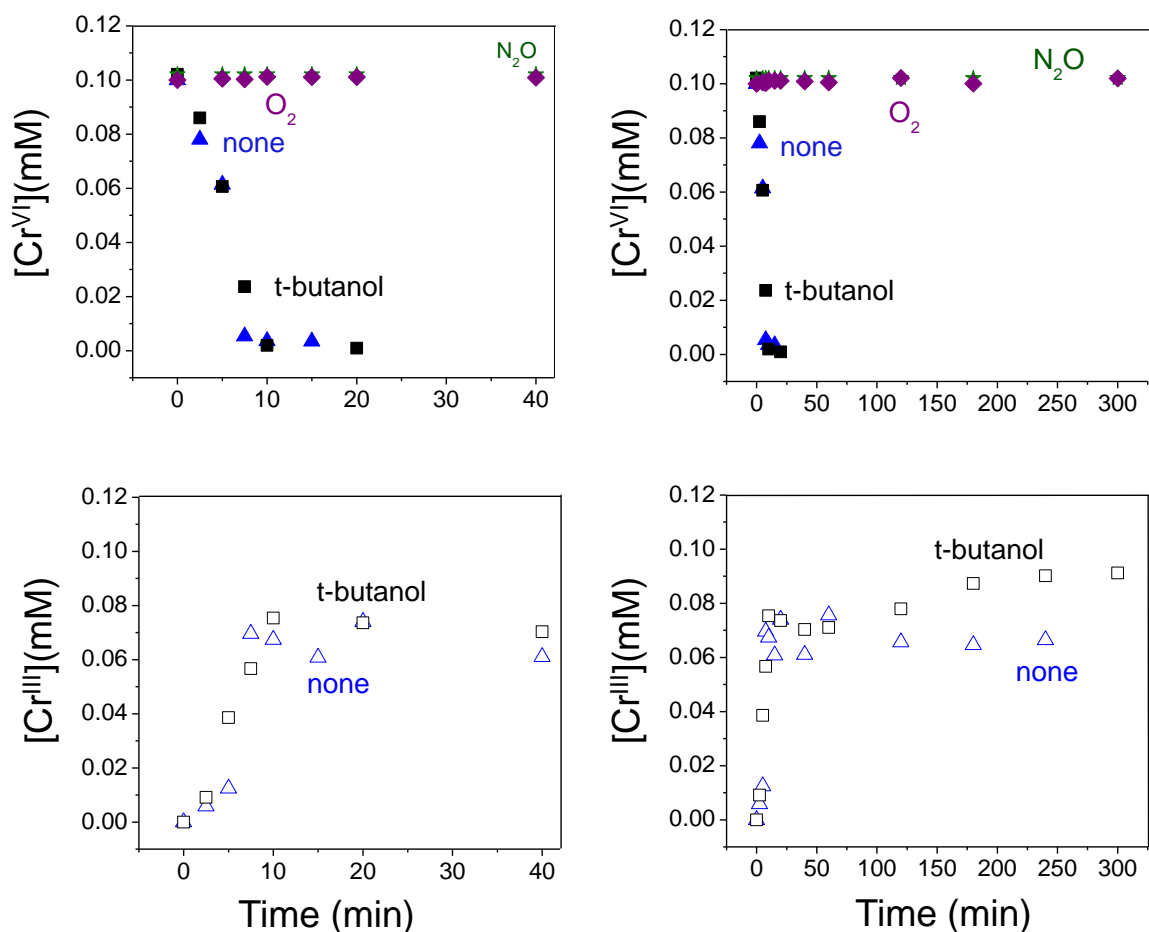


**Figure 6.7:** Concentrations of Cr<sup>VI</sup>(aq) (solid symbols) and Cr<sup>III</sup> (open symbols) observed as a function of time during radiolysis of 0.1 mM K<sub>2</sub>Cr<sub>2</sub>O<sub>7</sub> solutions containing no scavenger (▲, △) and one scavenger: 0.1 M *t*-butanol (■, □); O<sub>2</sub> (◆) and N<sub>2</sub>O (★). The two sets of graphs present the data on two different time scales.

In Figure 6.8, the conversion kinetics observed in the solutions that produced the particles shown in Figure 6.1 are compared. The [Cr<sup>VI</sup>(aq)] decreases at a much slower rate in solutions containing two scavengers (O<sub>2</sub> + *t*-butanol) than in the deaerated solutions. The rate of decrease is also faster than that seen in aerated solutions with no *t*-butanol (see Figure 6.7). These results arise because O<sub>2</sub> suppresses the concentration of

• $e_{aq}^-$  and this slows down the reduction of  $Cr^{VI}(aq)$  to  $Cr^{III}$  while *t*-butanol suppresses the concentration of •OH and this prevents oxidation of  $Cr^{III}$  back to  $Cr^{VI}(aq)$ . The net effect of the two scavengers is a slower conversion of  $Cr^{VI}(aq)$  to  $Cr^{III}$  at short times than that which occurs in solutions with *t*-butanol only, but a faster conversion than that which occurs in the solutions with only  $O_2$  present.

In solutions with  $O_2 + t$ -butanol the rate of production of  $Cr^{III}$  in Stage 1 is very slow and there is a delay in the production of detectable amounts of  $Cr^{III}$ . Following this delay,  $[Cr^{III}]$  quickly increases at a rate similar to that observed for deaerated solutions with and without *t*-butanol, but it reaches a steady concentration (Stage 2) sooner in solutions with  $O_2 + t$ -butanol. In these solutions Stage 2, in which  $[Cr^{VI}(aq)]$  continues to decrease and  $[Cr^{III}]$  is at a low steady-state level, also lasts longer. In Stage 3  $[Cr^{III}]$  starts to increase again at a nearly linear rate until it reaches ~85% of the initial  $[Cr^{VI}(aq)]$ . Although the rate of increase in  $[Cr^{III}]$  is faster in solutions with  $O_2 + t$ -butanol, the final conversion yield is nearly the same as that observed in solutions with *t*-butanol only. In solutions without any scavengers  $[Cr^{III}]$  does not change in Stage 3 (see Figure 6.6).

In all tests there are some apparent mass imbalances. At all times, the total concentration of  $Cr^{VI}$  and  $Cr^{III}$  does not equal the initial concentration of  $Cr^{VI}$ . We do not fully understand the reason for this behaviour. As noted above, there are two important factors that could contribute to the behaviour, loss of  $Cr^{VI}(aq)$  to particle surfaces and loss of  $Cr^{III}$  particles to test vial surfaces. Another factor could be incomplete oxidation of  $Cr^{III}$  particles during the analysis process. The mass imbalance was the most serious in deaerated only solutions which showed the highest  $Cr^{III}$  yield in Stages 1 and 2 but no

further growth in  $[\text{Cr}^{\text{III}}]$  in Stage 3 (Figure 6.7), and which produced the smallest particles but the largest number of these small particles (Figure 6.1).

We think co-precipitation of the oxides and hydroxides of chromium in mixed oxidation states ( $\text{Cr}^{\text{VI}}/\text{Cr}^{\text{V}}/\text{Cr}^{\text{IV}}/\text{Cr}^{\text{III}}$ ) occurs in Stages 1 and 2, triggered by the rapid reduction of the poly-oxygenated  $\text{Cr}^{\text{VI}}$  ion ( $\text{Cr}_2\text{O}_7^{2-}$ ) to insoluble  $\text{Cr}^{\text{III}}$  species [31]. The faster the reduction, the smaller the precipitated particles, but more of these particles are formed. The smaller the particles, the higher the fraction of  $\text{Cr}^{\text{VI}}$  (or Cr species in higher oxidation states than  $\text{Cr}^{\text{III}}$ ) adsorbed on the individual particles. As discussed later, the reduction of the adsorbed  $\text{Cr}^{\text{VI}}$  to  $\text{Cr}^{\text{III}}$  occurs at a slower rate than the reduction in solution phase. The reduction of adsorbed species thus occurs at later times. The less redox active species such as the superoxide radical ( $\bullet\text{O}_2^-$ ) and  $\text{H}_2\text{O}_2$  become more effective in inducing surface redox reactions than the very reactive species such as  $\bullet\text{e}_{\text{aq}}^-$  and  $\bullet\text{OH}$ . The latter species are more effective in inducing solution redox reactions. Thus, if the solution environment does not promote the formation of  $\bullet\text{O}_2^-$  at a higher concentration, further reduction of  $\text{Cr}^{\text{VI}}$  does not occur in Stage III. In deaerated only solutions the formation of  $\bullet\text{O}_2^-$  is negligible and most of the  $\text{Cr}^{\text{VI}}$  reduction to  $\text{Cr}^{\text{III}}$  is induced by homogenous solution phase reactions, see further discussion in Section 6.4. The  $\text{Cr}^{\text{VI}}$ -covered  $\text{Cr}^{\text{III}}$  species will be difficult to oxidize by permanganate and may not be detected by the DPC method. Despite the uncertainties associated with the absolute values of the  $[\text{Cr}^{\text{VI}}(\text{aq})]$  and  $[\text{Cr}^{\text{III}}]$  the time dependent trends in those concentrations are still valid.

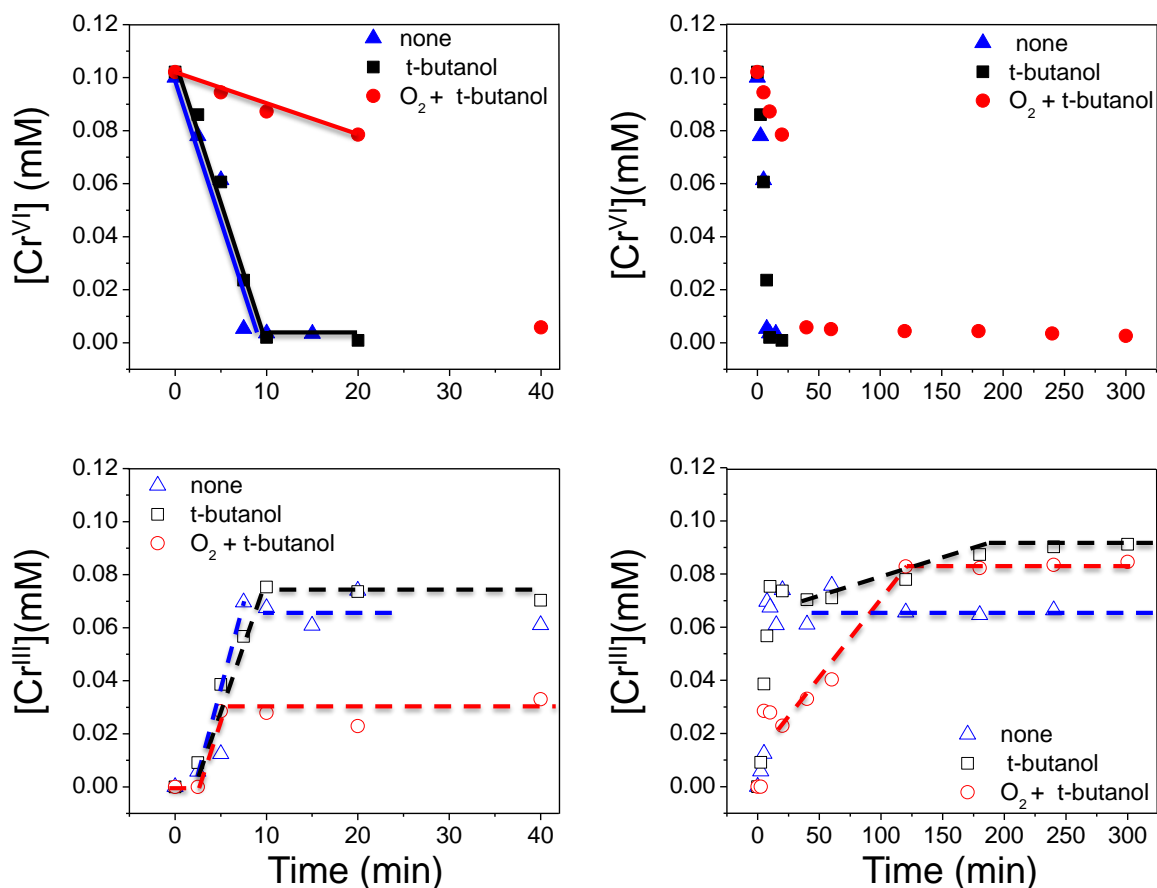


**Figure 6.8:** Concentrations of Cr<sup>VI</sup>(aq) (solid symbols) and Cr<sup>III</sup> (open symbols) observed as a function of time during radiolysis of 0.1 mM K<sub>2</sub>Cr<sub>2</sub>O<sub>7</sub> solutions with different scavengers: none (▲, △); 0.1 M *t*-butanol (■, □); and O<sub>2</sub> + 0.1 M *t*-butanol (●, ○). The two sets of graphs present the data on two different time scales.

## 6.4 DISCUSSION

The kinetic results presented above show that the presence of a scavenger can influence the yield and size of nanoparticles produced by irradiating a chromium solution. Different scavengers influence the kinetics of particle formation differently and this indicates that several different redox agents can participate in the particle formation

process. To explore this, it will consider the production of different oxidants and reductants and the changes in their concentrations with time, and the hydrolysis and phase equilibria of chromium species in an irradiated solution. A mechanism for radiation-induced chromium oxide particle formation that is consistent with the observations is then proposed.

Gamma-radiolysis of water produces a number of primary radiolysis products as shown in reaction (6.1). Under continuous irradiation these redox agents are continuously produced. They can then accumulate and undergo aqueous phase chemical reactions with each other and the water solvent species ( $\text{H}_2\text{O}$ ,  $\text{H}^+$ ,  $\text{OH}$ ) to form secondary products such as  $\text{O}_2$  and  $\bullet\text{O}_2^-$ . The concentrations of species in a system exposed to a continuous  $\gamma$ -radiation flux typically reach steady state within minutes [18,33].

The radiolysis products can also react with redox active solute species present in the solution. (The probability of solute species at a relatively low concentration ( $< 0.01$  M) directly interacting with incident radiation is very small and can be neglected.) These aqueous phase chemical reactions are typically much slower than the reactions leading to formation of the primary radiolysis products. (The half-life of an aqueous reaction is typically longer than a ms whereas a homogeneous distribution of primary radiolysis products is achieved in less than a  $\mu\text{s}$  [17,18].) However, solute reactions can have an impact on the steady-state concentrations of the radiolysis products that arise. Studies on steady-state radiolysis kinetics can be found in refs [39-41].

The radiolytic production of  $\text{Cr}^{\text{III}}$  particles from dissolved  $\text{Cr}^{\text{VI}}$  involves many competing oxidation and reduction reactions. The observed effects of different scavengers on the kinetics of this process and the final size of  $\text{Cr}_2\text{O}_3$  nanoparticles that



are formed can provide information on the key reactions involved in different stages. A reaction mechanism that is consistent with the observations is schematically presented in Figure 6.9. This mechanism is similar to a mechanism proposed by Wren et al. to explain the kinetics of Cr<sup>III</sup> oxide/hydroxide particle formation as a function of pH from [Cr<sup>VI</sup>(aq)]<sub>0</sub> solutions with no scavengers [31]. The mechanism is further refined here to accommodate the changes in reaction kinetics caused by the presence of selective radical scavengers.

The formation of Cr<sup>III</sup> oxide/hydroxide nanoparticles from irradiation of dissolved Cr<sup>VI</sup>(aq) ions (Cr<sub>2</sub>O<sub>7</sub><sup>2-</sup>/CrO<sub>4</sub><sup>2-</sup>) occurs in three kinetic stages.

Stage I: Radiolytic reduction of Cr<sup>VI</sup>(aq) to Cr<sup>III</sup>(aq) species followed by spontaneous condensation of Cr(OH)<sub>3</sub>. This provides nucleation sites onto which Cr<sup>VI</sup> and Cr<sup>III</sup> co-precipitate to form mixed Cr<sup>VI</sup>/Cr<sup>III</sup> oxide/hydroxide particles,

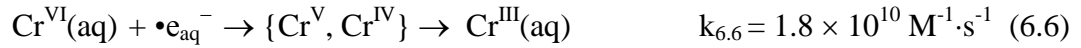
Stage II: Radiolytic redox reactions of Cr<sup>VI</sup>(aq) and Cr<sup>III</sup>(aq) in solution reach steady state and adsorption of Cr<sup>VI</sup> continues, growing the mixed Cr<sup>VI</sup>/Cr<sup>III</sup> oxide/hydroxide particles,

Stage III: Heterogeneous redox reactions of Cr<sup>VI</sup> and Cr<sup>III</sup> occur and the particles slowly convert from a mixed Cr<sup>VI</sup>/Cr<sup>III</sup> oxide/hydroxide to Cr(OH)<sub>3</sub> and then to Cr<sub>2</sub>O<sub>3</sub>.

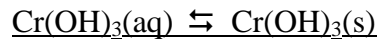
The standard reduction potential for the conversion of Cr<sub>2</sub>O<sub>7</sub><sup>2-</sup> to Cr<sup>3+</sup> (E°(Cr<sup>VI</sup>(aq)/Cr<sup>III</sup>(aq))) is 1.33 V<sub>SHE</sub> [42]. This high reduction potential indicates that the reduction of Cr<sup>VI</sup>(aq) to Cr<sup>III</sup>(aq) will occur very easily but its reverse process, oxidation of Cr<sup>III</sup>(aq) to Cr<sup>VI</sup>(aq), will not occur as easily. Thus, the chromium oxidation requires a

very strong oxidant, such as  $\bullet\text{OH}$  or  $\text{H}_2\text{O}_2$ . Dissolved oxygen ( $E^\circ(\text{O}_2/\text{H}_2\text{O}) = 1.229 \text{ V}_{\text{SHE}}$ ) is not a sufficiently strong oxidant to convert  $\text{Cr}^{3+}$  to  $\text{Cr}_2\text{O}_7^{2-}$ .

Water radiolysis produces  $\bullet\text{e}_{\text{aq}}^-$  which is a strong reducing agent that reacts very rapidly with  $\text{Cr}^{\text{VI}}(\text{aq})$ :



Since the solubility of  $\text{Cr}^{\text{III}}$  species is very low and several orders of magnitude lower than that of  $\text{Cr}^{\text{VI}}$  at nearly all pHs [43], once the concentration of  $\text{Cr}^{\text{III}}(\text{aq})$  reaches a critical level, spontaneous condensation of  $\text{Cr}^{\text{III}}(\text{aq})$  to  $\text{Cr}^{\text{III}}(\text{s})$  occurs. For simplicity we assume that the only  $\text{Cr}^{\text{III}}$  species that need be considered is  $\text{Cr}(\text{OH})_3$  (there may be other  $\text{Cr}^{\text{III}}$  hydroxides also in equilibrium in solution):



For simplicity chromium species with oxidation states in-between VI and III may be formed [31] but they are not considered in the discussion (they are considered to exist as transient species and will not be detected by post-irradiation analyses used in this study).

The condensed  $\text{Cr}^{\text{III}}$  particles provide surfaces for the  $\text{Cr}_2\text{O}_7^{2-}(\text{aq})$  to adsorb:



The overall effect of reactions (6.6) to (6.8) is a faster decrease in  $[\text{Cr}^{\text{VI}}(\text{aq})]$  than the rate of increase in  $[\text{Cr}^{\text{III}}]$  observed in Stage I in all solutions. The difference is caused by the amount of  $\text{Cr}^{\text{VI}}(\text{ad})$ . The rate of decrease in  $[\text{Cr}^{\text{VI}}(\text{aq})]$  in Stage 1 will depend mainly on the concentration of  $\bullet\text{e}_{\text{aq}}^-$ . Hence, the presence of any radical scavenger which can influence  $[\bullet\text{e}_{\text{aq}}^-]$  will also have an impact on the rate of decrease in  $[\text{Cr}^{\text{VI}}(\text{aq})]$  in Stage 1.

Water radiolysis also produces  $\bullet\text{OH}$  and  $\text{H}_2\text{O}_2$  and both of these species are sufficiently strong oxidizers to convert  $\text{Cr}^{\text{III}}(\text{aq})$  back to  $\text{Cr}^{\text{VI}}(\text{aq})$ , e.g.,



Since the radical/ion reactions (6.6) and (6.9) are fast, the concentrations of  $\text{Cr}^{\text{VI}}(\text{aq})$  and  $\text{Cr}^{\text{III}}(\text{aq})$  soon reach pseudo steady state and the ratio of their concentrations can be approximated by:

$$\frac{[\text{Cr}^{\text{III}}(\text{aq})]}{[\text{Cr}^{\text{VI}}(\text{aq})]} \approx \frac{k_{6,6}[\bullet\text{e}_{\text{aq}}^-]}{k_{6,9}[\bullet\text{OH}]} \quad (6.10)$$

The pseudo steady state is reached in Stage 2 and the concentration of  $\text{Cr}^{\text{III}}$  in Stage 2 is determined by the steady-state concentrations of  $\bullet\text{e}_{\text{aq}}^-$  and  $\bullet\text{OH}$ . The presence of an  $\bullet\text{OH}$  scavenger (*t*-butanol) will then increase the  $\text{Cr}^{\text{III}}$  to  $\text{Cr}^{\text{VI}}(\text{aq})$  ratio while the presence of an  $\bullet\text{e}_{\text{aq}}^-$  scavenger ( $\text{O}_2$ ) will decrease the ratio. The conversion yield achieved in Stage 2 is high (~ 70%) in the absence of any scavengers (Figure 6.6) and hence the effect of an  $\bullet\text{OH}$  scavenger (*t*-butanol) in deaerated solutions is small (Figure 6.7). As expect, addition of dissolved oxygen (a good  $\bullet\text{e}_{\text{aq}}^-$  scavenger) is effective in suppressing the production of  $\text{Cr}^{\text{III}}$ . In a system with mixed scavengers ( $\text{O}_2 + t$ -butanol) the competition for  $\bullet\text{e}_{\text{aq}}^-$  and  $\bullet\text{OH}$  slows the production of  $\text{Cr}^{\text{III}}$ .

The mixed  $\text{Cr}^{\text{VI}}/\text{Cr}^{\text{III}}$  oxides/hydroxides continue to grow in Stage 2 until most of the initial  $\text{Cr}^{\text{VI}}(\text{aq})$  has been oxidized and/or adsorbed onto particles. The subsequent increase in  $[\text{Cr}^{\text{III}}]$  observed in Stage 3 is due to the reduction of adsorbed  $\text{Cr}^{\text{VI}}$  to  $\text{Cr}^{\text{III}}$  and incorporation in the solid particle phase. The heterogeneous reaction and solid state conversion is slow, in part because it requires diffusion of reactants in solution to the particle surface. Redox active species such as  $\bullet\text{O}_2^-$  and  $\text{H}_2\text{O}_2$  become more important

contributors to long-term kinetics because these secondary radiolysis products can accumulate to higher concentrations at longer times [34]:



The radiolytic formation of  $\bullet\text{O}_2^-$  in aerated solutions promotes the solid state conversion of  $\text{Cr}^{\text{VI}}$  to  $\text{Cr}^{\text{III}}$  (reaction 6.11) in Stage 3. This can explain the faster rate of increase in  $[\text{Cr}^{\text{III}}]$  in Stage 3 in solutions with ( $\text{O}_2 + t$ -butanol) compared to the rate in solutions with  $t$ -butanol only. Note that scavenging of  $\bullet\text{OH}$  by  $t$ -butanol also increases  $[\bullet\text{O}_2^-]$  because the reaction of  $\bullet\text{O}_2^-$  with  $\bullet\text{OH}$  is suppressed:



Thus, in the solutions with  $t$ -butanol only  $[\text{Cr}^{\text{III}}]$  increases in Stage 3 at a slower rate than that which occurs in solutions with  $\text{O}_2$  and  $t$ -butanol.

The kinetics observed in different scavenging environments are consistent with the sizes and morphologies of the final particles formed. When the homogeneous  $\text{Cr}^{\text{VI}}$  to  $\text{Cr}^{\text{III}}$  conversion in solution (reaction 6.6) is very fast, such that most of the conversion occurs in Stages 1 and 2, a large number of mixed  $\text{Cr}^{\text{VI}}/\text{Cr}^{\text{III}}$  oxides/hydroxides (or  $\text{Cr}^{\text{VI}}$ -adsorbed  $\text{Cr}^{\text{III}}$  particles) will be formed very quickly. The overall concentration of  $\text{Cr}^{\text{VI}}$  in the mixed oxide will be small, and the final  $\text{Cr}^{\text{III}}$  particles won't be large. This is what we observed in deaerated water (Figure 6.1).

The addition of  $t$ -butanol (in both aerated or deaerated water) increases the size of  $\text{Cr}^{\text{III}}$  particles. This is consistent with the increase in  $[\text{Cr}^{\text{III}}]$  seen in Stage 3. The presence of bigger micelle-like particles in these solutions is attributed to the agglomeration of the mixed  $\text{Cr}^{\text{VI}}/\text{Cr}^{\text{III}}$  oxides/hydroxides which may be more effective with a higher  $\text{Cr}^{\text{VI}}$

concentration in the mixed oxide. As the reduction of Cr<sup>VI</sup> to Cr<sup>III</sup> continues in Stage 3, the Cr<sup>III</sup> oxide/hydroxide becomes more crystalline Cr<sub>2</sub>O<sub>3</sub>. The Cr<sub>2</sub>O<sub>3</sub> has a higher surface hydration energy than Cr(OH)<sub>3</sub> and less affinity to dissolved Cr<sup>VI</sup> ions, and the micelle-like agglomerates lose Cr<sup>III</sup> particles.

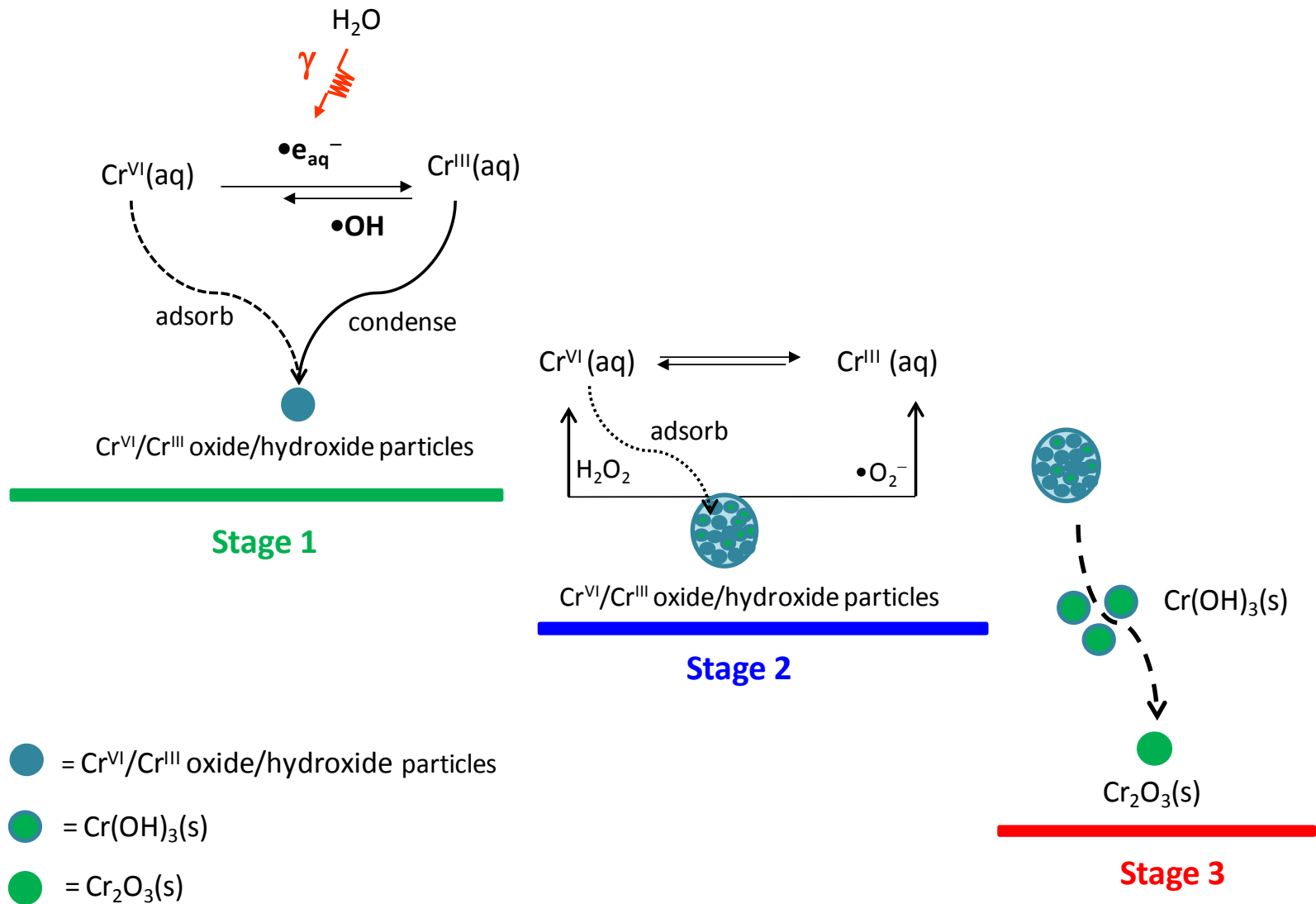


**Figure 6.9:** Schematic of a mechanism for radiation-induced chromium oxide nanoparticle formation

The proposed mechanism can also explain the observed effect of the scavengers on the composition and the size and morphology of the final  $\text{Cr}^{\text{III}}$  particles. The final size of  $\text{Cr}_2\text{O}_3$  is determined by the ratio of the rates of net reduction of  $\text{Cr}^{\text{VI}}$  to  $\text{Cr}^{\text{III}}$  in solution (Stages 1 and 2) versus on particle surface (Stage 3). The reduction rate in solution is determined by the ratio of steady-state concentrations of  $\bullet\text{e}_{\text{aq}}^-$  and  $\bullet\text{OH}$  while the reduction on particle surface is determined by the concentration of  $\bullet\text{O}_2^-$ . Dissolved oxygen scavenges  $\bullet\text{e}_{\text{aq}}^-$  but converts it to  $\bullet\text{O}_2^-$ . In the presence of  $\bullet\text{OH}$  at a high concentration  $\bullet\text{O}_2^-$  cannot accumulate to any substantial level. However, in the presence of *t*-butanol, an  $\bullet\text{OH}$  scavenger,  $\bullet\text{O}_2^-$  can accumulate a sufficiently high concentration. Thus, our study suggests that a combination of concentrations of dissolved oxygen and *t*-butanol, as well as the initial concentration of  $[\text{Cr}^{\text{VI}}(\text{aq})]$  may be used to control the size of the  $\text{Cr}_2\text{O}_3$  particles.

## 6.5 CONCLUSIONS

A mechanism for radiation-induced formation of  $\text{Cr}_2\text{O}_3$  nanoparticles is proposed that is consistent with the observed effects of radical scavengers on the kinetics of reduction of  $\text{Cr}^{\text{VI}}(\text{aq})$ . The radiation-induced formation of  $\text{Cr}_2\text{O}_3$  nanoparticles occurs in three stages. Stage 1 involves radiolytic reduction of  $\text{Cr}^{\text{VI}}(\text{aq})$  to  $\text{Cr}^{\text{III}}(\text{aq})$  species in the solution phase, followed by spontaneous condensation of  $\text{Cr}(\text{OH})_3$  particles. This provides sites onto which  $\text{Cr}^{\text{VI}}$  and  $\text{Cr}^{\text{III}}$  co-precipitate and form mixed  $\text{Cr}^{\text{VI}}/\text{Cr}^{\text{III}}$  oxide/hydroxide particles. In Stage 2, radiolytic interconversion of  $\text{Cr}^{\text{VI}}(\text{aq})$  and  $\text{Cr}^{\text{III}}(\text{aq})$  in solution reach steady state while the adsorption of  $\text{Cr}^{\text{VI}}$  on particles continues, growing mixed  $\text{Cr}^{\text{VI}}/\text{Cr}^{\text{III}}$  oxide/hydroxide particles. In Stage 3 solid-state conversion of  $\text{Cr}^{\text{VI}}$  and

Cr<sup>III</sup> in the particles, slowly converting the oxide from a mixed Cr<sup>VI</sup>/Cr<sup>III</sup> oxide/hydroxide to Cr(OH)<sub>3</sub> and then to Cr<sub>2</sub>O<sub>3</sub>. This study shows how appropriate adjustment of solution conditions and radical scavenger concentrations can be used to produce Cr<sub>2</sub>O<sub>3</sub> nanoparticles with tailored sizes.

## 6.6 REFERENCES

- [1] T. Brock, M. Groteklaes, P. Mischke, in *European Coating Handbook*, Vincentz, Hannover, Germany, 2000.
- [2] B.M. Abu-Zied, *Appl. Catal. A: Gen.*, 198 (2000) 139.
- [3] P. Berdhal, *Trans. Am. Soc. Mech. Eng. J. Heat Transfer.*, 117 (1995) 355.
- [4] H. Kitsunai, K. Hokkirigawa, N. Tsumaki, K. Kato, *Wear*, 151 (1991) 279.
- [5] T. Ivanova, K. Gesheva, A. Cziraki, A. Szekeres, E. Vlaikova, *J. Phys.: Conf. Ser.*, 113 (2008) 012030.
- [6] Z. Pei, H. Xu, Y. Zhang, *J. Alloys Compd.*, 468 (2009) L5.
- [7] M.D. Lima, R. Bonadimann, M.J. de Addrade, J.C. Toniolo, C.P. Bergmann, *J. Eur. Ceram. Soc.*, 26 (2006) 1213.
- [8] N. Arul Dash, Y. Koltypin, A. Gedanken, *Chem. Mater.*, 9 (1997) 3159.
- [9] G. Peters, K. Jerg, B. Schramn, *Mater. Chem. Phys.*, 55 (1998) 197.
- [10] Z. Gui, R. Fan, W. Mo, X. Chen, L. Yang, U. Hu, *Mater. Res. Bull.*, 38 (2003) 169.
- [11] L. Znaidi, C. Pommier, *Eur. J. Solid State Inorg. Chem.*, 35 (1998) 405.



- [12] A. Kawabata, M. Yoshinaka, K. Hirota, O. Yamaguchi, *J. Am. Ceram. Soc.*, 78 (1995) 2271.
- [13] D.W. Kim, S.I. Shin, J.D. Lee, S.G. Oh, *Mater. Lett.*, 58 (2004) 1894.
- [14] U. Balachandran, R.W. Siegel, Y.X. Liao, T.R. Askew, *Nanostruct. Mater.*, 5 (1995) 505.
- [15] D. Vollath, D.V. Szabo, J.O. Willis, *Mater. Lett.*, 29 (1996) 271.
- [16] C. Zhu, Y. Hong, J. Zhang, B. Zhou, *Key Eng. Mater.*, 353 (2007) 2111.
- [17] J.W.T. Spinks, R.J. Woods, *An Introduction to Radiation Chemistry*, Wiley, New York, 1990.
- [18] J.C. Wren, Steady-state radiolysis: effect of dissolved additives in ACS Symposium Series: *Nuclear Energy and the Environment*, 2010.
- [19] A. Henglein, M. Giersig, *J. Phys. Chem. B*, 103 (1999) 9533.
- [20] Y. Ni, X. Ge, Z. Zhang, Q. Ye, *Chem. Mater.*, 14 (2002) 2002.
- [21] J. Belloni, M. Mostafavi, H. Remita, J.-L. Marignier, M.-O. Delcourt, *New J. Chem.*, 22 (1998) 1239.
- [22] S. Chen, Y. Liu, G. Wu, *Nanotechnology*, 16 (2005) 2360.
- [23] H. Remita, M. Tréguer, J. Amblard, J. Belloni, J. Khatouri, *Z. Phys. D*, 40 (1997) 127.
- [24] M. Treguer, C. De Cointet, H. Remita, J. Khatouri, M. Mostafavi, J. Amblard, J. Belloni, R. De Keyzer, *J. Phys. Chem. B*, 102 (1998) 4310.
- [25] A. Abedini, A.R. Daud, M.A. Abdul Hamid, N. Kamil Othman, E. Saion, *Nanoscale Res. Lett.*, 8 (2013) 474.

- [26] M. Mirdamadi-Esfahani, M. Mostafavi, B. Keita, L. Nadjo, P. Kooyman, H. Remita, *Gold Bull.*, 43 (2010) 49.
- [27] S. Gasaymeh, S. Radiman, *Am. J. Applied Sci.*, 7 (2010) 892.
- [28] K. Torigoe, H. Remita, P. Beaunier, J. Belloni, *Radiat. Phys. Chem.*, 64 (2002) 215.
- [29] P.A. Yakabuskie, J.M. Joseph, P. Keech, G.A. Botton, D. Guzonos, J.C. Wren, *Phys. Chem. Chem. Phys.*, 13 (2011) 7167.
- [30] L.M. Alrehaily, J.M. Joseph, M.C. Biesinger, D. Guzonas, J.C. Wren, *Phys. Chem. Chem. Phys.*, 15 (2013) 1014.
- [31] L.M. Alrehaily, J.M. Joseph, A.Y. Musa, D.A. Guzonas, J.C. Wren, *Phys. Chem. Chem. Phys.*, 15 (2013) 98.
- [32] M. Von Piechowski, M.-A. Thelen, J. Hoigné, R. E. Bühler, *Berichte der Bunsengesellschaft für Phys. Chemie*, 96 (1992) 1448.
- [33] M. Schuchmann, C. Von Sonntag, *J. Phys. Chem.*, 83 (1979) 780.
- [34] J.M. Joseph, B.S. Choi, P.A. Yakabuskie, J.C. Wren, *Radiat. Phys. Chem.*, 77 (2008) 1009.
- [35] T. Shigematsu, S. Gohad, H. Yamazaki, Y. Nishikawa, *Bull. Inst. Chem. Res., Kyoto Univ.*, 55 (1977) 55.
- [36] W. Kunerth, *Phys. Rev.*, 19 (1922) 512.
- [37] M. Biesinger, B. Payne, A. Grosvenor, L. Lau, A. Gerson, R. Smart, *Appl. Surf. Sci.*, 257 (2011) 2717.
- [38] F. Djouider, M.S. Aljohani, *J. Radioanal. Nucl. Chem.*, 2010, 285, 417.
- [39] J.C. Wren, J.M. Ball, *Rad. Phys. Chem.*, 60 (2001) 577.

- [40] P. Driver, G. Glowa, J.C. Wren, *Rad. Phys. Chem.*, 57 (2000) 37.
- [41] J.C. Wren, G.A. Glowa, *Rad. Phys. Chem.*, 58 (2000) 341.
- [42] P. Atkins, J. de Paula, (7<sup>th</sup> ED). *Atkins' Physical Chemistry*, Oxford University Press Inc., New York, 2002.
- [43] C.F. Baes, R.E. Mesmer (2<sup>nd</sup> ED). *Hydrolysis of Cations*, Krieger Pub. Co. Malabar, Florida, 1986.

## Chapter 7

### Summary and Future Work

#### 7.1 SUMMARY

This thesis examined radiation-induced colloid formation. The study showed that radiolysis of dilute cobalt and chromium solutions can produce highly uniform, nanometer-sized particles. The process for particle formation can involve either oxidation or reduction driven by water radiolysis products. The particle formation mechanism depends on the different solubilities of the particular metal oxide/hydroxides and the redox potentials of the metal ions. In both metal systems, the nanoscale particles that are formed have uniform and narrow size distributions. By understanding the physical and chemical factors controlling particle formation there is a potential to tailor a practical method of synthesizing nanoparticles.

Nanometer sized  $\text{Co}_3\text{O}_4$  particles were synthesized by the  $\gamma$ -irradiation of aerated  $\text{CoSO}_4$  solutions at a dose rate of  $5.5 \text{ kGy}\cdot\text{h}^{-1}$ . At pH 6.0, no particles could be made and there was no oxidation of  $\text{Co}^{\text{II}}$  to  $\text{Co}^{\text{III}}$ . At pH 10.6, the  $\text{Co}^{\text{II}}$  is converted to  $\text{Co}^{\text{III}}$  with the reaction reaching completion after about 150 min of irradiation and particles were formed. Analysis showed the presence of two types of particles having very different sizes: larger particles of  $\sim 200 \text{ nm}$  in width and having a thin hexagonal shape, and smaller spherical particles with sizes 8–20 nm. With an increase in irradiation time, the larger particles convert into smaller particles. These smaller spherical particles were determined to be  $\text{Co}_3\text{O}_4$  using Raman spectroscopy and XPS.

The XPS results analysis showed that the fraction of  $\text{Co}(\text{OH})_2$  in a particle decreases with irradiation time while the fraction of  $\text{Co}_3\text{O}_4$  increases. The fraction of the particle that is an intermediate species,  $\text{CoOOH}$ , initially increases with time, reaches a maximum at  $\sim 50$  min, and then decreases. The particles collected from solutions irradiated for long times ( $> 300$  min) contain only  $\text{Co}_3\text{O}_4$ . These results show that the particles evolve and become more fully oxidized with irradiation time.

A mechanism was proposed for the radiation-induced  $\text{Co}_3\text{O}_4$  nanoparticle formation. The homogeneous radiolytic oxidation of dissolved  $\text{Co}^{\text{II}}$  is slow due to the higher oxidation potential for  $\text{Co}^{\text{II}}$ . However, some  $\text{Co}(\text{OH})_2$  formed by hydrolysis of dissolved  $\text{Co}^{\text{II}}$  can spontaneously condense with some  $\text{Co}(\text{OH})_3$  formed by the homogeneous oxidation to provide nucleation sites for the nanoparticle growth. This condensation cannot occur at pHs where the solubility of  $\text{Co}(\text{OH})_2$  is high. Hence no particle formation was seen in solutions with pH 6.0. At pH 10.6 the solubility of  $\text{Co}(\text{OH})_2$  is much lower and the co-condensation can occur. Exposure of the cobalt solution to  $\gamma$ -irradiation leads to the production of redox active water radiolysis products and particularly  $\bullet\text{OH}$  and  $\text{H}_2\text{O}_2$ . The heterogeneous oxidation of the  $\text{Co}^{\text{II}}$  adsorbed on the nucleates by these species can oxidize the  $\text{Co}(\text{OH})_2$  to form  $\text{CoOOH}$ . The formation of  $\text{CoOOH}$  stabilizes the particle nuclei since  $\text{CoOOH}$  is nearly insoluble at pH 10.6. At longer times the  $\text{CoOOH}$  then reacts with  $\text{Co}(\text{OH})_2$  to form  $\text{Co}_3\text{O}_4$  in a process that is coupled with the reduction and oxidation of  $\text{H}_2\text{O}_2$  (Fenton-like reaction).

The  $\text{Co}_3\text{O}_4$  nanoparticle formation from  $\gamma$ -irradiation of  $\text{CoSO}_4$  solution was also investigated in the presence of radical scavengers, *t*-butanol, nitrous oxide and dissolved oxygen. The concentrations of  $\text{Co}^{\text{II}}$  and  $\text{Co}^{\text{III}}$  species in the system and the chemical

composition and sizes of particles that were formed were measured as a function of irradiation time. The size of the particles formed depends on the scavenging environment and follows the following order: 8–20 nm in the aerated only solutions, 10–30 nm in the aerated with 0.1 mM *t*-butanol solutions and 60–80 nm in the N<sub>2</sub>O/Ar purged solutions.

A mechanism for the radiation-induced particle formation was proposed that is consistent with the observed effects of the scavengers on the kinetics of oxidation of Co<sup>II</sup> and the sizes of the Co<sub>3</sub>O<sub>4</sub> nanoparticles that are formed. The cobalt oxidation occurs in three stages: Stage 1 involves the oxidation of Co<sup>2+</sup>(aq) to Co<sup>3+</sup>(aq) in solution followed by spontaneous condensation of Co<sup>II</sup>Co<sup>III</sup>(OH)<sub>x</sub> nucleation particles; in Stage 2 the Co<sup>II</sup> species continues to adsorb onto the condensation nuclei as Co(OH)<sub>2</sub> and oxidize to CoOOH(s); and Stage 3 involves the solid-state conversion of Co(OH)<sub>2</sub>(s) and CoOOH(s) to form Co<sub>3</sub>O<sub>4</sub>(s) particles. A radical scavenger in solution can affect the kinetics of particle formation and growth depending on the water radical that it removes.

The different particle sizes observed in different scavenging environments are attributed to different rates of oxidation of Co(OH)<sub>2</sub>(s) to CoOOH(s). The final size of Co<sub>3</sub>O<sub>4</sub> nanoparticles formed is larger in N<sub>2</sub>O/Ar purged solutions than in aerated only solutions. The size of the nanoparticles in the aerated solutions with 0.1 M *t*-butanol added is in-between. This study shows how steady-state water radiolysis kinetics, hydrolysis and phase equilibria of cobalt ions and oxide species are linked. It also shows how appropriate adjustment of solution conditions and radical scavenger concentrations can be used to produce Co<sub>3</sub>O<sub>4</sub> nanoparticles with tailored sizes.

Nanoscale chromium (III) oxide particles were synthesized by  $\gamma$ -radiolysis of deaerated Cr<sup>VI</sup> solutions (CrO<sub>4</sub><sup>2-</sup> or Cr<sub>2</sub>O<sub>7</sub><sup>2-</sup>) at pHs 6.0, 8.5 and 10.6. The reduction of

soluble  $\text{Cr}^{\text{VI}}$  to insoluble  $\text{Cr}(\text{OH})_3$  by the hydrated electron ( $\bullet e_{\text{aq}}^-$ ), a powerful reducing agent, leads to the particle formation. The rate of  $\text{Cr}^{\text{VI}}$  to  $\text{Cr}^{\text{III}}$  reduction was determined using the diphenyl carbazide method to measure the concentrations of those species in solution as a function of irradiation time. Two stages are clearly observed in the reduction process. In Stage 1 there is a fast linear decrease in the  $\text{Cr}^{\text{VI}}$  concentration with time. This is associated with a corresponding linear increase in the concentration of  $\text{Cr}^{\text{III}}$  with time. In Stage 2 (after ~30 min) most of the  $\text{Cr}^{\text{VI}}$  has been converted to  $\text{Cr}^{\text{III}}$  and the system trends towards steady state.

The FTIR spectra of the particles formed match the reference spectrum of  $\text{Cr}(\text{OH})_3$ . The particle chemistry could be altered by post-formation treatment by washing and heating. Data obtained by XPS show that washed particles contain a high fraction of  $\text{Cr}(\text{OH})_3$  (72.9%) and less  $\text{Cr}_2\text{O}_3$  (18.5%). However heating of these particles removes adsorbed water from the particles and converts the  $\text{Cr}(\text{OH})_3$  to  $\text{Cr}_2\text{O}_3$  (98.6%). The average size of the particles produced were nearly independent of the solution pH.

The mechanism for the radiation-induced formation of  $\text{Cr}_2\text{O}_3$  particle occurs in two stages. Stage 1 involves the homogeneous aqueous reduction of  $\text{Cr}^{\text{VI}}$  to  $\text{Cr}^{\text{III}}$  by  $\bullet e_{\text{aq}}^-$ . Growth of the particles occurs slowly during this phase by agglomeration of  $\text{Cr}(\text{OH})_3$  that is governed by the Brownian motion. In Stage 2, most of the initial  $\text{Cr}^{\text{VI}}$  has been converted to  $\text{Cr}(\text{OH})_3$  and this continues to condense onto the particle nuclei. As the  $\text{Cr}(\text{OH})_3$  particles grow, the interior of the particle dehydrates to form  $\text{Cr}_2\text{O}_3$  while the outer layer remains hydrated. The dehydration rate is very slow since  $\text{Cr}(\text{OH})_3$  is a relatively stable phase. In Stage 2, the redox reactions on the particle surface reach an equilibrium with both  $\text{Cr}^{\text{III}}$  oxidation by  $\bullet\text{OH}$  and  $\text{H}_2\text{O}_2$  and  $\text{Cr}^{\text{VI}}$  reduction by  $\bullet e_{\text{aq}}^-$  and

H<sub>2</sub>O<sub>2</sub> occurring. The particle size distribution is determined by the steady-state redox conditions at the water-solid interface.

The synthesis of Cr<sub>2</sub>O<sub>3</sub> nanoparticles by gamma irradiation of CrO<sub>4</sub><sup>2-</sup> solutions was also investigated in presence of radical scavengers, *t*-butanol, nitrous oxide and dissolved oxygen. As for the chromium system, a mechanism was proposed that is consistent with the observed effects of scavengers on the kinetics of reduction of Cr<sup>VI</sup> in solution to solid Cr<sup>III</sup> and the final sizes of Cr<sub>2</sub>O<sub>3</sub> nanoparticles that are formed. The chromium reduction occurs in three stages. Stage 1 involves homogeneous aqueous reduction of Cr<sup>VI</sup>(aq) to Cr<sup>III</sup>(aq) followed by spontaneous condensation of Cr(OH)<sub>3</sub>, providing nucleation sites onto which Cr<sup>VI</sup> and Cr<sup>III</sup> co-precipitate and form mixed Cr<sup>VI</sup>/Cr<sup>III</sup> oxide/hydroxide particles. In Stage 2 the aqueous reduction of Cr<sup>VI</sup>(aq) and Cr<sup>III</sup>(aq) reaches steady state but the adsorption of Cr<sup>VI</sup> continues, growing the mixed Cr<sup>VI</sup>/Cr<sup>III</sup> oxide/hydroxide particles. Stage 3 involves the solid-state conversion of Cr<sup>VI</sup> and Cr<sup>III</sup> and the particles slowly convert from mixed Cr<sup>VI</sup>/Cr<sup>III</sup> oxide/hydroxide to Cr(OH)<sub>3</sub> and then to Cr<sub>2</sub>O<sub>3</sub>. The nature of the radical scavenger in solution affects the kinetics of particle formation and growth in different stages differently.

## 7.2 FUTURE WORK

This research has demonstrated that  $\gamma$ -irradiation of cobalt and chromium solutions under the appropriate conditions can be used to form nano-scale particles. The work has laid the groundwork for understanding how this process occurs and how it can be controlled by choices of solution pH, cover gas, metal ion concentration and radical scavenger additives. However, the nanoparticle formation studies were limited to only



two transition metals, chromium and cobalt, considered separately. A more interesting target for future work would be a study of the synthesis of mixed metals oxide nanoparticles. Mixed oxides, such as  $\text{CoCr}_2\text{O}_4$  and  $\text{FeCr}_2\text{O}_4$ , are found naturally as products of the corrosion of industrial alloys. The radiolytic formation of such mixed metal, insoluble oxide particles is a particular concern of water-cooled nuclear reactors. In addition, studies of more complex systems can lead to more general understanding of the colloid formation in transition metal systems.

There are growing applications for the use of nano-scale particles that are tailored for size and chemical composition. Radiation-induced particle formation is a new process that offers an improved route to such particle formation. Exploring and exploiting this process requires more information and understanding on how other transition metals and mixtures of metals can be combined and treated to yield particles of value and utility.

Appendix A.

## **Copyrights**

## ELSEVIER LICENSE TERMS AND CONDITIONS

Jan 22, 2015

This is a License Agreement between Leena M Alrehaily ("You") and Elsevier ("Elsevier") provided by Copyright Clearance Center ("CCC"). The license consists of your order details, the terms and conditions provided by Elsevier, and the payment terms and conditions.

**All payments must be made in full to CCC. For payment instructions, please see information listed at the bottom of this form.**

Supplier	Elsevier Limited The Boulevard, Langford Lane Kidlington, Oxford, OX5 1GB, UK
Registered Company Number	1982084
Customer name	Leena M Alrehaily
Customer address	
License number	3554300286870
License date	Jan 22, 2015
Licensed content publisher	Elsevier
Licensed content publication	Radiation Physics and Chemistry
Licensed content title	A combined experimental and model analysis on the effect of pH and O <sub>2</sub> (aq) on $\gamma$ -radiolytically produced H <sub>2</sub> and H <sub>2</sub> O <sub>2</sub>
Licensed content author	Jiju M. Joseph, Byung Seon Choi, Pam Yakabuskie, J. Clara Wren
Licensed content date	September 2008
Licensed content volume number	77
Licensed content issue number	9
Number of pages	12
Start Page	1009
End Page	1020
Type of Use	reuse in a thesis/dissertation
Portion	figures/tables/illustrations
Number of figures/tables/illustrations	1
Format	both print and electronic

Are you the author of this Elsevier article?	No
Will you be translating?	No
Original figure numbers	2
Title of your thesis/dissertation	GAMMA-RADIATION INDUCED REDOX REACTIONS AND COLLOIDAL FORMATION OF CHROMIUM AND COBALT OXIDE NANOPARTICLES
Expected completion date	Jan 2015
Estimated size (number of pages)	220
Elsevier VAT number	GB 494 6272 12
Permissions price	0.00 USD
VAT/Local Sales Tax	0.00 USD / 0.00 GBP
Total	0.00 USD

Terms and Conditions

## INTRODUCTION

1. The publisher for this copyrighted material is Elsevier. By clicking "accept" in connection with completing this licensing transaction, you agree that the following terms and conditions apply to this transaction (along with the Billing and Payment terms and conditions established by Copyright Clearance Center, Inc. ("CCC"), at the time that you opened your Rightslink account and that are available at any time at <http://myaccount.copyright.com>).

## GENERAL TERMS

2. Elsevier hereby grants you permission to reproduce the aforementioned material subject to the terms and conditions indicated.

3. Acknowledgement: If any part of the material to be used (for example, figures) has appeared in our publication with credit or acknowledgement to another source, permission must also be sought from that source. If such permission is not obtained then that material may not be included in your publication/copies. Suitable acknowledgement to the source must be made, either as a footnote or in a reference list at the end of your publication, as follows:

“Reprinted from Publication title, Vol /edition number, Author(s), Title of article / title of chapter, Pages No., Copyright (Year), with permission from Elsevier [OR APPLICABLE SOCIETY COPYRIGHT OWNER].” Also Lancet special credit - “Reprinted from The Lancet, Vol. number, Author(s), Title of article, Pages No., Copyright (Year), with permission from Elsevier.”

4. Reproduction of this material is confined to the purpose and/or media for which

permission is hereby given.

5. **Altering/Modifying Material: Not Permitted.** However figures and illustrations may be altered/adapted minimally to serve your work. Any other abbreviations, additions, deletions and/or any other alterations shall be made only with prior written authorization of Elsevier Ltd. (Please contact Elsevier at [permissions@elsevier.com](mailto:permissions@elsevier.com))

6. If the permission fee for the requested use of our material is waived in this instance, please be advised that your future requests for Elsevier materials may attract a fee.

7. **Reservation of Rights:** Publisher reserves all rights not specifically granted in the combination of (i) the license details provided by you and accepted in the course of this licensing transaction, (ii) these terms and conditions and (iii) CCC's Billing and Payment terms and conditions.

8. **License Contingent Upon Payment:** While you may exercise the rights licensed immediately upon issuance of the license at the end of the licensing process for the transaction, provided that you have disclosed complete and accurate details of your proposed use, no license is finally effective unless and until full payment is received from you (either by publisher or by CCC) as provided in CCC's Billing and Payment terms and conditions. If full payment is not received on a timely basis, then any license preliminarily granted shall be deemed automatically revoked and shall be void as if never granted. Further, in the event that you breach any of these terms and conditions or any of CCC's Billing and Payment terms and conditions, the license is automatically revoked and shall be void as if never granted. Use of materials as described in a revoked license, as well as any use of the materials beyond the scope of an unrevoked license, may constitute copyright infringement and publisher reserves the right to take any and all action to protect its copyright in the materials.

9. **Warranties:** Publisher makes no representations or warranties with respect to the licensed material.

10. **Indemnity:** You hereby indemnify and agree to hold harmless publisher and CCC, and their respective officers, directors, employees and agents, from and against any and all claims arising out of your use of the licensed material other than as specifically authorized pursuant to this license.

11. **No Transfer of License:** This license is personal to you and may not be sublicensed, assigned, or transferred by you to any other person without publisher's written permission.

12. **No Amendment Except in Writing:** This license may not be amended except in a writing signed by both parties (or, in the case of publisher, by CCC on publisher's behalf).

13. **Objection to Contrary Terms:** Publisher hereby objects to any terms contained in any purchase order, acknowledgment, check endorsement or other writing prepared by you, which terms are inconsistent with these terms and conditions or CCC's Billing and

Payment terms and conditions. These terms and conditions, together with CCC's Billing and Payment terms and conditions (which are incorporated herein), comprise the entire agreement between you and publisher (and CCC) concerning this licensing transaction. In the event of any conflict between your obligations established by these terms and conditions and those established by CCC's Billing and Payment terms and conditions, these terms and conditions shall control.

14. **Revocation:** Elsevier or Copyright Clearance Center may deny the permissions described in this License at their sole discretion, for any reason or no reason, with a full refund payable to you. Notice of such denial will be made using the contact information provided by you. Failure to receive such notice will not alter or invalidate the denial. In no event will Elsevier or Copyright Clearance Center be responsible or liable for any costs, expenses or damage incurred by you as a result of a denial of your permission request, other than a refund of the amount(s) paid by you to Elsevier and/or Copyright Clearance Center for denied permissions.

### LIMITED LICENSE

The following terms and conditions apply only to specific license types:

15. **Translation:** This permission is granted for non-exclusive world **English** rights only unless your license was granted for translation rights. If you licensed translation rights you may only translate this content into the languages you requested. A professional translator must perform all translations and reproduce the content word for word preserving the integrity of the article. If this license is to re-use 1 or 2 figures then permission is granted for non-exclusive world rights in all languages.

16. **Posting licensed content on any Website:** The following terms and conditions apply as follows: Licensing material from an Elsevier journal: All content posted to the web site must maintain the copyright information line on the bottom of each image; A hyper-text must be included to the Homepage of the journal from which you are licensing at <http://www.sciencedirect.com/science/journal/xxxxx> or the Elsevier homepage for books at <http://www.elsevier.com>; Central Storage: This license does not include permission for a scanned version of the material to be stored in a central repository such as that provided by Heron/XanEdu.

Licensing material from an Elsevier book: A hyper-text link must be included to the Elsevier homepage at <http://www.elsevier.com>. All content posted to the web site must maintain the copyright information line on the bottom of each image.

**Posting licensed content on Electronic reserve:** In addition to the above the following clauses are applicable: The web site must be password-protected and made available only to bona fide students registered on a relevant course. This permission is granted for 1 year only. You may obtain a new license for future website posting.

**17. For journal authors:** the following clauses are applicable in addition to the above: Permission granted is limited to the author accepted manuscript version\* of your paper.

**\*Accepted Author Manuscript (AAM) Definition:** An accepted author manuscript (AAM) is the author's version of the manuscript of an article that has been accepted for publication and which may include any author-incorporated changes suggested through the processes of submission processing, peer review, and editor-author communications. AAMs do not include other publisher value-added contributions such as copy-editing, formatting, technical enhancements and (if relevant) pagination.

You are not allowed to download and post the published journal article (whether PDF or HTML, proof or final version), nor may you scan the printed edition to create an electronic version. A hyper-text must be included to the Homepage of the journal from which you are licensing at <http://www.sciencedirect.com/science/journal/xxxxx>. As part of our normal production process, you will receive an e-mail notice when your article appears on Elsevier's online service ScienceDirect ([www.sciencedirect.com](http://www.sciencedirect.com)). That e-mail will include the article's Digital Object Identifier (DOI). This number provides the electronic link to the published article and should be included in the posting of your personal version. We ask that you wait until you receive this e-mail and have the DOI to do any posting.

**18. Posting to a repository:** Authors may post their AAM immediately to their employer's institutional repository for internal use only and may make their manuscript publically available after the journal-specific embargo period has ended.

Please also refer to [Elsevier's Article Posting Policy](#) for further information.

**19. For book authors** the following clauses are applicable in addition to the above: Authors are permitted to place a brief summary of their work online only.. You are not allowed to download and post the published electronic version of your chapter, nor may you scan the printed edition to create an electronic version. **Posting to a repository:** Authors are permitted to post a summary of their chapter only in their institution's repository.

**20. Thesis/Dissertation:** If your license is for use in a thesis/dissertation your thesis may be submitted to your institution in either print or electronic form. Should your thesis be published commercially, please reapply for permission. These requirements include permission for the Library and Archives of Canada to supply single copies, on demand, of the complete thesis and include permission for Proquest/UMI to supply single copies, on demand, of the complete thesis. Should your thesis be published commercially, please reapply for permission.

### **Elsevier Open Access Terms and Conditions**

Elsevier publishes Open Access articles in both its Open Access journals and via its Open

Access articles option in subscription journals.

Authors publishing in an Open Access journal or who choose to make their article Open Access in an Elsevier subscription journal select one of the following Creative Commons user licenses, which define how a reader may reuse their work: Creative Commons Attribution License (CC BY), Creative Commons Attribution – Non Commercial - ShareAlike (CC BY NC SA) and Creative Commons Attribution – Non Commercial – No Derivatives (CC BY NC ND)

### **Terms & Conditions applicable to all Elsevier Open Access articles:**

Any reuse of the article must not represent the author as endorsing the adaptation of the article nor should the article be modified in such a way as to damage the author's honour or reputation.

The author(s) must be appropriately credited.

If any part of the material to be used (for example, figures) has appeared in our publication with credit or acknowledgement to another source it is the responsibility of the user to ensure their reuse complies with the terms and conditions determined by the rights holder.

### **Additional Terms & Conditions applicable to each Creative Commons user license:**

**CC BY:** You may distribute and copy the article, create extracts, abstracts, and other revised versions, adaptations or derivative works of or from an article (such as a translation), to include in a collective work (such as an anthology), to text or data mine the article, including for commercial purposes without permission from Elsevier

**CC BY NC SA:** For non-commercial purposes you may distribute and copy the article, create extracts, abstracts and other revised versions, adaptations or derivative works of or from an article (such as a translation), to include in a collective work (such as an anthology), to text and data mine the article and license new adaptations or creations under identical terms without permission from Elsevier

**CC BY NC ND:** For non-commercial purposes you may distribute and copy the article and include it in a collective work (such as an anthology), provided you do not alter or modify the article, without permission from Elsevier

Any commercial reuse of Open Access articles published with a CC BY NC SA or CC BY NC ND license requires permission from Elsevier and will be subject to a fee.

Commercial reuse includes:

- Promotional purposes (advertising or marketing)



- Commercial exploitation ( e.g. a product for sale or loan)
- Systematic distribution (for a fee or free of charge)

Please refer to [Elsevier's Open Access Policy](#) for further information.

## 21. Other Conditions:

v1.7

## ROYAL SOCIETY OF CHEMISTRY LICENSE TERMS AND CONDITIONS

Jan 26, 2015

This is a License Agreement between Leena M Alrehaily ("You") and Royal Society of Chemistry ("Royal Society of Chemistry") provided by Copyright Clearance Center ("CCC"). The license consists of your order details, the terms and conditions provided by Royal Society of Chemistry, and the payment terms and conditions.

**All payments must be made in full to CCC. For payment instructions, please see information listed at the bottom of this form.**

License Number	3556530863016
License date	Jan 26, 2015
Licensed content publisher	Royal Society of Chemistry
Licensed content publication	Physical Chemistry Chemical Physics
Licensed content title	Iron oxyhydroxide colloid formation by gamma-radiolysis
Licensed content author	P. A. Yakabuskie,J. M. Joseph,P. Keech,G. A. Botton,D. Guzonas,J. C. Wren
Licensed content date	Mar 11, 2011
Volume number	13
Issue number	15
Type of Use	Thesis/Dissertation
Requestor type	academic/educational
Portion	figures/tables/images
Number of figures/tables/images	1
Format	print and electronic
Distribution quantity	10000
Will you be translating?	no
Order reference number	None
Title of the thesis/dissertation	GAMMA-RADIATION INDUCED REDOX REACTIONS AND COLLOIDAL FORMATION OF CHROMIUM AND COBALT OXIDE NANOPARTICLES
Expected completion date	Jan 2015
Estimated size	220
Total	0.00 USD

## Terms and Conditions

This License Agreement is between {Requestor Name} ("You") and The Royal Society of Chemistry ("RSC") provided by the Copyright Clearance Center ("CCC"). The license consists of your order details, the terms and conditions provided by the Royal Society of Chemistry, and the payment terms and conditions.

## RSC / TERMS AND CONDITIONS

### INTRODUCTION

The publisher for this copyrighted material is The Royal Society of Chemistry. By clicking "accept" in connection with completing this licensing transaction, you agree that the following terms and conditions apply to this transaction (along with the Billing and Payment terms and conditions established by CCC, at the time that you opened your RightsLink account and that are available at any time at .

### LICENSE GRANTED

The RSC hereby grants you a non-exclusive license to use the aforementioned material anywhere in the world subject to the terms and conditions indicated herein. Reproduction of the material is confined to the purpose and/or media for which permission is hereby given.

### RESERVATION OF RIGHTS

The RSC reserves all rights not specifically granted in the combination of (i) the license details provided by your and accepted in the course of this licensing transaction; (ii) these terms and conditions; and (iii) CCC's Billing and Payment terms and conditions.

### REVOCATION

The RSC reserves the right to revoke this license for any reason, including, but not limited to, advertising and promotional uses of RSC content, third party usage, and incorrect source figure attribution.

### THIRD-PARTY MATERIAL DISCLAIMER

If part of the material to be used (for example, a figure) has appeared in the RSC publication with credit to another source, permission must also be sought from that source. If the other source is another RSC publication these details should be included in your RightsLink request. If the other source is a third party, permission must be obtained from the third party. The RSC disclaims any responsibility for the reproduction you make of items owned by a third party.

### PAYMENT OF FEE

If the permission fee for the requested material is waived in this instance, please be advised that any future requests for the reproduction of RSC materials may attract a fee.

### ACKNOWLEDGEMENT

The reproduction of the licensed material must be accompanied by the following acknowledgement:

Reproduced (“Adapted” or “in part”) from {Reference Citation} (or Ref XX) with permission of The Royal Society of Chemistry.

If the licensed material is being reproduced from New Journal of Chemistry (NJC), Photochemical & Photobiological Sciences (PPS) or Physical Chemistry Chemical Physics (PCCP) you must include one of the following acknowledgements:

For figures originally published in NJC:

Reproduced (“Adapted” or “in part”) from {Reference Citation} (or Ref XX) with permission of The Royal Society of Chemistry (RSC) on behalf of the European Society for Photobiology, the European Photochemistry Association and the RSC.

For figures originally published in PPS:

Reproduced (“Adapted” or “in part”) from {Reference Citation} (or Ref XX) with permission of The Royal Society of Chemistry (RSC) on behalf of the Centre National de la Recherche Scientifique (CNRS) and the RSC.

For figures originally published in PCCP:

Reproduced (“Adapted” or “in part”) from {Reference Citation} (or Ref XX) with permission of the PCCP Owner Societies.

#### **HYPertext LINKS**

With any material which is being reproduced in electronic form, you must include a hypertext link to the original RSC article on the RSC’s website. The recommended form for the hyperlink is <http://dx.doi.org/10.1039/DOI suffix>, for example in the link <http://dx.doi.org/10.1039/b110420a> the DOI suffix is ‘b110420a’. To find the relevant DOI suffix for the RSC article in question, go to the Journals section of the website and locate the article in the list of papers for the volume and issue of your specific journal. You will find the DOI suffix quoted there.

#### **LICENSE CONTINGENT ON PAYMENT**

While you may exercise the rights licensed immediately upon issuance of the license at the end of the licensing process for the transaction, provided that you have disclosed complete and accurate details of your proposed use, no license is finally effective unless and until full payment is received from you (by CCC) as provided in CCC's Billing and Payment terms and conditions. If full payment is not received on a timely basis, then any license preliminarily granted shall be deemed automatically revoked and shall be void as if never granted. Further, in the event that you breach any of these terms and conditions or any of CCC's Billing and Payment terms and conditions, the license is automatically revoked and shall be void as if never granted.

Use of materials as described in a revoked license, as well as any use of the materials beyond the scope of an unrevoked license, may constitute copyright infringement and the RSC reserves the right to take any and all action to protect its copyright in the materials.

#### WARRANTIES

The RSC makes no representations or warranties with respect to the licensed material.

#### INDEMNITY

You hereby indemnify and agree to hold harmless the RSC and the CCC, and their respective officers, directors, trustees, employees and agents, from and against any and all claims arising out of your use of the licensed material other than as specifically authorized pursuant to this licence.

#### NO TRANSFER OF LICENSE

This license is personal to you or your publisher and may not be sublicensed, assigned, or transferred by you to any other person without the RSC's written permission.

#### NO AMENDMENT EXCEPT IN WRITING

This license may not be amended except in a writing signed by both parties (or, in the case of "Other Conditions, v1.2", by CCC on the RSC's behalf).

#### OBJECTION TO CONTRARY TERMS

You hereby acknowledge and agree that these terms and conditions, together with CCC's Billing and Payment terms and conditions (which are incorporated herein), comprise the entire agreement between you and the RSC (and CCC) concerning this licensing transaction, to the exclusion of all other terms and conditions, written or verbal, express or implied (including any terms contained in any purchase order, acknowledgment, check endorsement or other writing prepared by you). In the event of any conflict between your obligations established by these terms and conditions and those established by CCC's Billing and Payment terms and conditions, these terms and conditions shall control.

#### JURISDICTION

This license transaction shall be governed by and construed in accordance with the laws of the District of Columbia. You hereby agree to submit to the jurisdiction of the courts located in the District of Columbia for purposes of resolving any disputes that may arise in connection with this licensing transaction.

#### LIMITED LICENSE

The following terms and conditions apply to specific license types:

##### Translation

This permission is granted for non-exclusive world English rights only unless your license was granted for translation rights. If you licensed translation rights you may

only translate this content into the languages you requested. A professional translator must perform all translations and reproduce the content word for word preserving the integrity of the article.

#### Intranet

If the licensed material is being posted on an Intranet, the Intranet is to be password-protected and made available only to bona fide students or employees only. All content posted to the Intranet must maintain the copyright information line on the bottom of each image. You must also fully reference the material and include a hypertext link as specified above.

#### Copies of Whole Articles

All copies of whole articles must maintain, if available, the copyright information line on the bottom of each page.

#### Other Conditions

v1.2

Gratis licenses (referencing \$0 in the Total field) are free. Please retain this printable license for your reference. No payment is required.

If you would like to pay for this license now, please remit this license along with your payment made payable to "COPYRIGHT CLEARANCE CENTER" otherwise you will be invoiced within 48 hours of the license date. Payment should be in the form of a check or money order referencing your account number and this invoice number {Invoice Number}.

Once you receive your invoice for this order, you may pay your invoice by credit card.

Please follow instructions provided at that time.

**ROYAL SOCIETY OF CHEMISTRY LICENSE  
TERMS AND CONDITIONS**

Jan 29, 2015

---

This is a License Agreement between Leena M Alrehaily ("You") and Royal Society of Chemistry ("Royal Society of Chemistry") provided by Copyright Clearance Center ("CCC"). The license consists of your order details, the terms and conditions provided by Royal Society of Chemistry, and the payment terms and conditions.

**All payments must be made in full to CCC. For payment instructions, please see information listed at the bottom of this form.**

License Number	3554260658876
License date	Jan 22, 2015
Licensed content publisher	Royal Society of Chemistry
Licensed content publication	Physical Chemistry Chemical Physics
Licensed content title	Iron oxyhydroxide nanoparticles formed by forced hydrolysis: dependence of phase composition on solution concentration
Licensed content author	Dong Fu, Peter G. Keech, Xueliang Sun, J. Clara Wren
Licensed content date	Sep 22, 2011
Volume number	13
Issue number	41
Type of Use	Thesis/Dissertation
Requestor type	academic/educational
Portion	figures/tables/images
Number of figures/tables/images	1
Format	print and electronic
Distribution quantity	100
Will you be translating?	no
Order reference number	None
Title of the thesis/dissertation	GAMMA-RADIATION INDUCED REDOX REACTIONS AND COLLOIDAL FORMATION OF CHROMIUM AND COBALT OXIDE NANOPARTICLES
Expected completion date	Jan 2015
Estimated size	220
Total	0.00 CAD
Terms and Conditions	

This License Agreement is between {Requestor Name} ("You") and The Royal Society of Chemistry ("RSC") provided by the Copyright Clearance Center ("CCC"). The license consists of your order details, the terms and conditions provided by the Royal Society of Chemistry, and the payment terms and conditions.

## RSC / TERMS AND CONDITIONS

### INTRODUCTION

The publisher for this copyrighted material is The Royal Society of Chemistry. By clicking "accept" in connection with completing this licensing transaction, you agree that the following terms and conditions apply to this transaction (along with the Billing and Payment terms and conditions established by CCC, at the time that you opened your RightsLink account and that are available at any time at .

### LICENSE GRANTED

The RSC hereby grants you a non-exclusive license to use the aforementioned material anywhere in the world subject to the terms and conditions indicated herein. Reproduction of the material is confined to the purpose and/or media for which permission is hereby given.

### RESERVATION OF RIGHTS

The RSC reserves all rights not specifically granted in the combination of (i) the license details provided by your and accepted in the course of this licensing transaction; (ii) these terms and conditions; and (iii) CCC's Billing and Payment terms and conditions.

### REVOCAATION

The RSC reserves the right to revoke this license for any reason, including, but not limited to, advertising and promotional uses of RSC content, third party usage, and incorrect source figure attribution.

### THIRD-PARTY MATERIAL DISCLAIMER

If part of the material to be used (for example, a figure) has appeared in the RSC publication with credit to another source, permission must also be sought from that source. If the other source is another RSC publication these details should be included in your RightsLink request. If the other source is a third party, permission must be obtained from the third party. The RSC disclaims any responsibility for the reproduction you make of items owned by a third party.

### PAYMENT OF FEE

If the permission fee for the requested material is waived in this instance, please be advised that any future requests for the reproduction of RSC materials may attract a fee.

### ACKNOWLEDGEMENT

The reproduction of the licensed material must be accompanied by the following



acknowledgement:

Reproduced (“Adapted” or “in part”) from {Reference Citation} (or Ref XX) with permission of The Royal Society of Chemistry.

If the licensed material is being reproduced from New Journal of Chemistry (NJC), Photochemical & Photobiological Sciences (PPS) or Physical Chemistry Chemical Physics (PCCP) you must include one of the following acknowledgements:

For figures originally published in NJC:

Reproduced (“Adapted” or “in part”) from {Reference Citation} (or Ref XX) with permission of The Royal Society of Chemistry (RSC) on behalf of the European Society for Photobiology, the European Photochemistry Association and the RSC.

For figures originally published in PPS:

Reproduced (“Adapted” or “in part”) from {Reference Citation} (or Ref XX) with permission of The Royal Society of Chemistry (RSC) on behalf of the Centre National de la Recherche Scientifique (CNRS) and the RSC.

For figures originally published in PCCP:

Reproduced (“Adapted” or “in part”) from {Reference Citation} (or Ref XX) with permission of the PCCP Owner Societies.

#### HYPertext LINKS

With any material which is being reproduced in electronic form, you must include a hypertext link to the original RSC article on the RSC’s website. The recommended form for the hyperlink is <http://dx.doi.org/10.1039/DOI suffix>, for example in the link <http://dx.doi.org/10.1039/b110420a> the DOI suffix is ‘b110420a’. To find the relevant DOI suffix for the RSC article in question, go to the Journals section of the website and locate the article in the list of papers for the volume and issue of your specific journal. You will find the DOI suffix quoted there.

#### LICENSE CONTINGENT ON PAYMENT

While you may exercise the rights licensed immediately upon issuance of the license at the end of the licensing process for the transaction, provided that you have disclosed complete and accurate details of your proposed use, no license is finally effective unless and until full payment is received from you (by CCC) as provided in CCC’s Billing and Payment terms and conditions. If full payment is not received on a timely basis, then any license preliminarily granted shall be deemed automatically revoked and shall be void as if never granted. Further, in the event that you breach any of these terms and conditions or any of CCC’s Billing and Payment terms and conditions, the license is automatically revoked and shall be void as if never granted. Use of materials as described in a revoked license, as well as any use of the materials

beyond the scope of an unrevoked license, may constitute copyright infringement and the RSC reserves the right to take any and all action to protect its copyright in the materials.

#### WARRANTIES

The RSC makes no representations or warranties with respect to the licensed material.

#### INDEMNITY

You hereby indemnify and agree to hold harmless the RSC and the CCC, and their respective officers, directors, trustees, employees and agents, from and against any and all claims arising out of your use of the licensed material other than as specifically authorized pursuant to this licence.

#### NO TRANSFER OF LICENSE

This license is personal to you or your publisher and may not be sublicensed, assigned, or transferred by you to any other person without the RSC's written permission.

#### NO AMENDMENT EXCEPT IN WRITING

This license may not be amended except in a writing signed by both parties (or, in the case of "Other Conditions, v1.2", by CCC on the RSC's behalf).

#### OBJECTION TO CONTRARY TERMS

You hereby acknowledge and agree that these terms and conditions, together with CCC's Billing and Payment terms and conditions (which are incorporated herein), comprise the entire agreement between you and the RSC (and CCC) concerning this licensing transaction, to the exclusion of all other terms and conditions, written or verbal, express or implied (including any terms contained in any purchase order, acknowledgment, check endorsement or other writing prepared by you). In the event of any conflict between your obligations established by these terms and conditions and those established by CCC's Billing and Payment terms and conditions, these terms and conditions shall control.

#### JURISDICTION

This license transaction shall be governed by and construed in accordance with the laws of the District of Columbia. You hereby agree to submit to the jurisdiction of the courts located in the District of Columbia for purposes of resolving any disputes that may arise in connection with this licensing transaction.

#### LIMITED LICENSE

The following terms and conditions apply to specific license types:

##### Translation

This permission is granted for non-exclusive world English rights only unless your license was granted for translation rights. If you licensed translation rights you may only translate this content into the languages you requested. A professional translator

must perform all translations and reproduce the content word for word preserving the integrity of the article.

#### Intranet

If the licensed material is being posted on an Intranet, the Intranet is to be password-protected and made available only to bona fide students or employees only. All content posted to the Intranet must maintain the copyright information line on the bottom of each image. You must also fully reference the material and include a hypertext link as specified above.

#### Copies of Whole Articles

All copies of whole articles must maintain, if available, the copyright information line on the bottom of each page.

#### Other Conditions

v1.2

Gratis licenses (referencing \$0 in the Total field) are free. Please retain this printable license for your reference. No payment is required.

If you would like to pay for this license now, please remit this license along with your payment made payable to "COPYRIGHT CLEARANCE CENTER" otherwise you will be invoiced within 48 hours of the license date. Payment should be in the form of a check or money order referencing your account number and this invoice number {Invoice Number}.

Once you receive your invoice for this order, you may pay your invoice by credit card.

Please follow instructions provided at that time.



# Leena M. Alrehaily

## EDUCATION

---

- Jan. 2010 – Jan. 2014** Ph.D. candidate in physical chemistry, University of Western Ontario, London Ontario, Canada
- Sep. 2004 -Feb. 2007** M.Sc. Chemistry (Physical Chemistry), King Abdulaziz University, Jeddah, Kingdom of Saudi Arabia
- Sep. 1999-Aug. 2002** B.Sc. Chemistry, Taibah University (Girl College), Madinah, Kingdom of Saudi Arabia

## POSTERS, PRESENTATIONS & PUBLICATIONS

---

### PUBLISHED PAPERS

- **L.M. Alrehaily**, J.M. Joseph, M.C. Biesinger, D. A. Guzonas, J.C. Wren. Gamma-Radiolysis Assisted Cobalt Oxide Nanoparticles Formation. Phys. Chem. Chem. Phys., 2013,15, 1014
- **L.M. Alrehaily**, J.M. Joseph, A.Y. Musa, D. Guzonas, J.C. Wren. Gamma-Radiation induced Formation of Chromium oxide Nanoparticles from dissolved dichromate. Phys. Chem. Chem. Phys., 2013, 15,98

### ARTICLES PUBLISHED IN PEER-REVIEWED CONFERENCE PROCEEDINGS

- J.M. Joseph, **L.M. Alrehaily**, P.A. Yakabuskie, D.A. Guzonas and J.C. Wren, Radiation-Induced Nanoparticle Formation under Steady-State Radiolysis: Comparison of the Fe, Co and Cr Systems. 34<sup>th</sup> Annual Conference of the Canadian Nuclear Society, 2013.
- **L.M. Alrehaily**, J.M. Joseph, D.A. Guzonas and J.C. Wren, Formation of Chromium Oxide Nanoparticles by Gamma-Irradiation of dissolved Chromium Species. Nuclear Plant Chemistry Conference, 2012.
- J.M. Joseph, P.A. Yakabuskie, **L.M. Alrehaily**, P. Keech, D.A. Guzonas, and J.C.Wren. The Effect of Steady-State Water Radiolysis on Metal Ion Solubility.

Nuclear Plant Chemistry Conference, 2010.

#### POSTER AND PRESENTATION

- **L.M. Alrehaily**, J.M. Joseph and J.C. Wren, Radiolytic formation of Cr<sub>2</sub>O<sub>3</sub> nanoparticles: particle size control using tert-butanol. 35<sup>th</sup> Annual Canadian Nuclear Society Conference and 38th Annual CNS/CNA Student Conference, Vancouver, BC, August 24-28, 2014. (Poster)
- **L.M. Alrehaily**, J.M. Joseph and J.C. Wren, The Effect of •OH Scavenger on the Formation of cobalt oxide nanoparticles by gamma-radiolysis. 34<sup>th</sup> Annual Canadian Nuclear Society Conference and 37th Annual CNS/CNA Student Conference, Toronto, ON, June 9-12, 2013. (Poster)
- N. Yousefi, J.M. Joseph, **L.M. Alrehaily** and J.C. Wren, Effect of high temperature on the steady state radiolysis product behavior. 34<sup>th</sup> Annual Canadian Nuclear Society Conference and 37th Annual CNS/CNA Student Conference, Toronto, ON, June 9-12, 2013. (Poster)
- **L.M. Alrehaily**, J.M. Joseph, D.A. Guzonas and J.C. Wren, Formation of Chromium Oxide Nanoparticles by Gamma-Irradiation of dissolved Chromium Species. Nuclear Plant Chemistry Conference, Paris, France, September 24-28, 2012. (Poster)
- **L.M. Alrehaily**, J.M. Joseph, A.Y. Musa and J.C. Wren, Formation of Cobalt Oxide Nanoparticles by Gamma-Radiolysis. Gordon Research Conference on Radiation Chemistry and Radiation Driven Processes in Physics, Chemistry and Biology. Andover, NH, USA, July 28-August 3rd, 2012. (Poster)
- **L.M. Alrehaily**, J.M. Joseph, \*A.Y. Musa and J.C. Wren, Formation of Cobalt Oxide Nanoparticles by Gamma-Radiolysis. 33rd Annual Canadian Nuclear Society Conference and 36th Annual CNS/CNA Student Conference, Saskatoon,

SK, June 10-13, 2012. (Poster)

- **L.M. Alrehaily**, J.M. Joseph, and J.C. Wren, Formation of ChromiumOxide Nanoparticles by Gamma-Radiolysis. 32nd Annual Canadian Nuclear Society Conference and 35th Annual CNS/CNA Student Conference, Niagara Falls, ON, June 5-8, 2011. (Poster)
- J.M. Joseph, P.A. Yakabuskie, **L.M. Alrehaily**, P. Keech, D.A. Guzonas, and J.C. Wren. The Effect of Steady-State Water Radiolysis on Metal Ion Solubility. Nuclear Plant Chemistry Conference Quebec City, QC, October 3-7, 2010. (Poster)
- P.A. Yakabuskie, J.M. Joseph, **L.M. Alrehaily**, P. Keech, D.A. Guzonas, and J.C. Wren. The Effect of Steady-State Water Radiolysis on Metal Ion Solubility. Gordon Research Conference on Radiation Chemistry and Radiation Driven Processes in Physics, Chemistry and Biology. Andover, NH, USA, July 18- 23, 2010. (Poster)